4-2015

DEVELOPMENT OF A THERAPEUTIC MODEL OF EARLY LIVER CANCER USING CROCIN-COATED MAGNETITE NANOPARTICLES

Rkia El-Kharrag

United Arab Emirates University

College of Science

DEVELOPMENT OF A THERAPEUTIC MODEL OF EARLY LIVER CANCER USING CROCIN-COATED MAGNETITE NANOPARTICLES

Rkia El-kharrag

This dissertation is submitted in partial fulfilment of the requirements for the degree of Doctor of Philosophy

Under the Supervision of Professor Amr Amin

April 2015

Declaration of Original Work

I, Rkia El-Kharrag, the undersigned, a graduate student at the United Arab Emirates University (UAEU), and the author of this PhD dissertation, entitled "*Development of a Therapeutic Model of Early Liver Cancer Using Crocin-Coated Magnetite Nanoparticles*", hereby, solemnly declare that this dissertation is an original research work that has been done and prepared by me under the supervision of Dr. Amr Amin, in the College of Science at the UAEU. This work has not been previously formed as the basis for the award of any academic degree, diploma or a similar title at this or any other university. The materials borrowed from other sources and included in my dissertation have been properly cited and acknowledged.

Student's Signature _____ Date _____

Approval of the Doctorate Dissertation

This Doctorate Dissertation is approved by the following Examining Committee Members:

1) Advisor (Committee Chair): Amr Amin
   Title: Professor
   Department of Biology
   College of Science

   Signature _____ Date _____

2) Member: Yaser Greish

   Title: Associate Professor
   Department of Chemistry
   College of Science

   Signature _____ Date _____

3) Member: Sherif Karam
   Title: Professor
   Department of Anatomy
   College of Medicine and Health Sciences

   Signature _____ Date _____

4) Member (Internal Examiner): Ernest Adeghate
   Title: Professor
   Department of Anatomy
   College of Medicine and Health Sciences

   Signature _____ Date _____

5) Member (External Examiner): Lily Yang
   Title: Professor
   College: School of Medicine, Department of Surgery
   Institution: Emory University, Atlanta, USA

   Signature _____ Date _____

This Doctorate Dissertation is accepted by:

1) Dean, College of Science: Professor Frederick Chi-Ching Leung

   Signature:_____ Date: _____

2) Dean, College of the Graduate Studies: Professor Nagi T. Wakim

   Signature:_____ Date: _____

Copy _____ of _____

Abstract

Hepatocellular carcinoma is one of the most common health problems that is difficult to treat. As a result of the side effects frequently experienced with conventional cancer treatments, there has been a growing interest to develop controlled drug delivery system that can reduce the mortality rate of liver cancer patients and un-harm healthy tissues. Magnetite nanoparticles are potentially important in hepatocellular carcinoma treatment, since they can be used as delivery system. Pure and coated magnetite nanoparticles were synthesized via modified co-precipitation method in air at low temperature. Various reaction parameters and coating materials have been investigated and characterized. Among these parameters and coating materials, 1.0 % of dextran was selected as an optimum coating for nanoparticles using a slow feeding rate for the Fe^{2+}/Fe^{3+} reactants, maintaining the stirring and soaking temperatures at 60ºC. After that dextran-coated magnetite nanoparticles were bound to crocin, a pharmacologically active component of saffron, via cross-linker. Crocin alone has shown anti-cancer activity in different *in vitro* and *in vivo* settings by several studies. The aim of this study was to synthesize dextran-coated magnetite nanoparticles containing crocin with a higher therapeutic index for hepatocellular carcinoma treatment. The nanoparticles with crocin were tested *in vitro* and *in vivo* for their anti-cancer effects as compared to free crocin. HepG2 cells treated with crocin-dextran-coated magnetite nanoparticles showed a decrease in cell proliferation compared to control (non-treated cells) or to those treated with free crocin or dextran-coated nanoparticles. The anti-cancer activity of crocin-dextran-coated nanoparticles was also evaluated in Balb/c mice. These mice were injected with carcinogenic agent, diethylnitrosamine. Histological examination revealed several

precancerous changes. The immunohistochemical analysis using antibodies indication of cell proliferation (Ki-67), apoptosis (M30-Cytodeath and Bcl-2), inflammation (cyclooxygenase-2) and angiogenesis (vascular endothelial growth factor), indicated that magnetite nanoparticles conjugated with dextran plus crocin does indeed improve its anti-tumorigenic activity over free crocin. These results provide the basis for designing new modalities for treatment of liver cancer which could hopefully reduce its high mortality rate.

Keywords: Magnetite nanoparticles, dextran, precancerous changes, crocin, diethylnitrosamine, immunohistochemical studies.

Title and Abstract (in Arabic)

إنشاء نموذج لعلاج سرطان الكبد المبكر باستخدام جزيئات النانو الممغنطة و المغلفة بالكروسين (crocin)

الملخص

يعتبر سرطان الكبد من اكثر المشاكل الصحية شيوعا التي يصعب علاجها. ونتيجة لآثار الجانبية التي عادة ما تصاحب وسائل العلاج التقليدية للسرطان، فقد كان هناك اهتمام متزايد لتطوير نظام التحكم في توجيه وتوصيل الادوية إلى مكان السرطان التي يمكن أن تقلل من معدل الوفيات بسرطان الكبد ولا تحدث ضرر بالأنسجة السليمة. جزئيات النانو الممغنطة يمكن أن تكون مهمة لعلاج سرطان الكبد لما لها من دور في زيادة كفاءة توجيه وتوصيل الأدوية. تم تحضير جزئيات النانو الممغنطة النقية والمغلفة بطريقة خاصة ومعدلة في الهواء وفي درجة حرارة منخفضة. كما تم دراسة مختلف عوامل ومعايير التفاعل ومواد التغليف. ومن بين العديد من تلك المعايير ومواد التغليف، فقد اختير 1.0% من الديكستران (dextran) كالتلغليف الأمثل لجزيئات النانو باستخدام معدل تنزيل بطيء للحديد الثنائي والثلاثي مع الحفاظ على درجات حرارة التحريك والتنقيع في 60 درجة مئوية. وبعد ذلك تم تحضير جزيئات النانو الممغنطة والمغلفة بالديكستران و بالكروسين. الكروسين هو العقار النشط في نبات الزعفران. وقد أثبت الكروسين عند استخدامه بمفرده قدرته في مكافحة السرطان في مختلف التجارب المخبرية بواسطة العديد من الدراسات.

وكان الهدف من هذه الدراسة هو انتاج جزيئات النانو الممغنطة و المغلفة بالديكستران والتي تحتوي على الكروسين ودراسة قدرتها العلاجية لسرطان الكبد حيث تم اختبار قدرة جزيئات النانو مع الكروسين في المختبر. ولقد تم اختبار قدرة جزيئات النانو مع الكروسين في المختبر على مكافحة السرطان. و لوحظ أن الخلايا السرطانية للكبد (HepG2) تراجعت في تكاثرها بعد معالجتها بجزيئات النانو المغلفة بالديكستران و الكروسين مقارنة مع الخلايا الغير معالجة، أو الخلايا المعالجة بالكروسين بمفرده أو بجزيئات النانو المغلفة بالديكستران وبدون الكروسين. كما تم تقييم قدرة جزيئات النانو المغلفة بالديكستران و الكروسين على مكافحة السرطان في فئران التجارب (Balb/c). حيث تم حقنها بمادة مسرطنة (diethylnitrosamine) . وكشف الفحص النسيجي على تواجد العديد من التغيرات المصاحبة للمراحل الأولى من الاصابه بالسرطان. كما أشار التحليل الكيمياء النسيجي المناعي (immunohistochemical) باستخدام الأجسام المضادة المعنية بالتعرف على

عامل التكاثر الخلوي (Ki-67)، وعامل موت الخلايا المبرمج (M30-Cytodeath and Bcl-2) ، وعامل الالتهابات الخلوية (cyclooxygenase-2) وعامل نمو الأوعية الدموية الجديدة (vascular endothelial growth factor) إلى أن جزيئات النانو المغلفة بالديكستران والكروسين أظهرت تحسنا ملموسا في مكافحة السرطان مقارنة بالكروسين بمفرده. تمثل تلك النتائج الأساس لتصميم طرق جديدة لعلاج سرطان الكبد الذي نأمل في أن يساهم في خفض معدلات الوفيات المرتفعة لهذا المرض العضال.

الكلمات الرئيسية: جزيئات النانو الممغنطة، ديكستران، التغيرات المصاحبة للمراحل الأولى من الاصابة بالسرطان، كروسين، المادة المسرطنة diethylnitrosamine، دراسات التحليل الكيميائي النسيجي المناعي.

Acknowledgments

First and foremost I thank Allah for giving me strength and ability to accomplish my Ph.D. degree. I am thankful to the UAE University for giving me this opportunity and providing me with scholarship and funding my research. I am grateful to my supervisor Dr. Amr Amin for his guidance, assistance and encouragement during the years of my project. It has been an honour to be his first Ph.D. student.

My sincere appreciation to Dr. Yaser Afifi and Dr. Sherif Karam for giving me the opportunity to gain from their experience and knowledge, use their laboratories, as well as for their support and confidence in me. They both encouraged me to explore new ideas, answer my questions and never failed to support me and advice in times where I felt uncertain despite being very busy. In addition to academic knowledge, they taught me to maintain a positive attitude and passion for science and research. As Dr. Yaser always says" Be optimistic and look at the filled half of the cup, not at the empty one". If I ever have given a chance, I think Dr. Yaser's and Dr. Sherif's names deserve to be in the front page of my dissertation, because without their help throughout the years of my Ph.D. I could not achieve what I achieved today.

I would like to thank the laboratory members of Dr. Yaser and Dr. Sheirf. These members are Nuha, Mariem, Hesa, Najwa, Dina, Rony, Wafa, Prashanth, Sneha, Somuya and Sheikha. They have contributed to my personal and professional sides of my life, and have been a source of friendships as well as good advices, assistance and collaboration.

I would like to sincerely acknowledge my other committee members, Dr. Lily Yang and Dr. Ernest Adeghate for their time, cooperation, advice and feedback. My thanks are extended to Dr. Abdulmajeed Al Khajeh, Dr. Khaled Al Amiri, Dr. Naim Anwar, Dr. Waleed Hamza, Mohamed Shahid, Dr. Nagi Wakim, Luna Jahan and Amal Al Hassani for assisting me in various administration matters.

I am very thankful to Dr. Ramzi Mohamed, Dr. Asfar Azmi, Osama Alian, Amro Kamel and Dr. Joshua Reineke from Wayne State University for their kind welcome and help during my staying in the US back in 2012. Additionally, I would like to thank who ever helped and supported me during my Ph.D., including: Dr. Michel Conlon, Dr. Soleiman Hisaindee, Bassam Al Hindawi, Heba Abou- Khousa, Leena Al-Kaabi, Sheikha, Mariam Alkayoumi, Dr. Salman Ashraf, Dr. Thies Thieman, Abdeltawab Ali, Khawla, Dr. Mohamed Mousa, Dr. Asma Al Menhali, Dr. Taoufik Ksiksi, Dr. Mohamed Enan, Salwa, Dr. Loay Lubbad, Ahmed Taha, Osama Kayal, Saeed Taraq, Rai, Bacheir, Achaq, Saeed, Abdel Gadir Hago, Mansour Qureshi, Mohamed El-Haj, Yassir Mohamed, Dr. Nawal Osman, Mohamed Waseela, Mustafa Ardah, Manjusha Sudhadevi, Rasheed Hameed, and others who I might forget their names.

Special thanks to my colleague and brother Ismail El Haty for his inspiring ideas, endless advices, patient, help and support all these years. I have to also acknowledge my lovely friends, Jincy, Karima, Rima, Heba, Crystal, and Ghada who always stayed by me, made my life more cheerful and helped me to get through the tough times. My time at the UAE University as a Ph.D. student was made enjoyable in large part due to the many friends, hostel-mates, colleagues and groups that became a part of my life. I am grateful for the nice time that I spent with them and for many special memories came alongside this journey.

I would like to thank the families' members of Momad and Ghoypa for their support and nice friendship all the years of my life. Finally, I would like to thanks my beloved family in the UAE and Morocco, my sisters Fatima, Moleed, Habiba, Naima and Nasseima, my brother Abul-Nabi and his family Amena and little Salma, and especially my parents. They have always inspired me to follow my dreams and always stayed by my side during my journeys. Their unconditional support, patient, love and faith in my ability have always been my driving force to achieve my goals.

Dedication

To my beloved parents and family in the UAE and Morocco,

To Morocco, the country that I am proud to be from and belong to.

Table of Contents

Title i
Declaration of Original Work ii
Copyright iii
Approval of the Doctorate Dissertation iv
Abstract vi
Title and Abstract (in Arabic) viii
Acknowledgments x
Dedication xiii
Table of Contents xiv
List of Tables xvii
List of Figures xviii
Chapter 1: Introduction 1
1.1. Cancer 1
1.2. Liver 2
1.2.1. Liver structure 3
1.2.2. Liver neoplasm 6
1.3. Liver neoplasm and Animal Model 8
1.3.1. Chemically-induced models 9
1.3.2. Xenograft models 16
1.3.3. Genetically modified models 17
1.4. Saffron 18
1.5. Crocin 21
1.5.1. Crocin metabolism 23
1.5.2. Crocin sources 23
1.5.3. Biological activities of crocin 24
1.5.4. Safety of crocin 26
1.6. Nanoparticles (NPs) 28
1.7. Magnetite nanoparticles (MNPs) 32
1.7.1. MNPs Crystal structure 33
1.7.2. Superparamagnetism property of MNPs 34
1.7.3. Synthesis of MNPs 37

1.7.4. Desirable features of MNPs 41
1.7.5. Surface modification of MNPs 41
1.7.6. Surface functionalization of MNPs 48
1.8. Aims of the study 50
Chapter 2: Materials and Methods 51
2.1. Pure MNPs 51
2.2. Functionalization of MNPs 52
2.2.1. SDS-coating onto MNPs 52
2.2.2. Chitosan coating onto MNPs 53
2.2.3. Dextran-coating onto MNPs 54
2.3. Benedict's test 56
2.4. Addition of cross linker and crocin to D-MNPs 56
2.5. Calculation of the crocin loading 57
2.6. Characterization techniques 58
2.7. *In vitro* release study of crocin 59
2.8. *In vitro* cytotoxicity 60
2.8.1. MTT Assay 60
2.9. *In vivo* study 61
2.9.1. Animals 61
2.9.2. Experimental design 62
2.9.3. Prussian blue stain 66
2.9.4. Immunohistochemistry (IHC) studies 66
2.9.5. Quantification analysis of primary antibodies expression 69
2.10. Statistics 69
Chapter 3: Results and Discussion 70
3.1. Characterization of pure MNPs 70
3.2. Characterization of different surface coating materials 95
3.2.1. FTIR of coated MNPs 97
3.2.2. TGA analysis of coated MNPs 108
3.2.3. Morphology of coated MNPs 117
3.2.4. N_2 adsorption and pore size distribution of coated MNPs 120
3.2.5. Magnetic properties of coated MNPs 124
3.3. Selection of organic-coated MNPs 127

3.4. Crocin loading characterization 131
3.5. *In vitro* release of crocin 137
3.6. *In vitro* cytotoxicity 140
3.7. *In vivo* anti-tumour efficacy 147
3.7.1. General Observation, Body and Liver Weight 148
3.7.2. Histopathological examination 151
3.7.3. Detection of D-MNPs *in vivo* 161
3.7.4. Immunohistochemistry studies 166
3.7.5. Proposed mechanism 199
Chapter 4: Conclusions 206
Chapter 5: Future Prospects and Limitations 207
Bibliography 209
List of Publications 232

List of Tables

Table 1: DEN administration to wild-type male mice strains via i.p. injection.....14
Table 2: Some of the approved or marketed nanomaterials for cancer treatment. 31
Table 3: Examples of FDA clinically approved, commercially available organic-materials coated MNPs. 44
Table 4: Primary antibodies used for IHC studies. 68
Table 5: Effect of different conditions on the agglomerate average particle size and surface area of MNPs prepared by a co-precipitation in an aqueous solution. 81
Table 6: Wavenumber of the absorption bands characteristic to the sulfate group in SDS as appeared in pure SDS and S-MNPs FTIR spectra.....98
Table 7: Wavenumber of the absorption bands characteristic of chitosan, both as neat and different concentrations coating the surface of MNPs. 102
Table 8: Wavenumber of the absorption bands characteristic of dextran, as seen in the pure and different concentrations coating the surface of MNPs. 105
Table 9: Analysis of crocin and iron content in different D-MNPs formulations. 131

List of Figures

Figure 1: Diagrammatic representation of anatomical lobule which is the structural unit of the liver 5
Figure 2: Each flower of *C. sativus L.* has three stigmas. 19
Figure 3: Schematic representation of crocin chemical structure 22
Figure 4: Diagrammatic representation of the behaviour of multiple domains of a ferromagnetic material, and the single-domain of superparamagnetic MNPs in the presence or absence of external magnetic field.....36
Figure 5: Schematic representation of chemical structures of organic coatings 55
Figure 6: A diagram representing the treatment regime of the DEN-induced animal model and groups assignment 64
Figure 7: Diagrammatic representations of liver sections that were processed to perform several studies 65
Figure 8: Pourbaix diagram for the iron-water system showing the thermodynamically stable phases in aqueous solutions with various pH values 71
Figure 9: XRD patterns of solid MNPs prepared at different feeding rates of Fe^{2+} and Fe^{3+} aqueous solutions 73
Figure 10: SEM micrographs of agglomerates of MNPs prepared at different feeding rates. 75
Figure 11: SEM micrographs of agglomerates of MNPs prepared under different stirring temperatures.....76
Figure 12: Diagrammatic representation of the nucleation and growing process of MNPs. 78
Figure 13: SEM micrographs of different concentrations of $Fe^{2+}$and Fe^{3+}.....80
Figure 14: XRD patterns of MNPs prepared using different initial concentrations of the starting iron ions Fe^{2+}/Fe^{3+} 83
Figure 15: FTIR spectrum of MNPs sample containing initial concentrations of 0.3 and 0.6 M of Fe^{2+} and Fe^{3+} ions, respectively.....84
Figure 16: TGA analysis of solid MNPs samples prepared in solutions containing different initial concentrations of Fe^{2+} /Fe^{3+} ions. 86
Figure 17: Adsorption isotherms of MNPs samples prepared in solutions containing different initial concentrations of Fe^{2+} /Fe^{3+} ions 87

Figure 18: Pore volume distribution in MNPs samples prepared in solutions containing different initial concentrations of Fe^{2+}/Fe^{3+} ions 89
Figure 19: TEM micrographs of MNPs prepared in solutions containing different initial concentrations of Fe^{2+} and Fe^{3+} ions 90
Figure 20: Magnetic susceptibility of MNPs prepared in solutions containing different initial concentrations of Fe^{2+} and Fe^{3+} ions. 92
Figure 21: Magnetization of MNPs prepared under optimum conditions as a function of applied magnetic field at room temperature. 94
Figure 22: FTIR spectra of pure SDS and MNPs coated with various concentrations of SDS. 99
Figure 23: Diagrammatic representation of the interaction between SDS functional groups and iron ions of MNPs to form S-MNPs. 100
Figure 24: FTIR of pure chitosan and MNPs coated with various concentrations of chitosan. 103
Figure 25: Diagrammatic representation of the interaction between chitosan functional groups and iron ions of MNPs to form C-MNPs 104
Figure 26: FTIR spectra of pure dextran and different concentrations of dextran coatings onto MNPs 106
Figure 27: Diagrammatic representation of the interaction between dextran functional groups and iron ions of MNPs to form D-MNPs. 107
Figure 28: TGA analysis of MNPs coated with various concentrations of SDS. Insert: TGA pattern of pure SDS.....109
Figure 29: TGA analysis of MNPs coated with various concentrations of chitosan. Insert: TGA pattern of pure chitosan. 110
Figure 30: TGA analysis of MNPs coated with various concentrations of dextran. Insert: TGA pattern of pure dextran. 111
Figure 31: A detailed TGA analysis of the removal of water and organic coatings from the surfaces of the MNPs 114
Figure 32: Diagrammatic representation of the possible construction of water and organic coatings onto the surface of MNPs 116
Figure 33: TEM micrographs of MNPs coated with 0.2% of different organic coatings 118

Figure 34: Average particle size distribution of neat MNPs and MNPs coated with different concentrations of organic coating materials 119
Figure 35: Adsorption-desorption hysteresis of MNPs coated with different concentrations of organic coating materials.....122
Figure 36: Pore size distribution of MNPs coated with different concentrations of organic coating materials 123
Figure 37: Magnetization of neat MNPs and MNPs coated with different concentrations of organic coating materials.....126
Figure 38: FTIR of pure MNPs and the D-MNPs.....129
Figure 39: TGA of pure MNPs and the D-MNPs. 130
Figure 40: UV-Visible spectral measurements of crocin, D-MNPs and 4 mg/ml crocin-loaded D-MNPs 133
Figure 41: FTIR of crocin, D-MNPs and 4 mg/ml crocin-loaded D-MNPs 134
Figure 42: Schematic representation of chemical synthesis of crocin-loaded D-MNPs. 135
Figure 43: TEM micrographs of (a) D-MNPs and (b) 4mg/ml crocin-loaded D-MNPs. 136
Figure 44: Release profiles of crocin from the prepared two formulations 138
Figure 45: MTT cell viability assay of HepG2 cells, which were incubated with different concentrations of crocin for 72 hrs.....142
Figure 46: Cytotoxicity of different iron concentrations of D-MNPs on HepG2 cells after 72 hrs.....144
Figure 47: Cytotoxicity effects of media alone as a control, 3 mg/ml crocin alone, D-MNPs with 0.09 mg Fe/ml and 3 mg/ml crocin-loaded D-MNPs with 0.09 mg Fe/ml on HepG2 cells.....146
Figure 48: Body and liver weights of Balb/c mice treated with different treatments. 150
Figure 49: Diagrammatic representation of liver normal structure and blood flow ...152
Figure 50: Liver's normal histology (H&E stain).....153
Figure 51: Formation of AHF in the liver of DEN-induced group 156
Figure 52: Histological examination of AHF arising in livers of Balb/c mice after DEN administration and treated with 11 mg/kg or 22 mg/kg free crocin.....159

Figure 53: Histological examination of AHF arising in livers of Balb/c mice post DEN administration and treated with 11 mg/kg crocin-loaded D-MNPs or 22 mg/kg crocin-loaded D-MNPs, both doses contained 17 mg Fe/kg 160
Figure 54: Prussian blue staining of liver sections.....162
Figure 55: Subcellular localization of 22 mg/kg crocin-loaded-DMNPs and stained with Prussian blue. 165
Figure 56: Effects of 11 mg/kg crocin and its NP formulations on GST-P expression in liver 169
Figure 57: Effects of 22 mg/kg crocin and its NP formulations on GST-P expression in liver 170
Figure 58: Quantification of percent stained GST-P area in the two tested crocin formulations 171
Figure 59: Effects of 11 mg/kg crocin and its NP formulations on Ki-67 expression in liver 174
Figure 60: Effects of 22 mg/kg crocin and its NP formulations on Ki-67 expression in liver 175
Figure 61: Estimated expression areas of Ki-67 positive cells in the two examined crocin formulations. 176
Figure 62: Diagrammatic representation of caspases cleavage cytokeratin 18.....179
Figure 63: Effects of 11 mg/kg crocin and its NP formulations on M30-Cytodeath expression in liver. 180
Figure 64: Effects of 22 mg/kg crocin and its NP formulations on M30-Cytodeath expression in liver 181
Figure 65: Estimated expression of M30-Cytodeath area in the two examined crocin formulations. 182
Figure 66: Diagrammatic representation of Bcl-2 and Bax regulate apoptosis. 184
Figure 67: Effects of 11 mg/kg crocin and its NP formulations on Bcl-2 expression in liver 186
Figure 68: Effects of 22 mg/kg crocin and its NP formulations on Bcl-2 expression in liver 187
Figure 69: Quantitative analysis of Bcl-2 expression in relative to IHC fields in the two tested crocin formulations 188

Figure 70: Effects of 11 mg/kg crocin and its NP formulations on COX-2 expression in liver 191
Figure 71: Effects of 22 mg/kg crocin and its NP formulations on COX-2 expression in liver 192
Figure 72: Estimated expression areas of COX-2 positive cells in the two examined crocin formulations 193
Figure 73: Effects of 11 mg/kg crocin and its NP formulations on VEGF expression in liver 196
Figure 74: Effects of 22 mg/kg crocin and its NP formulations on VEGF expression in liver 197
Figure 75: Quantitative analysis of VEGF-expression in the two examined crocin formulations 198
Figure 76: A diagram representing the changes that occur in bile ductule and oval cells due to DEN 200
Figure 77: A diagram representing the proposed steps of endocytosis of crocin-loaded D-MNPs into the cell.....202
Figure 78: Diagrammatic representation demonstrating the proposed anti-cancer activity of crocin on pre-cancer/cancer cell, *in vitro* and *in vivo* 205

Chapter 1: Introduction

1.1. Cancer

Cancer is a disease characterized by cells that uncontrollably outgrow their normal counterparts. The terms tumor and cancer are sometimes used synonymously, which can be misleading. A tumor is not necessarily a cancer. The word tumor refers to a mass or lumps that may refer to benign or malignant growths. Neoplasm is a synonym of tumor. A benign tumor is a non-malignant/non-cancerous tumor and is usually localized, grows slowly, and rarely spreads to other parts of the body. Malignant tumor is however, a cancer that is resistant to treatment, invades adjoining parts of the body, and might reoccur after removal [1, 2]. There are several hallmarks of cancer cells include stimulate their own growth, resist growth inhibitory signals, avoid apoptosis, stimulate angiogenesis, multiply endless by invade adjacent tissues and metastasize, and avoiding immune destruction [1, 2].

Cancer is among the leading causes of death worldwide, accounting for 8.2 million deaths and 32.6 million people living and suffering from cancer in 2012 alone. It was estimated that annual cancer cases would rise from 14 million in 2012 to 22 million within the next two decades. The most common causes of cancer death are lung [3], liver (745 000 deaths), stomach (723 000 deaths), colorectal (694 000 deaths) and breast (521 000 deaths) cancers [4]. In the United Arab Emirates (UAE) cancer is the third leading cause of death after cardiovascular diseases and accidents. Data from the Health Authority of Abu Dhabi indicated that cancer accounts for approximately 474 deaths cases in 2012, with 53% male and 47% female, and the majority are expatriates. Millions of dirhams are invested annually to treat cancer cases in the UAE [5]. There are over 100 different types of cancer, and each

classified according to the type of cell that is initially affected. Each organ consists of different cell types that may affected by cancer. Liver is one of the vital organs that might develop cancer.

1.2. Liver

The liver is a vital organ of the digestive system. It is the largest gland in the body and the heaviest internal organ (1200-1500 g). It maintains many of the body's homeostatic and physiological functions. The liver receives all absorbed substances from intestine where some foreign material may filter via portal vein. Systemically it receives it's oxygen via arterial blood supply (hepatic artery). The liver stores the nutrients and controls their release to the systemic circulation [6-9].

Liver functions are various and can be categorized into metabolic, catabolic, synthetic, storage and excretory functions. The liver has a central role in the regulation of metabolism of nutrients like carbohydrate (glycogenolysis and gluconeogenesis), protein, fat, hormone and various xenobiotics, such as food additives, drugs, or environmental pollutants. Liver produces albumin, blood coagulation factors, vitamins like vitamin A and iron. In addition, it sores glycogen, triglycerides, iron, copper and lipid soluble vitamins. It also catabolizes endogenous substance including hormones, serum proteins, old red blood cells, haemoglobin and bilirubin and maintain a balance between their production and removal. Drugs are catabolized and detoxified, then excreted via the kidney or the biliary system. The main excretory product of the liver is bile while stored in the gallbladder. The bile helps in heme catabolism and absorption of fat in the small intestine [8, 9].

1.2.1. Liver structure

The liver consists of multiple lobes; left, right (the largest), caudate, and quadrate or middle lobes. Caudate and quadrate lobes are located in the back of right lobe. Parietal and visceral surfaces of the liver are cover by a capsule. It is a thin connective tissue layer covered by peritoneal mesothelial cells. Liver has a dual blood supply, the hepatic portal vein and hepatic artery [10].

The histological or structural unit of the liver is a polyhedral anatomical lobules (**Figure 1**). Each lobule contains a central vein, and radiating sinusoids separated from each other by plates of hepatocytes, and peripheral portal tracts or triads. Portal triad includes branches of hepatic artery, portal vein and bile duct. The blood flows from portal vein into central vein, and the branches of central veins unit to form three main veins that enter the inferior vena cava. The bile flows in opposite direction from hepatocytes into the bile ducts and eventually store in gall bladder [10].

The main parenchymal cellular units of the liver are hepatocytes. The hepatocytes are arranged in plates or cords that radiate from the central vein to the portal areas (**Figure 1)**. Hepatocytes, on one side, they are separated from the sinusoidal wall by space of Disse, where they are exposed to tissue cytoplasm. On the opposite side, bile canaliculi are formed with hepatocytes in an adjacent hepatic cord. Desmosomes, and gap junctions connect neighbouring hepatocytes within a plate. In addition to hepatocytes and blood cells that exist in the sinusoids and blood vessels, the liver includes several other types of cells, including biliary duct cells, oval cells, endothelial cells, Kupffer cells, Ito cells (stellate cells), and pit cells [10].

Biliary cells form the bile ducts in the portal areas. Oval cells are stem cells located in Herring canals, the area where the biliary duct system connected with

hepatocytes. It has been shown that oval cells have a potency to generate and regenerate not only hepatocytes after injury, but also bile duct cells, intestinal epithelium and pancreatic acinar cells [9-11]. Fenestrated endothelial cells line the sinusoids and synthesize prostaglandins [10]. Kuppfer cells are mononuclear macrophages forming 10% of all liver cells. These cells are phagocytic, inflammation mediators, and catabolize lipids and proteins. They are also essential for paracrine interactions between hepatocytes and Ito cells. Ito cells are peri-sinusoidal cells that store vitamin A and fat and are the main source of collagen in the liver. Pit cells are lymphocytes that have characteristic features of natural killer cells and therefore exert cytotoxic activity against tumor cells, and are mostly located in periportal areas [10].

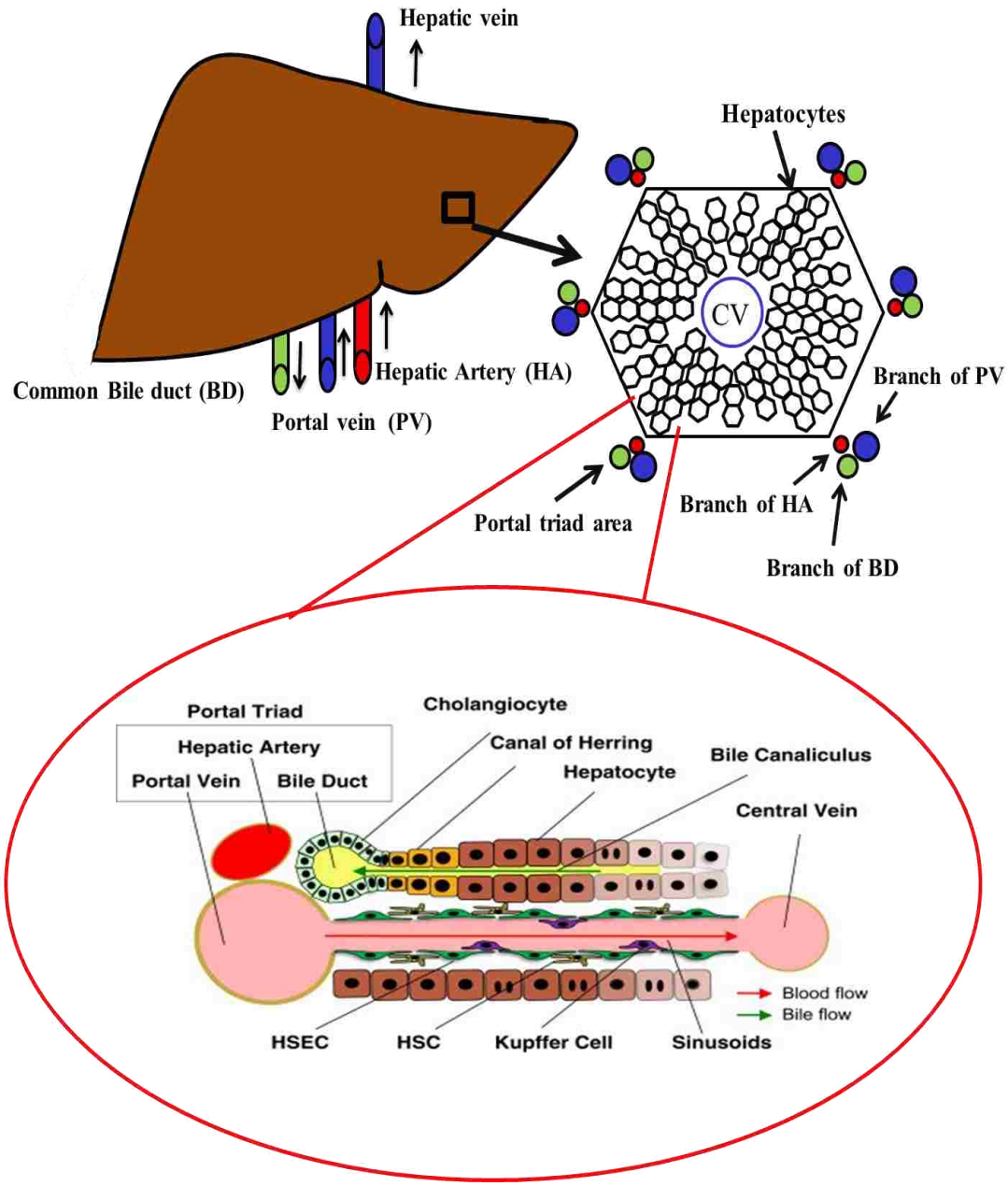

Figure 1: Diagrammatic representation of anatomical lobule which is the structural unit of the liver. Each lobule includes plates of hepatocytes, hepatic sinusoidal endothelial cells (HSEC); Hepatic stellate cells (HSC), and kupffer cells [12].

1.2.2. Liver neoplasm

Despite the liver capacity for regenerative growth by oval cells, it is a target organ for damage induced by a variety of factors such as toxins, alcohol, chronic inflammations, drugs, and genetic mutations. These may lead to various liver diseases including acute liver failure, viral hepatitis, cirrhosis, steatosis or fibrosis. If these diseases not treated early, may lead to development of liver cancer. Primary liver cancer occurs in different form, such as hepatocellular carcinoma (HCC), intrahepatic cholangiocarcinoma (ICC) and hepatoblastoma [13].

1.2.2.1. HCC

HCC is one of the most common primary malignant liver lesions, accounting for 70-80% of primary liver cancer cases [13, 14]. HCC is the fifth common cancer in the world. It kills almost half-million people around the world every year, and it is the third most common cause of cancer-related deaths [13-17]. The Health Authority of Abu Dhabi reported in 2013 that in UAE there are 17% of cancer patients died because of liver cancer and ICC. Among these patients 13% are men and 4 % women [5].

About 80% of HCC develop in cirrhotic livers and chronic hepatitis. Chronic viral infections, including the hepatitis B and hepatitis C viruses are major risk factors contributing to HCC development. Hepatitis B virus infection is most relevant in most parts of Asia and Africa, with ingestion of aflatoxin B1 from contaminated food an additional contributory factor. In the West and Japan, hepatitis C virus infection is the main risk factor. Apart from hepatotropic viruses, other major risk factor leading to cirrhosis includes excess alcohol intake. HCC is an aggressive cancer with a poor prognosis [14, 17-21].

Late diagnosis of HCC usually leads to a very short survival time. Enhancing the survival rate requires detection of small tumors at early stages, often present in asymptomatic individuals. Ultrasonography is the preferred imaging method for screening, because it can be tolerated and widely accessible. However, ultrasonography sensitivity for HCC detection is low, because small nodules can be easily missed in a cirrhotic liver. Contrast-enhanced ultrasonography can be used to improve the diagnostic performance of ultrasonography for HCC. The most common used serological test for screening is alpha-fetoprotein, but it is no longer considered as a surveillance test because of its low sensitivity. Contrast-enhanced computed tomography and magnetic resonance imaging (MRI) have a high sensitivity (55%–91%) and specificity (77%–96%) in diagnosing HCC. The diagnosis of HCC lesions measuring between 1 and 2 cm is confirmed when typical vascular pattern detected on CT and MRI. Otherwise, these lesions should not be treated as HCC without histological indication because of a rate of false positives is as high as 20% [19, 21, 22].

Therapeutic strategies for HCC patients include surgical resection or liver transplantation, which are only applicable to a small proportion of patients around 25% with early tumors. Other therapeutic methods are percutaneous ethanol injection, percutaneous radiofrequency ablation, and trans-arterial embolization. Due to late detection and advanced underlying liver diseases, these treatments are normally not recommended to the majority of the patients [18, 22-24].

Regarding the chemotherapy, the only drug that is currently being used for HCC is sorafenib. However, the patients survival remains low, and sorafenib may only improve life expectancy by approximately 3 months over placebo control [18, 22-24]. Sorafenib (also known as Nexavar), is a multikinase inhibitor that targets the

vascular endothelial growth factor receptor family (VEGFR-2 and VEGFR-3) and platelet-derived growth factor receptor family (PDGFR-beta). These receptors play key roles in cancer progression. It also inhibits activation of oncogenic RAF serine/threonine kinases along the RAF/MEK/ERK pathway (Ras/RAF pathway), which will inhibit proliferative signal resulting in blocking in tumour growth and development [25].

Prior sorafenib, doxorubicin was routinely used as a single drug for advanced HCC, but has been shown ineffective, with a response rate of about 15-20% [26]. Other chemotherapy agents, such as epirubicin, cisplatin, 5-fluorouracil, etoposide and their combinations, demonstrate even lower efficacy [18, 22, 23, 26].

One of the main reasons for which the patients with HCC have poor prognosis is the multicentric occurrence of HCC in the liver of patients with chronic hepatitis or cirrhosis caused by infection of hepatitis viruses. Thus, even if the first cancer is diagnosed and removed another malignant cell clone may arise to form a second primary cancer (Moriwaki, 2002). Therefore, due to the fact that the current treatments for HCC are not effective, new strategies are needed not only to prevent the development or post-therapeutic recurrence of HCC but also to prevent further deterioration of liver function [22-24, 27].

1.3. Liver neoplasm and Animal Model

The increase in the burden of liver cancer and specifically HCC require understanding the aetiology, cellular and molecular mechanisms leading to it. Thus, the development of animal models for better understanding is essential [13, 14, 16]. Currently, a wide range of HCC animal models are existing, which have provided researchers with the opportunity to: 1) evaluate cancer–host interactions, 2) perform drug screening and testing, 3) mimic the complex multistep process of liver

carcinogenesis in human, and 4) conduct various therapeutic experiments [13, 14, 16; 28].

Mice models are one of the preferred and convenient experimental systems, owing to the physiologic, molecular and genetic similarities to humans, their breeding capacity, short lifespan, affordable, easier to be handle and the unlimited options offered by genetic engineering. Mice are also small, easily housed, and maintained, and adapt well to the new surroundings [13, 16]. There are many ways to produce HCC using mice models, such as chemically-induced, xenograft implantation and genetically modified models [17].

1.3.1. Chemically-induced models

Several chemical reagents induce liver damage and HCC formation and development of tumours when timely administered in sufficient doses. There are two types of carcinogens: (1) Genotoxic compounds which are characterized by their ability to induce direct structural DNA changes. (2) Promoting compounds which enhance tumour formation after initiation, and lack direct genotoxic capability. Treatment with tumour promoting agent facilitates the clonal expansion of the preneoplastic cells. The advantage of chemically-induced models is that it mimics pathological events such as injury and malignancy steps that occur in humans. This makes them the preferred models for HCC research [13, 28].

1.3.1.1. Diethylnitrosamine

As mentioned earlier liver is the primary target location for many chemicals including pesticides, food additives, pharmaceuticals and industrial intermediates [13]. The genotoxic compound N-Nitrosodiethylamin, also known as diethylnitrosamine (DEN), is categorized as a potent hepatotoxin and hepatocarcinogen producing reproducible tumors after repeated administration in

experimental animals. DEN induces lesions in animals that mimic the process of different types of malignant cancers in human [29].

In 1956, the British John Barnes and Peter Magee are the first scientists who reported that DEN produced liver tumours in rats during toxicity screening test of chemicals. These chemicals were being proposed for the use as solvents in the dry cleaning industry [30]. DEN belongs to nitrosamine family. This family is structurally divided into N-nitrosamides and N-nitrosodialkylamines and both groups can induce DNA damage. DEN belongs to N-nitrosodialkylamines that require metabolic activation mediated by cytochrome P450 (CYP450) enzymes, in order to induce DNA damage. It is a slightly yellow liquid and soluble in water, saline, ethanol, diethyl ether and organic solvents [31, 32].

As DEN is known to produce cancer in many different species and due to its widespread occurrence in a variety of products consumed by human, the possibility of DEN being a main cause of cancer in humans has been the concern of public health agencies for a long time. DEN is found in various foods like cheese, milk and diary product, soybean, smoked, salted and dried fish, cured meat, fried bacon, soft drinks and alcoholic beverages like whiskey and beers [29, 32, 33]. DEN is also found in tobacco smoke at a concentration ranging from 1 to 28 ng/cigarette, and in baby bottle nipples at a level of 10 ppb. It is used also in the production of some cosmetics, pesticides, metal industry, and in most rubber and latex products such as balloons [29, 31].

DEN is metabolically activated to carcinogens by CYP2E1 isoforms (one of CYP450 enzymes). This isoform is highly conserved, having a high degree of sequence homology between various species, including humans. DEN causes carcinogenic activity in several different ways as the following:

1) DEN has capability of alkylating DNA structures leading to the formation of mutagenic DNA adducts. In the first step, DEN is hydroxylated to a-hydroxylnitrosamine. This bio-activation step is oxygen- and NADPH- dependent. An electrophilic ethyldiazonium ion is formed post cleavage of acetaldehyde. This ethyldiazonium ion causes DNA damage by reacting with DNA-bases. The resulting O^6-ethylguanine leads to GC–AT transitions [16, 31, 34].

2) DEN can cause reactive oxygen species (ROS) formation. The generated ROS including hydrogen peroxide and superoxide anions induce oxidative stress and cause carcinogenesis by destroying DNA, protein and lipid [13, 16, 17, 33]. Oxidative stress plays a vital role in hepatocarcinogenesis, particularly in the initiation and progression steps. ROS-mediated DNA damage is associated with breaks in single or double stranded DNA chain, and alterations in deoxyribose or nitrogenous bases. Such increased erroneous replication will lead to genomic instability and eventually causing carcinogenesis [34].

3) DEN develops cancer by inducing mutations in *H-ras* proto-oncogene (also known as *Ha-ras* gene). The mutation in *H-ras* gene was attributed to specific single-base substitutions at different bases of codon 61. These point mutations either a transversion in the first base (substitution of a purine (A and G) for a pyrimidine (C and T) or vice versa), or a transition in the second base (substitution of a purine for a purine, or pyrimidine for another pyrimidine) [35, 36]. *H-ras* gene produces H-ras protein that is involved in regulating normal cell division and proliferation in response to growth factor stimulation like epidermal growth factor (EGF). Then activates major effector pathways necessary for the propagation of the receptor's signal, such as Raf protein kinases and phosphatidyl inositol 3-kinase (PI3K). Raf

regulates cell cycle progression and transcription, and PI3K plays an impoetant role in reguatling cell grwoth, proliferation and survival [37].

4) DEN alone leads to the formation of lesions that overexpress the Bcl-2 gene [17].
5) DEN stimulates the proliferation of hepatic oval cells and bile duct cells leading to hyperplasia and the formation of microscopic intrahepatic cholangioma [38, 39].

The target organ in which DEN generates tumours is species specific. Hartwell and Shubik are the first who compiled a review of DEN carcinogenicity examining in between 1961-1967. Upon DEN exposure, mice have been shown to develop manily HCC, in addition to gastrointestinal, skin, respiratory and haematopoietic tumours. Rats were also primarily HCC, besides gastrointestinal cancer. Guinea pigs and Syrian hamsters developed HCC, gastrointestinal and respiratory cancer. Rabbits, dogs and monkeys had only HCC while pigs had both HCC and hematopoietic cancer [17, 40].

The time needed after DEN adminstration to develop HCC depend on sevral factors, including: dose concentration, gender, age, animal strain, dose repetitive administration, administration period (short or long term), route of adminstration, and individaul DEN injection or in association with promoting agents. The younger the mice, the faster HCC will develop because of the high hepatocyte proliferation rates of young animals. Due to the stimulating effect of androgens and the inhibitory effect of estrogens on hepatocarcinogenesis, HCC deveolps in males more than females [13, 16, 17, 41].

Because of genetic variations between strains, their susceptibility to both spontaneous and DEN-induced liver cancer are different. CBA and C3H inbred mice

strains are considered to be highly susceptible to spontaneous incidence of HCC. While inbred of C57BL/6 and Balb/c mice are relatively resistant to spontaneous incidence of HCC but relatively sensitive to DEN induced HCC (**Table 1**) [42].

Carcinogenesis in mice develops in three steps: initiation, promotion, and progression. Based on the dose of muliple DEN adminstration for around 8-16 weeks, development of liver cancer can be determined. For example, doses below 10 mg/kg of body weight only stimulate the initiation of carcinogenesis. Hepatic fibrosis is produced at 10-20 mg/kg of body weight, while promotion and progression of carcinogenesis will be developed at doses equal to or above 25–30 mg/kg of body weight [43].

The dose requiremnet, time and percentage of cancer development vary among different strains. For examples, C3H/HE mice strain at concendtration of 90 mg/kg DEN-induced 100% HCC after 45–75 weeks [44]. DEN-induced C57BL6 /J mice at concentration 5 mg/ kg produecd 84% HCC after 40–70 weeks [45]. When adult mice are injected weekely for a short time with DEN, it leads to a higher tumour rate in a shorter time (**Table 1**). Six weeks of intraperitoneal injections (i.p.) (3 weeks with 75 mg/ kg followed by 3 weeks with 100 mg/kg) lead to 100% tumour incidence after 7 months in male mice [46]. Weekly administration of 50 mg/kg DEN to mice leads to 100% pre-neoplastic lesions dvelopment after 8 months [47]. Hepatocarcinogenesis model can be also be obtained by using initiatione/promotion protocol that will leads to genomic alterations. While DEN is usually the initator, promoter agents can be phenobarbital, carbon tetrachloride, partial hepatectomy, or a high fat diet [17].

Table 1**:** DEN administration to wild-type male mice strains via i.p. injection.

Wild-type Strain	**Age**	**Dose repetition**	**Dose concentration (per body weight)**	**HCC development**	**References**
Balb/c	15 days	Single	25 or 50 µglg	6- 10 months	[48]
Balb/c	15 days	Single	10 µglg	8 months	[49]
Balb/c	5 weeks	Multiple; Each dose Once/week for 3weeks	75mg/kg followed by 100mg/kg	5months (pre-neoplastic lesions) 7 months-HCC	[46]
C57BL/6	15 days	single	25mg/kg	8months	[50]
C57BL/6	4 weeks	Once/week for 8 weeks	50mg/kg	6 months (pre-neoplastic lesions)	[47]

HCC development using DEN model is a multistep process, where DEN works as a complete carcinogen to induce HCC and cycles of de-generation and re-generation activate pre-neoplastic transformations. The progression of early dysplastic lesions to malignant tumors is associated with an increased occurrence of genomic alterations. Such genomic alterations are very similar to those associated with HCC development in humans. Thus, DEN model is consider one of the best models used to study HCC pathogenesis mechanism in human [17, 51].

1.3.1.2. The aflatoxin model

The aflatoxin B1 is hepatotoxin produced by particular fungi of the Aspergillus genus, for example *Asparagillus flavum* and *Aspergillus parasiticus* which are widespread in nature. There are four of aflatoxin (B1, B2, G1 and G2) known to be carcinogenic to both humans and animals. Aflatoxin B1 is the most potent hepatocarcinogenic of those agents. The Aflatoxin B1 is found in food, such as corn, rice, oil seeds, dried fruits and peanuts, that have been stored in hot, humid and inappropriate conditions. It is found in the milk, meat and eggs of farm animals that feed on contaminated foods with aflatoxin [16, 17, 52, 53].

CYP450 is necessary for the metabolic activity of aflatoxin B1 causing sister chromatide exchange, chromosomal strand breaks, DNA-adducts, and uncontrolled DNA synthesis [16, 17, 52, 53].

1.3.1.3. Carbon tetrachloride

Another potent hepatotoxin is carbon tetrachloride (CCl_4). The hepatotoxicity of CCl_4 is exerted in several different ways. CCl_4 damages hepatocytes directly by altering the permeability of the plasma, lysosomal, and mitochondrial membranes. CCl4 is metabolized by CYP2E1, CYP2B1 or CYP2B2 to form trichloromethyl radicals. These radicals are highly reactive and can bind to cellular molecules, such

as nucleic acid, protein and lipid impairing vital cellular processes such as lipid metabolism, with the result of fatty degeneration (steatosis). Adduct formation between CCl_4 and DNA lead to hepatic cancer [16, 17, 54, 55].

1.3.1.4. Choline deficient diet

Several studies reported that mice subjected to choline deficient diet could develop HCC in 13 months post 3 weeks continous adminstration of the diet [56]. Abnormal proliferation of oval cells has been proposed as the mechanism through which carcinogenicity by choline deficient diet was developed. The abnormal proliferation of oval cells was a result of ROS generation and oxidative DNA damage and chromosomal instability because of the depletion of hepatic antioxidant mechanisms [16, 17].

1.3.2. Xenograft models

Xenograft tumours is one of the most widely used models to study HCC. In this model, human cancer cells are injected into immune deficient micesuch as athymic (nude) or severe combined immune deficient (SCID) mice. Depending on the number of HCC cells injected, the cancer will take to develop around 1–8 weeks. There are several types of xenograft models including: (1) The ectopic model, in which human cancer cells are injected subcutaneously in the flanks of mice. (2) The orthotopic model, in which tumour cells are injected directly into the mice liver. (3) Hollow fibre assay, in which different cells from different cancer cell lines placed into small indivial semi-permeable tubes [13, 16, 17, 57]. The advantages of xenograft models are the rapid tumor grwoth and development. These models also allow investigation of *in vivo* toxicity, absorption and pharmacokinetics of the compounds/drugs. However, the pathological events of tumor development in these models do not mimic that occur in humans [16, 17].

1.3.3. Genetically modified models

Genetically modified animals are engineered to resemble pathophysiological and molecular features of HCC. The genetic profile of these mice is changed, in a way that one or several genes that involved in the molecular stages leading to the cancer are mutated, deleted or overexpressed. Genetically modified animals enable detailed investigation of carcinogenic pathways, exmanine the effect of the modified genes alone or in combination with carcinogenic agents, and the therapeutic responses [13, 16, 17, 57].

There are large numbers of HCC transgenic mice, including transgenic mice over-expressing oncogenes like Myc protein (a transcription factor that upon mutation it forces cells to proliferate continuously and prevent apoptosis), and mice over-expressing growth factors, such as Epidermal growth factor that regulate cell growth, proliferation and differentiation [17, 58].

Because the existing treatments for HCC are not efficient, new treatment sources are needed to prevent the progress of HCC and deterioration of liver functions. Many investigations are being carried out worldwide to discover naturally occurring compounds which can suppress or prevent the development of liver carcinogenesis. It is well known that many anticancer drugs derived from plants include Taxol (mitotic inhibitor) from Pacific Yew tree, Vinblastine (anti-microtubule drug) from Catharanthus roseus, and Campothecin (inhibits DNA topoisomerase I) from Camptotheca acuminate. The current research suggests that many herbs and spices contain chemicals that may decrease the incidence of cancer [59, 60].

1.4. Saffron

Saffron is world's most expensive spice that has been widely used as an herbal medicine, spice, food colouring, and a flavouring agent since ancient times because of its distinct colour, odor, and taste. It is obtained from the dried stigma derived from the flower of the plant *Crocus sativus Linnaeus* (*C. sativus L.*) [60-63]. The genus *Crocus* contains around 88 species among which *C. sativus L.* is the most investigated species. This herb is cultivated in many different countries, such as Spain, Kashmir, and Nepal [60-62, 64]. However, Iran accounts for 70% of saffron worldwide [65].

C. sativus L. grows under hot and dry weather in the summer, but its vegetative growth is during cold winter. The seeding of saffron takes place in the months of June and July, while harvesting is end of October-beginning of November. Saffron can tolerates tempertaure of maximum 45ºC and minimum of ˉ18º C. The plant is proliferating by bulbs**,** which divides to yield new plants, and each bulb produces one to seven flowers [65].

C. sativus L. produces flowers once a year and the flower has three stigmas **(Figure 2**). The flowers should be collected immediately because the stigmas might lose their colour and their volatile aroma components might evaporate. Once the flowers are gathered, stigmas are removed from the rest of the flowers. The stigmas and their flowers must be hand-picked because they are delicate [60-62, 64].

Figure 2: Each flower of *C. sativus L*. has three stigmas [66].

More than 85,000 flowers needed to produce only one kilogram (kg) of stigmas. It is necessary to dry (roasting process) stigmas well for good preservation, because they have a high level of moisture. After the roasting, 1 kg of raw stigmas will obtain nearly 200 gram (g) of saffron [60, 62, 63, 66, 67].

While saffron can tolerate high temperatures, it easily degrades in the presence of light and oxidizing agents. Usually the best saffron sold as whole stigmas (not powdered) in airtight containers away from light sources to maintain its integrity. The limited production yield, time and difficult seeding and harvesting procedures that should be done by hand, these reasons make saffron expensive, around $40–50 per g [60, 62, 63, 66, 67].

Chemical analysis has shown the presence of estimated 150 volatile and non-volatile compounds in saffron. It has also some carbohydrates like starch, vitamins, amino acids, and fats. Saffron's major components are as the following:

1) Crocin (Di-glycosyl polyene esters of crocetin, hydro-soluble) is responsible for 80% of saffron colour.
2) Crocetin (Dicarboxylic acid precursor of crocin, lipo-soluble) is also responsible for 20% of saffron colour.
3) Picrocrocin (Monoterpene glycoside precursor of safranal) is responsible for the bitter taste. It is the second most abundant component in saffron.
4) Safranal (De-glycosylated form of picrocrocin) is an aromatic aldehyde that is responsible for saffron volatile oil's odor.

Dehydration process is not only critical for the preservation of saffron, but is important for the release of safranal from picrocrocin via enzymatic activity. Then the reaction produces D-glucose and safranal [62]. Recent studies showed that saffron has many medicinal properties including anti-oxidants, anti-tumorigenic [68],

memory enhancer, anti-depressant and cardio-protective agent [60, 62, 67]. As a major component of saffron, crocin is a main contributing active ingredient to saffron's bioactivity. Thus, the following section will focus on crocin.

1.5. Crocin

Crocin is one of the few water-soluble carotenoids found in nature; therefore, it has various applications as a food colorant and medicinal properties. It is the diester formed from the disaccharide gentiobiose and the dicarboxylic acid of crocetin. Gentiobiose is a disaccharide composed of two units of D-glucose, and due to these sugar moieties crocin has high water solubility [67, 69]. Crocin has a deep red colour, quickly dissolves in water to form an orange to yellow colour. Crocin chemical formula is $C_{44}H_{64}O_{24}$ (**Figure 3**), with molecular weight is 976.96 g/mol. The recommended storage temperature is 2-8 °C, and it is light sensitive. It forms crystals with a melting point of 186 °C. In addition to crocin water solubility, it is also soluble in methanol and ethanol. [60, 62, 67].

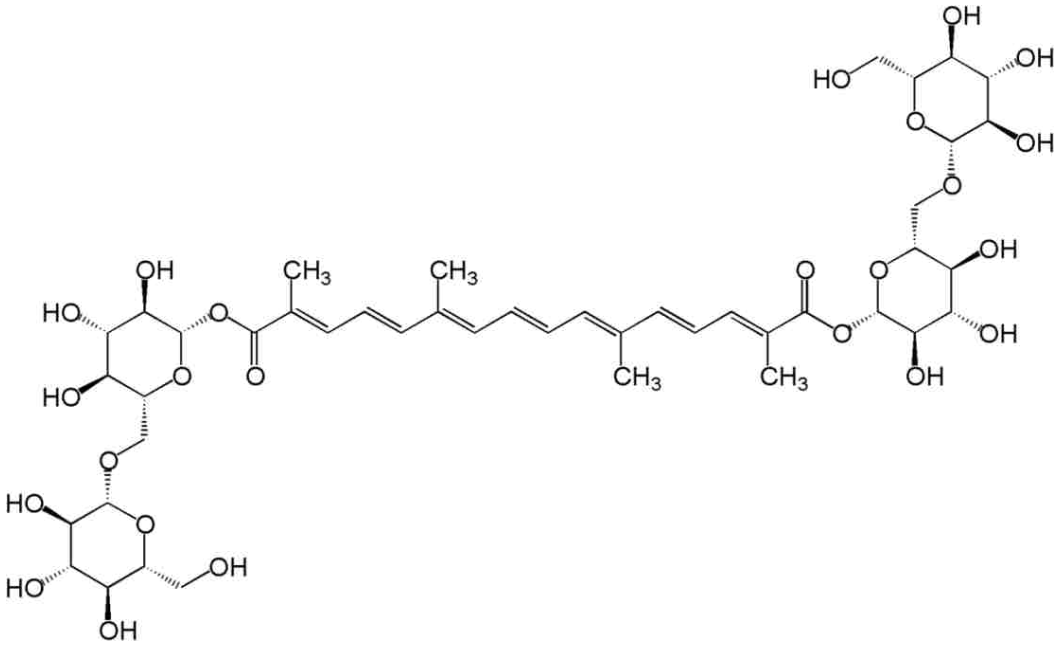

Figure 3: Schematic representation of crocin chemical structure [67].

1.5.1. Crocin metabolism

Orally administered crocin hydrolyzed into crocetin before circulated into the blood, after a single dose or repeated doses for six days of 40mg/kg crocin into rats and mice. Crocin hydrolyzed into crocetin before or during intestinal absorption. Crocetin was then partly metabolized into mono- and di-glucuronide conjugates. The plasma concentration of crocetin was decreasing, after 1 hr of single oral dose of crocin. This indicates that crocetin might rapidly be eliminated without accumulation in the body. This is consistent with the short plasma half-life of crocetin [70-72]

Crocin as intact form was largely present in feces and intestinal contents, but not in the urine post 24 hrs of administration. The amount of crocin lost in the colon was greater than other parts of intestine (Duodenum, Jejunum and Ileum), that probably because of higher basic condition within the colon. Consequently, the intestinal tract serves as an important site for crocin hydrolysis [70, 71]. However, another study reported that crocin could be excreted by the urine after long term exposure, 21 days, of 180mg/kg crocin i.p. administrated (Hosseinzadeh, Shariaty, Sameni, & Vahabzadeh, 2010.

1.5.2. Crocin sources

Crocin found to be the main pigment of the saffron as mentioned earlier. The amount of crocin in saffron is varying depending on the growing conditions, drying processes, duration and storage methods. Greek and Kashmiri saffron have the highest concentration of crocin followed by India and New Zealand [67, 69]. In addition, crocin obtained from the fruits and flowers of gardenia, in specific *Gardenia jasminoides Ellis* species. This species has traditionally used as a folk medicine in few Asian countries like china, Japan, India and Pakistan. This species is less common compared to *C. sativus L.* [73].

1.5.3. Biological activities of crocin

Many beneficial effects of crocin against different illnesses have been reported inclduing being a potent anti-cardiovascular, anti-cancer, anti-oxidant, anti-inflammatory, and anti-depressant and as a promoting agent of learning and memory [67].

1.5.3.1. Anticancer effect

Several studies have shown that the crocin can inhibit the growth of different types of cancers such as leukaemia, osteosarcoma, fibrosarcoma and ovarian carcinoma and breast cells. Crocin decreased MCF-7 and Hela cell lines by down-regulating the expression of Bcl-2, and up-regulating the expression of Bax. Crocin induced apoptosis and G1 cell cycle arrest in human pancreatic and tongue squamous cancer cell lines [67]. It was also reported that crocin inhibit the proliferation of three colorectal cell lines (HCT-116, SW- 480, and HT-29) and human non-small cell lung cancer (NSCLC) cells. On the other hand, no toxic effect was reported on normal cells, non-cancer young adult mouse colon (YAMC) cells [74].

Crocin also reduced the formation of mouse skin papillomas when they were injected subcutaneously with 85 nmol of crocin [75]. The life span of rats was increased and colon tumor growth was decreased in female rats without showing any significant toxic effects, after long-term treatment of crocin. The treatment was weekly for 13 weeks with subcutaneous administration of crocin 400mg/kg [76].

1.5.3.2. Effect on gastric disorders

Several studies reported that crocin decreased the gastric diseases. Kianbakht et al. have shown that orally administrated of crocin at 10mg/kg reduced ulcer formation, due to it is antioxidant properties. Crocin prevented indomethacin-induced gastric mucosa damage by increasing glutathione levels and preventing lipid

oxidation [77]. A similar study tested the capability of crocin to prevent stomach lesions in rats treated with indomethacin, an anti-inflammatory drug known to cause ulcers. The results showed that crocin protected the stomach mucosa from damage compared to un-treated group [78]. These studies also emphasized the safety of crocin since the rats did not display gastric ulceration at the highest crocin doses of 10 mg/kg or 50 mg/kg in normal tested animals [77, 78].

1.5.3.3. Antioxidant effect

As a potential radical scavenging agent, crocin is a potent neuro-protective, anti-aging, anti-inflammatory, and anti-cancer biomolecule. Bors et al. in 1982 was the first to report the anit-oxidant activity of crocin [79]. The anti-oxidant mechanisms of crocin are mainly attributed to its scavenging ability of superoxide anions and nitrite, 2,20-azino-bis (3-ethylbenzthiazoline-6-sulfonic acid) radical cations inhibition, superoxide dismutase-like activity and the reduction of intracellular ROS production [80].

Santhosh et al. studied the role of crocin in treating the secondary complications of snakebite. Rats treated i.p. with venom mixed crocin. The results indicated that in crocin reduced the level of pro-inflammatory cytokines, such as IL-1ß, IL-6, and TNF-α, and decreased the oxidative stress induced by venom [81]. The protective role of crocin against beryllium chloride toxicity in rats was investigated at a dose of 200mg/kg i.p. treatment for 7 days prior to beryllium chloride intake resulted in significant reduction in beryllium chloride-induced oxidative stress, combined with initiation of mRNA expression of catalase and superoxide dismutase genes. The hematological and biochemical parameters such as lactate dehydrogenase levels were restored near the normal levels [82].

1.5.3.4. Anti-inflammation effect

Recent studies revealed that crocin exerts anti-inflammatory and anti-nociceptive activities. Tamaddonfard et al. tested the effects of i.p. treatment of crocin at doses of 25, 50, and 100 mg/kg on local inflammation and inflammatory pain responses induced by intra-plantar injection of carrageenan in rats. The results showed anti-inflammatory and anti-nociceptive activities of crocin in a dose dependent manner by decreasing the inflammatory pain responses and number of neutrophils in carrageenan model [83].

A study by Xu et al. evaluated the anti-inflammatory effects of crocin *in vitro* and *in vivo*. *In vitro*, cyclooxygenase inhibition assays showed that crocin concentrations (0.01, 0.1, 1.0, 10, 30, and 100 μM) displayed a dual inhibitory activity against the cyclooxygenase-1 (COX-1) and cyclooxygenase-2 (COX-2) enzymes in lipopolysaccharide-challenged RAW 264.7 murine macrophages cells in a dose dependent manner. Crocin also suppressed the productions of prostaglandin E2 [78]. Anti-inflammatory activity *in vivo* examined using two animal edema model tests. Pre-treatment with crocin at doses 12, 25, and 50mg/kg were administered orally, inhibited the xylene-induced ear edema in mice and carrageenan-induced paw edema in rats in a dose dependent manner. These results indicated that crocin exhibits obvious anti-inflammatory effects [78].

1.5.4. Safety of crocin

Several studies conducted by researchers to investigate the potential safety of crocin. Wang et al. reported that crocin caused reversible and dose dependent black pigmentation of the liver, and acute hepatic damage related to discoloration. In rats orally administered with crocin daily at dose of 50 mg/kg for 8 days, the liver function was normal. However, higher daily dosage of 100 mg/kg for longer

duration, 2 weeks, induced reversible hepatic damage and black pigmentation. These results suggested that the crocin has low toxicity in rats even in high experimental dosage, which would hardly happen in human practice; therefore, crocin is safe for human consumption [84].

Hosseinzadeh et al. reported a more comprehensive study in 2010 to investigate biochemical, hematological and pathological toxic effect of crocin in mice and rats in major organs, like heart, liver, lung, spleen, and kidney. The acute toxicity studied at doses 3 g/kg given orally and i.p. once a day for 2 days, and the sub-acute toxicity at doses 15, 45, 90 and 180 mg/kg, i.p. daily for 21 days (Hosseinzadeh, Shariaty, Sameni, & Vahabzadeh, 2010). Oral and i.p. doses of 3 g/kg crocin did not cause any pathological changes and death within 2 days of study. However, there was a reduction in appetite, weight, and in alveolar size in lungs only at 180 mg/kg group compared to control group. Regardless the excessive loss of crocin in 180 mg/kg group that made the urine orange-yellow color, there was no pathologic change in kidney. The results obtained indicated that crocin at pharmacological doses less than 180 mg/kg did not cause damage to all the major organs of the body, and it might has low toxicity at 180mg/kg post long time administration [85].

In 2013, crocin tablets 20mg/day for 4 weeks were evaluated by Mohamadpour et al., for short-term safety and tolerability in healthy adult male and female volunteers. General health measures recorded before, after and during the study, such as hematological, biochemical, hormonal and urinary parameters. The results of this clinical safety evaluation showed a relatively safe and normal profile for crocin in healthy volunteers at the given doses within the trial period [86]. In addition, saffron as a whole extract has a high LD_{50}=20 g/kg, that is why recently

toxicology researchers consider it to be safe for human intake. The amount used in daily food consumption is actually much lower than the dose causing any of the reported side effects [62].

Attaching or conjugating crocin on delivery systems like nanoparticles (NPs) can improve the therapeutic effects of crocin as anticancer agent. Crocin-conjugated NPs may offer several advantages including: (1) Prolonging crocin circulation time. (2) Preserving crocin as intact form not to convert to crocetin. (3) Reducing the crocin doses concentration. (4) Specific delivering to cancer site, due to passive targeting that lead to increase accumulation of crocin in cancer tissue, because of their leaky microvessels and the lack of efficient lymphatic drainage that do not exist in normal tissue.

1.6. Nanoparticles (NPs)

Nanotechnology is a multidisciplinary branch of science, which is dynamically growing field of both academic and industrial interest. In this branch advanced materials are used for various applications such as biomedical, pharmaceutical, agricultural, environmental, and comprised different fields of science, engineering and medicine. As a result of rapid development in these fields, there is a significant increase in the development of novel nanomaterials [87-89]. The prefix ‘nano’ derives from the Greek meaning ‘dwarf’. The European Committee for Standardization defines nanomaterials as materials with an external dimension at the nanoscale, or that have nanoscale internal or surface structures. Nanoscale describes the size range from approximately 1 to 100 nm (ISO/TS 27687:2008) [88].

Various structures of nanomaterials were produced and applied such as NPs, nanocapsules, nanotubes, and nanofibers. NPs are the one of the most widely studied and used nanomaterials. NPs can be spherical, tubular, or irregularly shaped, and can

occur in the form of fused or agglomerated forms. NPs can be divided into two main types; natural and engineered. Natural NPs present in the environment result from events such as terrestrial dust storms, erosion, and volcanic eruptions that happened naturally. While, engineered NPs were manufactured by human using different materials. These materials, including metals (Ag, Zn, Au, Ni, Fe, and Cu), metal oxides (TiO_2, Fe_3O_4, SiO_2, and Al_2O_3), non-metals (silica and quantum dots), carbon (nanotubes), polymers (alginate, chitosan, hydroxymethylcellulose, and polycaprolactone), and lipids (soybean lecithin and stearic acid) [88, 89]. Some of the nanomaterials approved by Food and Drug Administration (FDA) and commercialized for biomedical applications, especially for the treatment of cancer, are listed in **Table 2** [90, 91]. Many engineered NPs have been developed for biomedical applications.

Superparamagnetic iron-oxide NPs (SPIONs) are among the different types of Engineered NPs, that are considered to be promising candidates in cancer therapeutic and diagnostic (theranostics) applications due to their unique properties. These properties include superparamagnetic behaviour, biocompatibility, flexible surface-modification, and high surface to volume ratio by virtue of their small size. These kinds of NPs are also biodegradable, because they can be metabolized, transported, and stored in proteins like ferritin, transferritin and hemosiderin [92, 93].

Due to their unique features, SPIONs have various applications in biomedical fields such as magnetic separation, biosensing, gene therapy, detection of biological entities like cells and proteins, and tissue repair. Moreover, SPIONs were investigated in the area of cancer therapeutics, where they were found to have a potential in improving the contrasting features in MRI, biological labelling, drug delivery, and hyperthermia. Recently, several SPIONs formulations have been

approved for clinical use, for MRI as contrast agents and therapeutic purposes, such as: Lumiren for bowel imaging, Feridex IV for liver and spleen imaging, Combidex for lymph node metastases imaging, and Ferumoxytol for iron replacement therapy [93-95].

Table 2: Some of the approved or marketed nanomaterials for cancer treatment.

Name	Nanomaterial/ active agent	Cancer	Status	Company/ Reference
Doxil/Caelyx 1	PEGylated liposome/doxorubicin hydrochloride	Ovarian cancer	Approved 11/17/1995 FDA50718	Ortho Biotech (acquired by JNJ)
Myocet	Non-PEGylated liposomal doxorubicin nanomedicine	Metastatic breast cancer	Approved in Europe and Canada, in combination with cyclophosphamide	Sopherion erapeutics, LLC in North America and Cephalon, Inc. in Europe
DaunoXome	Liposomal daunorubicin	First-line treatment for patients with advanced HIV-associated Kaposi's sarcoma	Approved in the USA	Galen Ltd.
ThermoDox	Heat-activated liposomal encapsulation of doxorubicin	Breast cancer, primary liver cancer	Approved	Celsion
Abraxane	Paclitaxel albumin nanoparticle	Various cancers	Approved 1/7/2005 FDA21660	Celgene
Rexin-G	Targeting protein tagged phospholipid/microRNA- 122 (Targeted gene Therapy)	Sarcoma, osteosarcoma, pancreatic cancer, and other solid tumour	Phase II/III, approved in Philippines	Epeius Biotechnologies Corp.

The concept of using magnetic NPs for drug delivery was proposed in the late 1970s by Widder and his colleagues [96, 97]. However, the idea of using magnetic NPs as a carrier that can be targeted to a certain site using external magnetic field date back to early 1940s, as a new methodology in waste water treatment [98]. Magnetite is among the most commonly studied SPIONs [87, 99].

1.7. Magnetite nanoparticles (MNPs)

MNPs are one of the most attractive used SPIONs in cancer therapy and other biomedical applications, due to their chemical stability, biodegradability, reactive surface that can be modified, and magnetic properties [89, 92-94]. Magnetite (MN) with a chemical formula Fe_3O_4 is a mineral and one of the three naturally occurring iron oxides (maghemite; γ-Fe_2O_3, and hematite; α-Fe_2O_3) [92]. MN is considered the most magnetic of all the naturally occurring minerals on Earth [100].

MN is black or brownish-black with molecular weight of 231.55 g/mol. It has a density of 5.18 g/cm^3, a melting point of 1583-1597 °C, and a hardness of 5-6 on Mohs scale of mineral hardness. The chemical name of MN according to International Union of Pure and Applied Chemistry (IUPAC) is iron (II,III) oxide, and the common name is ferrous-ferric oxide. The chemical formula of MN can also be written as $FeO{\cdot}Fe_2O_3$ [100-103]. MNPs have been widely investigated in the last decades for a wide range of applications. In biomedical applications, they have been studied as MRI contrast agent, immunoassay, detoxification of biological fluids, hyperthermia, cell separation, and drug delivery [87, 99, 104].

To be used in biomedical applications, the composition, size, charge, and surface chemistry of the MNPs are important and strongly affect both the blood circulation time as well as bioavailability of these nanoparticles within the body. In

addition, magnetic properties and internalization process of MNPs depend strongly on their size [94].

For the systemic administration, smaller particles with diameters of smaller than 10 nm can be rapidly removed by renal clearance. On the other hand, particles with diameters bigger than 100-200 nm are usually sequestered by the spleen and liver as a result of mechanical filtration and are eventually removed by the cells of the phagocyte system, resulting in decreased blood circulation times. NPs in the range of 10-100 nm are optimal, safe, and demonstrate the most prolonged blood circulation times. Most endothelial barriers allow MNPs less than 150 nm to pass, more stringent barriers, such as the blood brain barrier allow 15 to 50 nm to pass with molecular weight smaller than 500 Da [92, 94, 105-107] [102, 108].

1.7.1. MNPs Crystal structure

MN has a cubic inverse spinel structure. The large oxygen ions form a close-packed cubic lattice, with the Fe ions filling the gap between them. The iron ions in the gaps arranged in two different sites: (1) Tetrahedral site: Fe ion is surrounded by four oxygens, and form a magnetic sublattice. These sites are exclusively occupied by the smaller ferric iron Fe^{3+} atoms. (2) Octahedral site: Fe ion is surrounded by six oxygens, and form B magnetic sublattices. These sites are randomly occupied by subequal numbers of ferric (Fe^{3+}) and ferrous (Fe^{2+}) iron atoms.

The spins on the A sublattice are antiparallel to those on the B sublattice. The two crystal sites are very different and result in complex forms of exchange interactions of the iron ions between and within the two types of sites. MN exhibits a variety of characteristics that depend on the temperature [100, 109].

1.7.2. Superparamagnetism property of MNPs

MN is a ferrimagnetic material at room temperature, with populations of atoms with opposite direction of magnetic moments. Ferrimagnetic materials can be magnetized by an external magnetic field and remain magnetized after removing the external field. MN has a Curie temperature of 850 K (577ºC), which is temperature where a material's permanent magnetism changes to induced magnetism [110]. MNPs are also known as superparamagnetic; SPIONs. The term superparamagnetism refers to a specific NPs size of 1– 30 nm [111]. In other studies the size is smaller than 10 nm at room temperature [103]. Goya et al. investigated the magnetic properties of MNPs of size between 5 and 150 nm and he concluded that the magnetization was increased as the particle size decreased [112].

The bulk of MNPs contains multiple domains and expresses ferromagnetic behaviour. The material with a higher number of domains produces less internal energy, and vice versa. As the size of the particles decrease to less than 30 nm, the number of domains decreases to be single domain. In such a state of superparamagnetic behaviour, the MNPs show ferromagnetic or paramagnetic properties, according the presence or absence of external magnetic field, receptively. Paramagnetism is the type of magnetism that occurs only in the presence of an externally applied magnetic field [93, 111].

When an external magnetic field is applied, the single-domain of MNPs aligns all their magnetic moments in the same direction as this external magnetic field, resulting in a high magnetization (**Figure 4**). Due to the superparamagnetic behaviour of MNPs, they have been used as MRI contrast agents in diagnosis, as heat mediators in hyperthermia treatments and additionally as magnetic guidance in drug delivery applications [101, 103, 111].

MNPs magnetic properties strongly depend on the methods used in their synthesis. Moreover, Teja et al. reported that the magnetic properties of MNPs appeared to depend strongly on changes in the crystal morphology. The crystal morphology affects coercivity in the order: spheres < cubes < octahedra in line with the increase in the number of magnetic axes along this series of shapes. Coercivity is the intensity of the applied magnetic field required to reduce the magnetization of that material to zero after the magnetization of the sample has been driven to saturation. MNPs with coercivities ranging from 2.4 to 20 kA/m have been produced by controlling their synthesis conditions [101, 103].

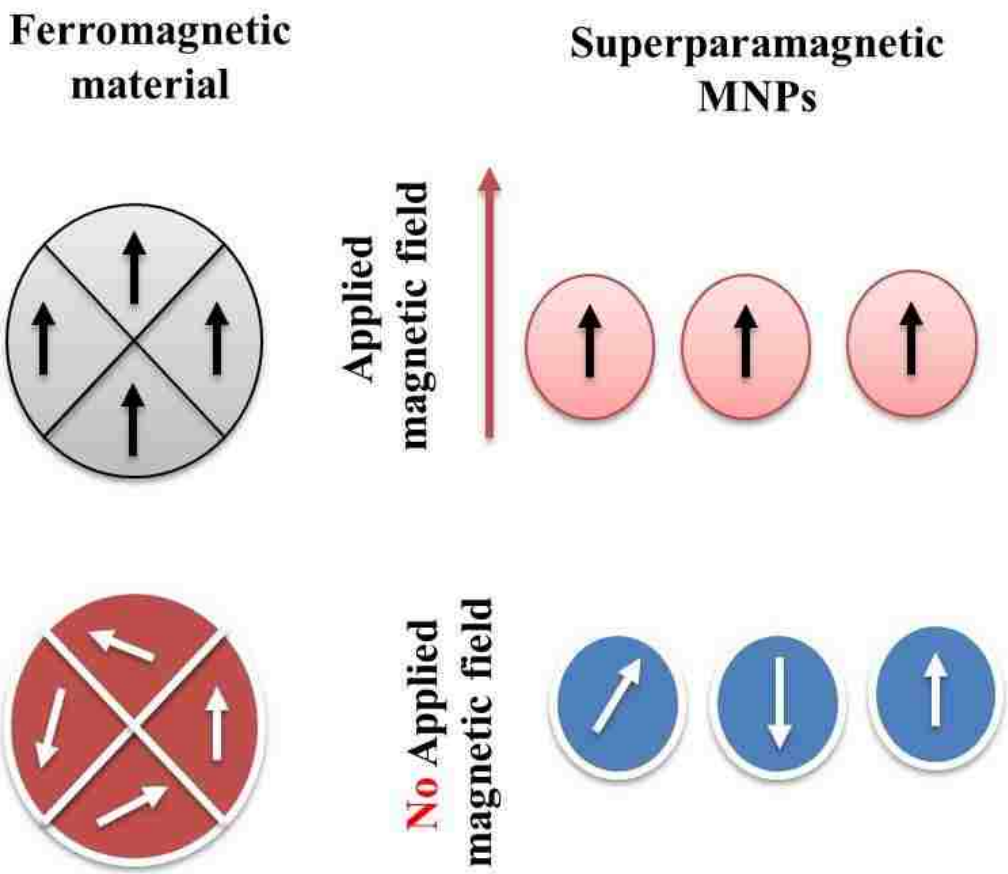

Figure 4: Diagrammatic representation of the behaviour of multiple domains of a ferromagnetic material, and the single-domain of superparamagnetic MNPs in the presence or absence of external magnetic field, modified from [113].

1.7.3. Synthesis of MNPs

Considering the increasing number of potential applications for MNPs, it is not surprising that various synthetic routes have been described with different abilities to control the size and size distribution, shape, polydispersity, surface charge, magnetic susceptibility, crystallinity, surface chemistry and the yield of production. These methods include: wet or co-precipitation, hydrothermal reactions, thermal decomposition, microemulsions, sol-gel syntheses, sonochemical reactions, hydrolysis and thermolysis of precursors, flow injection syntheses and others [102, 103, 107, 111]. Some of these methods are described in the following sections.

1.7.3.1. *Co*-precipitation method

Co-precipitation is a method where Fe^{2+} and Fe^{3+} salts co-precipitate in the presence of an alkaline aqueous media. It is the simplest, the most common, most efficient, and universally used chemical pathway to obtain MNPs. The precipitated MNPs are dark or brownish-black in colour. The chemical reaction describing precipitation of Fe_3O_4 is given in the following **equation**:

$$Fe^{2+} + 2Fe^{3+} + 8OH^- \rightarrow Fe_3O_4 + 4H_2O \qquad \textbf{Equation 1}$$

According to the thermodynamics of this reaction, a complete precipitation of MNPs should be expected at a pH between 8 and 14 where the precipitated MNPs acquire negative charges on their surfaces, while maintaining a stoichiometric ratio of 2:1 (Fe^{3+}/Fe^{2+}) under a non-oxidizing environment. Otherwise, MNPs might also be oxidized to other impure phases like maghemite. Oxidation in air is not the only way to transform magnetite into maghemite (γ-Fe_2O_3). Various electron or ion transfer incidents, depending upon the pH of the suspension, are involved, according to the following **equation:**

$Fe_3O_4 + 2H^+ \rightarrow \gamma\text{-}Fe_2O_3 + Fe^{2+} + H_2O$ **Equation 2**

This would critically affect the physical and chemical properties of the MNPs. Bubbling nitrogen gas through the solution not only prevents critical oxidation of magnetite, but also reduces the particle size when compared to methods that use an oxygenated environment [114-117].

The size, monodispersity, and shape of MNPs can be tailored or adjusted by a number of factors, such as pH, addition of alkaline solution before or after the addition of Fe^{2+}/Fe^{3+} ions solution, altering the feeding rate of the iron ions solution, ionic strength of Fe^{2+} and Fe^{3+}, stirring and soaking temperatures, nature of the iron salts, and addition of the coating layers before, during or after MNPs synthesis [111, 114, 116-118]. Despite the above mentioned advantages of the co-precipitation method, few disadvantages may arise due to experimental parameters variation, such as large particles of varying diameters, polydispersity, and poor crystallization. These disadvantages can be overcome by monitoring the previous mentioned factors [93, 102]. Several studies explored the preparation of MNPs in an oxygen-free atmosphere. For example, Iwasaki et al. prepared MNPs to test the effect of pressure on their size. These NPs synthesized using the co-precipitation method by adding alkaline solution to ferric and ferrous ions in an argon atmosphere. After that, a cooled ball mill was used as a synthesis reaction medium in which MNPs of about 10 nm were prepared by mechanochemical effect without heating the starting suspension and annealing the product [119].

Yazdani et al. sealed the reaction vessel after being filled with iron ions then injected with an alkaline solution, following which different pressures of nitrogen gas were applied. By increasing the nitrogen reaction pressure from 300 to 6000 mbar, the

particle size increased from 8.3 to 16.8 nm at 25°C [120]. In addition, Sun et al. synthesized MNPs with a size range of 8-20 nm using a modified, chemically controlled co-precipitation method. Sodium oleate, as surfactant, was added during the reaction to enhance the compatibility of the nanoparticles [121].

1.7.3.2. Hydrothermal method

A hydrothermal process was used to produce MNPs due to its advantages in producing high yield of NPs with excellent crystallinity and controllable size and morphology. Furthermore organic reagents are not needed, so this method is comparatively environmentally benign, and is relatively cost-effective [116]. In this method, synthesis of MNPs is usually carried out by precipitating ferrous and ferric ions in an alkaline medium with a molar ratio 1:2 similar to the co-precipitation method. Dilute acid is also added to avoid the precipitation of other iron oxides before the addition of alkaline solution. The mixture is then added into a nitrogen gas blanketed three neck flask and stirred at a constant rate for a short time. After that, the precipitated black product is immediately added into a Teflon-lined stainless steel autoclave and subsequently placed in a furnace at high temperature (200°C) [116, 122-125].

Control of the particle size and morphology in this hydrothermal method take place through the processes of nucleation and grain growth. Nucleation might be faster than grain growth at higher temperatures and results in a decrease in particle size. In addition, prolonging the reaction time would favour grain growth [116, 122-125].

MNPs with an average particle size of 17.22 nm were obtained at 200°C and were coated with chitosan to modify their surfaces [122]. Also, MNPs with a diameter of 27 nm were prepared by this method in the presence of a surfactant; sodium bis (2 ethylhexyl) sulfosuccinate [126]. In addition, size control using lactate and sulfate ions

was investigated by Mizutani et al., who prepared also MNPs in an argon atmosphere and then autoclaved at 120°C for 20 hr in an electric oven. The median particle size obtained varied from 9.5 to 38.6 nm. This was found strongly dependent on the stability of iron complexes and the surface potential of anions-adsorbed precipitates [127].

1.7.3.3. Thermal decomposition

MNPs with a high level of monodispersity and size control were also obtained by a thermal decomposition procedure. In this method, iron precursors decomposed in hot organic solvents in the presence of stabilizing surfactants (e.g. oleylamine, oleic acid, and steric acid) and organic solvents (such as hexane and toluene). Iron precursors include iron (III) acetylacetonate; $Fe(acac)_3$, iron pentacarbonyl; $Fe(CO)_5$, and iron (III) cupferronates; $Fe(Cup)_3$ [114, 128].

Sun et al. have described a high-temperature reaction of $Fe(acac)_3$ with 1,2-hexadecanediol in the presence of oleic acid and oleylamine to obtain monodispersed MNPs. The particle diameter could be tuned from 3 to 20 nm under a flow of nitrogen gas, and the hydrophobic particles could be transformed into hydrophilic ones by adding a bipolar surfactant [129-131]. Also, thermal decomposition of $Fe(CO)_5$ in octyl ether solution of oleic acid with consecutive aeration resulted in MNPs with a narrow size distribution. [132].

Li et al. and other researchers described the synthesis of water-dispersible MNPs in acidic or basic media by thermal decomposition of $Fe(acac)_3$ [133-136] or inexpensive ferric chloride ($FeCl_3$) in refluxing 2-pyrrolidone. The latter is not only a high boiling solvent but also a stabilizer because of its coordination capacity with metal ions. According to the reflux time, size could be controlled to obtain MNPs with diameters of 4, 12 and 60 nm [134].

1.7.4. Desirable features of MNPs

Using different manufacturing procedures, the desirable features of synthesized MNPs for biomedical applications, specifically cancer treatment, are: stable at physiological pH, with high magnetization, size is 10-100 nm in diameter to avoid elimination from biological system, narrow size distribution, high reactive surface, biocompatible, biodegradable and able to respond to stimuli, such as magnetic field, heat, and pH.

However, there are significant issues with naked MNPs that affect and reduce their efficacy in cancer treatment application, including:

1) They tend to agglomerate and aggregate, because of hydrophobic–hydrophobic interactions between the MNPs, and magnetic properties with a large surface area to volume ratio.
2) Because of their agglomeration, they will be rapidly eliminated from the circulation; hence their half-life will be short.
3) They have low stability and dispersibility.
4) They are toxic, because they circulate inside the body without any specific interaction with the organs or tissues.

To overcome these issues, the development of a proper surface coating is needed to improve MNPs efficacy in clinical applications [116, 137-141].

1.7.5. Surface modification of MNPs

The surface coating of MNPs with various coating materials play an important role in the stabilization of aqueous MNPs suspensions, as well as in their further functionalization. The surface modifications provide and offer the following advantages for MNPs [87, 99, 104, 142, 143]:

1) Reduce the agglomeration.
2) Improve their stability in various solvents to extend their half-life and blood circulation time in physiological conditions.
3) Control their growth and size.
4) Prevent the oxidation of MNPs.
5) Improve their biocompatibility and reduce toxicity.
6) Limit non-specific cell binding by being targeted.
7) Modify the physical and chemical properties of MNPs, such as electronic, optical, spectroscopic, and surface charge
8) Provide functional groups for further modification, such as attachment of optical dyes, therapeutic and targeting agents
9) Reduce of the therapeutic drugs dose quantity.

The stabilization of the MNPs is crucial to obtain magnetic colloidal ferrofluids that are stable against aggregation in a biological medium and a magnetic field. MNPs coatings can be comprised of several types of materials, including monomeric stabilizers such as carboxylates and phosphates, polymeric, non-polymeric like oleic acid, and stearic acid, liposomes, micelles, and inorganic materials such as silica and gold [87, 89, 94, 102]. These materials together with various surfactants, such as sodium oleate, dodecylamine and sodium dodecyl sulfate (SDS), are all used to enhance dispersibility of the NPs in the solution, and they bind differently to their surfaces. Some researchers explored the use of more than one coating materials (such as co-polymers) to coat MNPs to perform specific functions. The NPs coating can be achieved via a number of approaches, including pre-synthesis, in situ coating and post-synthesis [94, 116, 144,

145]. **Table 3** list examples of FDA clinically approved organic-materials coated MNPs [90, 91, 146].

Table 3: Examples of FDA clinically approved, commercially available organic-materials coated MNPs, commonly used as contrast agents in MRI imaging (except NanoTherm for hyperthermia treatment).

Name (half-life)	Size (nm)	Target	Coating type	Status	Company
Feridex IV/ Endorem (8-30 minutes)	80-150	Liver/spleen	Dextran	Approved	Berlex Laboratories
Resovist/supravist	80-150	Liver/spleen	Carboxy-dextran	Approved	Bayer Schering Pharma
Combidex (25-30 hrs)	15-30	Lymph node metastases	Dextran	Phase III	AMAG Pharma
Clariscan (45–120 minutes)	20	Tumor microvasculature	PEG	Discontinued due to safety concern	Nycomed Imaging
GastroMARK (4 -7hrs)	400	Bowel	Silicone	Approved	AMAG Pharma
Abdoscan	300	Bowel	Sulphonated styrene-divinybenzene	Approved	Nycomed Imaging
Feraheme (15hrs)	30	Vasculature	Polyglucose sorbitol carboxymethylether	Phase II	AMAG Pharma
NanoTherm (hyperthermia)	10-20	In situ injection (e.g. brain & prostate cancer)	aminosilane	Approved	MagForce, Nanotechnologies AG

1.7.5.1. Surface modification with polymeric materials

Polymeric coatings prevent the agglomeration of the MNPs and limit their non-specific cell binding in the biological system. Structural features of the polymeric coatings may affect the performance of coated MNPs. These include the nature of the chemical structure of the polymer (such as hydrophobicity and biodegradation characteristics), the length or molecular weight of the polymer, the type of chemical bond in which the polymer is attached (for example covalent bonding), the conformation of the polymer, and the degree of particle surface coverage. Polymeric coating materials are classified into natural and synthetic. Examples of natural polymers are dextran, chitosan, starch, and cellulose. The synthetic polymers include polyethylene glycol (PEG), poly-vinylpyrrolidone and poly-ethyleneimine. Dextran and chitosan are two of the most commonly used natural and synthetic polymers will be discussed in details in the following sections [114, 117, 118, 144, 147, 148].

1.7.5.1.1. Dextran

Dextran is a natural branched polysaccharide polymer comprised of glucose subunits, which can be prepared with sizes ranging from 10 to 150 kDa. Dextran has been widely used as a polymeric coating mostly because of it is biocompatibility, non-toxicity and polar interactions (chelation and hydrogen bonding) that give dextran a high affinity towards MNPs surfaces. Dextran bind to MNPs surface by covalent bond between oxygen and iron II and III ions along the MNPs surfaces [94, 116, 118, 149]. In 1982, Molday and Mackenzie were the first to report the formation of MNPs in the presence of dextran. They prepared MNPs by a co-precipitation method with *in situ* coating by dextran of 40 kDa molecular weight and produced MNPs with 15-30 nm in diameter. Since then, various forms of dextran polymers, including carboxydextran and

carboxymethyl dextran were used to coat surfaces of MNPs with varying hydrodynamic sizes [148, 150, 151].

Other approaches were also explored for applying dextran coating onto MNPs. Sonvico et al. modified the surfaces of MNPs with amino-propylsilane, followed by covalent conjugation of partially oxidized dextran via a secondary amine bond. Another study performed by Woo et al., who modified the hydrophobic surface of MNPs to hydrophilic via Fe-S covalent bond with bi-functional 3-mercaptopronic acid, and then the terminal carboxylic acid group was esterified with dextran to improve biocompatibility [149, 150]. Mykhaylyk et al. also prepared MNPs via precipitation from iron (II) sulphate aqueous. Then the surface of freshly prepared MNPs were immediately modified by spontaneous adsorption of dextran from aqueous solution. The modified MNPs (24 nm in diameter) were able to target rat glial tumors by disrupting the blood-brain barrier immediately prior to particle injection [137, 152].

1.7.5.1.2. Chitosan

Chitosan is one of the most abundant natural linear poly-aminosaccharide, hydrophilic, non-toxic, biocompatible, and biodegradable polymer. It has enormous applications in the pharmaceutical industry, such as drug carrier, absorption enhancement, gene delivery, and is a metal chelating agent. Chitosan possesses both amino and hydroxyl functional groups, which can bind with other functional molecules that are commonly used as targeting, imaging and therapeutic agents (Jana Chomoucka et al., 2010; Dash, Chiellini, Ottenbrite, & Chiellini, 2011). Chitosan is soluble in acidic media and is also used as a surfactant agent. Adding chitosan on the surface of the MNPs will enhance their stability and biocompatibility to be used in different applications [94, 115, 153-156].

Several studies have investigated the preparation of chitosan coated MNPs for different applications. For examples, Tran et al. and Boddu et al. formed chitosan coated MNPs (C-MNPs) to remove metal ions pollutants from aqueous solution [157-159]. C-MNPs were prepared by co-precipitation of MNPs in the presence of chitosan followed by hydrothermal treatment. Another study used C-MNPs as MRI contrast agent, which can be used for cell tracking, cancer detection and therapeutically response assessment [122, 160-162]. Similarly, Kim et al. synthesized MNPs by sonochemical method. From these MNPs, they synthesized ferrofluids for use as MRI contrast agents by coating them with oleic acid as a cross-linker and then dispersing them in chitosan, yielding spherically shaped MNPs with 15 nm in diameter [94, 163]. In a study carried out by Qu et al. C-MNPs with core-shell structure with 11 nm in diameter have been prepared using cross-linking method. Oleic acid modified MNPs were firstly prepared and then chitosan was added to coat the surface of the MNPs by physical absorption. The C-MNPs were obtained by cross-linking the amino groups on the chitosan using glutaraldehyde (cross-linker) [155, 161, 164].

1.7.5.2. Surfactant coating material

1.7.5.2.1. SDS

SDS is one of the most used anionic alkyl sulfate surfactants. SDS synthesis is a relatively simple procedure involving the sulfation of 1-dodecanol followed by neutralization with a cation source. Because of its high reactive surface properties, it is important in industrial cleaners, and cosmetics. In addition, it has been used in different kinds of industrial manufacturing procedures, as a delivery aid in pharmaceuticals, and in biochemical research [165, 166]. In the physiological system, SDS can enhance absorption of chemicals through skin, gastrointestinal mucosa, and other mucous

membranes. SDS is known for its fast uptake, distribution, and excretion. It accumulates selectively in the hepatopancreas and gall bladder, and gets absorbed via the intestine, colon, and skin. Metabolism procedure of SDS takes place by proceeding from initial omega-oxidation to a carboxylic acid, then to beta-oxidation to butyric acid 4-sulfate, which is finally non-enzymatically de-sulfurated to gamma-butyrolactone and inorganic sulfate. SDS stimulates both physical and biochemical effects on cells, and specifically targets the membrane [165].

Shariati et al. investigated the ability of S-MNPs to efficiency remove the safranin O dye from waste water. In this study, MNPs were synthesized via co-precipitation method in the presence of SDS to the mixture solutions of iron ions. The effects of various parameters on the removal efficiency of dye, such as the type and amount of surfactant, pH of solution, salt effect, and contact time were studied and optimized. The results suggested that S-MNPs with size less than 40 nm can be used as an efficient adsorbent material for adsorption of cationic dyes from aqueous solutions with high removal at acidic media pH 2 [166]. On the other hand, S-MNPs were synthesized by Adeli et al. using a co-precipitation method. S-MNPs prepared herewith were applied for the removal and recovery of copper, nickel and zinc from industrial waste water due to high concentration of these metal ions in the real samples. The obtained results reported that S-MNPs were efficient adsorbent material for removal of the metal ions from wastewater samples [167].

1.7.6. Surface functionalization of MNPs

The modified surfaces of the MNPs not only stabilize the magnetic core, but they can also provide functional groups for further modification. Those functional groups can bind to different molecules, such as targeting agents, optical dyes, therapeutic agents,

enzymes, and nucleic acids. When the MNPs functionalized with more than one type of molecule, they are termed multifunctional. These molecules can be conjugated on the surface or incorporated within MNPs. They also can bind to the modified surface by chemical bonds or by avidin-biotin protein coupling technique. These chemical bonds include amide, ester, hydrogen and other bonds. The functionalization of MNPs surface is a method for tuning the overall properties of particles to fit targeted applications [87, 92-94].

Surface modification of MNPs using functional molecules has different tasks to fulfil, such as:

1) Improve the mechanical and chemical performance of the modified surface of the MNPs.
2) Improve the effect of anti-cancer drugs/bioactive molecules.
3) Target desired chemical, physical, or biological environments.

In the current study, crocin has been selected to be added to the surface of dextran coated MNPs. It was found that among several new drug delivery systems, functionalized MNPs have emerged as a promising technology to deliver crocin to their site of actions. By reducing the uptake of crocin by phagocytic cells, prolonging crocin circulation time, preserving crocin as intact form and passively accumulate in the tumour location, leading to improve the therapeutic effect of crocin versus free crocin [87, 92-94].

1.8. Aims of the study

Crocin has been shown to have the potential of inhibiting tumorigenesis in a variety of cancers including hepatocellular carcinoma. Among several drug delivery systems, MNPs coated with natural polymers like dextran have emerged as a promising technology to deliver biomolecules to their target site of actions. Coated MNPs can improve the therapeutic effects of crocin as anti-cancer agents versus free crocin because of several reasons. These reasons include that coated MNPs can reduce the uptake by phagocytic cells, prolong the circulation time, and passively accumulate in the cancer areas due to the leaky microvasculature and the lack of efficient lymphatic drainage in those sites.

The main objective of the present study was set to mainly assess the anti-cancer effect of crocin-loaded NPs both *in vitro* and *in vivo*.

The detailed objectives are:

1. To prepare and characterize MNPs with uniform particle size distribution, and to conjugate their surfaces with different biocompatible organic coatings.
2. To load crocin efficiently onto the functionalized MNPs.
3. To assess anti-cancer effects of crocin-loaded NPs *in vitro* utilizing HepG2 cells.
4. To develop HCC animal model utilizing Balb/c mice and then assess the anti-cancer effect of crocin-loaded NPs.

Chapter 2: Materials and Methods

2.1. Pure MNPs

Chemicals used to prepare pure MNPs included iron (II) chloride tetrahydrate ($FeCl_2$-$4H_2O$), iron (III) chloride ($FeCl_3$), sodium hydroxide (NaOH) and ammonia solution. All reagents were analytical-grade and were purchased from Sigma-Aldrich (St. Louis, MO, USA). Aqueous solutions of Fe^{2+} and Fe^{3+} were separately prepared by dissolving the respective amounts of $FeCl_2$-$4H_2O$ and $FeCl_3$ in de-ionized water. An aqueous solution of NaOH of pH 13 was also prepared by dissolving the corresponding amount of NaOH in de-ionized water. A 50 ml aqueous NaOH solution was heated at 60-90^oC in an open round flask. A mixture containing equal volumes of Fe^{2+} and Fe^{3+} was injected into the NaOH solution at feeding rates of 20, 40 or 60 ml/hr using syringe pump with vigorous stirring. At the end of addition, a brownish-black precipitate was formed. The whole solution was vigorously stirred for 60 minutes at a constant temperature, which is the same as the stirring temperature; 60-90^oC. MN suspensions were then soaked at 60, 75 or 90 ^oC for 24 hrs in the incubator. To study the effect of varying the ionic strengths of the starting solutions on the characteristics of the formed NPs, Fe^{2+}/Fe^{3+} solutions containing 0.075/0.15, 0.15/0.3, 0.3/0.6 or 0.6/1.2 were prepared and initially injected in the NaOH aqueous solution at the optimized feeding rate, stirring and soaking temperatures.

The MN suspensions were then centrifuged at 3000 rpm for 15 minutes followed by a successive decantation/washing with 12% ammonia solution for 3 times to maintain high basic conditions. After final decantation, MN deposits were collected and dried at

60 ºC for 24 hrs. Dried powders were finely ground to be characterized for its composition, morphology, surface area, magnetic susceptibility, and magnetization.

Based on the experiments carried out in the previous section, lists of optimized conditions were obtained. A mixture containing equal volumes of ferrous and ferric salts was injected into the 5M NaOH solution at feeding rates of 40 ml/hr using a syringe pump with vigorous stirring. At the end of the addition, a brownish-black precipitate was formed. The whole solution was vigorously stirred at the same constant temperature 60°C for 60 minutes. MNPs suspensions were then soaked at 60ºC for 24 hrs without stirring. The MNPs suspensions were then centrifuged at 3000 rpm for 15 minutes followed by successive decantation/washing with 25% ammonia solution three times. After the final decantation, the MNPs deposits were collected and dried at 60°C in the incubator for 24 hrs. The dried powders were finely ground to be characterized in respect of their composition, morphology, surface area, and magnetic properties.

2.2. Functionalization of MNPs

MNPs were chemically functionalized by applying organic coatings onto its surfaces. Three types of biocompatible organic compounds were considered; SDS, chitosan and dextran. The chemical structures of these compounds are shown in **Figure 5**. In the following sections, the method of applying each of the coatings will be explained:

2.2.1. SDS-coating onto MNPs

To prepare SDS-coating MNPs, similar process as described above was repeated with the SDS being initially dissolved in 50 ml water at concentrations of 0.2, 0.5, 1.0 and 2.0% by weight. Each of these solutions was added to 50 ml of 5M NaOH solution prior to injection of the $Fe^{2+/}Fe^{3+}$ solution. SDS dissolved gradually when the

temperature increase to 60°C. The injection of 0.3 M of Fe^{2+} and 0.6 M of Fe^{3+} iron ions into 5 M NaOH solution was at a feeding rate of 40 ml/hr at 60°C in a normal atmosphere. At the end of addition, a brownish precipitate was formed. The whole solution was vigorously stirred at 60^{o}C for 1hr. SDS-coated MNPs (called S-MNPs hereafter) suspensions were then soaked at 60ºC for 24 hrs without stirring. The S-MNPs suspensions were then centrifuged at 3000 rpm for 15 minutes followed by successive decantation/washing with 25% ammonia solution three times. Then S-MNPs deposits were collected and dried at 60°C in the incubator for 24 hrs. The dried powders were finely ground to be characterized for their composition, morphology, surface area, and magnetic properties.

2.2.2. Chitosan coating onto MNPs

To prepare chitosan-coating MNPs, chitosan solutions containing 0.2, 0.5, 1.0 and 2.0 % by weight were prepared by dissolving the corresponding weight of chitosan in a 0.2 % acetic acid solution. An equal volume of each of the chitosan solutions (around 50 ml) was vigorously blended with 0.3 M of Fe^{2+} and 0.6 M of Fe^{3+} solutions (25ml Fe^{2+} + 25 ml Fe^{3+}), and then injected into 5M NaOH solution at a feeding rate of 40 ml/hr at 60°C in a normal atmosphere. At the end of addition, a brownish precipitate was formed. The whole solution was vigorously stirred at a constant temperature of 60^{o}C for 1hr. Suspensions of chitosan-coated MNPs (called C-MNPs hereafter) were then left to cool to room temperature. The suspension was then decanted and centrifuged at 3000 rpm for 15 minutes followed by a successive decantation/washing with 25% ammonia solution for 3 times. After washing out the un-attached chitosan, a Benedict's test was used to confirm the complete removal of unattached chitosan. C-MNPs were

finally dried in air at 60^{o}C for 24 hrs. Completely dried powders were finely ground and characterized for their composition, morphology, thermal and magnetic properties.

2.2.3. Dextran-coating onto MNPs

To prepare dextran-coating MNPs, dextran solutions containing 0.2, 0.5, 1.0 and 2.0 % by weight were prepared by dissolving the corresponding weight of dextran in a 5M NaOH solution (dissolved completely at room temperature). MN precursors (0.3 M of Fe^{2+} and 0.6 M of Fe^{3+} iron salt solutions) were separately prepared, then injected into the NaOH solution at a feeding rate of 40 ml/hr at 60°C in air. At the end a brownish precipitate was formed. The whole solution was vigorously stirred at 60^{o}C for 1hr. Suspensions of the dextran-coated MNPs (called D-MNPs hereafter) were then left to cool to room temperature. This was followed by decantation, washing the completely dried. Dry powders were finely ground and characterized for their composition, morphology, thermal and magnetic properties.

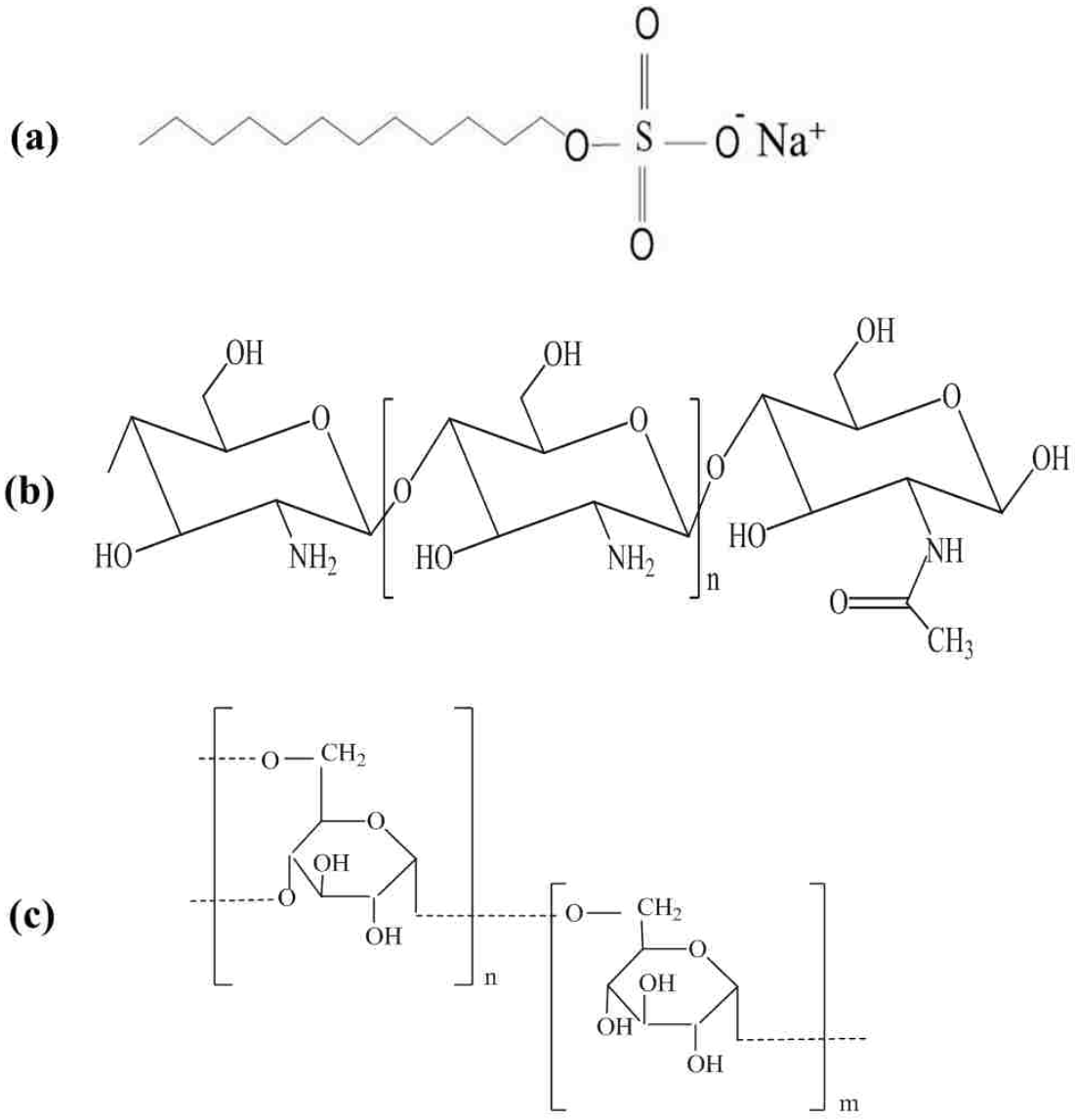

Figure 5: Schematic representation of chemical structures of organic coatings. a) SDS, b) chitosan and c) dextran.

2.3. Benedict's test

A Benedict's test was used to detect the un-attached chitosan and dextran in the coated MNPs solutions. A Benedict reagent was prepared by dissolving 173 g sodium citrate and 100 g sodium carbonate in about 500 ml de-ionized water. Separately, 17.3 g copper sulfate was dissolved in about 100 ml de-ionized water. After that both solutions were mixed together with stirring and the volume was completed to 1000 ml with de-ionized water. To test for unattached chitosan or dextran, few drops of the test solution were added to 2ml of Benedict reagent, and then boiled for five minutes in a water bath. Formation of coloured precipitate qualitatively indicates presence of chitosan or dextran in the solution.

2.4. Addition of cross linker and crocin to D-MNPs

Based on the characterization results of the organic-coated MNPs, 1.0 weight % of dextran coating MNPs were chosen for further functionalization with crocin. However, it was found that a linker molecule was required to be immobilized onto the D-MNPs prior to be functionalized with crocin. To do that, pre-calculated amounts of 1.0% D-MNPs were suspended in autoclaved de-ionize water and under sterilized conditions until completely dried. The dry powders were divided into two groups: one group D-MNPs with a linker but without crocin (negative control), and another D-MNPs group with linker and crocin. The preparations of the D-MNPs groups were performed simultaneously.

Synthesis of the D-MNPs derivatives were carried out in a dry fresh dimethylacetamide (DMAC), as a solvent in the absence of moisture. Succinic anhydride was added to the groups in a large excess (D-MNPs: succinic anhydride, 1:20). The succinic anhydride-D-MNPs mixture in DMAC was stirred at 90°C for 8 hrs

in oil bath in a closed environment. At this point, the two groups were treated differently. D-MNPs with linker but without crocin: unreacted succinic anhydride, from the above mixture, was removed by repeated washing of the D-MNPs with sterile de-ionized and stored in fresh sterile de-ionized water. D-MNPs with linker but with crocin: the second group of D-MNPs was washed three times with DMAC to remove un-bound succinic anhydride. Each step was followed by centrifugation at 3000 rpm for 15 minutes at room temperature and decantation for 3 times. After that, fresh DMAC and 2 mmol of 1-ethyl-3-(3-dimethylaminopropyl) carbodiimide hydrochloride (EDCI.HCl) were added to D-MNPs with stirring at room temperature for 12 hrs under moisture-free conditions.

Following that, 50 or 100 mg/ml Crocin (Sigma-Aldrich, St. Louis, MO, USA) was added to the DMAC mixture and stirred for 24 hrs at room temperature. Coated NPs centrifugation and washing with sterile de-ionized water were thoroughly carried out 6 times at 4000 rpm, 15°C for 15 minutes. The resultant crocin-loaded D-MNPs were precipitated and re-suspended in de-ionized water. UV-Visible spectroscopy and Fourier transform infrared (FTIR) spectroscopy were performed to confirm the presence of crocin onto the surfaces of D-MNPs. It should be mentioned that D-MNPs with crocin samples were named according the concentration tested *in vitro* or *in vivo,* 2 mg/ml, 3 mg/ml or 4 mg/ml crocin-loaded D-MNPs formulations.

2.5. Calculation of the crocin loading

Crocin conjugation efficiency was determined by an indirect method. Indirect method involved detection of total free crocin concentration in the decanted solutions, after reaction, by measuring the absorbance at 440 nm (visible range) using a UV–Visible spectrophotometer. The amount of crocin loaded in (or entrapped within) the D-

MNPs was calculated by the difference between the total amount of crocin initially used to prepare the NPs and the amount of free crocin present in the decanted solutions [168, 169]. Then the loading efficiency was calculated as the following **equation:**

$$Loading\ \ efficiency\ (\%) = \frac{(amount\ of\ loaded\ crocin)}{(amount\ of\ \ initially\ added\ crocin)}\ x\ 100 \quad \textbf{Equation 3}$$

2.6. Characterization techniques

All neat and coated MNPs were characterized for their composition, morphology and properties using various characterization techniques:

The composition was studied by X-ray diffraction (XRD), FTIR spectroscopy, and thermogravimetric analysis (TGA). An automated Phillips X-ray diffractometer (Phillips, Amsterdam, Netherland), with a step size of 0.02^o, scan rate of 2^o per min, and a scan range from $2\theta = 10^o$ to 70^o was used on dry sample. FTIR analysis was conducted using a Nicolet Nexus 470 infrared spectrophotometer (Massachusetts, USA), where samples were pre-pressed with KBr, then scanned over the normal range of 4000–400 cm^{-1}. Thermogravimetric analysis (TGA) was carried out using a TGA-50 Shimadzu thermogravimetric analyser (Kyoto, Japan), where pre-weighed powder samples were heated to 600°C at a heating rate of 20°C/min using aluminium pan in air, and the percent weight loss was followed and correlated with the original composition of the NPs.

Solid NPs samples were evaluated for their microstructures using a JEOL Scanning electron microscopy (SEM; XL-30 Phillips, Amsterdam, Netherland) at an accelerating voltage of 15 kV. Detailed description of the morphology of the NPs was examined by Transmission electron microscopy (TEM; CM10-Phillips Amsterdam, Netherland). Samples were prepared for imaging by spreading drops of NPs diluted

dispersion on a copper grid that was coated with a thin layer of carbon and then air dried.

Porosity, pore size distribution and pore volume of the dried solid samples were measured using liquid nitrogen adsorption at 77 K employing a Quantochrome NOVA 1000 volumetric gas sorption instrument; Autosorb (Boynton Beach, FL,USA).

Magnetic properties of the NPs were studied by measuring the magnetic susceptibility of the neat and coated NPs as a function of coating concentration. Moreover, the magnetization of these NPs as a function of applied magnetic field at room temperature and was measured using a vibrating sample magnetometer (VSM, Quantum design Inc, San Diego, CA, USA) instrument.

2.7. *In vitro* release study of crocin

Crocin release behaviour of the prepared crocin conjugated D-MNPs was studied in physiological pH (7.4) as well as in acidic media at pH 5.5. Two samples of 2 and 4 mg/ml crocin loaded D-MNPs with 3 mg Fe/ml were prepared in 1.5 ml of 1x phosphate buffered saline (PBS) at pH values 5.5 and 7.4. The samples were kept in the incubator at 37ºC under constant mixing. In order to determine crocin concentration, and thereby follow up the time dependent crocin release profile, clear 1.5 ml of supernatant samples were taken out after precipitating the NPs at pre-determined time intervals. Each removed volume was replaced by 1.5 ml of fresh buffer solution of the same pH value. Then the NPs were maintained back at 37 ºC after mixed and re-suspended properly. The concentration of drug released was determined by UV–Visible spectrophotometry at 440 nm and using calibration curve of free crocin. The percentage of crocin released was calculated as in the following **equation**:

$$Release\ (\%) = \frac{(amount\ of\ free\ crocin\ \text{ in supernatant after release test})}{(amount\ \text{of crocin initially in D−MNPs before release test})}\ x\ 100 \qquad \textbf{Equation 4}$$

To calculate the percentage of cumulative release of crocin, individual percentage release values were added to each other.

2.8. *In vitro* cytotoxicity

HepG2, a human hepatocellular carcinoma cell line, was purchased from American Type Culture Collection (ATCC, Manassas, VA, USA). The cells were maintained in 75 cm^2 culture flasks using Dulbecco´s Modified Eagle´s Medium (DMEM) (Life Technologies, Grand Island, NY, USA), supplemented with 10% heat-inactivated fetal bovine serum (Life Technologies, Grand Island, NY, USA) and 1% penicillin/streptomycin. Cells were grown in 5% CO2 at 37 °C and 100% humidity. Media were changed every 48 hrs, and the cells were sub-cultured after 5 - 6 days using 1x trypsin- Ethylenediaminetetraacetic acid (EDTA), (Life Technologies, Grand Island, NY, USA).

2.8.1. MTT Assay

The viability of HepG2 cells was determined by measuring the reduction of 3-[4,5-dimethylthiazol-2-yl]-2,5-diphenyl tetrazolium bromide (MTT) to insoluble purple formazan (Sigma-Aldrich, St. Louis, MO, USA). The yellow tetrazolium salt MTT is reduced by metabolically active cells, in part by the action of dehydrogenase enzymes (reductase) in mitochondria, to generate reducing equivalents such as NADH and NADPH. The resulting intracellular purple formazan can be solubilized and quantified by spectrophotometry. So the living cells were purple, while dead cells were colourless.

HepG2 cells were seeded at density of 8000 cells/well in a 96-well plate for 24 hrs for the cells to attach to the plate. Then, the medium was changed into fresh medium

with following treatments. Various concentrations of crocin including 0.025, 0.05, 0.5, 3, 5, 8, 10, 15 or 20 mg/ml were tested. Different iron concentrations including 0.05, 0.07, 0.09 or 0.1 mg Fe/ml in D-MNPs were tested. Cells were incubated with 3 mg/ml crocin, D-MNPs and 3 mg/ml crocin-loaded D-MNPs. D-MNPs that have been tested contained 0.09 mg/ml (9 µg/100 µl) iron content in D-MNPs [3]. After 72 hrs incubation period, cells were washed with 1x PBS and then 100 µl new medium was added to each well in addition to 20 µl of MTT (5 mg/ml). Cells were then incubated at 37°C for 1 hr. After that the formazan solubilized using 100 µl isopropanol for 30 minutes at room temperature and the absorbance was measured at 560 nm.

All the tested groups were well dissolved/suspended in DMEM prior incubating them with the cells. The relative cell viability (%) related to control wells containing cells culture medium without any treatment was calculated as the following **equation**:

$$Cell\ viability\ (\%) = \frac{(\text{Absorbance of tested compound})}{(\text{Absorbance of control})}\ x\ 100 \quad \textbf{Equation 5}$$

2.9. *In vivo* study

2.9.1. Animals

Balb/c mice were obtained from the animal facility of the College of Medicine and Health Sciences, UAE University. Animals were housed under a 12 hrs light/dark cycle each at 24–26°C. They were maintained on standard laboratory animal diet with food and water *ad libitum*. All animal studies were carried out in accordance with, and after approval of, the Animal Research Ethics Committee of the College of Medicine and Health Sciences, UAE University.

2.9.2. Experimental design

In the present study, 3-weeks old male Balb/c mice were used. These mice were randomly divided into 2 groups; **Normal** group (n=3) which did not receive any treatment and **experimental** group (n=9). The experimental group was treated with 50 mg/kg body weight of DEN (Sigma-Aldrich, St. Louis, MO, USA) dissolved in saline (0.9% NaCl) and given i.p. injections twice a weeks for 8 weeks, total of 16 injections. Then, the mice of **experimental** group were randomly divided into four sub-groups (n=3) and injected intravenously (i.v.) in the tail as the following: **Sub-group 1** (**DEN-induced)** received 100 µl of saline twice a week for two weeks, total of 4 injections. **Sub-group 2 (Crocin)** received 100 µl of crocin dissolved in saline twice a week for two weeks, total of 4 injections. The injected concentrations were 11 mg/kg or 22 mg/kg in two different experiments. **Sub-group 3 (Crocin-loaded D-MNPs)** received 100 µl of 11 mg/kg or 22 mg/kg crocin loaded D-MNPs formulations in saline twice a week for two weeks, total of 4 injections. The injected concentrations were equivalent to 17 mg Fe/kg (0.3 mg Fe/100 µl) of D-MNPs as iron concentration in the two different formulation experiments. This dose was chosen 0.3 mg/100µl twice a week for two weeks was reported non-toxic [170].

At the end of experimental period, that was 24 hrs after the last i.v. injection, mice were weighed, anesthetized by mild Diethyl ether and dissected **(Figure 6).** The whole liver was removed, weighed, and examined for the presence of visible lesions or tumour. The right lobe was cut into small parts and fixed in 10% buffered formalin for 24 hrs. Fixed tissues were then processed for dehydration in ascending grades of ethanol (70% and 90% each for 1 hr, after that 100% twice and each was for 2 hrs). Tissues were then cleared in xylene and finally impregnated and embedded in paraffin.

A total of 4 different livers (representative of each normal and experimental groups) were embedded in the same block. Paraffin tissue blocks were cut at 5 microns thickness, mounted on gelatine-coated slides and then used for histopathological and immunohistochemical (IHC) studies **(Figure 7)**. For histopathological examination the slides were stained with hematoxylin and eosin (H&E).

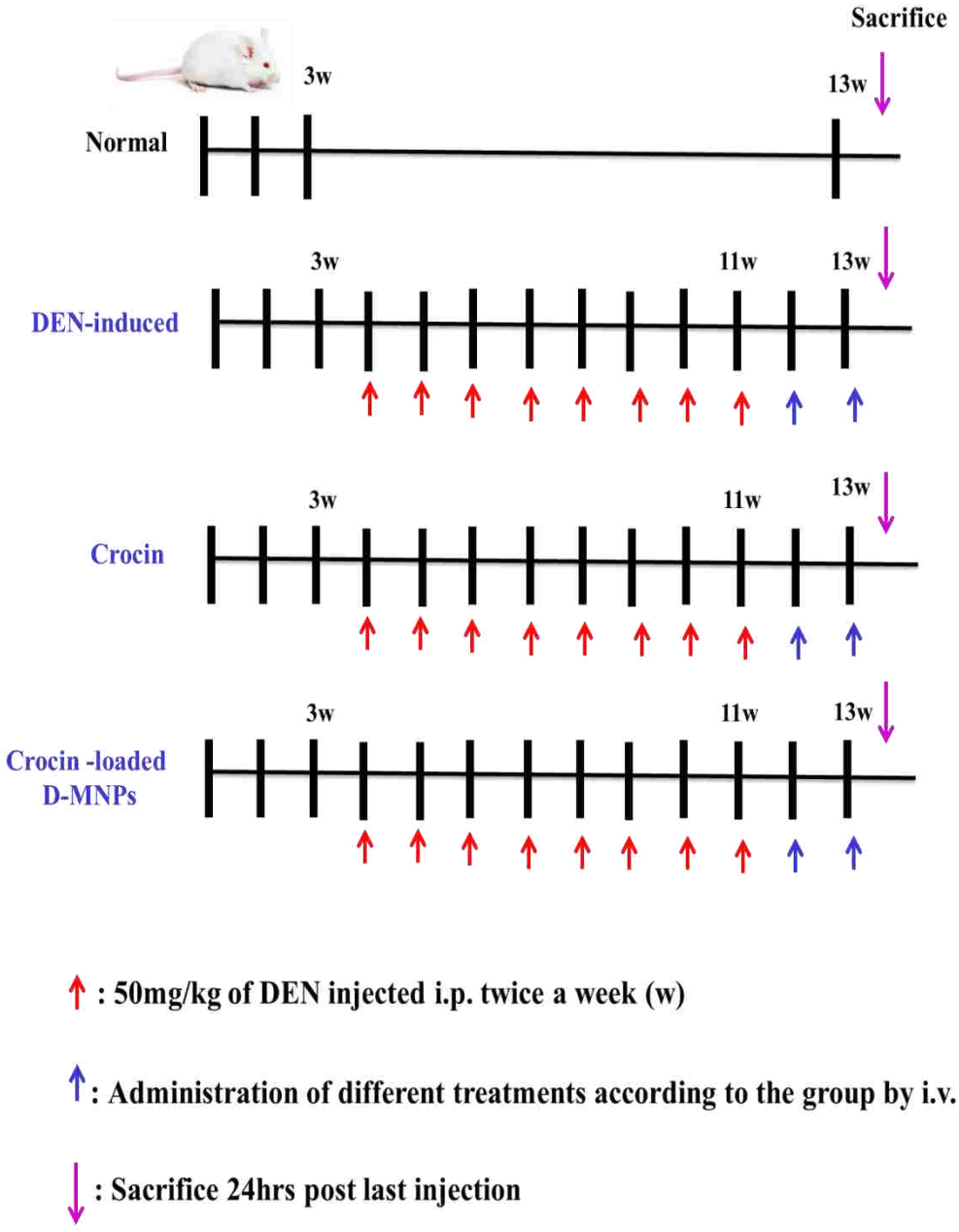

Figure 6: A diagram representing the treatment regime of the DEN-induced animal model and groups assignment.

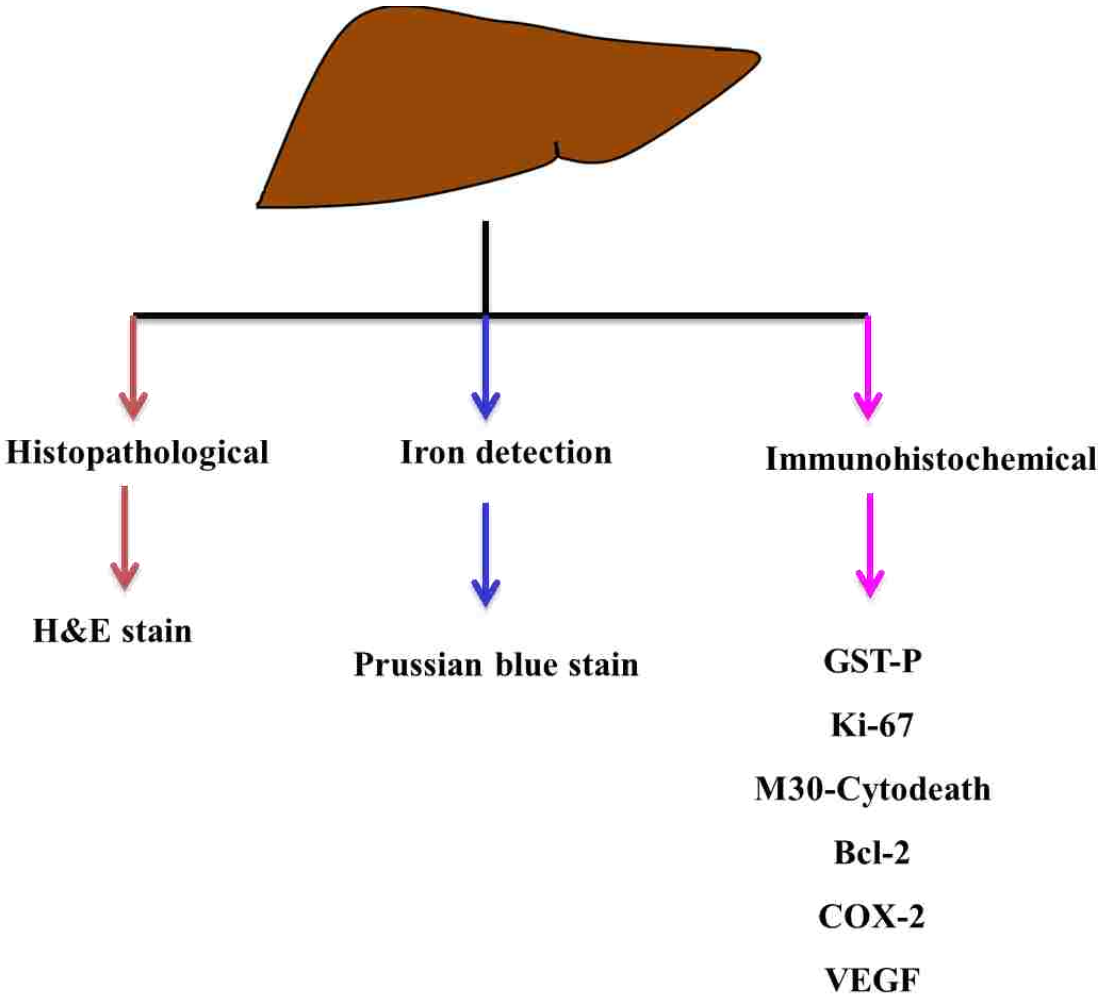

Figure 7: Diagrammatic representations of liver sections that were processed to perform several studies.

2.9.3. Prussian blue stain

Prussian blue staining was used to study the presence of iron. Tissue sections were deparaffinized in xylene, rehydrated in descending grades of ethanol (100%, 95%, 90%, 70% and 50% each for 3 minutes), and washed in distilled water. Equal parts of ready prepared solutions of 20% hydrochloric acid and 10% potassium ferrocyanide were mixed immediately before used for slide incubation for 35 minutes. Sections were washed with distilled water and counterstained with neutral red for 25 minutes or with H&E stain.

2.9.4. Immunohistochemistry (IHC) studies

Liver tissue sections were deparaffinized in xylene, rehydrated in descending grades of alcohol (100%, 95%, 90%, 70% and 50% each for 3 minutes), and washed in 1x PBS. Sections were incubated in antigen retrieval solution 10 mM Citrate buffer at pH 6 and heated at 98°C for 45 minutes. To inhibit endogenous peroxidase activity, sections were incubated in 3% hydrogen peroxide in methanol for 1 hr at room temperature. A circle with a thin film using PAP-pen (Dako, Glostrup, Denmark) was draw around the tissue sections to ensure that all tissue sections were exposed simultaneously to the same solution/ reagents.

To ensure similar conditions to all tissue sections, all the tested groups were run at the same time and slide using similar conditions. Tissue sections from all tested animal groups were included on the same slide (Normal, DEN-induced, Crocin, and Crocin-loaded D-MNPs). To block non-specific binding, sections were incubated in 1% bovine serum albumin containing 0.5% Tween-20 in 1x PBS for 45 minutes. Sections were then incubated 1 hr at room temperature or overnight at 4°C with rabbit polyclonal primary antibodies as mentioned in **Table 4.**

Following a PBS wash, tissue sections were incubated with biotinylated donkey or sheep anti-rabbit antibodies (Jackson ImmunoResearch, West Grove, PA, USA; 1:500) for 2 hrs at room temperature. To use avidin-biotin-peroxidase complex (ABC) method, Extravidine peroxidase conjugate (Sigma-Aldrich, St. Louis, MO, USA; 1:1000) was added for 1 hr at room temperature in 1% bovine serum albumin. The antigen-antibody binding sites were revealed by using 3,3'-diaminobenzidine tetrahydrochloride (DAB, Sigma-Alrdich, St. Louis, MO, USA). Some of the tissues were counterstained briefly with the hematoxylin being added for around 1 minute. After that sections were dehydrated through graded ethanol, cleared in xylene and mounted using DPX. Negative control slides were prepared by replacing the primary antibody with PBS.

Table 4: Primary antibodies used for IHC studies.

Antibody	**Dilution factor**	**Incubation Time**	**Manufacture**
Glutathione S-transferase placental form (GST-P)	1:1500	1hr	MBL Co.,Ltd., Nagoya, Japan
Ki-67	1:1000	1hr	Abcam, Cambridge, MA, USA
M30-Cytodeath	1:100	Overnight	Roche, Penzberg, Germany
Bcl-2	1:200	Overnight	Abcam, Cambridge, MA, USA
COX-2	1:200	Overnight	Abcam, Cambridge, MA, USA
VEGF	1:100	Overnight	Abcam, Cambridge, MA, USA

2.9.5. Quantification analysis of primary antibodies expression

To provide a quantification evaluation of the primary antibodies expression in the stained tissue, DAB labeled tissue sections were calculated using a computerized method. This method depended on automated process of quantification of DAB stained cells in different tissue samples, by using digital image processing via Image Pro 6 software. The method was estimating the percentage (%) area of expression per image or field at 400 magnifications. A total of 20 fields per antibody labeled tissue sections were quantified. The automated quantification was followed, because it minimized the human error and gave more accurate data.

2.10. Statistics

The resulted data were represented as mean ± the standard error of the means. The mean of the groups were compared using GraphPad Prism 5 software and one-way analysis of variance (ANOVA) with Tuckey post-hoc procedure. Data were considered significantly different at a value of $P \leq 0.05$ and highly significant at $P \leq 0.001$.

Chapter 3: Results and Discussion

3.1. Characterization of pure MNPs

MNPs were prepared in the current study using a modified wet method in air. Formation of different types of iron oxides in aqueous media has been studied from the electrochemical point of view using Pourbaix diagrams [171]; **Figure 8**. In highly basic aqueous media, Pourbaix diagrams indicated that other phases such as FeO_4^{2-}, Fe_2O_3, $Fe(OH)_2$ and $HFeO^{2-}$ may also exist under these conditions. These phases could be distinguished from each other using various characterization techniques such as XRD and FTIR. In addition, MN, Fe_3O_4, has been viewed as an assembly of FeO and Fe_2O_3 within a unified crystal lattice of MN [172].

When synthesized in air, FeO gets oxidized to Fe_2O_3, leaving a phase-pure Fe_2O_3, according to **Equation 6:**

$$2(FeO.Fe_2O_3) + ½\ O_2 \rightarrow 3\ Fe_2O_3 \qquad \textbf{Equation 6}$$

$$Fe_3O_4 + ¼\ O_2 + 4½\ H_2O \rightarrow 3Fe\ (OH)_3 \qquad \textbf{Equation 7}$$

Oxidation reactions shown in **Equations 6 and 7** explain why synthesis of MNPs in alkaline media in air has been always abandoned to avoid the formation of phase-impure Fe_3O_4. However, if solutions were pre-adjusted to be highly alkaline prior the addition of Fe^{2+} and Fe^{3+} ions then MN would be spontaneously precipitated as the highest thermodynamically stable phase despite the fact that all preparations were carried out in air. In the current study, aqueous media used for the preparation of MNPs were pre-adjusted at a pH 13 using NaOH to avoid the formation of non-MN phases.

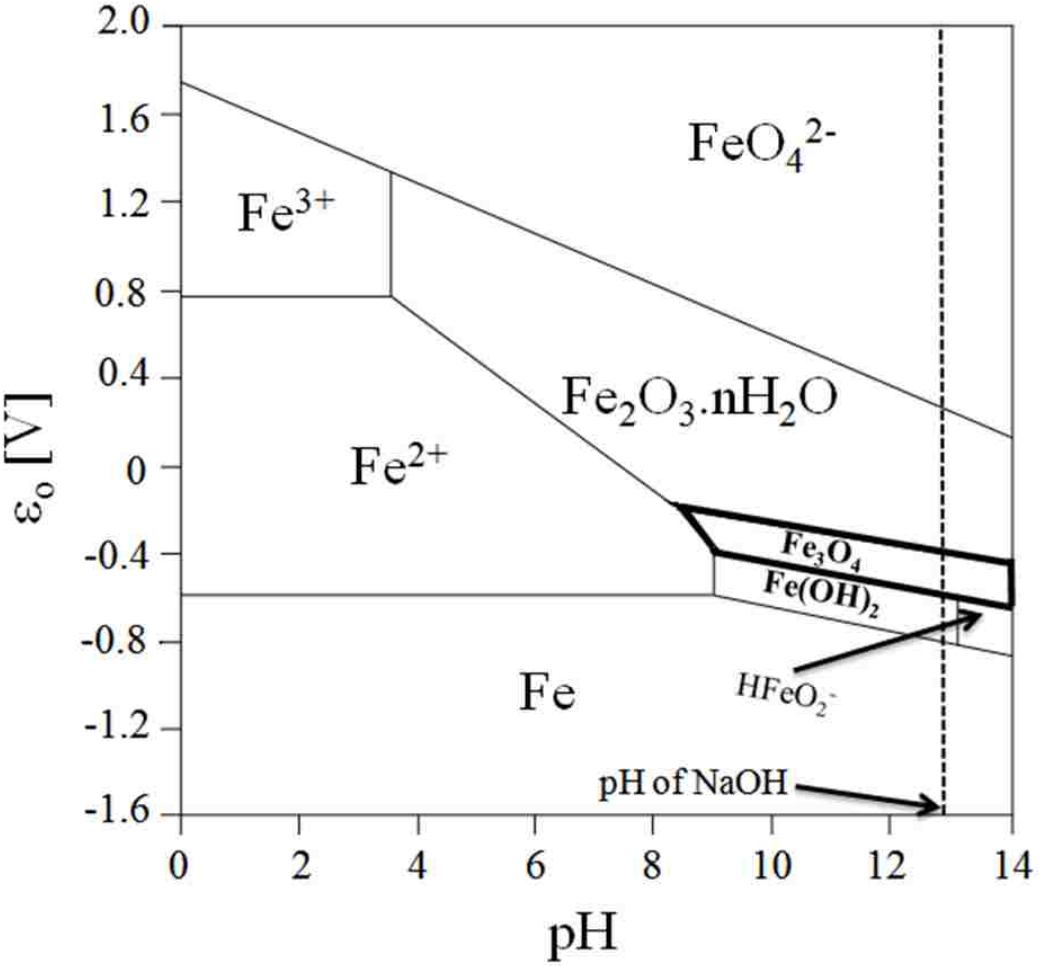

Figure 8: Pourbaix diagram for the iron-water system showing the thermodynamically stable phases in aqueous solutions with various pH values.

Various parameters were investigated for their effect on the purity of the deposited MNPs. **Figure 9** shows XRD patterns of the phases evolved during the formation of MN as a function of the feeding rate, while keeping the stirring and soaking temperatures as well as the starting concentrations of Fe^{2+} and Fe^{3+} constant.

The XRD patterns in **Figure 9** compare the phase purity and crystallinity of MNPs formed at feeding rates 20, 40 or 60 ml/hr. A standard JCPDS pattern of pure MN is also shown for comparison. At a fast feeding rate of 60 ml/hr, the deposited MN nuclei rapidly formed and accumulated without further crystallization leading to an amorphous phase, which also shows a relatively weak intensity peak at 2θ value of 35.2º for the 311 plane. These results indicated the need for a slower rate of addition of the iron reactants. At a slower feeding rate of 40 ml/hr, relatively more time was given for the deposited nuclei to crystallize. This was even increased by decreasing the feeding rate to 20 ml/hr, as indicated by the presence of the MNPs characteristic peaks at 2θ values of 29.9º (220), 35.2º (311), and 43.1º (400). In addition to these findings, no indication for the presence of non-MN phases was observed despite the fact that the entire preparation process took place in air.

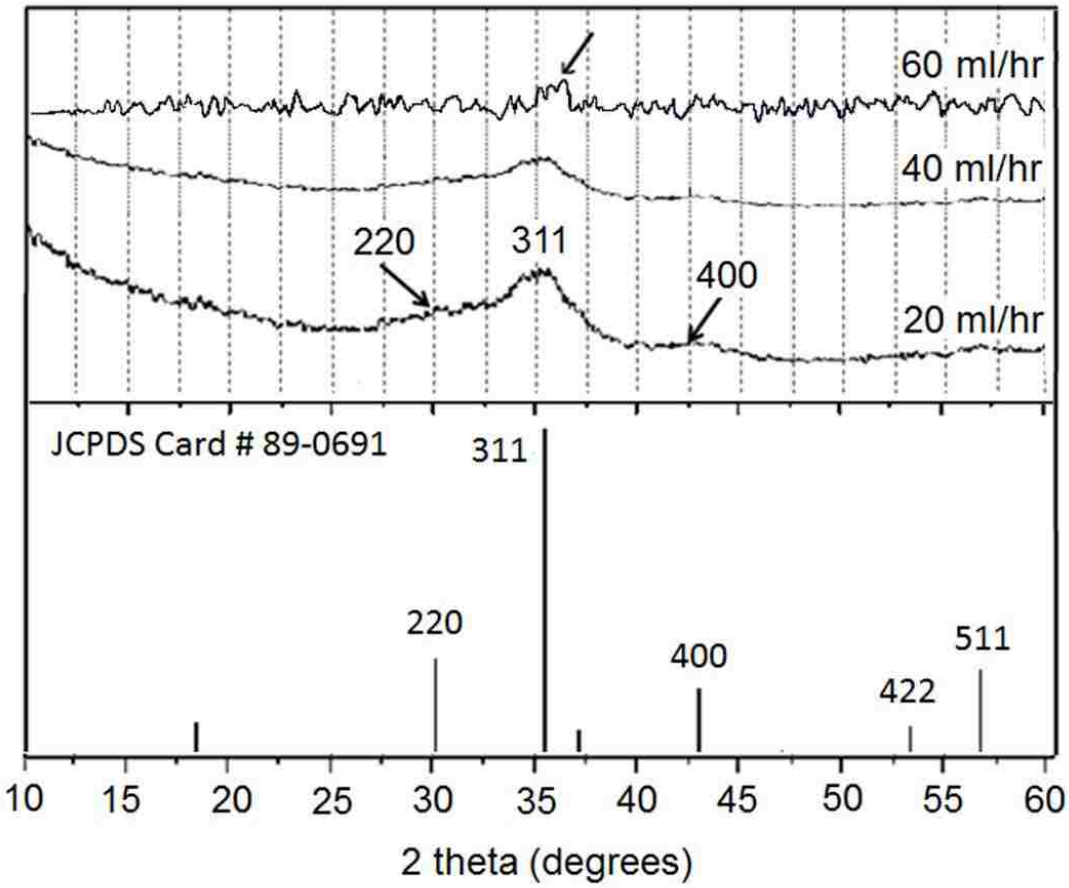

Figure 9: XRD patterns of solid MNPs prepared at different feeding rates of Fe^{2+} and Fe^{3+} aqueous solutions. JCPDS: Joint Committee on Powder Diffraction Standards.

Figure 10 shows SEM micrographs of agglomerates of MNPs prepared at different feeding rates. These micrographs indicate the formation of rounded NPs with homogeneous size distribution at all feeding rates. The average agglomerate size and surface area of the deposited MNPs is shown in **Table 5-black colour**. Despite the difference in crystallinity of the formed NPs at different feeding rates, a less pronounced variation in the average particle size was detected.

Given the phase purity of MNPs formed at these conditions, a feeding rate of 40 ml/hr was chosen for the optimization of the following preparation parameters. Stirring temperature during and after the addition of the Fe^{2+} and Fe^{3+} ions to the pre-adjusted alkaline solution was varied at 60, 70, 80 or 90 ºC. This is shown in **Table 5-blue colour** to have a pronounced effect on the average particle size and surface area of the formed NPs without affecting the overall crystallinity or purity of the MNPs. The least agglomerate average particle size of 55 nm was achieved at a stirring temperature of 60ºC. Size increased by raising the stirring temperature up to 90ºC.

Figure 11 shows SEM micrographs of agglomerates of MNPs prepared under different stirring temperatures. An overall homogeneous size distribution of the NPs forming these agglomerates is evident. Moreover, increasing the size of the NPs with increasing the stirring temperature was also reflected in an increase in the size of the agglomerates.

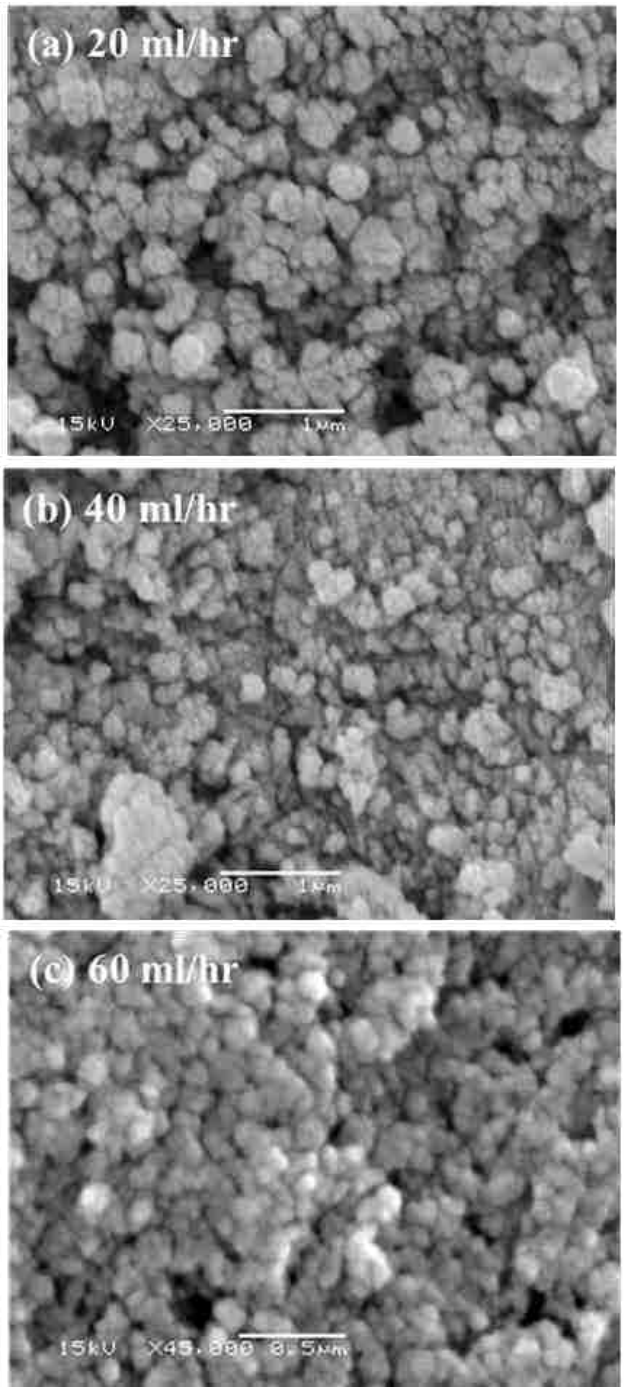

Figure 10: SEM micrographs of agglomerates of MNPs prepared at different feeding rates. a) 20ml/hr, b) 40ml/hr and c) 60ml/hr.

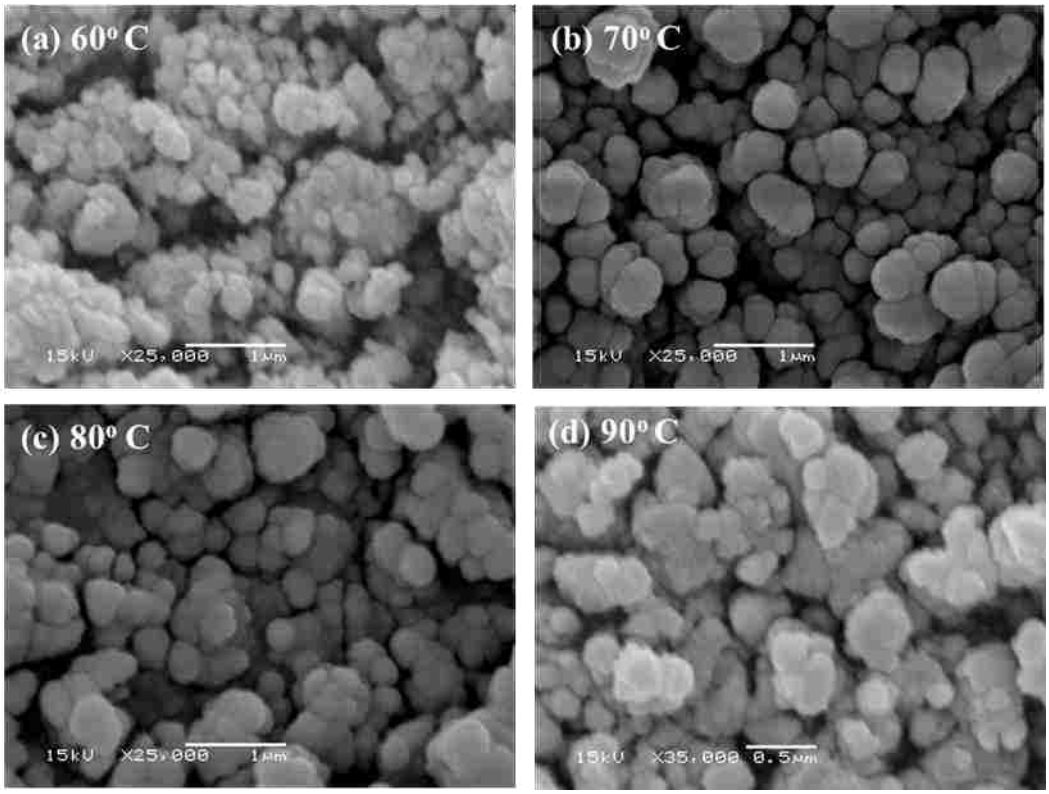

Figure 11: SEM micrographs of agglomerates of MNPs prepared under different stirring temperatures. a) 60°C, b) 70°C, c) 80°C and d) 90°C.

Previous researchers showed that only kinetic factors control the growth of the crystal. In a coprecipitation process where Fe^{2+} and Fe^{3+} ions are added at the same time, the mechanism of precipitation of MNPs takes place over two stages [102]. The first stage involves a short burst of nucleation as the concentration of the species reached critical super-saturation. This step is followed by a slow growth of the nuclei by diffusion of the ionic species in solution to the surface of the formed MN crystallites as in **Figure 12**. This step is believed to be enhanced by increasing the stirring temperature during the addition of the iron species**.**

Moreover, and in contrast to an average size of 15 and 26.5 nm of the MNPs obtained at a stirring temperature of 80 ºC under N_2 gas in the work of Zhang et al. [173] and Lee et al.[174], the relatively higher size obtained in the current study; at 60 ºC, could be attributed to the fact that all preparations were carried out in air. At a lower temperature range (4–37 ºC), and using $NaNO_2$ as an oxidant, a controlled oxidation of Fe^{2+} in an alkaline media under N_2 gas took place forming MNPs with a size range of 30–100 nm [175]. Although reactants used in this system were different from the currently studied one, its findings indicate that despite the presence of N_2 atmosphere, NPs with a relatively large size could be obtained at temperatures below 60 ºC.

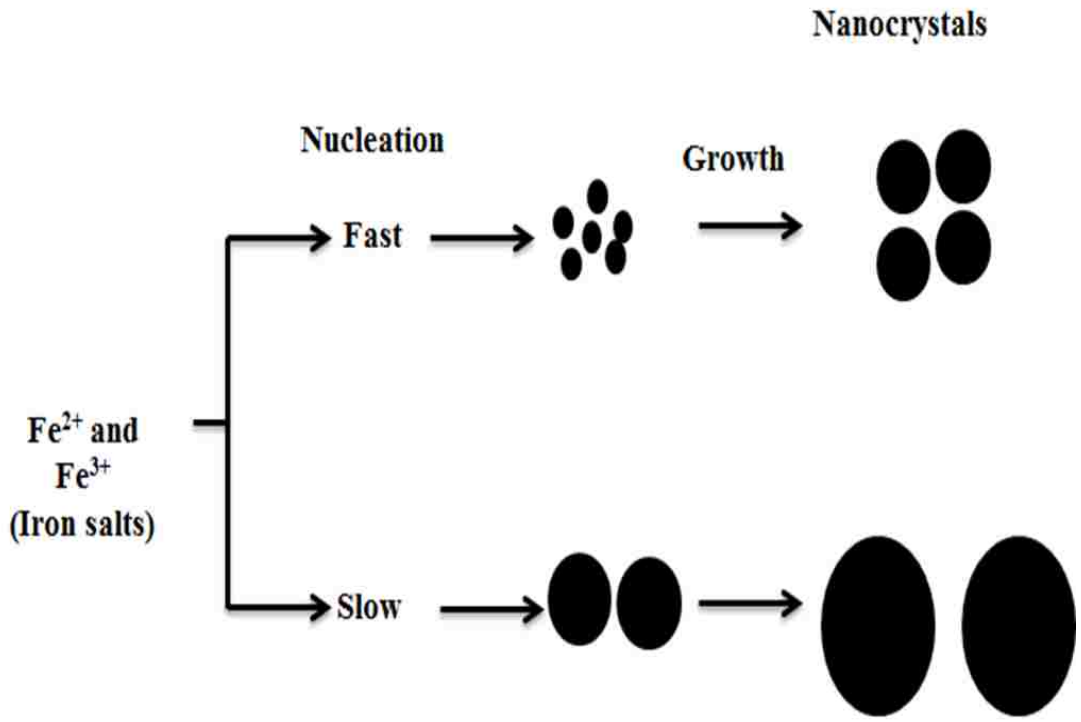

Figure 12: Diagrammatic representation of the nucleation and growing process of MNPs, modified from [176].

After complete addition of reactants, precipitated MNPs were maintained in contact with their alkaline solutions for 24hr at soaking temperatures of 60, 75 or 90 ºC (**Table 5-red colour**). Soaking of the MNPs at relatively high temperatures following their co-precipitation was previously shown to enhance crystallinity, which was also shown to be a function of the soaking temperature [177].

The effect of varying the soaking temperature on the average particle size and surface area of the NPs is given in **Table 5-red colour.** No change was observed in the size and surface area of the NPs when the suspensions were soaked at the same temperature as that maintained during the addition and stirring of reactants. Increasing the soaking temperature up to 90ºC led to an increase in the particle size accompanied by a consequent decrease in the surface area of the formed NPs. This indicates that the observed growth of the formed NPs is temperature-dependent. It should be mentioned that varying the soaking temperature did not affect the crystallinity of the formed NPs. It was, therefore, recommended to maintain the stirring and soaking temperatures at the same value whereas the optimized temperature was at 60ºC at a 40 ml/hr feeding rate.

Based on these findings, MNPs prepared in solutions containing different concentrations of Fe^{2+} and Fe^{3+} were further characterized in more details. These concentrations included: 0.075/0.15, 0.15/0.3, 0.3/0.6 and 0.6/1.2 of Fe^{2+} and Fe^{3+}, respectively. The data shown in **Table 5-green colour** indicate that doubling the initial concentrations, while maintaining a fixed solution volume, resulted in a pronounced increase in the agglomerate average size of the precipitated NPs, with a consequent decrease in the surface area of the NPs. This was also shown in the SEM micrographs of these samples; as shown in **Figure 13.** This was also reflected in an increase in the crystallinity of the formed MNPs.

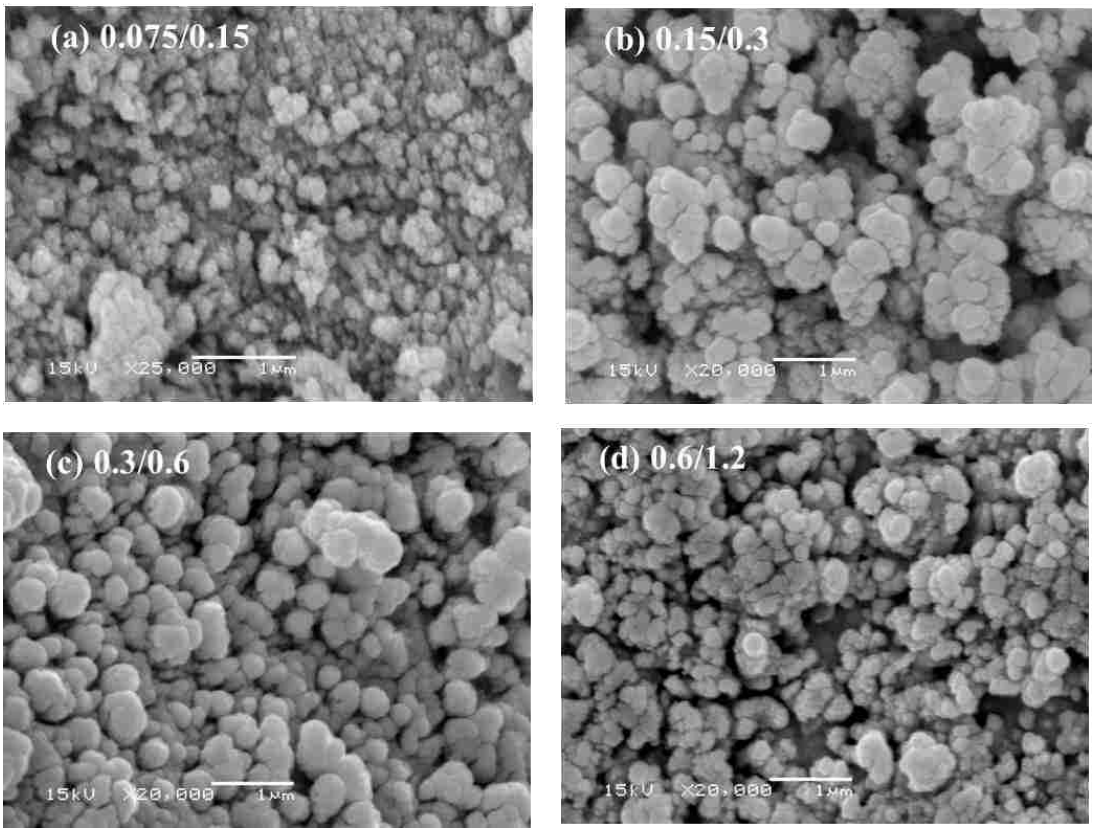

Figure 13: SEM micrographs of different concentrations of Fe^{2+} and Fe^{3+}. a) 0.075/0.15, b) 0.15/0.3, c) 0.3/0.6 and d) 0.6/1.2 of Fe^{2+} and Fe^{3+}, respectively.

Table 5: Effect of different conditions on the agglomerate average particle size and surface area of MNPs prepared by a co-precipitation in an aqueous solution.

$[Fe^{2+}]/Fe^{3+}]$	**Feeding Rate (ml/hr)**	**Stirring Temperature (^oC)**	**Soaking Temperature (^oC)**	**Average Particle Size (nm)**	**Surface Area (m^2/g)**
0.30/0.60	20	60	60	76	197
0.30/0.60	40	60	60	55	215
0.30/0.60	60	60	60	85	167
0.30/0.60	40	60	60	55	215
0.30/0.60	40	70	60	165	140
0.30/0.60	40	80	60	290	81
0.30/0.60	40	90	60	350	72
0.30/0.60	40	60	60	55	215
0.30/0.60	40	60	75	165	140
0.30/0.60	40	60	90	189	122
0.075/0.15	40	60	60	25	460
0.15/0.30	40	60	60	40	230
0.30/0.60	40	60	60	55	215
0.60/1.20	40	60	60	175	162

Figure 14 shows XRD patterns of MNPs prepared using different initial concentrations of the starting iron ions. Peaks appeared at 2θ values of 29.9º (220), 35.2º (311), 43.1º (400), 53.4º (422), 57.1º (511), and 62.8º (440) were observed in all samples, and were consistent with the standard data of phase-pure MNPs shown in **Figure 9** [102, 174]. Despite the fact that the current experiments were carried out in air, no sign of oxidation of the formed MN was found, reflecting its chemical stability. The relative broadening of the peaks at 29.9º, 35.3º and 62.8º in samples made of solutions containing Fe^{2+}/Fe^{3+} 0.075/0.15 ratio is attributed to relatively small particle size, which is known to be as a result from dilute solutions [174], and is shown in **Figure 13a**. The absence of maghemite in the XRD patterns of the MNPs prepared in the current study confirms the phase purity of the prepared MNPs.

Figure 15 shows a FTIR spectrum of a selected MNPs sample prepared in solutions containing initial concentrations of 0.3 and 0.6 M of Fe^{2+} and Fe^{3+} ions, respectively. Bands at wavenumbers of 430, 584and 622 cm^{-1} are characteristic to the Fe-O stretching absorption in MN phase, while the broad band around 3400 cm^{-1} is characteristic to the stretching mode of absorption of the O-H bond in the physically adsorbed water molecules [178]. Being prepared in aqueous media, MNPs show the presence of physically adsorbed water molecules even after drying in air, since there is no possibility for water molecules to be included within the crystalline structure of MN.

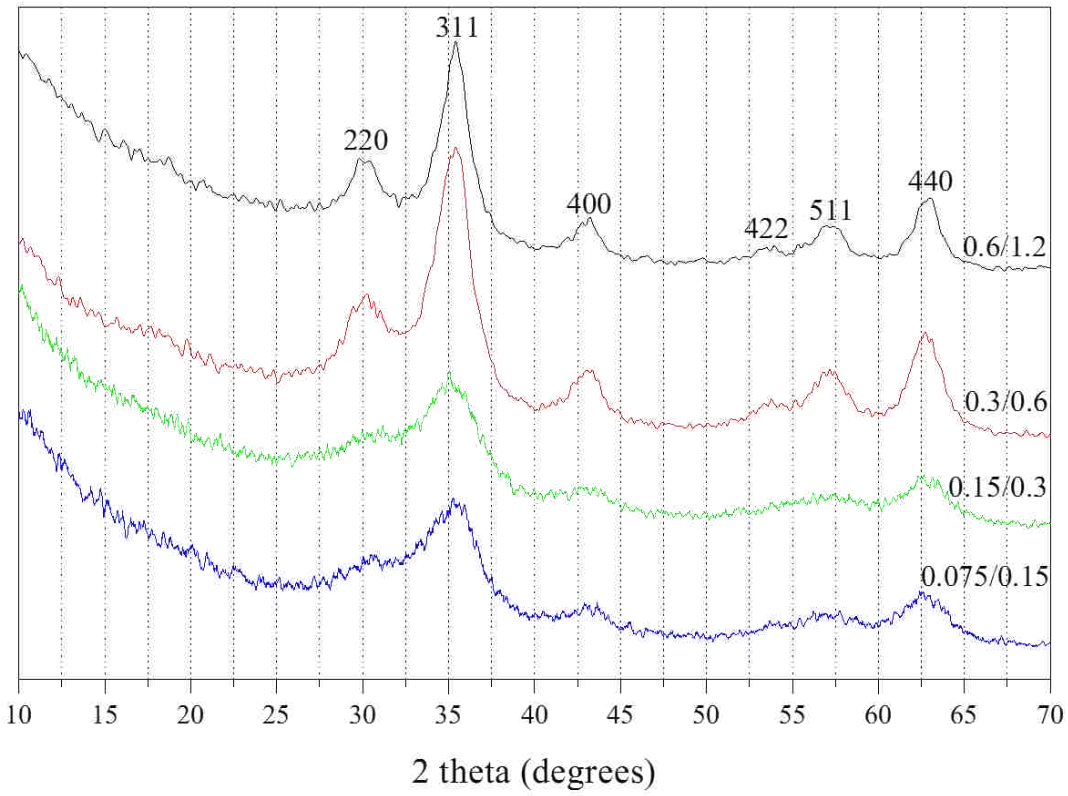

Figure 14: XRD patterns of MNPs prepared using different initial concentrations of the starting iron ions Fe^{2+}/Fe^{3+}.

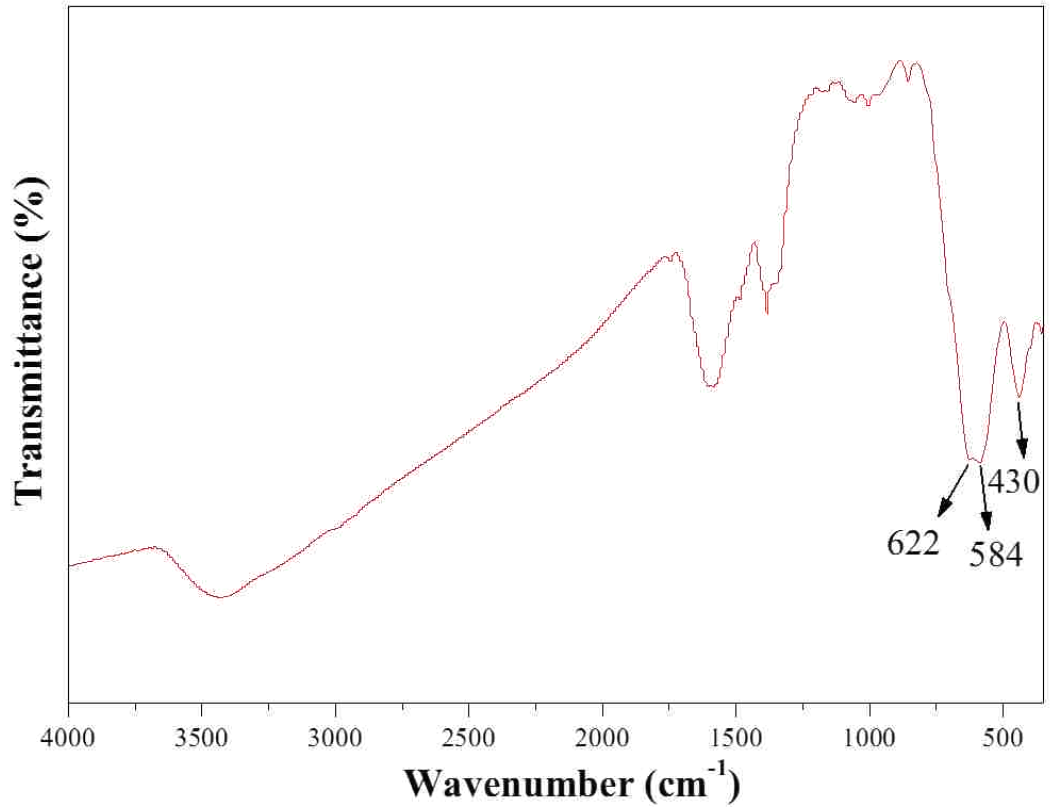

Figure 15: FTIR spectrum of MNPs sample containing initial concentrations of 0.3 and 0.6 M of Fe^{2+} and Fe^{3+} ions, respectively.

The presence of physically adsorbed water was also confirmed by TGA analysis; **Figure16**, which shows the percent weight loss of solid MNPs when heated up to 600^{o}C in air. These TGA curves were collected for MNPs samples that were prepared from solutions containing various concentrations of the initial Fe^{2+} and Fe^{3+} solutions. All samples showed weight loss values in the range of 14–17% taking place at a mid-temperature of 100 ºC. This is attributed to the evaporation of the physically adsorbed water. This loss continued to take place with a slower rate as temperature increased. This could be attributed to the presence of multi layers of water of hydration onto the surfaces of the NPs. It should be mentioned that after complete dryness of all powders, NPs were highly agglomerated, which a common characteristic of small NPs is prepared in aqueous media [101, 111].

The MNPs prepared in the current study are intended to be used as drug delivery vehicles to treat hepatic cancer. Therefore, in addition to biocompatibility of the NPs, size and surface area of the NPs are considered important parameters that will determine the affinity towards the immobilization of drugs onto their surfaces as well as the efficiency of drug delivery. MNPs prepared from solutions containing various initial concentrations of the Fe^{2+} and Fe^{3+} ions were subjected to surface area, porosity and pore size distribution measurements using liquid Nitrogen adsorption technique. **Figure 17** shows the adsorption isotherms of N_2 on agglomerated powders prepared under these conditions. All samples showed hysteresis loops of type IV where the lower curve represents the adsorption of N_2 gas on the surfaces of the NPs, while the upper curve represents the progressive withdrawal; desorption, of the adsorbed N_2 gas [179].

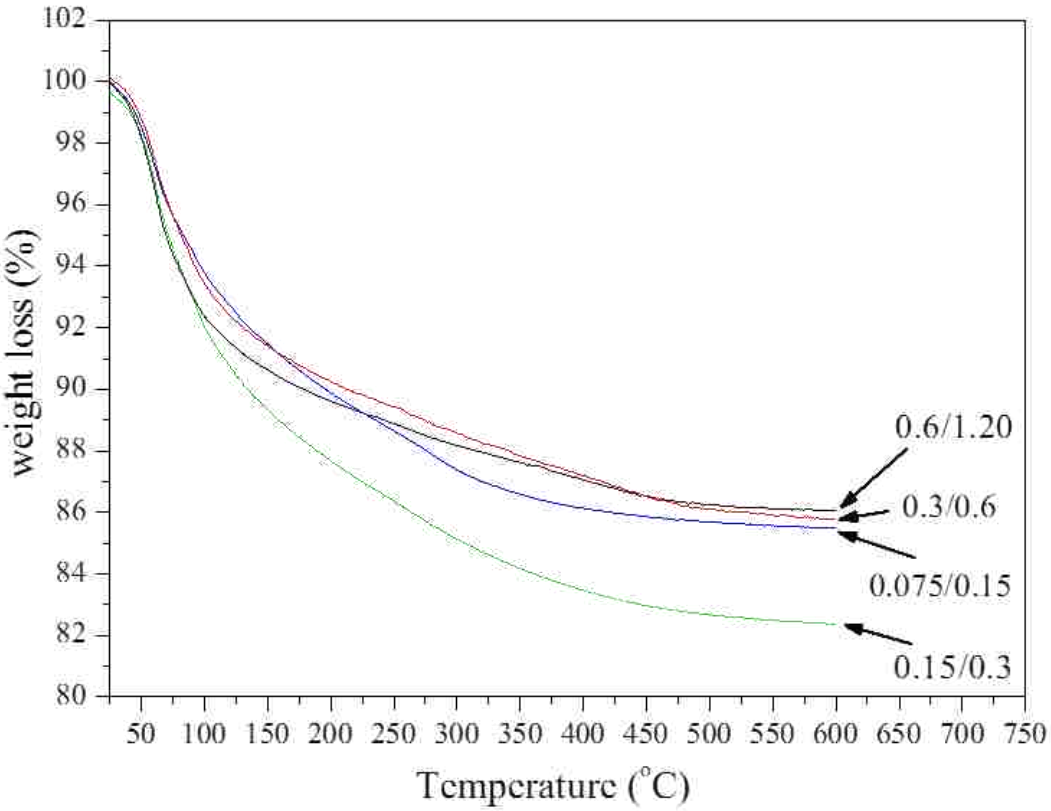

Figure 16: TGA analysis of solid MNPs samples prepared in solutions containing different initial concentrations of Fe^{2+} /Fe^{3+} ions.

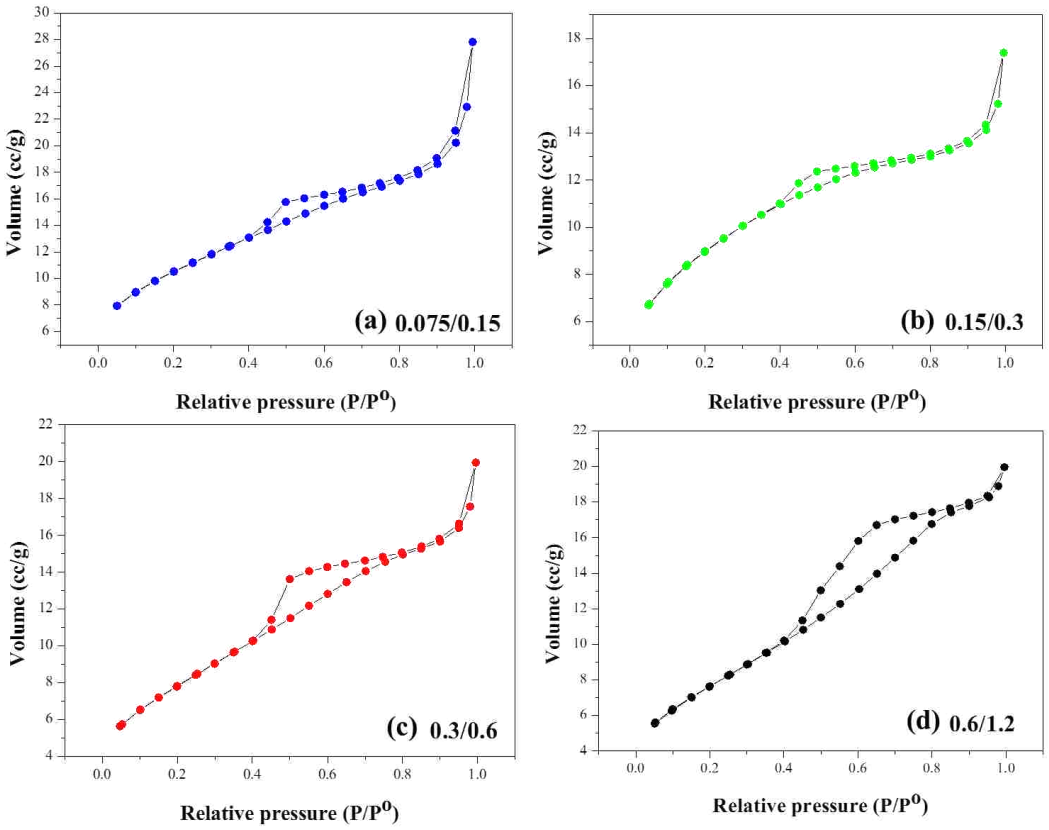

Figure 17: Adsorption isotherms of MNPs samples prepared in solutions containing different initial concentrations of Fe^{2+} /Fe^{3+} ions. a) 0.075/0.15, b) 0.15/0.3, c) 0.3/0.6 and d) 0.6/1.2 of Fe^{2+} and Fe^{3+}, respectively.

As a result of the isotherms in **Figure 17**, pore size distributions were calculated using the BJH method for the desorption segment of the hysteresis curves. Results are plotted in **Figure 18**. All samples showed homogeneous pore size distributions with maxima in the range of 30–40 nm. This range denotes the presence of mesoporosity in the agglomerates of the prepared NPs [179]. A mesoporous material is a material containing pores with diameters between 2 and 50 nm. The monodispersity in the pore size distribution within the agglomerates relatively reflects the homogeneity of the particle size distribution in these samples. No pronounced difference in the pore size or its distribution was observed among samples prepared from solutions containing various concentrations. The homogenous distribution of mesopores in the aggregates of the prepared NPs offers an advantage for these NPs if they are used for environmental applications.

Detailed morphology of the MNPs prepared in solutions containing 0.075/0.15 and 0.3/0.6 M concentrations of Fe^{2+} and Fe^{3+} ions, respectively is shown in the TEM micrographs in **Figure 19**. MNPs shown in the TEM micrographs are spherical in shape with a homogeneous size distribution. The average sizes of these individual NPs were 12 ±5 and 25 ±5 nm, for samples prepared from relatively dilute solutions (Fe^{2+}/Fe^{3+} = 0.075/0.15) and relatively more concentrated solutions (Fe^{2+}/Fe^{3+} = 0.3/0.6), respectively. The relatively smaller particle size shown in **Figure19a** explains the relatively small crystallite size of this sample that was previously shown in **Figure 14**.

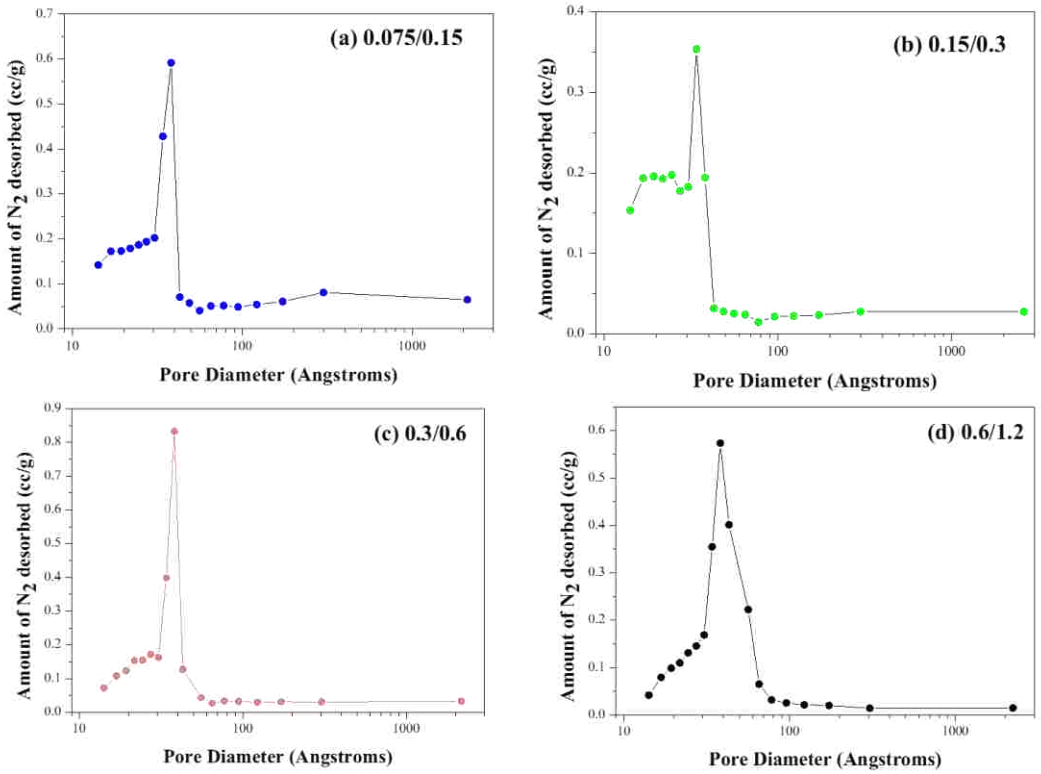

Figure 18: Pore size distribution in MNPs samples prepared in solutions containing different initial concentrations of Fe^{2+}/Fe^{3+} ions. a) 0.075/0.15, b) 0.15/0.3, c) 0.3/0.6 and d) 0.6/1.2 of Fe^{2+} and Fe^{3+}, respectively.

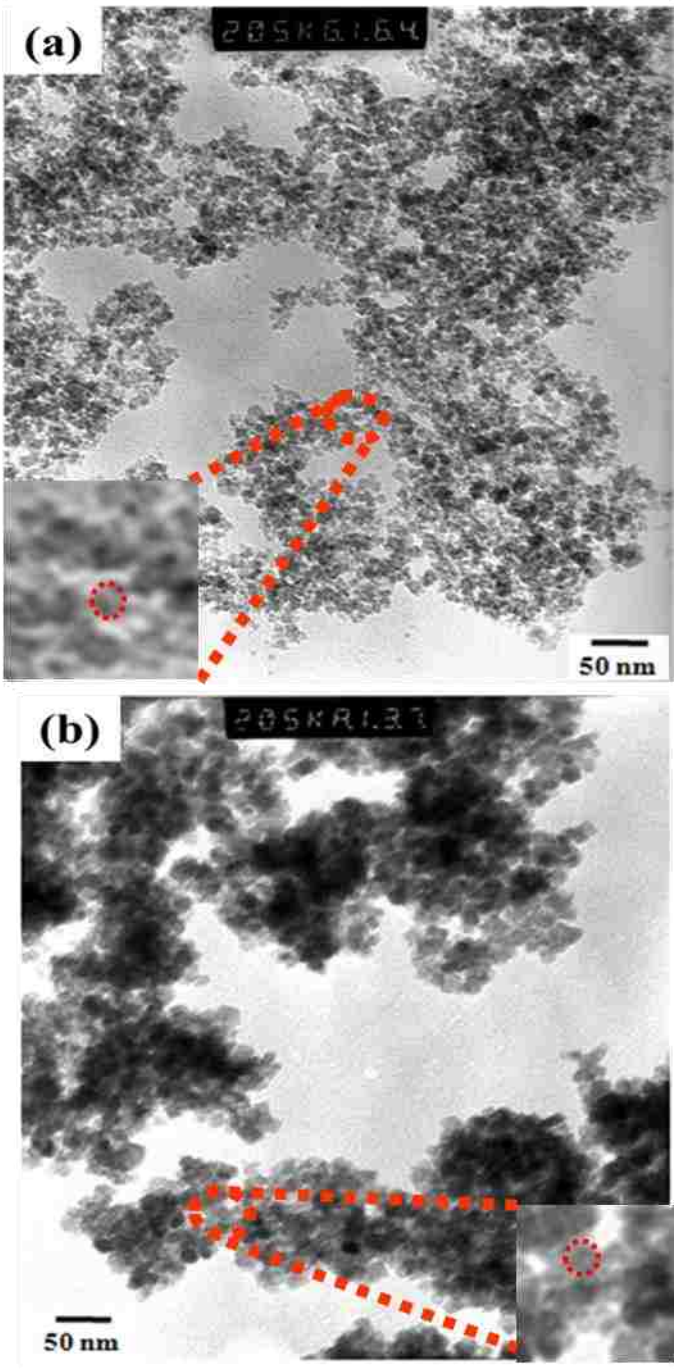

Figure 19: TEM micrographs of MNPs prepared in solutions containing different initial concentrations of Fe^{2+} and Fe^{3+} ions. a) 0.075/0.15 and b) 0.3/0.6 M of Fe^{2+}/Fe^{3+} ions. Insets: individual round shaped MNP.

The magnetic susceptibility results of MNPs samples prepared at different starting concentrations of Fe^{2+} and Fe^{3+} ions are shown in **Figure 20.** Magnetic susceptibility is the degree to which a material can be magnetized in an external magnetic field, and is directly proportional to its magnetization [180]. Moreover, the magnetic size is known to be directly proportional to the magnetic susceptibility of solid NPs [181].

Susceptibility results indicate an opposite behaviour, but are still explained by their agglomeration and size characteristics. Previous results by Thapa et al. [182] attributed the increase in the magnetization of MN with the decrease of particle size to the decrease in the oxygen content in the MN samples and the subsequent increase of [Fe^{2+}] in the MN lattice, which is the main cause of magnetic character of MNPs. Moreover, Ma and Liu related the decrease in magnetic properties with increasing size of MNPs to the agglomeration of the particles, which is caused by the hydrophobic interaction between them [183].

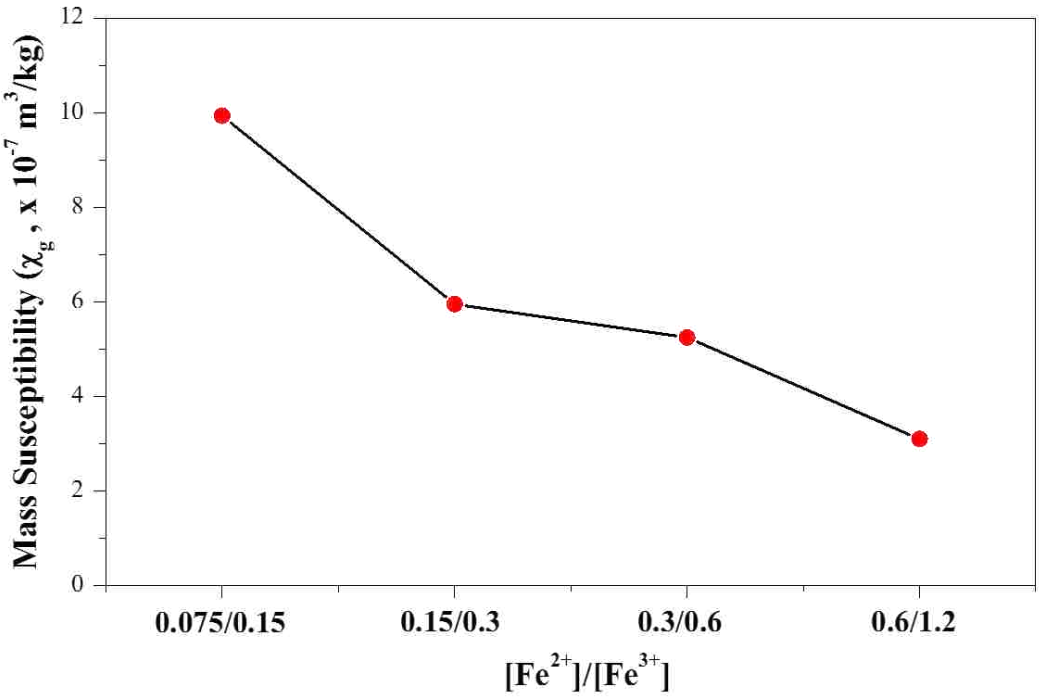

Figure 20: Magnetic susceptibility of MNPs prepared in solutions containing different initial concentrations of Fe^{2+} and Fe^{3+} ions.

Based on the previous results, MNPs prepared using the following optimum conditions were used for the next stage of experimentation where organic coating materials were developed onto their surfaces:

a) Fe^{2+}/Fe^{3+} = 0.3/0.6 M
b) Feeding rate of 40 ml/hr
c) Stirring temperature of 60^{o}C
d) Soaking temperature of 60^{o}C

Under these conditions, monolithic MNPs with a spherical shape that exhibited superparamagnetic behavior at room temperature [184]. The average particle size of these MNPs were in the size of 25 nm with the high surface area; around 215 m^2/g as seen in **Table 5.** However, and due to small size of MNPs that form high surface-to-volume ratio and magnetic properties of the NPs, agglomeration took place giving rise to mesoporous agglomerates with an average size of 55 nm. MNPs prepared under these optimum conditions were further subjected to magnetization measurements as a function of applied field at a room temperature. Results are shown in **Figure 21.** A maximum magnetization of 25 emu/g was obtained, which is lower than that mentioned in the literature for NPs prepared under similar conditions. This could be attributed to agglomeration of the NPs.

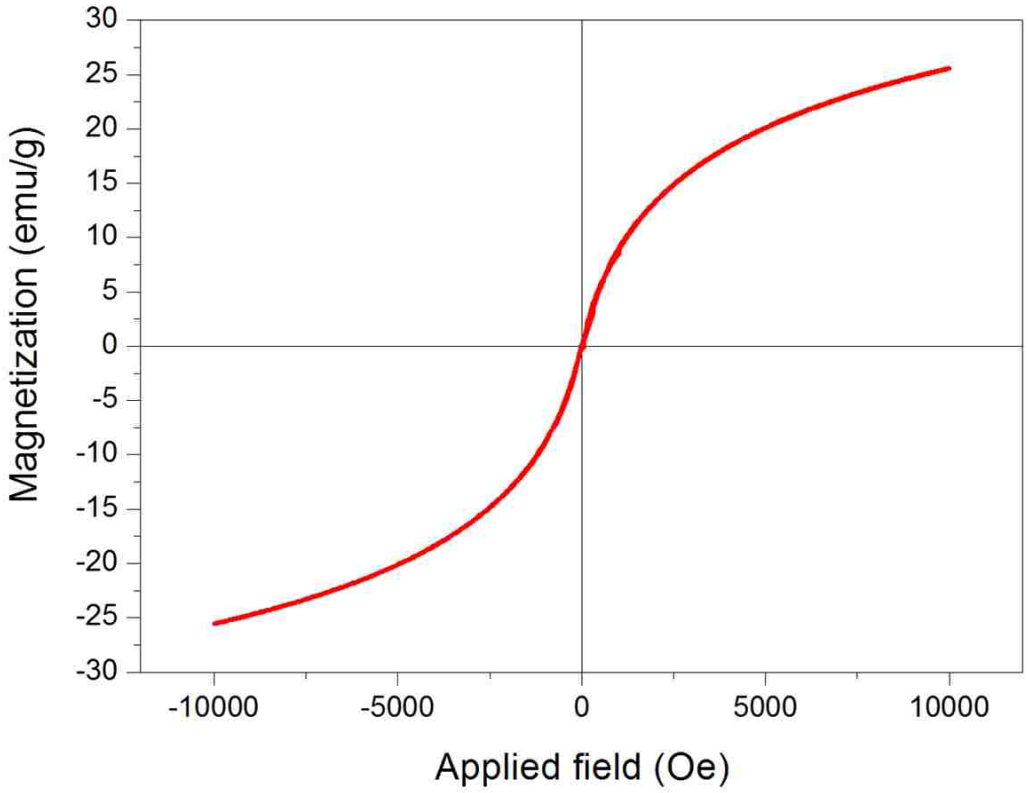

Figure 21: Magnetization of MNPs prepared under optimum conditions as a function of applied magnetic field at room temperature.

3.2. Characterization of different surface coating materials

MNPs have been widely explored for their applications as MRI contrast agents, in immunoassays, in the detoxification of biological fluids, in hyperthermia, drug delivery, cell separation, in addition to their environmental applications in the removal of inorganic contaminants from the aqueous media [102, 185]. However, MNPs tend to agglomerate in solution, which may limit their applications. For example, neat MNPs undergo non-specific interactions with the serum proteins *in vivo* leading to their rapid elimination from the body. Therefore, it has been recognized by researchers that the surfaces of the MNPs need to be hydrophilic in nature for *in vitro* and *in vivo* applications, so that it will be stable for prolonged circulation inside the body [95].

In order to widen the scope of these applications, researchers have explored the functionalization of the surfaces of these NPs using various organic and inorganic coatings [87, 92, 178, 186-189]. The choice of coating is application driven. In biomedical applications, a pre-requisite is to have a biocompatible coating. In addition, if these coated NPs are to be used to deliver certain bioactive drugs into infection or tumor sites, the chemical characteristics of the coating should match those of the bioactive drugs to ensure bonding between them until delivery takes place [186, 190, 191].

Applying an organic coating onto the surfaces of MNPs takes place by synthesizing the NPs in the presence of these organic molecules or by chemically treating the fresh MNPs in solutions of these organic compounds by direct immersion. The first route provides two advantages over the second one. First, when organic molecules are initially added to the preparation solution, they tend to act as capping agents. They adsorb onto the surfaces of the freshly formed MN nuclei,

hence limiting their size and size distribution. Second, the presence of organic functionalities onto the surfaces of all formed MNPs helps separating the NPs, consequently minimize their aggregation. To summarize, the presence of organic functionalities onto the surfaces of MNPs provides the following advantages:

1) Reduces the aggregation between the MNPs, therefore increases the stability of the MNPs in various solvents.
2) Controls the size of the MNPs and might help in determine their shape.
3) Improves the biocompatibility of coated MNPs.
4) Limits non-specific cell binding in biomedical application.
5) Provides functional groups for further modification, such as attachment of optical dyes, therapeutic and targeting molecules.

In the current study, coating of the optimally prepared MNPs was investigated in details in order to choose the type of functionality that will be further modified for targeted drug delivery application. Three organic compounds were studied; SDS, chitosan and dextran. Chemical structure of these organic compounds is shown in **Figure 5.** SDS is a known ionic organic compound that has been previously shown to stabilize NPs in solutions by providing surface charges onto their surfaces [165, 166]. Chitosan and dextran are natural polymers, and both have also been shown to stabilize MNPs in solution [114, 117, 118, 144, 147, 148]. The following sections discuss the characterization of the coated MNPs with each of these compounds.

S-MNPs and D-MNPs were prepared by addition of Fe^{2+} and Fe^{3+} solutions into an aqueous NaOH solution that was pre-adjusted at pH 13 and containing 0.2, 0.5, 1.0 and 2.0% by weight of SDS or dextran. After precipitation of NPs, they were centrifuged, washed, dried, and then subjected to characterization. Due to the

insolubility of chitosan in aqueous and basic media, C-MNPs were prepared by a different approach. Initially, chitosan solutions containing 0.2, 0.5, 1.0 and 2.0 % by weight were prepared by dissolving the corresponding weight of chitosan in 0.2 % acetic acid solution. An equal volume of each of the chitosan solutions was then added and vigorously mixed with the Fe^{2+}/Fe^{3+} solutions (pre-coating procedure), then injected into the NaOH solution at a feeding rate of 40 ml/hr at 60°C in air (optimal conditions). At the end of addition, extra chitosan was washed out by cycles of washing and decantation with de-ionized water and confirmed by Benedict's test, which is used to detect carbohydrates. The formed C-MNPs were separated by decantation, centrifuged, washed, and then dried before being characterized for its composition.

3.2.1. FTIR of coated MNPs

Figures 22-27 show FTIR spectra of S-MNPs, C-MNPs, and D-MNPs, respectively as a function of the initial concentration of the organic coating; 0.2-2 weight %. A spectrum of pure organic coating; SDS, chitosan and dextran, is also shown in the respective graph for comparison. In all spectra, MN is represented by its bands at 430, 584 and 622 cm^{-1}, with band intensities decreasing and shifting to lower wavenumbers with increasing the concentration of the organic coating. This is attributed to possible chemical interaction between the functionalities of the organic coating and the underlying MNPs surfaces. On the other hand, bands of each of the organic coating compounds were shown to dominate the spectra with increasing the initial concentration of the organic coating.

The FTIR spectrum of pure SDS in **Figure 22** shows the presence of bands at 998.5, 1019.3 and 1082.2 cm^{-1} for its symmetric absorption, and at 1223.1 and 1248.9 cm^{-1} for its asymmetric absorption of the $-OSO_3^-$- in the $-OSO_3Na$ groups in

SDS [192]. Position, shape, and sharpness of these bands in the FTIR spectra of S-MNPs samples in **Figure 22** changed as a result of the interaction between the SDS coating and the underlying MNPs. Details of these changes are given in **Table 6.** Shifts in the band position of the corresponding bands in S-MNPs are attributed to the formation of ionic bonds between the sulfate group and the Fe^{2+} and Fe^{3+} ions along the surfaces of the underlying MNPs (**Figure 23**), which was previously shown in comparable oxide systems [192]. This shift was shown to increase with increasing the concentration of SDS initially added to solution, and was more evident in the FTIR spectra of S-MNPs samples containing 1.0 and 2.0% of SDS. It should be mentioned that un-adsorbed SDS was removed from all samples by washing, which confirms that the observed bands are solely related to SDS coatings.

Table 6: Wavenumber of the absorption bands characteristic to the sulfate group in SDS as appeared in pure SDS and S-MNPs FTIR spectra.

	s ($-OSO_3^-$)			**as ($-OSO_3^-$)**	
SDS	998.5	1019.3	1082.2	1223.1	1248.9
0.2 %	1010.2		***	***	
0.5 %	1005.3		***	1247.6	
1.0 %	969.2		1062.8	1242.1	
2.0 %	957.8		1062.8	1229.9	
*** bands were not observed in the FTIR spectra of these samples					

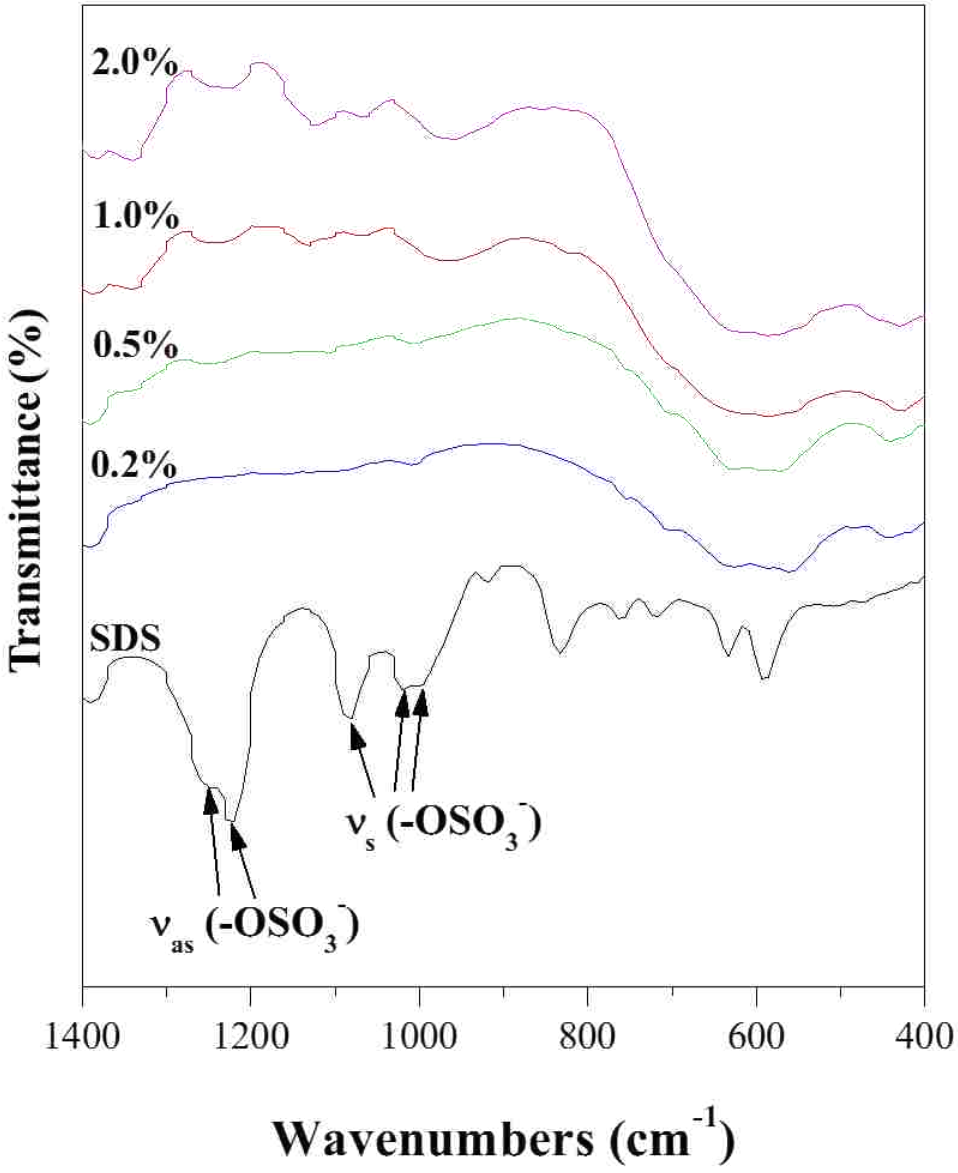

Figure 22: FTIR spectra of pure SDS and MNPs coated with various concentrations of SDS.

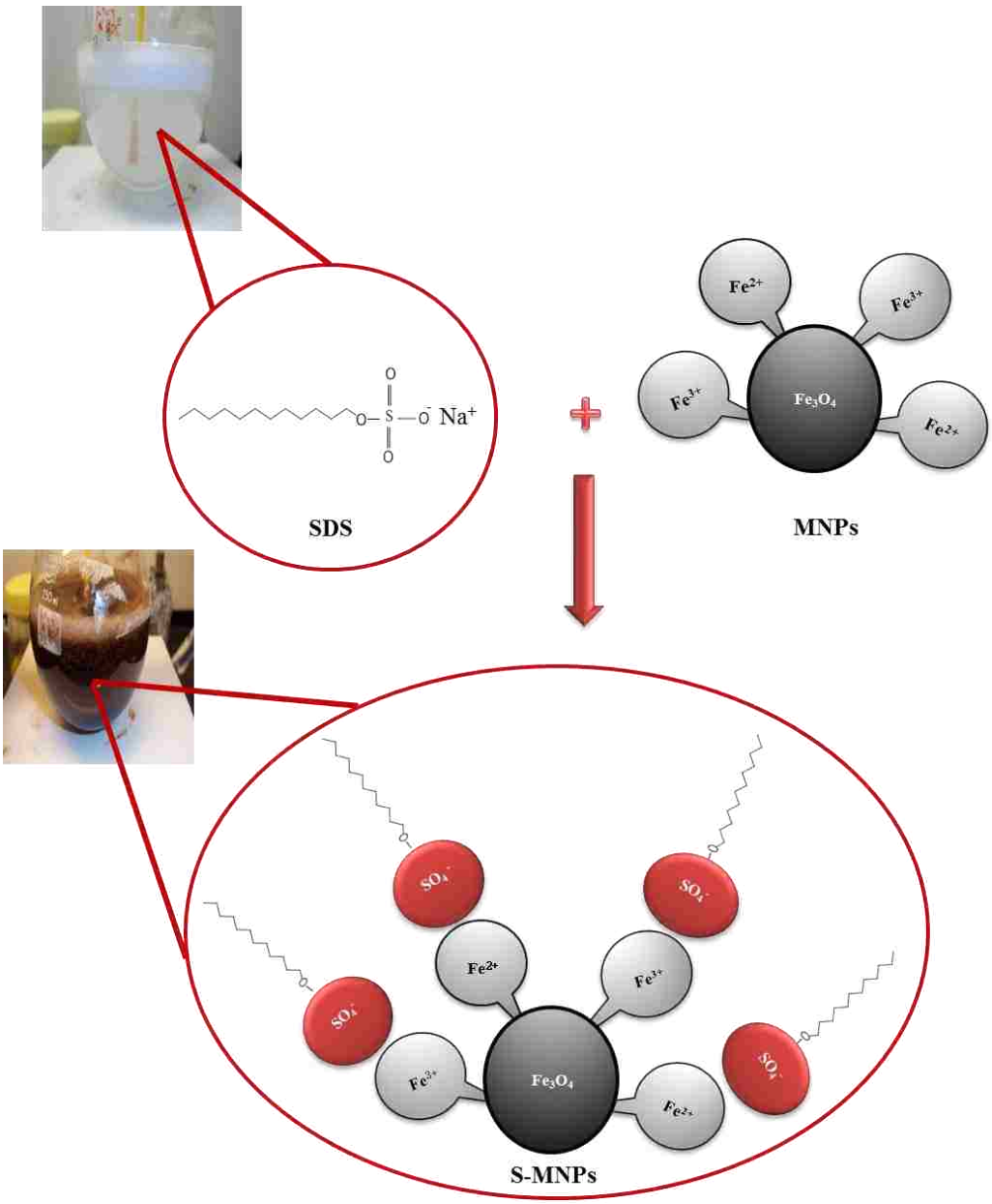

Figure 23: Diagrammatic representation of the interaction between SDS functional groups and iron ions of MNPs to form S-MNPs.

The characteristic bands of pure chitosan are shown in **Figure 24**. Those bands appeared at 1082, 1382 and 1655 cm^{-1}, and are attributed to the absorption of C-O, C-N, and C=O groups, respectively. In addition, a weak-medium intensity broad band appears at 3449 cm^{-1}, which is attributed to the absorption of both O-H and N-H groups, as shown in the chemical structure of chitosan. A summary of these bands as a function of coating concentrations is shown in **Table 7.**

A shift towards a shorter wavenumbers was observed in the bands characteristic to C-O, and O-H/N-H groups, while no pronounced shift was observed in the bands characteristic to the C-N bond of the amide group. Moreover, another shift was observed in the absorption band of the amide C=O group. Variation of the bands of MNPs and those of chitosan in the FTIR spectra of C-MNPs collectively indicates the formation of bonds between the chitosan coating, as a capping molecule, and the underlying MNPs surfaces.

These chemical interactions are expected to take place between the MN surface Fe^{2+} and Fe^{3+} ions and the $C\text{-}O^{-}$ groups that result from the ionization of the C-OH groups under the high basic conditions of the experiments (**Figure 25**). In addition, coordination bond is expected to form between the C=O group and both MN Fe^{2+} and Fe^{3+} cations, as a result of the extra electronic density on the oxygen atom of the C=O group. According to the chemical structure of chitosan, it can be concluded that this interaction takes place at the pending primary alcoholic group along the chitosan chains as well as the terminal OH groups in every chitosan chain. Secondary alcoholic groups; directly attached to the hexagonal rings of chitosan, are sterically hindered and are therefore slightly expected to participate in this interaction with the MN surfaces. It should be mentioned that un-adsorbed chitosan was removed by successive centrifuge and washing to eliminate the possibility of un-

reacted chitosan remain in the powder. Therefore, the relative increase in intensity of the bands characteristic to chitosan, mentioned in **Table 7** with the increase in the concentration of chitosan indicates the adsorption of more chitosan molecules or the development of thicker chitosan coatings on the surfaces of the MNPs [173, 193].

Table 7: Wavenumber of the absorption bands characteristic of chitosan, both as neat and different concentrations coating the surface of MNPs.

[Chitosan] (Weight %)	Band location (cm^{-1})			
	υ_s (C-O)	**υ_s (amide)**	**υ_s (C=O)**	**υ_s (O-H & N-H)**
100	1082	1382	1655	3449
0.2	1076.3	1384.7	1630.4	3399.8
0.5	1074.7	1384.7	1628.8	3399.8
1.0	1074.7	1384.7	1630.4	3402.6
2.0	1069.4	1384.7	1631.1	3402.6

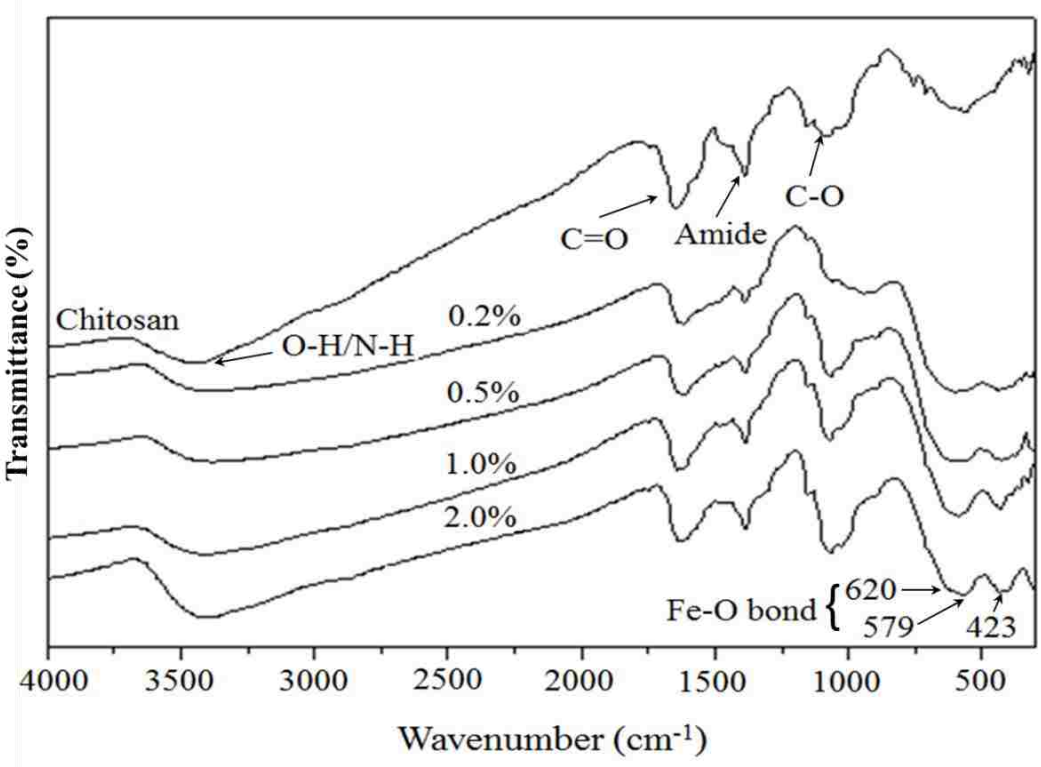

Figure 24: FTIR of pure chitosan and MNPs coated with various concentrations of chitosan.

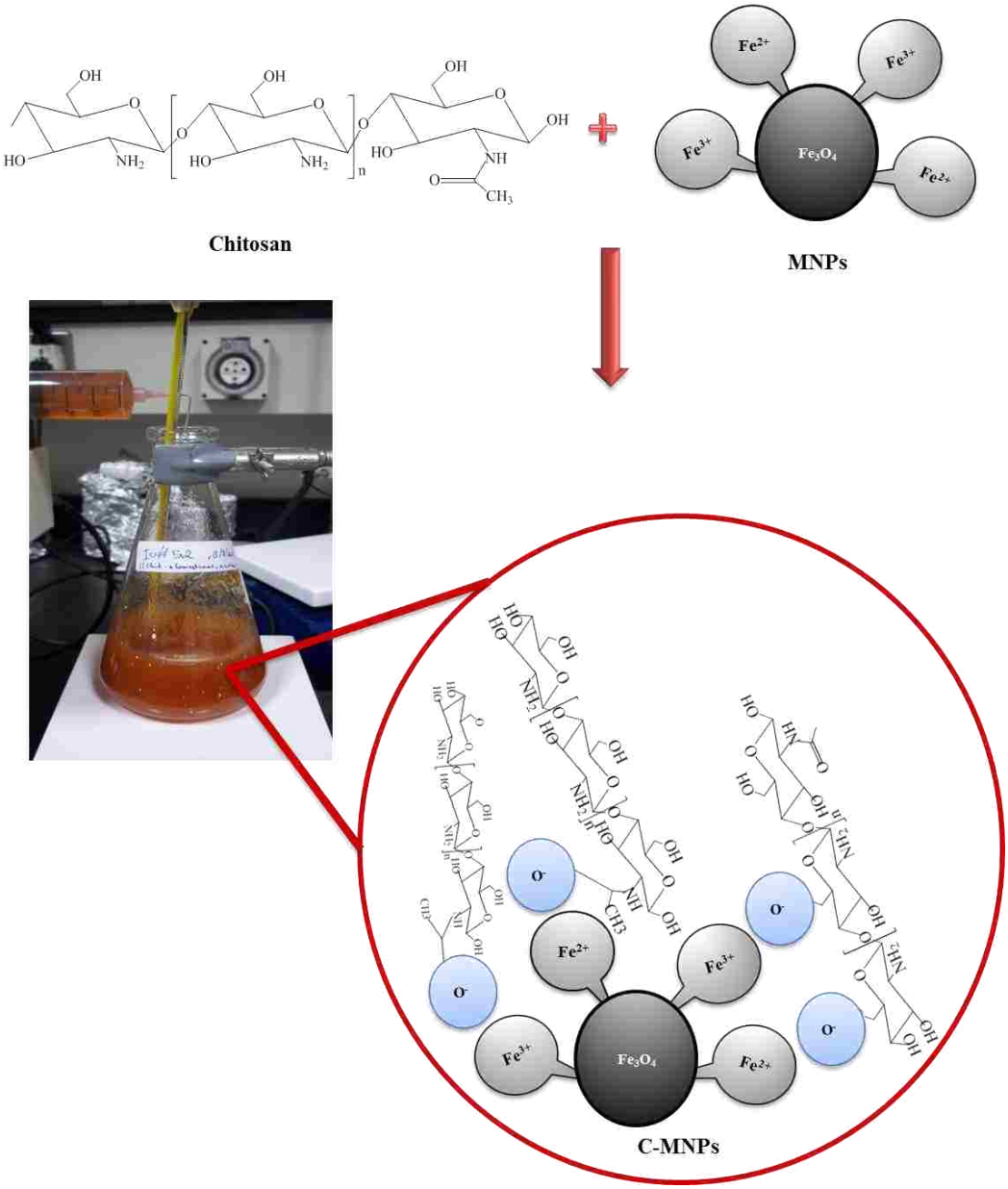

Figure 25: Diagrammatic representation of the interaction between chitosan functional groups and iron ions of MNPs to form C-MNPs.

Figure 26 compares the FTIR spectra of pure dextran and different concentrations of dextran coatings onto MNPs. The spectra present vibrational modes characteristic of the organic structure of dextran, such as the α-glucopyranose ring of dextran at 907 cm^{-1}. The α-glucopyranose ring in a pure dextran is also represented by two bands at 759 and 838 cm^{-1}. In addition, bands of pure dextran at 1279 and 1373 cm^{-1} are due to C-H vibrational modes, while bands at 1019 and 1152 cm^{-1} are attributed to C-O vibrations (**Figure 27**). Vibrational bands at 1645 and 3400 cm^{-1} are representative of O-H group of adsorbed water in the samples. All dextran bands were shifted and changed their intensities upon the formation of coatings onto MNPs, as a result of the interaction between dextran and Fe^{2+} and Fe^{3+} ions in the MNPs surfaces, as summarized in **Table 8** [178, 194, 195].

Table 8: Wavenumber of the absorption bands characteristic of dextran, as seen in the pure and different concentrations coating the surface of MNPs.

[Dextran] (Weight %)	Band location (cm^{-1})				
	υ_s (α-glucopyranose)	υ_s (C-O)		υ_s (C-H)	
100	907	1019	1152	1279	1373
0.2	917	1019	1152	1328	1386
0.5	917	1019	1152	1328	1386
1.0	917	1019	1152	1328	1386
2.0	917	1019	1152	1328	1386

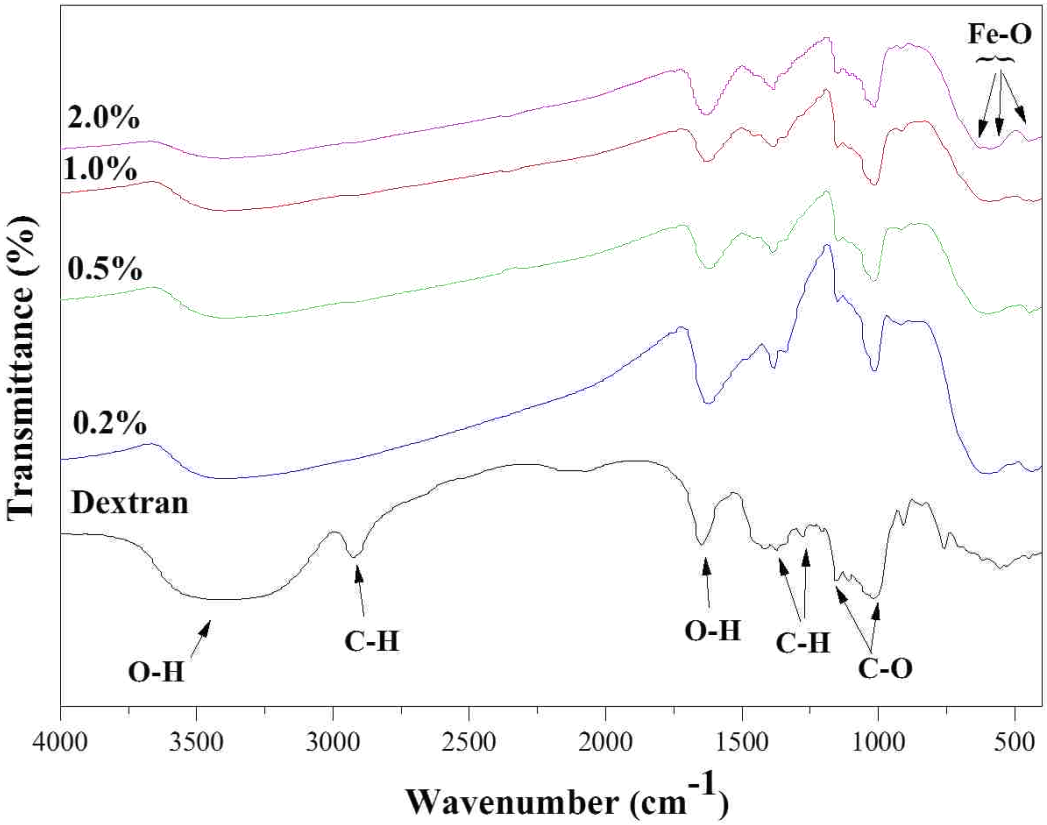

Figure 26: FTIR spectra of pure dextran and different concentrations of dextran coatings onto MNPs.

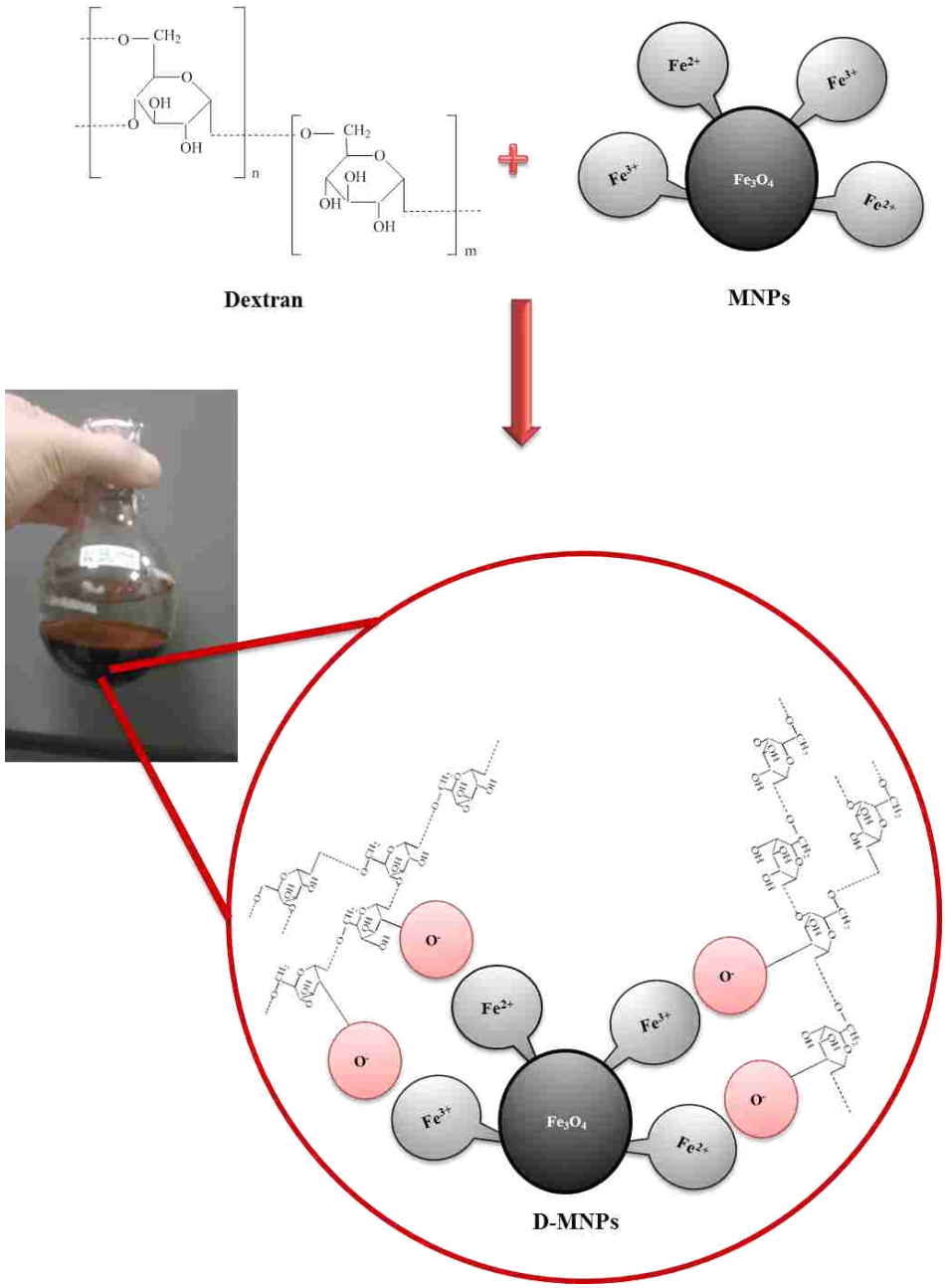

Figure 27: Diagrammatic representation of the interaction between dextran functional groups and iron ions of MNPs to form D-MNPs.

3.2.2. TGA analysis of coated MNPs

Pure MNPs showed an average weight loss of 14%, as was previously shown in **Figure 16**. This was attributed to the removal of water that was physically adsorbed onto the surfaces of the NPs. **Figures 28-30** show TGA curves of S-MNPs, C-MNPs, and D-MNPs, respectively, as a function of the concentration of each of the organic compounds initially added to the preparation reaction medium. Weight loss of pure organic coating has been added to each of these figures for comparison.

SDS shows a major single step weight loss at a temperature of 180 ºC, which denotes its degradation; **Figure 28**. This process increases until it levels off at a temperature of 470ºC with an overall weight loss of 75.3% where SDS was completely degraded. Pure chitosan shows an overall weight loss of 80% took place after heating it to 600^{o}C; **Figure 29**. This weight loss takes place over two stages, where the first loss around 100^{o}C and is attributed to the removal of physically and chemically adsorbed water. This was followed by a major weight loss around 300°C due to the degradation of chitosan that takes place through thermal and oxidative decomposition [192].

Pure dextran, on the other hand, shows an initial weight loss at 100-150 ºC, and is attributed to the removal of physically and chemically adsorbed water, accounting for 10% of total weight loss. This was followed by a major weight loss around 300°C that corresponds to the degradation of the polysaccharide dextran chains; **Figure 30**. The overall weight loss at the end of heating of pure dextran amounted to 92% due to the complete burn out of dextran [196].

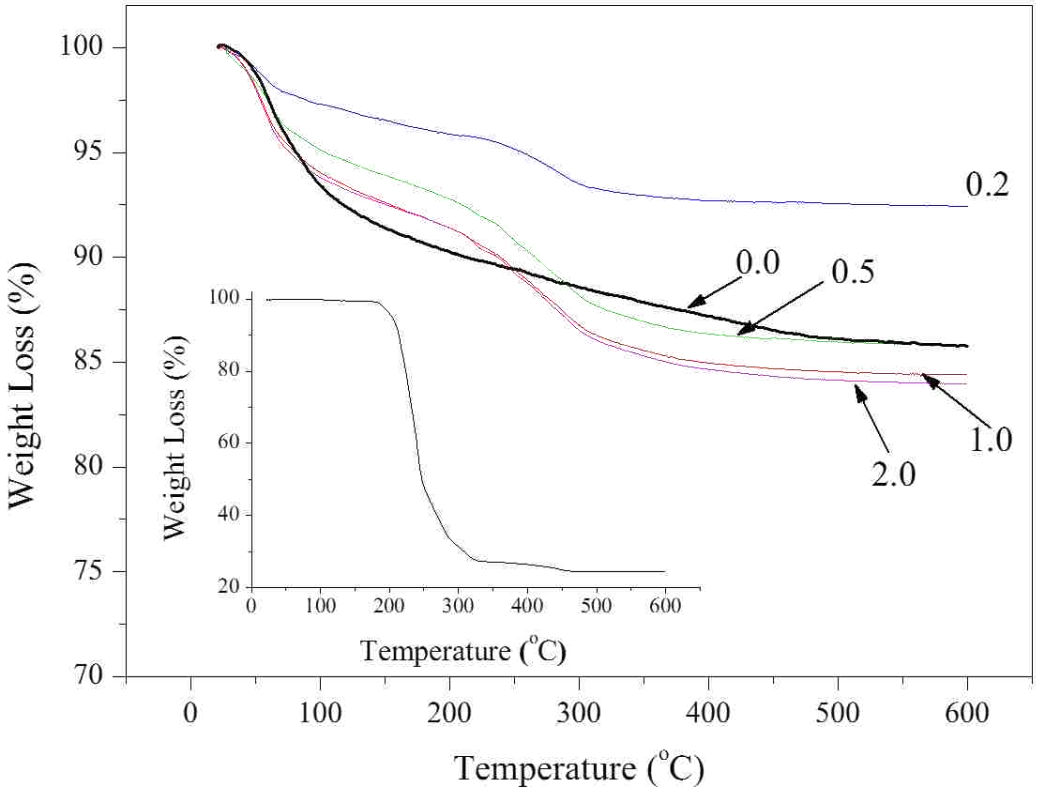

Figure 28: TGA analysis of MNPs coated with various concentrations of SDS. Insert: TGA pattern of pure SDS.

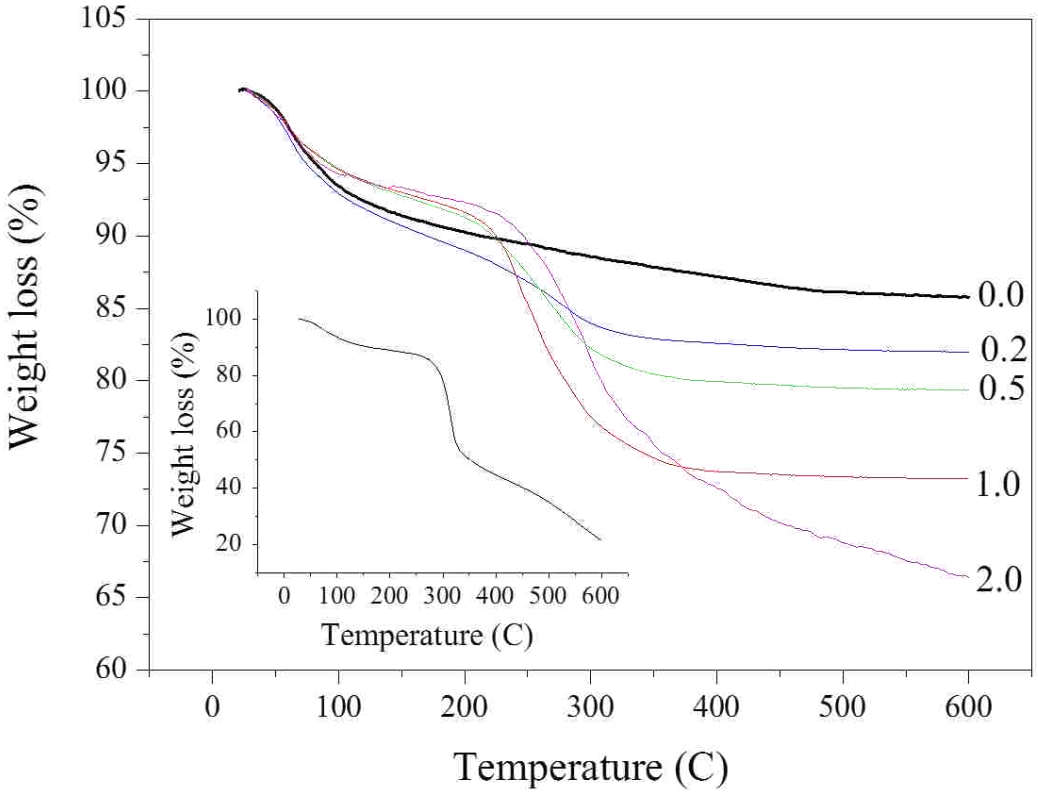

Figure 29: TGA analysis of MNPs coated with various concentrations of chitosan. Insert: TGA pattern of pure chitosan.

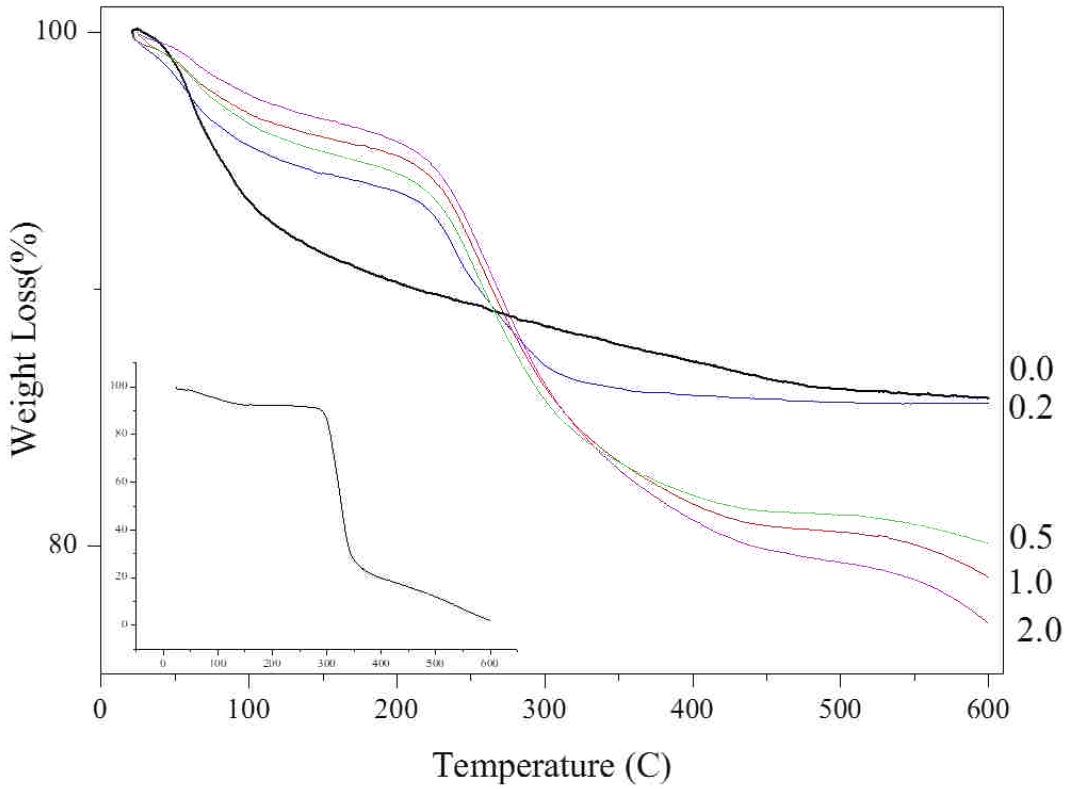

Figure 30: TGA analysis of MNPs coated with various concentrations of dextran. Insert: TGA pattern of pure dextran.

With the presence of these organic compounds as coatings onto the surfaces of MNPs, TGA thermograms showed variable behaviour based on the type of coating and its concentration that was initially added during preparation. **Figure 28** indicates that all S-MNPs showed two steps of weight loss; an initial step that started at a temperature slightly below 100 °C, and a second step that started at a temperature close to 200 °C. The first step is related to the evaporation of physically and chemically attached water, while the second step is related to the degradation of the SDS coating the MNPs. These results confirm the presence of SDS as a coating on the surface of the prepared MNPs, as was previously shown in the FTIR spectra of these samples in **Figure 22**. These findings also confirm the presence of multi-layers of SDS coating the MNPs on which water was adsorbed.

Similarly, TGA thermograms of C-MNPs showed in **Figure 29** indicated the presence of two stages of weight loss. The first event of weight loss accounts for the evaporation of physically and chemically adsorbed water; around 100^{o}C, while the second event took place at 300±10^{o}C and is attributed to the degradation of chitosan linked onto the surfaces of the MNPs.

D-MNPs showed similar pattern, where two stages of weight loss were also observed; **Figure 30**. The first weight loss took place at 100-200^{o}C, and is attributed to the evaporation of physically and chemically adsorbed water molecules. The second step, on the other hand, appeared at 250±100^{o}C, with a higher temperature achieved in samples containing higher concentration of dextran. In addition to these events, a third event was observed around 500±50^{o}C, which was slightly evident in the TGA thermogram of pure dextran. This event appeared in an increasing manner in the thermograms of samples containing ≥ 0.5 weight % of dextran, and could be attributed to a delayed degradation of dextran-bonded MNPs. In addition, the overall

early degradation of dextran coatings, as compared to pure dextran could be attributed to the effect of MNPs in catalyzing the thermal decomposition of dextran, which was previously reported in the literature [196].

Figure 31 shows a detailed analysis of the removal of water and organic coating from the surfaces of the MNPs during their TGA analysis. These data were derived from the TGA thermogarms in **Figure 28-30**. In the absence of organic coatings, the weight loss is related to water only. As the concentration of the organic coating was increased, a pronounced decrease in the weight loss owing to water was observed and a consequent increase in the weight loss owing to the organic coating was observed. This behavior continued up to 0.5% of SDS. As the percentage of SDS was increased to 1%, its contribution to the overall weight loss was decreased with a subsequent increase in the contribution of water to the overall weight loss; **Figure 31a.** The same criterion was also observed when 2% of SDS was initially added.

Figure 31b shows, on the other hand, that the amount of water adsorbed onto the MNPs was largely reduced by the presence of chitosan, and that this amount slightly decreased concurrently with the increase of concentration of chitosan initially added to the system. The decrease in the slope between 1 and 2% chitosan as compared with lower percentages of chitosan may indicate a relative decrease in the affinity of the MNPs towards further addition of chitosan on their surfaces after 1% concentration.

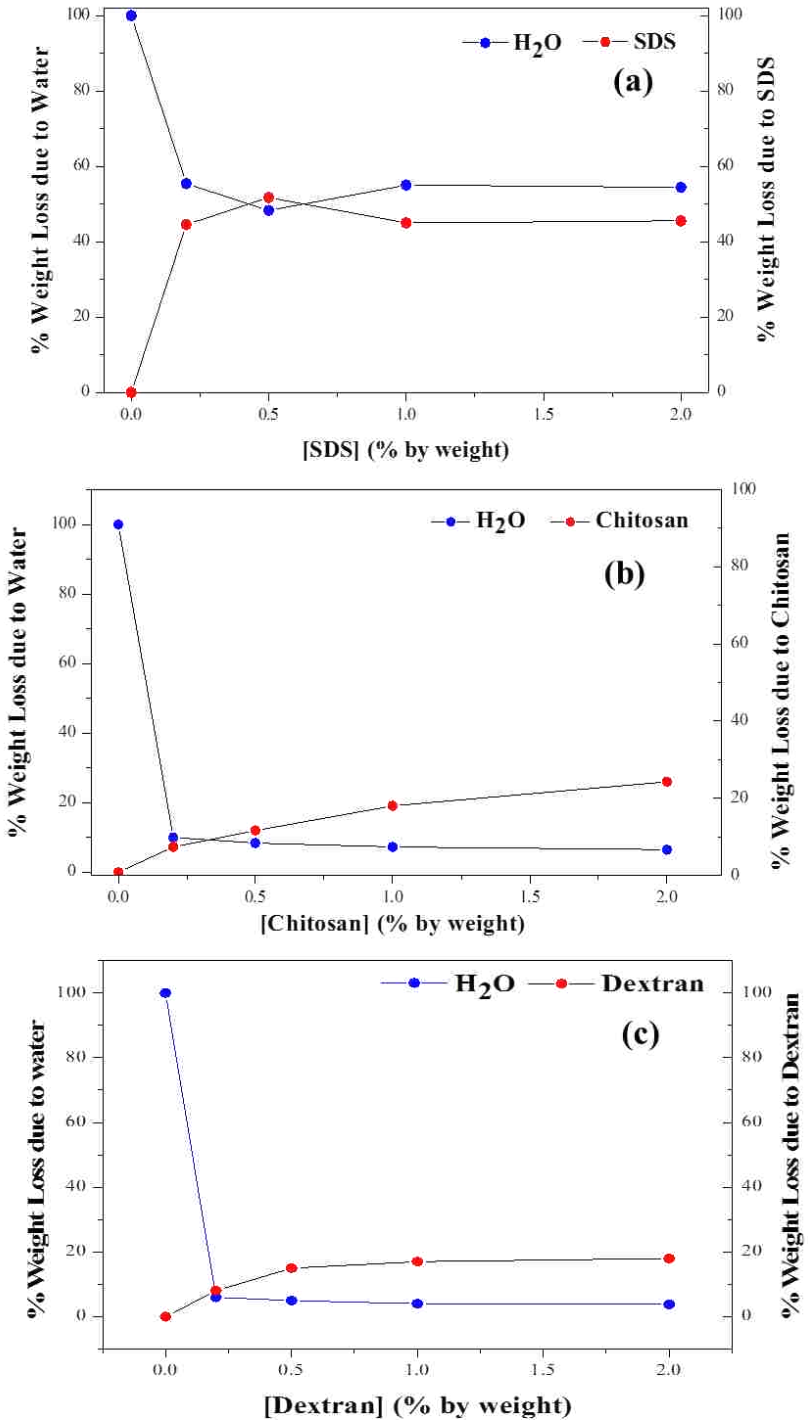

Figure 31: A detailed TGA analysis of the removal of water and organic coatings from the surfaces of the MNPs. a) SDS, b) chitosan and c) dextran.

In the presence of dextran as a coating, a similar pattern was observed where the amount of adsorbed water was highly reduced as the MNPs coated with dextran; **Figure 31c.** As the concentration of dextran increased up to 1% the amount of water decreased. This was followed by a slight addition of dextran onto the MNPs surfaces from 1 to 2% as compared to lower dextran concentrations. This indicates the decreased affinity of MNPs towards further addition of dextran on their surfaces after 1% concentration.

These results suggest that at SDS percentages above 0.5 %, its molecules detach from the coating and are replaced by water. Detachment of adsorbed molecules takes place when these molecules are weakly bonded to the substrate, i.e. the MNPs. This indicates that the desorbed molecules are in the outermost layer of SDS coating the MNPs. It should be mentioned that the primary layers are thermodynamically known to strongly bond to the underlying substrate, whereas this bonding decreases in strength for molecules in the external layers of the coating. The same concept could be applied to the first layers of chitosan and dextran, which are directly bonded to the underlying MNPs' surfaces, as was explained in the previous section; FTIR analysis of coated MNPs.

In the presence of chitosan and dextran, a possible increase in the thickness of the chitosan coating layer was observed, and could be attributed to the development of intermolecular forces, such as H-bonding and dispersion forces, amongst chitosan molecules and dextran molecules in their coatings, respectively. In all cases, the first layer(s) of organic coatings are secondarily covered with an external hydrated layer through H-bonding. These findings explains the removal of water, as a first event, from the surfaces of the organic-coated NPs, followed by the removal of the organic coating, as shown in the TGA thermograms in **Figures 28-30**. Based on these

discussions, a diagram showing the possible construction of coatings onto MNPs is given in **Figure 32**.

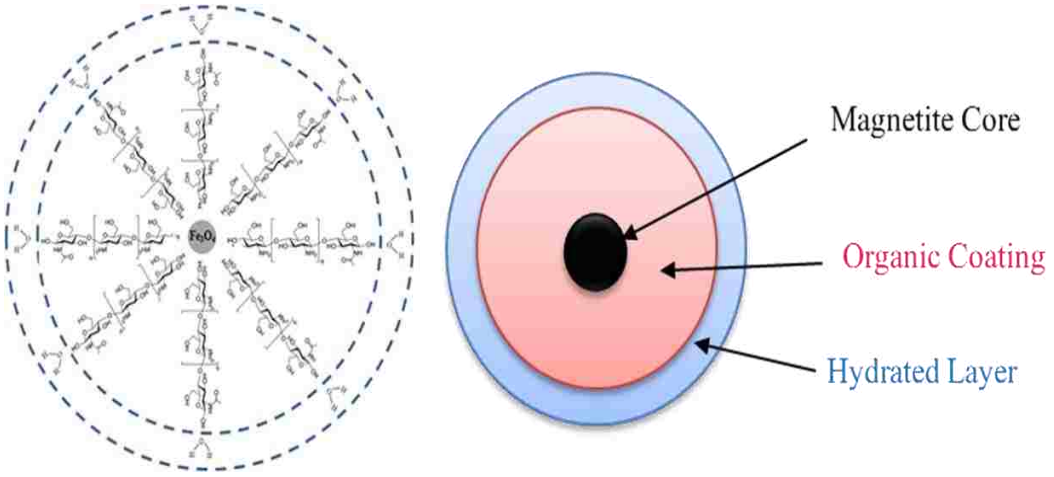

Figure 32: Diagrammatic representation of the possible construction of water and organic coatings onto the surface of MNPs.

3.2.3. Morphology of coated MNPs

TEM micrographs of coated MNPs are shown in **Figure 33**. Neat MNPs were previously shown in **Figure 19b** as spherical in shape, uniform in size and with an average particle size of around 25 nm. In the presence of organic coatings in the reaction medium, NPs maintained their shape and size distribution, but an overall decrease in the particle size of the NPs was observed. This decrease was shown to increase with increasing the concentration of the organic coating initially added to the reaction medium; **Figure 34**. The lowest sizes of coated NPs achieved were 9, 10, and 10 nm when 2 weight % of SDS, chitosan or dextran, respectively, were added to reaction medium during the precipitation of MNPs. These results confirms the role of these organic compounds as capping agents that limited the size of MNPs nuclei formed during precipitation in the aqueous medium. It is also evident that the size of particles could be controlled by adjusting the type and concentration of the organic material added during the formation of MNPs.

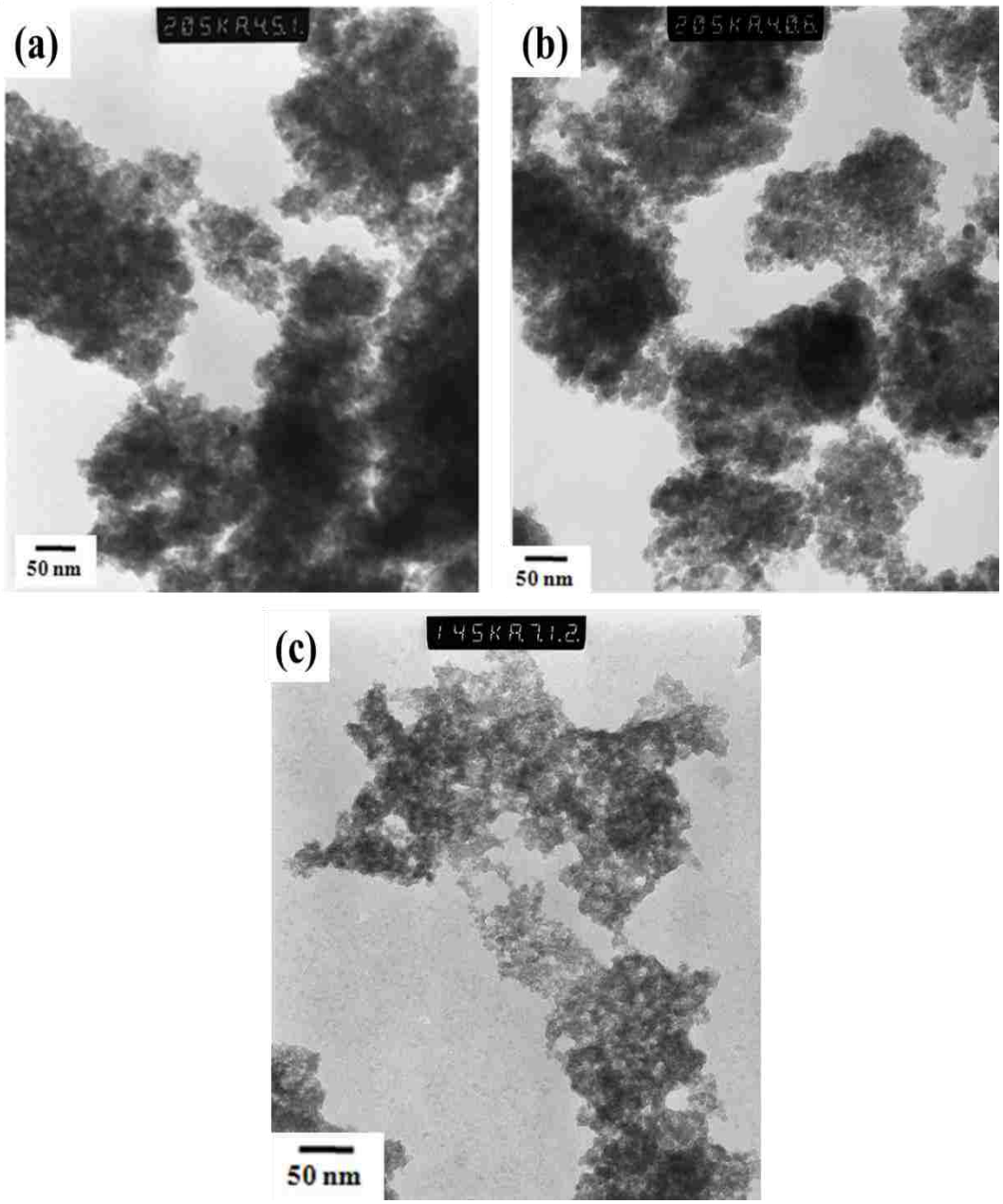

Figure 33**:** TEM micrographs of MNPs coated with 0.2% of different organic coatings. a) SDS, b) chitosan and c) dextran.

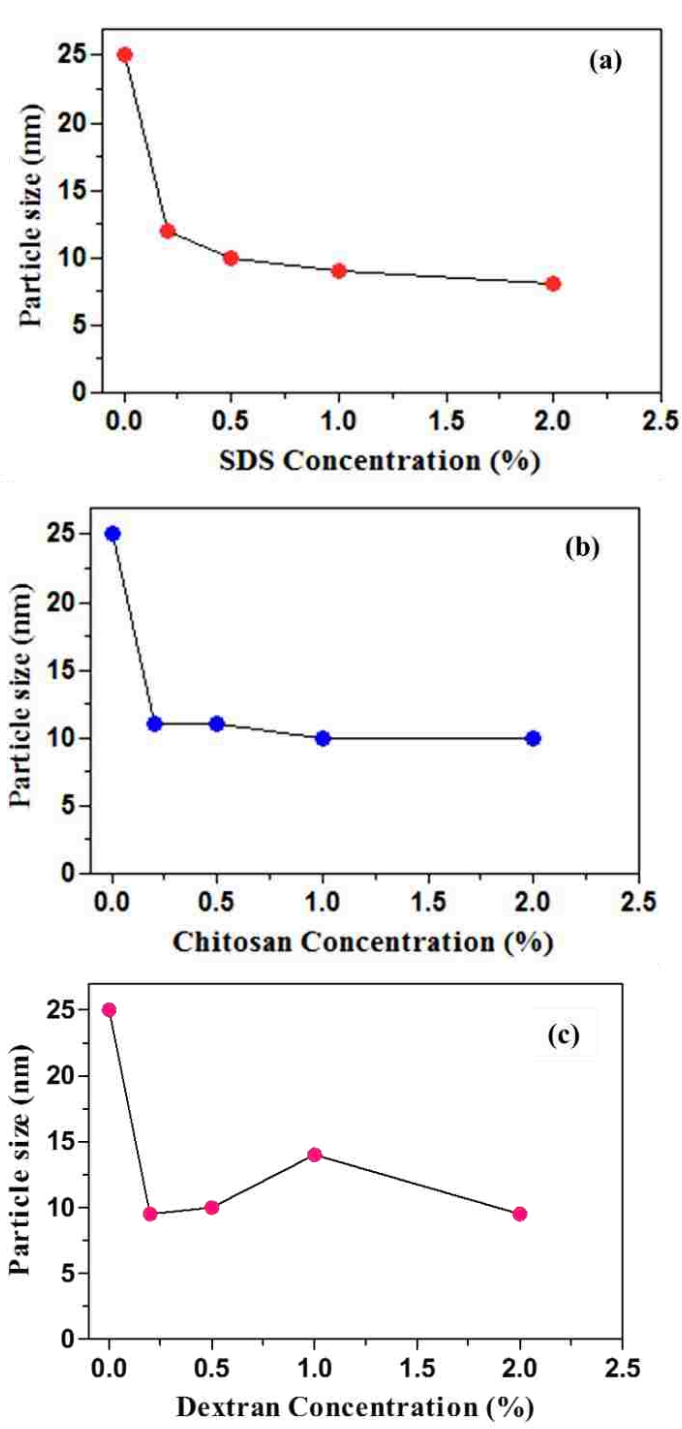

Figure 34: Average particle size distribution of neat MNPs and MNPs coated with different concentrations of organic coating materials. a) SDS, b) chitosan and c) dextran.

3.2.4. N_2 adsorption and pore size distribution of coated MNPs

Organic-coated MNPs were subjected to N_2-adsorption measurements to assess their surface area, pore size and pore size distribution. These measurements also provide information about the texture and topography of the NPs, especially if their ultimate applications require special surface characteristics.

Figure 35 shows adsorption-desorption hysteresis of MNPs coated with different concentrations of SDS, chitosan and dextran. All samples showed hysteresis loops of type IV where the lower curve represents the adsorption of N_2 gas on the surfaces of the NPs, while the upper curve represents the progressive withdrawal, i.e. desorption, of the adsorbed N_2 gas [192]. As a result of these experiments, and applying the BJH method of calculations, pore size distribution in each of the examined MNPs systems was calculated. Results are shown in **Figure 36**. It should be mentioned that these measurements are usually carried out on dry samples, where NPs tend to agglomerate as a result of their magnetic characteristics in addition to possible intermolecular forces between the organic-coated NPs.

Figure 36a indicates that NPs coated with 0.2% SDS appear to have macroporosity with a larger pore volume of 150 nm, which is a reflection of the larger particle size of these particles. By increasing the concentration of SDS, all samples showed the presence of mesoporosity as a sole type of porosity. In the presence of chitosan and dextran, all samples showed the presence of mesoporosity with a unified monodisperse pore size distribution; **Figure36b,c**. Comparing the results of adsorption isotherms and pore size distribution curves of organic-coated MNPs with those in pure MNPs, indicates that the mesoporosity of the neat MNPs aggregates is maintained even after coating with various concentrations of SDS, chitosan and dextran. Both monodispersity in particle size and mesoporosity in these

agglomerates are considered advantageous if these coated NPs are to be used as drug delivery vehicles or adsorbents or catalysts for various chemical reactions with potential environmental importance [179].

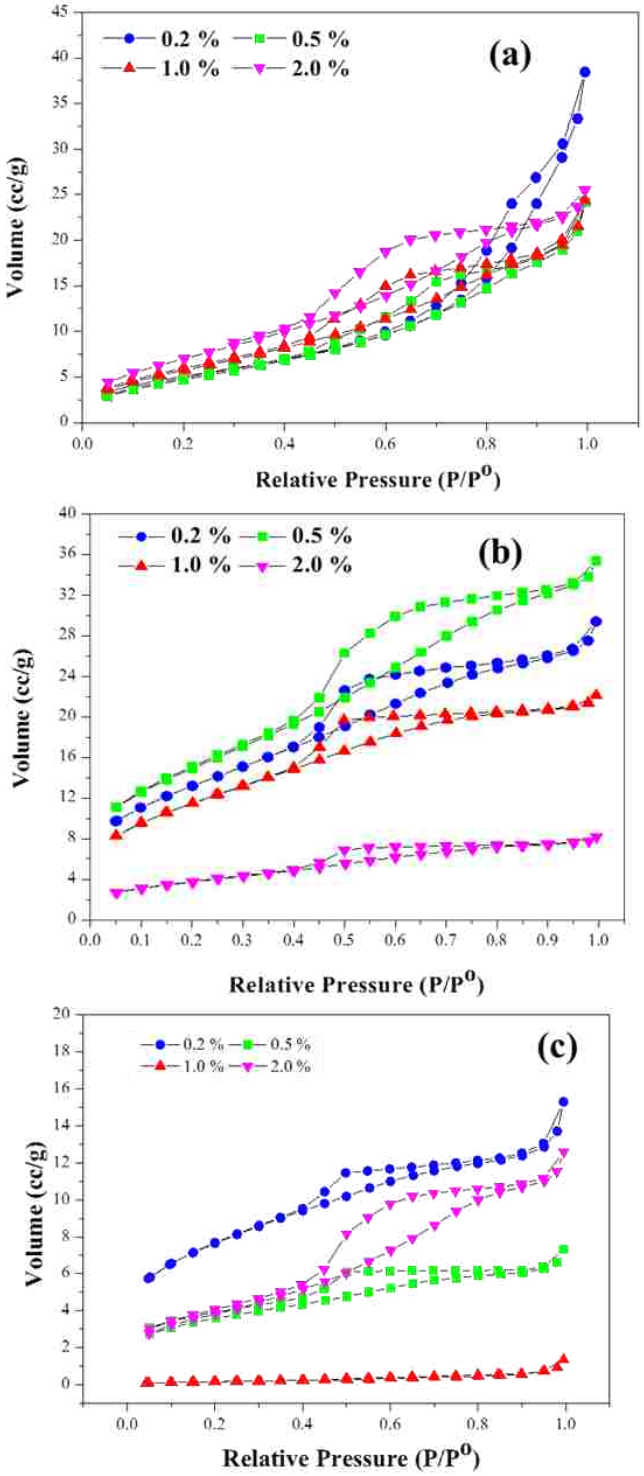

Figure 35**:** Adsorption-desorption hysteresis of MNPs coated with different concentrations of organic coating materials. a) SDS, b) chitosan and c) dextran.

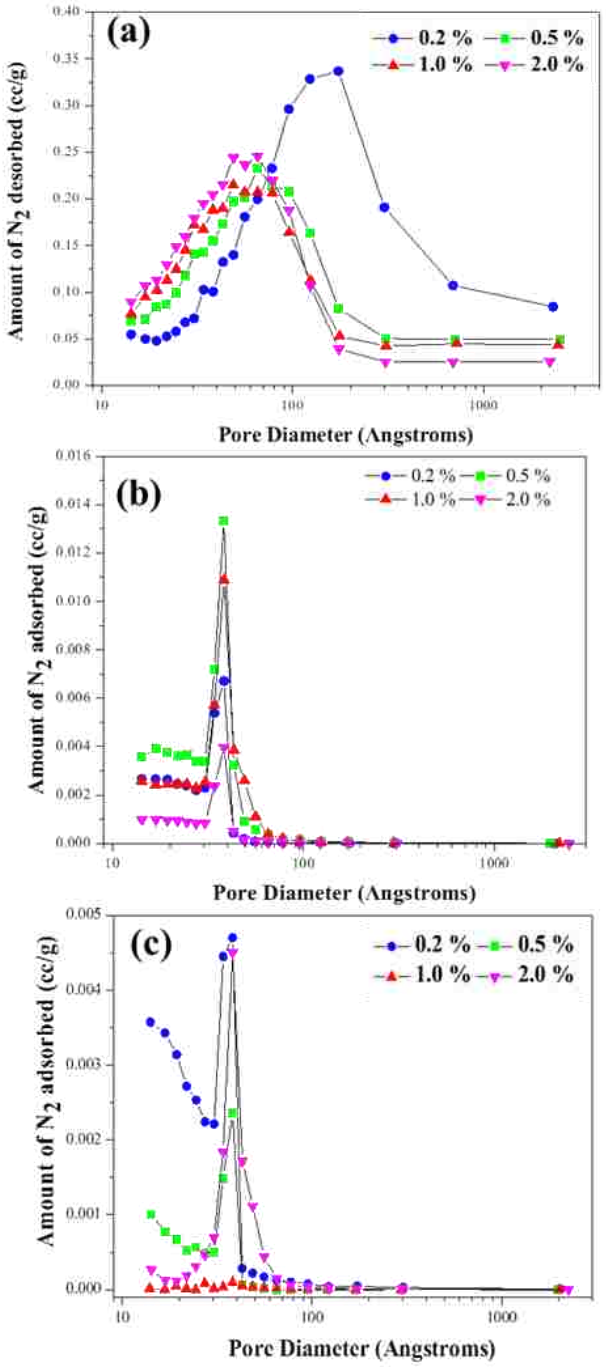

Figure 36: Pore size distribution of MNPs coated with different concentrations of organic coating materials. a) SDS, b) chitosan and c) dextran.

3.2.5. Magnetic properties of coated MNPs

The presence of an organic coating onto the surfaces of MNPs provides more advantages to the NPs where the newly established surface functionality could be used to immobilize other reagents to be used in drug delivery applications. However, increased thickness of the coating might lead to a decrease in the magnetic properties of the NPs, which is expected to decrease their potential for biomedical applications. Therefore, the effect of varying the concentration of organic coatings on the magnetic properties of the coated MNPs was investigated using a common VSM instrument.

Results are shown in **Figure 37**, where magnetization was measured as a function of the applied magnetic field at room temperature (300K). Neat MNPs and NPs coated with 0.2 and 1.0 weight % coating were selected for these measurements and for comparison. All Magnetization curves exhibited a typical behaviour of an ideal superparamagnetic material with zero coercivity and zero remanence. This is also confirmed with the fact that the average particle size of the neat and coated MNPs is below 30 nm, which is considered a maximum threshold for superparamagnetic character [197].

The superparamagnetic behaviour means the MNPs are a single-domain core and the magnetization at room temperature is reduced to zero, but when an external field is applied, the magnetic moments align with the field having magnetic field. Non-coated MNPs showed a saturation magnetization (*Ms*) of 25.9 emu/g. The presence of SDS as a coating onto the MNPs surprisingly resulted in an increase in the magnetization of the coated NPs. The NPs coated with 0.2 weight % SDS showed a magnetization of 50 emu/g, while increasing the SDS coating concentration to 1.0 weight % showed a magnetization of 38 emu/g; **Figure 37a.**

The increase in magnetization with the presence of SDS could be related to the surface charges of the ionic SDS groups on the coating. Increasing the concentration of SDS results in the formation of multilayers of SDS coating, which might decrease the surface charge as a result of the interlocking between the SDS molecules in the coating with increased thickness. This behaviour was not observed in the magnetization of chitosan and dextran-coated MNPs; **Figure 37b,c**.

The presence of chitosan and dextran coatings with variable weight percentages showed a range of magnetization of 7.0 - 21.3 emu/g. This could be related to the charge neutrality of the chitosan and dextran molecules. It was observed that the presence of chitosan and dextran resulted in a decrease in the particle size of the coated MNPs, the development of a non-magentic organic coating on the surfaces of these NPs in the presence of chitosan could be considered the main reason for the decrease in magnetization. This is also a common phenomenon in coated MNPs [173, 193].

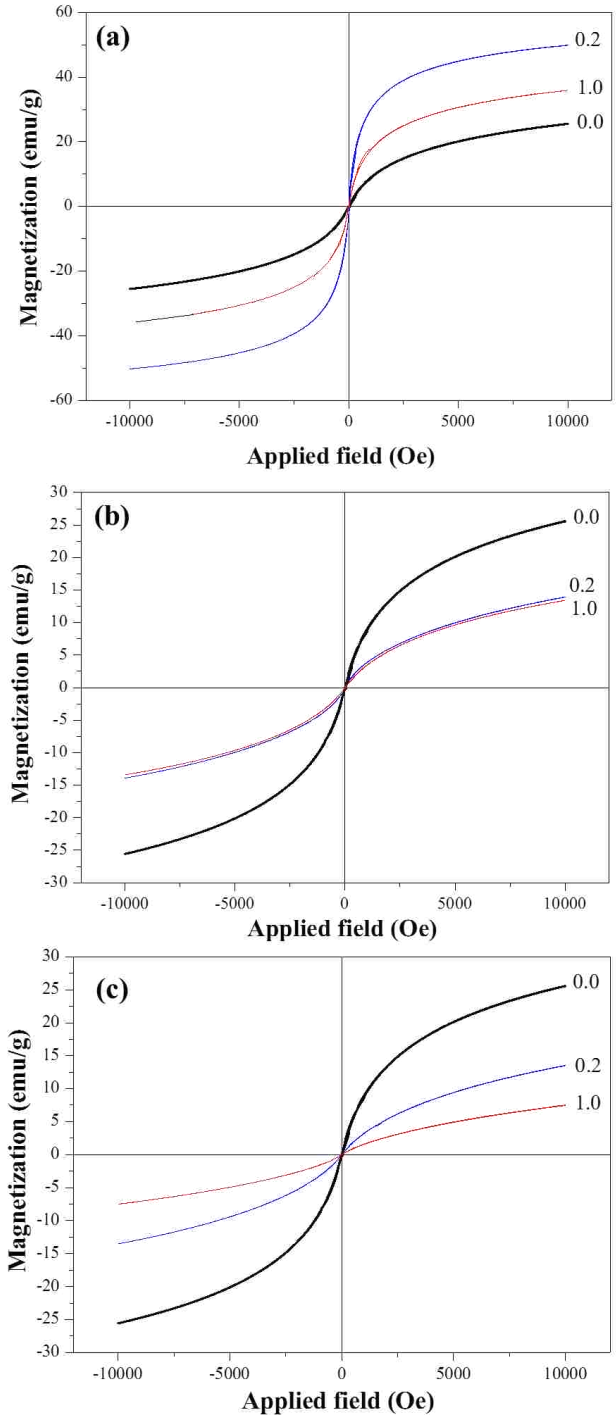

Figure 37: Magnetization of neat MNPs and MNPs coated with different concentrations of organic coating materials. a) SDS, b) chitosan and c) dextran.

3.3. Selection of organic-coated MNPs

Based on the previous results, MNPs coated with 1% by weight of dextran were selected to be further functionalized for drug delivery objectives. These were selected based on the following criteria:

1) Dextran is biocompatible and biodegradable.
2) Chemical Structure of dextran provides sites for further functionalization.
3) Dextran is a naturally occurring polysaccharide that can provide steric hindrance for further stabilization of the NPs in aqueous media.
4) Average size according to TEM was around 14 nm, which is reasonable for drug delivery applications [88].
5) Washing the extra unattached dextran was much easier than chitosan and SDS, during preparation.

In order to increase the yield of D-MNPs while maintaining the phase purity and monodispersity of the NPs, preparation of the dextran-coated MNPs was further modified and optimized. In the modified procedure, MNPs were pre-formed from more concentrated Fe^{2+} and Fe^{3+} solutions, MNPs were post-coated with 1% dextran. Starting iron solutions were 1.2M Fe^{2+} and 2.4M Fe^{3+}. After precipitation of the MNPs in a highly alkaline NaOH solution, they were soaked at a temperature of 60ºC for 38 hrs. MNPs suspensions were then centrifuged and subjected to successive decantation/centrifugation using sterile de-ionized water. Solutions containing suspended MNPs were separated by centrifuge, to be coated by dextran. A highly alkaline solution of NaOH containing 1 weight % dextran was used, so that the weight ratio of MNPs-to-dextran was 3:1. Extra un-attached dextran was removed by successive centrifugation and decantation, and was confirmed by Benedict's test. It should be mentioned that all preparation were carried out under

sterile conditions in a biological hood using sterile equipments and reagents. To confirm phase composition, D-MNPs were separated by centrifuge, dried and characterized using FTIR and TGA techniques.

Figure 38 shows FTIR of pure MNPs (0.0 % coating) and the D-MNPs (1.0% coating). Bands representing pure MNPs Fe-O bonds were appeared at 429, 561 and 618 cm^{-1} in the spectrum of pure MNPs. These bands were shifted to at 428, 571 and 619 cm^{-1} bands, respectively, in the FTIR spectrum of 1% D-MNPs. In addition, the presence of dextran as a coating was confirmed by its bands at 1010 and 1150 cm^{-1} for C-O group, and 1342 cm^{-1} for C-H group in D-MNPs.

Moreover, the presence of dextran as a coating onto MNPs was confirmed by TGA analysis; **Figure 39**, where weight loss of D-MNPS indicated the presence of dextran as a coating. This was evident through the major weight loss around 200^{o}C, and the minor weight loss around 450^{o}C, which were attributed to the degradation of dextran. It should be mentioned that TEM analysis of these NPs showed an average particle size of 16 nm with and without the coating, which may indicate the presence of a thin coating of dextran onto the MNPs.

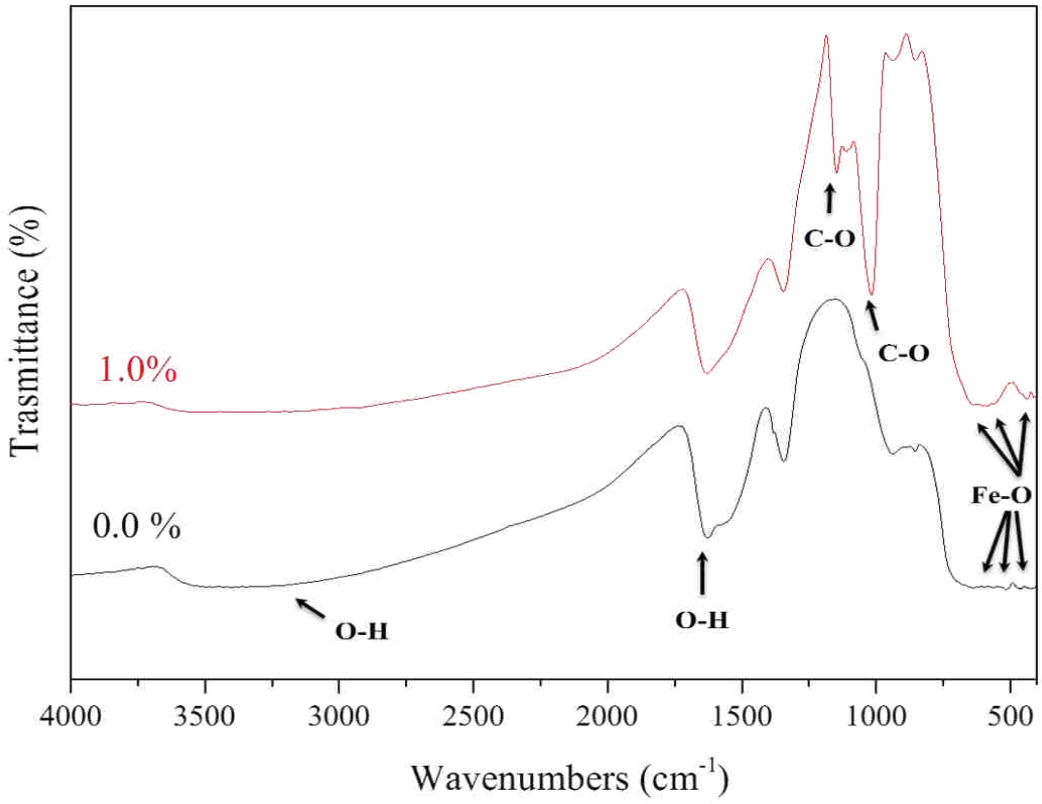

Figure 38: FTIR of pure MNPs and the D-MNPs.

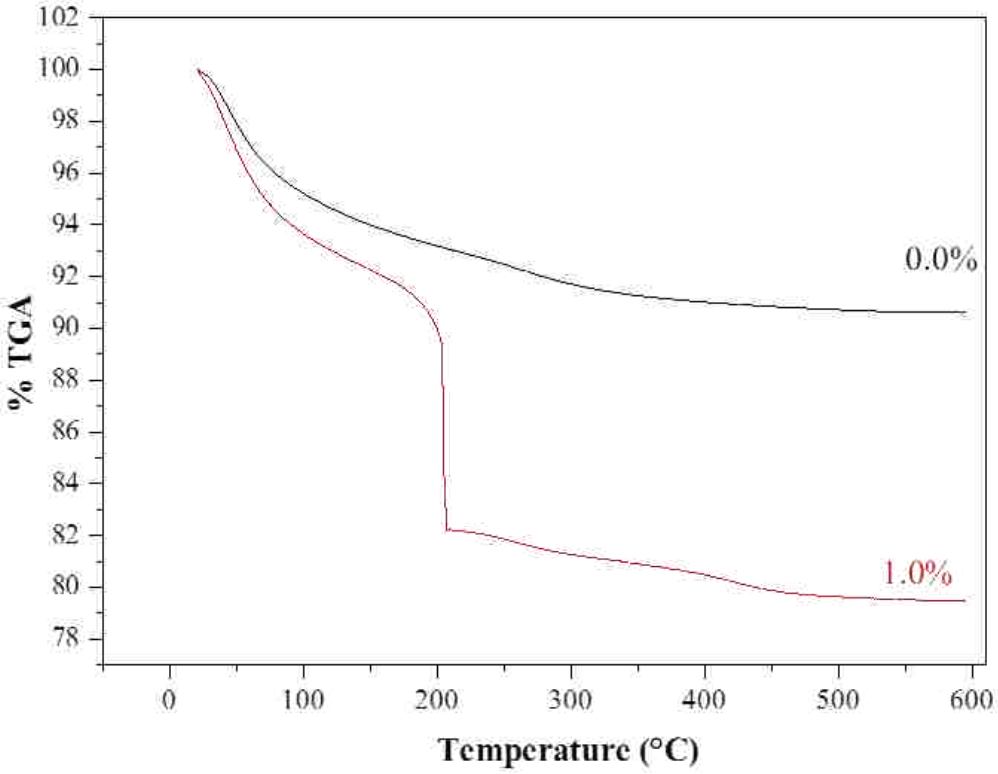

Figure 39: TGA of pure MNPs and the D-MNPs.

3.4. Crocin loading characterization

Crocin was chemically conjugated, via succinic anhydride as a cross linker, onto the surface of functionalized D-MNPs synthesized in this study. Results of three formulations are presented in this dissertation. Each formulation was numbered according to the crocin concentration that was used *in vitro* or *in vivo* experiments **(Table 9)**. The iron concentration used, was considered safe based on our previous studies.

The remained attached crocin was 70 mg/ml in 3 mg/ml formulation, 33 mg/ml attached crocin was in 2 mg/ml formulation, and in 4 mg/ml formulation the attached crocin was 40 mg/ml (**Table 9** and **Figure 40**). The difference in attached crocin might be because of the difference in the percentage of the coating with dextran among the NPs them self.

Table 9: Analysis of crocin and iron content in different D-MNPs formulations.

Tested crocin concentration	Initial crocin concentration (mg/ml)	Crocin loading efficiency (%)	Attached crocin concentration (mg/ml)	Non-toxic Fe concentration (NPs with and without crocin)
3 mg/ml (*in vitro*)	100	70	70	0.09mg/ml-9µg/100µl
2 mg/ml = 11 mg/kg (*in vivo*)	100	33	33	17mg/kg-0.3mg/100µl
4 mg/ml = 22 mg/kg (*in vivo*)	50	80	40	17mg/kg-0.3mg/100µl

The results of FT-IR spectrum of pure crocin showed the bands at 1515 and 1631 cm^{-1} due to C=C. Also it shows 1697 cm^{-1} because of C=O [153], 2933 cm^{-1} band caused by C-H and the broad stretch between 3262 and 3441 cm^{-1} corresponds to the presence of O-H groups [198]. FTIR spectrum of D-MNPs with crocin shows the unique bands of C=C at 1534 and 1637 cm^{-1} which is only present in crocin, confirming the successful addition of crocin in the D-MNPs as seen in **Figure 41**.

The synthesis reaction of crocin-loaded D-MNPs was as follows. Free hydroxyl groups on dextran reacted with succinic anhydride to form covalent ester bonds and a free carboxylic acid. The latter is used to link the hydroxyl group of crocin via esterification. Succinic anhydride is an organic compound with the molecular formula $C_4H_4O_3$ (**Figure 42**). It can form a strong ester bonds between itself and crocin or dextran as mentioned earlier. These bonds can break specifically in acidic environment as in cancer site to release crocin in active form, dextran and succinic acid. EDCI was used during the esterification reaction as the coupling reagent to activate succinic acid enabling crocin to bind. It did not interfere in the chemical structure and its end product (urea derivative) can be washed out easily by water **Figure 42.**

Figure 43 shows the TEM of D-MNPs and 4 mg/ml crocin-loaded D-MNPs as representative formulation. The size of synthesized crocin conjugated D-MNPs by esterification process was uniform and monodisperse. The average diameter of D-MNPs with and without crocin was 16 nm, indicating that the addition of dextran and crocin layers were very thin and did not affect the main core size of MNPs.

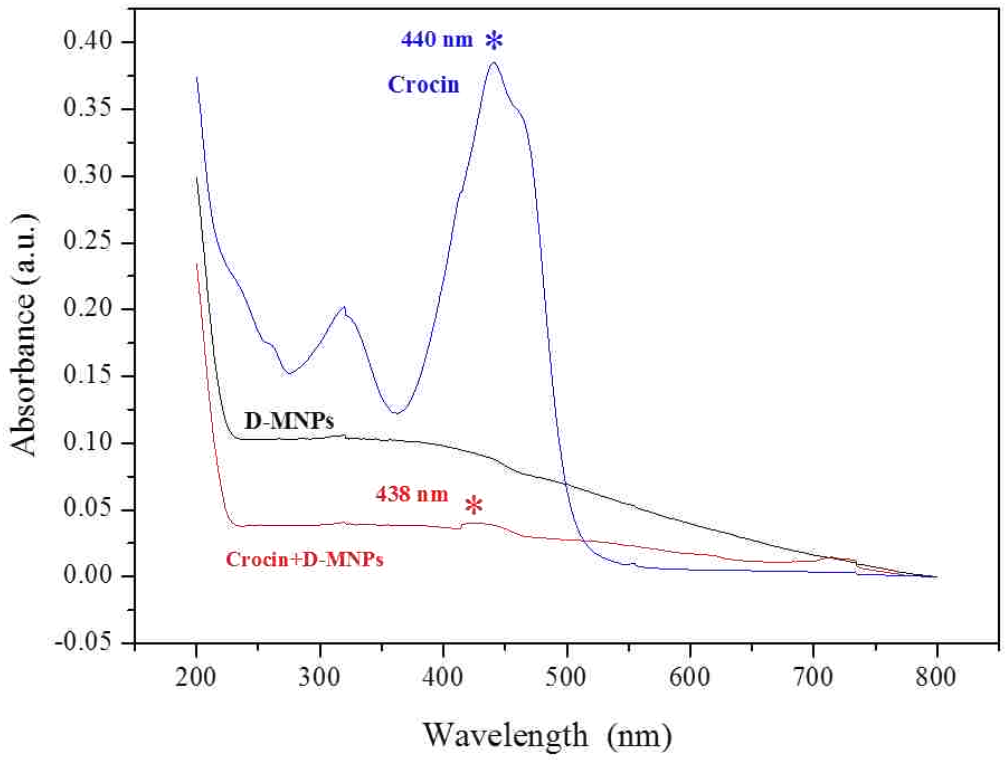

Figure 40: UV-Visible spectral measurements of crocin, D-MNPs and 4 mg/ml crocin-loaded D-MNPs.

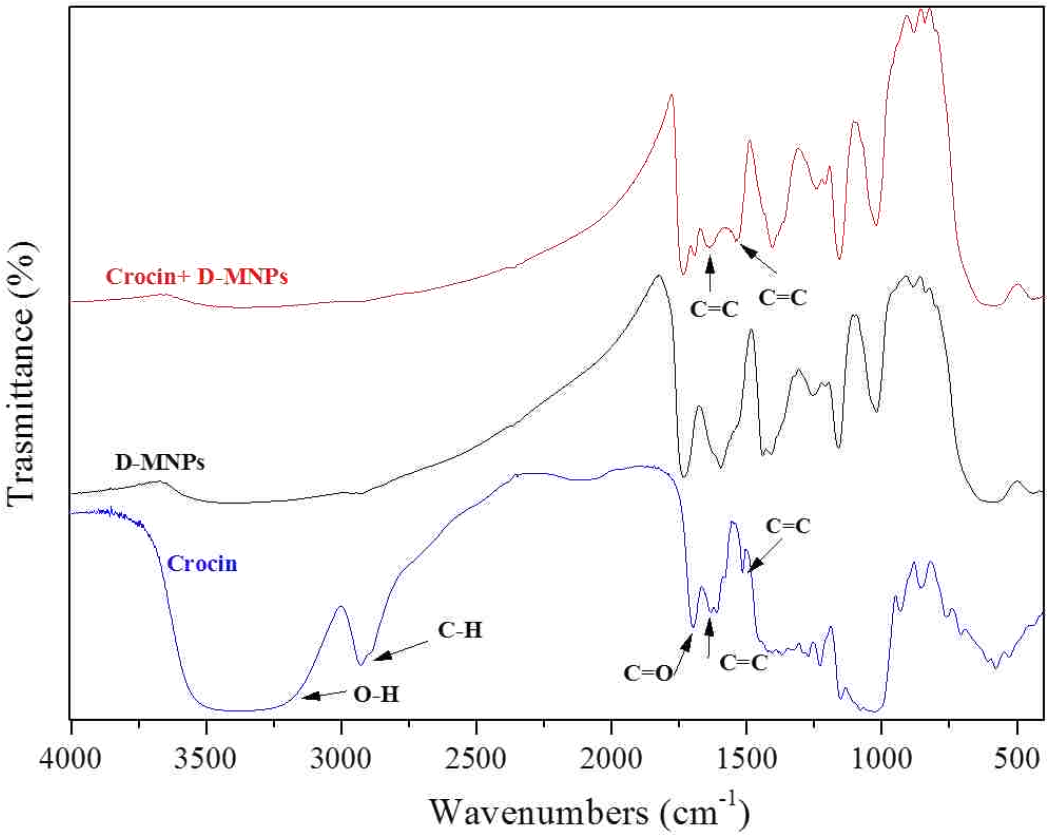

Figure 41: FTIR of crocin, D-MNPs and 4 mg/ml crocin-loaded D-MNPs.

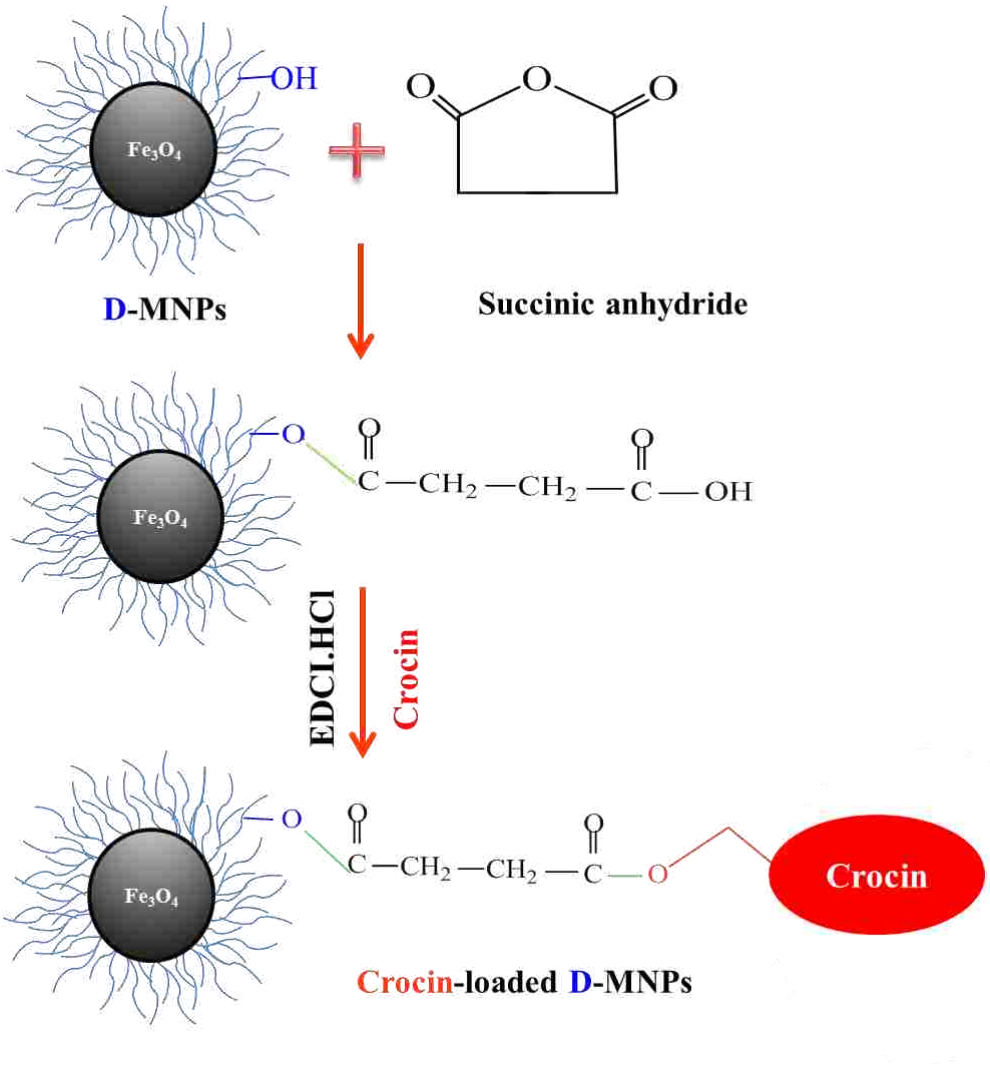

Figure 42: Schematic representation of chemical synthesis of crocin-loaded D-MNPs.

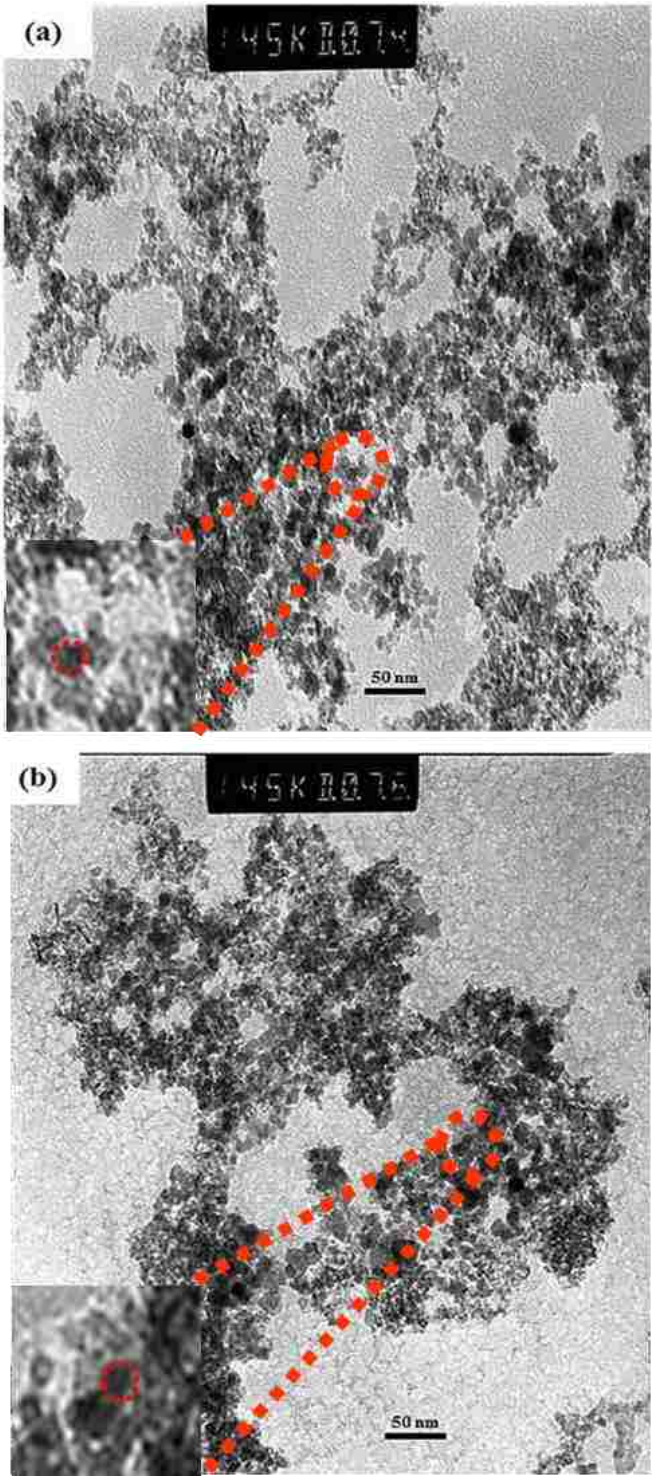

Figure 43: TEM micrographs of (a) D-MNPs and (b) 4 mg/ml crocin-loaded D-MNPs. Insets: individual round shaped MNP.

3.5. *In vitro* release of crocin

The cumulative release of crocin from the prepared D-MNPs carrier was investigated at pH values of 5.5 and 7.4 at the physiological temperature of 37 ºC. The cumulative drug release was expressed as the percent of de-attached crocin from D-MNPs and released to the surrounding aqueous media as a function of time. The drug release activity depends on many characteristics of the NPs, such as surface characteristics and forces of interaction between crocin and the underlying D-MNPs. The *in vitro* drug release behaviour of crocin loaded D-MNPs was studied in PBS at pH 7.4 and a temperature of 37ºC to maintain the experimental condition similar to the physiologic conditions. The tumour tissue has acidic nature with pH 5-6 compared to the healthy tissues at pH 7.4 [168, 199, 200], because of that the release study was investigated at pH 5.5 at temperature of 37ºC to understand the release mechanism in cancer site.

Figure 44 shows the percentage of cumulative release of crocin from 2 and 4 mg/ml crocin loaded D-MNPs formulations and both with 3 mg Fe/ml. The release behaviour of 2 mg/ml crocin loaded D-MNPs at 0.0 hr was 16% at pH 5.5, whereas at pH 7.4 it showed a percent release of 4%. The release increased as the time increased to reach 47 % and 38 % at pH 5.5 and 7.4, respectively after 15 day.

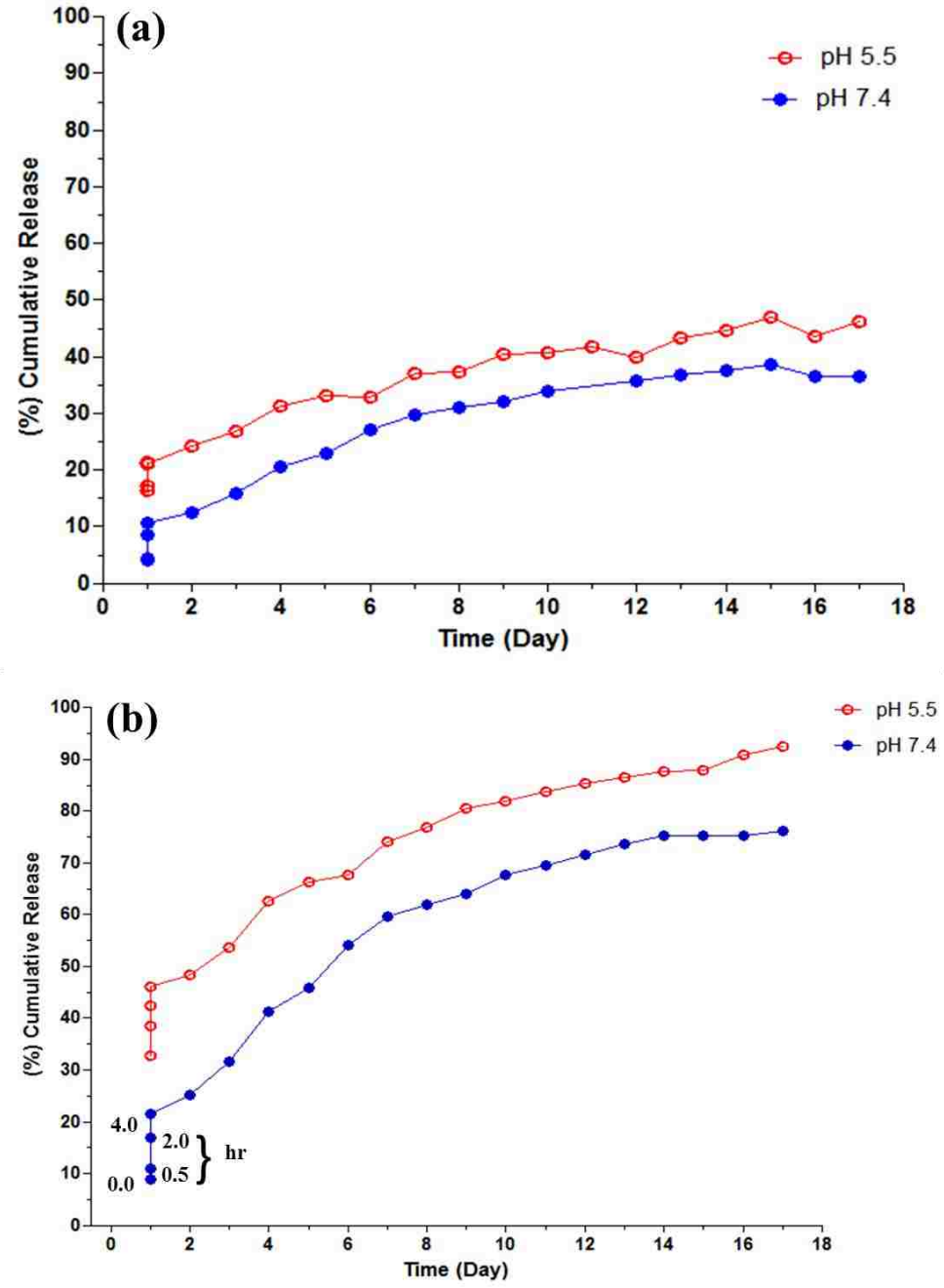

Figure 44**:** Release profiles of crocin from the prepared two formulations. a) 2 mg/ml and b) 4 mg/ml crocin conjugated D-MNPs with 3 mg Fe/ml in PBS at pH 5.5 and 7.4.

On another hand, there was initial burst release in 4 mg/ml crocin loaded D-MNPs with 33% at pH 5.5 compared with 9% at pH7.4. The release rate at 5.5 pH increased to reach 46% in the first 4 hrs. Then it was accelerated constantly as the time prolonged to reach 88% in day 15^{th} and 92% in day 17^{th}. In addition, the crocin release at pH 7.4 was lower than 5.5. In the first 4 hrs it was 21%, and then the release was increased regularly till day 15^{th} to be 75%. But it started to increase slowly to reach 76% after 17 days. In General, the release behaviour in 4 mg/ml crocin loaded D-MNPs were faster than 2 mg/ml formulation.

In this study crocin release in both buffer solutions showed sustained release behaviour with time in both formulations. Release of crocin might be attributed to the slow cleavage or hydrolysis of hydrogen bond between crocin and cross linker that was directly attached to the D-MNPs. A maximum percentage of crocin release was 92% and was obtained under acidic conditions (pH 5.5) compared to 76% in physiological conditions (pH 7.4) after 17 days. This difference in release is significant ($P = 0.0127 < 0.05$, student t-test). The higher percentage of release was obtained due to the increase in hydrolysis of carboxylic esters linkage between crocin and succinic acid that bound to D-MNPs. After hydrolysis each compound returned to its original structure producing; crocin, succinic anhydride, and dextran attached to MNPs, while the MNPs might degrade to free iron that will bind to ferritin protein in the cells.

Because of leaky and pre-mature blood vessels of cancer tissues, the chance of crocin loaded D-MNPs to accumulate inside these tissues by passive targeting will be higher than normal tissues. Leading to an increase in the concentration of crocin loaded D-MNPs to 10-100 times higher in cancer tissues within 1-2 days compared

to normal ones. Consequently, this will increase the hydrolysis and release of crocin in cancer tissues [90, 201-203].

The current results are consistent with the findings of previous researchers, who demonstrated that acidic conditions accelerate the cleavage of the bonds connecting the linker to the crocin and underlying D-MNPs, and the passive targeting can accumulate the NPs in tumour tissues more than normal one [168, 200].

3.6. *In vitro* cytotoxicity

In this study, the human hepatocellular carcinoma cell line HepG2 was selected as a model of cancer cells for *in vitro* experiments. Cell proliferation and viability were evaluated by MTT assay. HepG2 cells were incubated for 72hrs with 9 different concentrations of crocin including 0.025, 0.05, 0.5, 3, 5, 8, 10, 15 or 20 mg/ml as well as crocin-free control. Compared to control group, microscopic examination of crocin treated cells showed morphological changes such as rounding of cells, reduced cytoplasm, cell shrinkage and pyknotic nuclei, suggesting apoptosis induction [68, 204].

Similar apoptotic-related changes have been reported in HeLa cells after being treated with crocin. IC_{50} of crocin-treated HeLa cells was 3 mg/ml (3mM) 18hrs post incubation. Crocin was also found to be more effective than other saffron bioactive ingredients such as crocetin and safranal [205].

MTT assay results showed that crocin decreased the cell viability in a dose-dependent manner. There were significant reductions ($P \leq 0.001$) from 3 to 20 mg/ml concentrations compared with control as in **Figure 45**. The IC_{50} of crocin was around 6 mg/ml, which is equivalent to 6 mM.

Noureini et al. reported that crocin has a significant cell viability inhibitory impact in both dose- and time-dependent manners on HepG2 cells. This anti-proliferative effect was proposed to be due to the telomerase inhibition that resulted

from down regulating hTERT (catalytic subunit of telomerase gene) [206]. Studies have shown that the crocin has the potential to inhibit growth of different types of cancer cell lines. The IC_{50} of crocin on HL-60 leukemic cells was 2 µM (µg/ml). Other cell lines including K562, HeLa, HCT-116 and HT-29, had IC_{50} of 0.4, 3, 10 and 1 mg/ ml, respectively [67, 207].

Sun et al. suggested that crocin (0.625-5 mg/ml) reduced cell proliferation in human leukemia HL-60 cell line, and caused apoptosis and cell cycle arrest at G0/G1 phase, in concentration- and time-dependent manners [208]. These results are in agreement with the investigation of Hoshyar et al. who also found that crocin triggered the apoptosis through increasing the Bax/Bcl-2 ratio and caspase activation in human gastric adenocarcinoma, AGS cells [209].

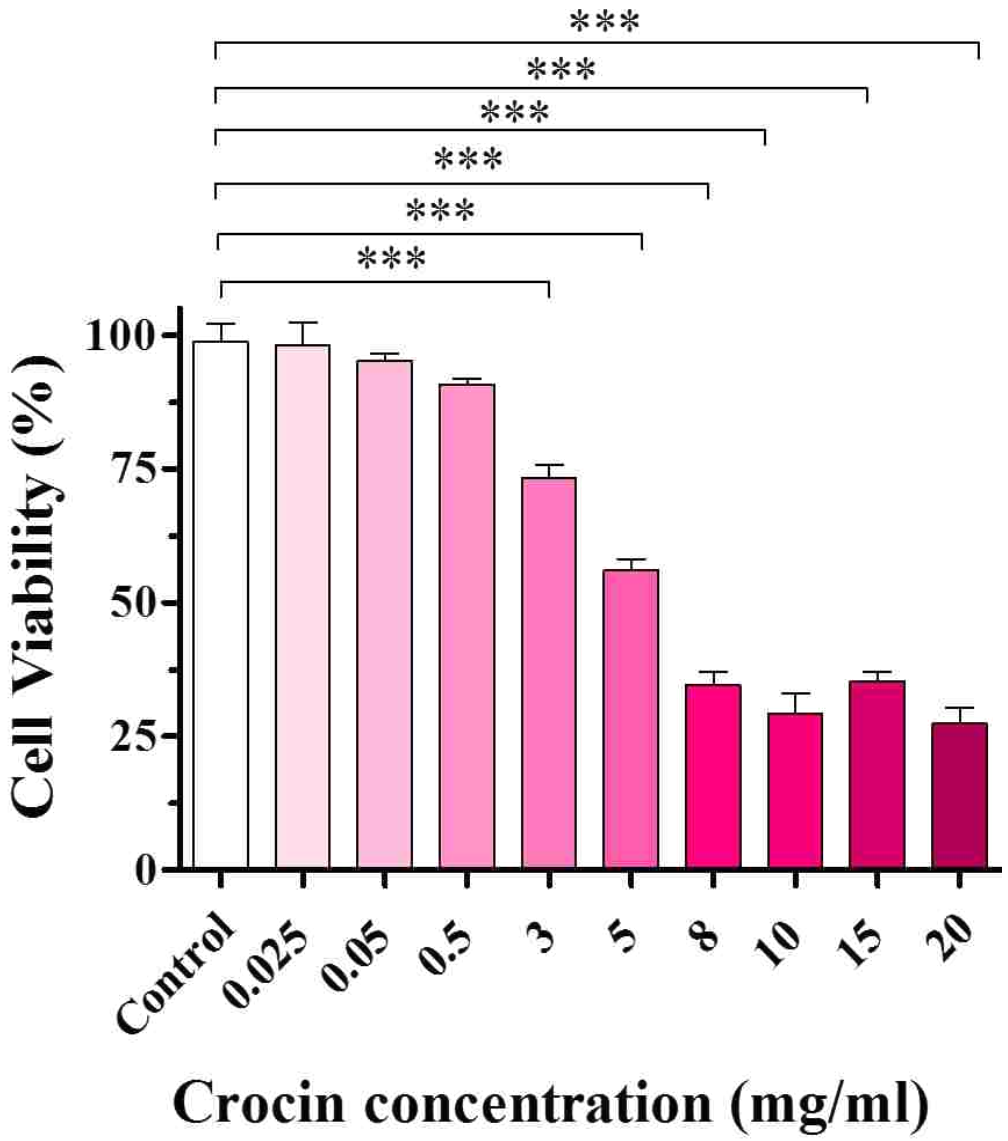

Figure 45: MTT cell viability assay of HepG2 cells, which were incubated with different concentrations of crocin for 72 hrs. All the values are expressed as mean ±SEM; ***$P \leq 0.001$.

Crocin also inhibited the proliferation of human tongue squamous cell carcinoma cell line, Tca8113, through reducing the nucleic acid synthesis and inducing apoptosis [210]. It also induced apoptosis and G1-phase cell cycle arrest in a human pancreatic cancer cell line, BxPC-3, and colorectal cell line, HCT-116, while decreasing cell viability in dose-and time-dependent manners [207, 211]. However, crocin has no toxic effects on normal cells such as human normal fibroblast skin cells, HFSF-PI3 [67, 209].

MTT assay was then used to study the effect of D-MNPs on viability of HepG2 cells. Different concentration of iron contents of applied D-MNPs were incubated with HepG2 cells for 72 hrs and the corresponding cell viability were plotted in **Figure 46.** The cell viability decreased as the iron concentration increased in a concentration-dependent manner. There was no significant inhibition at 0.05 mg/ml compared to the control. The cell viability was obtained at 90 to 60% in a broad concentration range of 0.05 mg/ml to 0.1 mg/ml. This demonstrated that the MNPs carrier coated with dextran had good biocompatibility due to its sugar components. The increase in cytotoxicity might be because of some MNPs lost their dextran coating, consequently exposing MNPs to the cells [200].

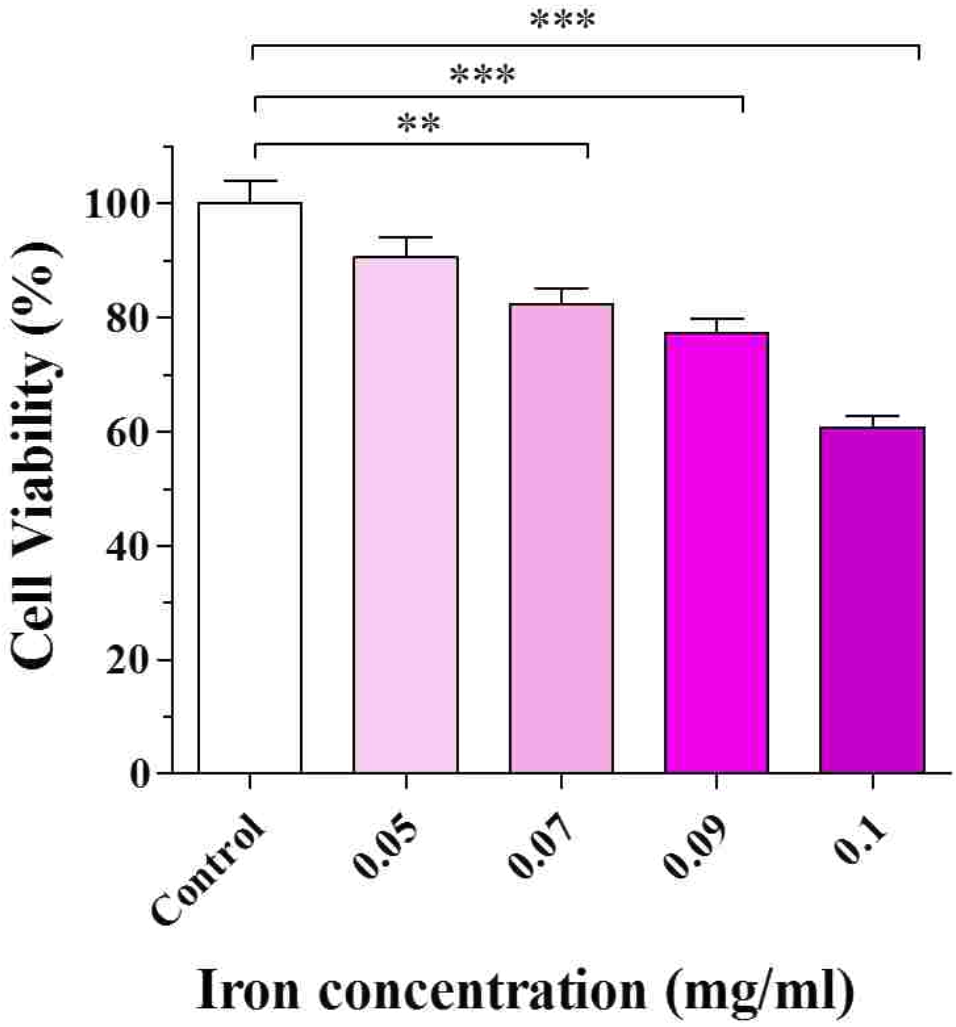

Figure 46: Cytotoxicity of different iron concentrations in D-MNPs on HepG2 cells after 72 hrs. All values are expressed as mean ±SEM; $^{**}P \leq 0.01$, $^{***}P \leq 0.001$.

Kumar et al. demonstrated that the cell viability of human breast cancer cell line MCF-7 cells was obtained at 90 to 78% in concentration range of 0.01-0.1 mg/ml for 24 hrs compared with control cells. They also concluded that the MNPs coated with dextran had good biocompatibility [200]. In other study, a range of MNPs with varying physico-chemical properties primarily demonstrated low cytotoxicity at doses of 0.1 mg/ml or higher [3]. Therefore, 0.09 mg/ml (9 µg/100µl) iron-content D-MNPs were loaded with crocin for further *in vitro* studies.

MTT assay at 72 hrs of HepG2 cells was also used to evaluate the anti-cancer effect of 3 mg/ml crocin-loaded D-MNPs with 0.09 mg Fe/ ml and compare it with control, 3 mg/ml crocin or D-MNPs with 0.09 mg Fe/ml as in **Figure 47**. Three mg/ml crocin was selected from the previous free crocin screening to test if crocin-loaded D-MNPs enhance the crocin-inhibitory effect over free crocin by reduce the proliferation of HepG2 cells. Inverted microscope observations showed that the cell viability of the HepG2 incubated with free crocin and crocin-loaded D-MNPs decreased as incubation time increased from 24 to 72 hrs. However, D-MNPs had no significant effect on the cell viability compared to control. Villanueva et al. revealed that the viability of cell culture of D-MNPs with HeLa cells at 24 hrs was not significantly affected by the presence of the NPs compared to control [212].

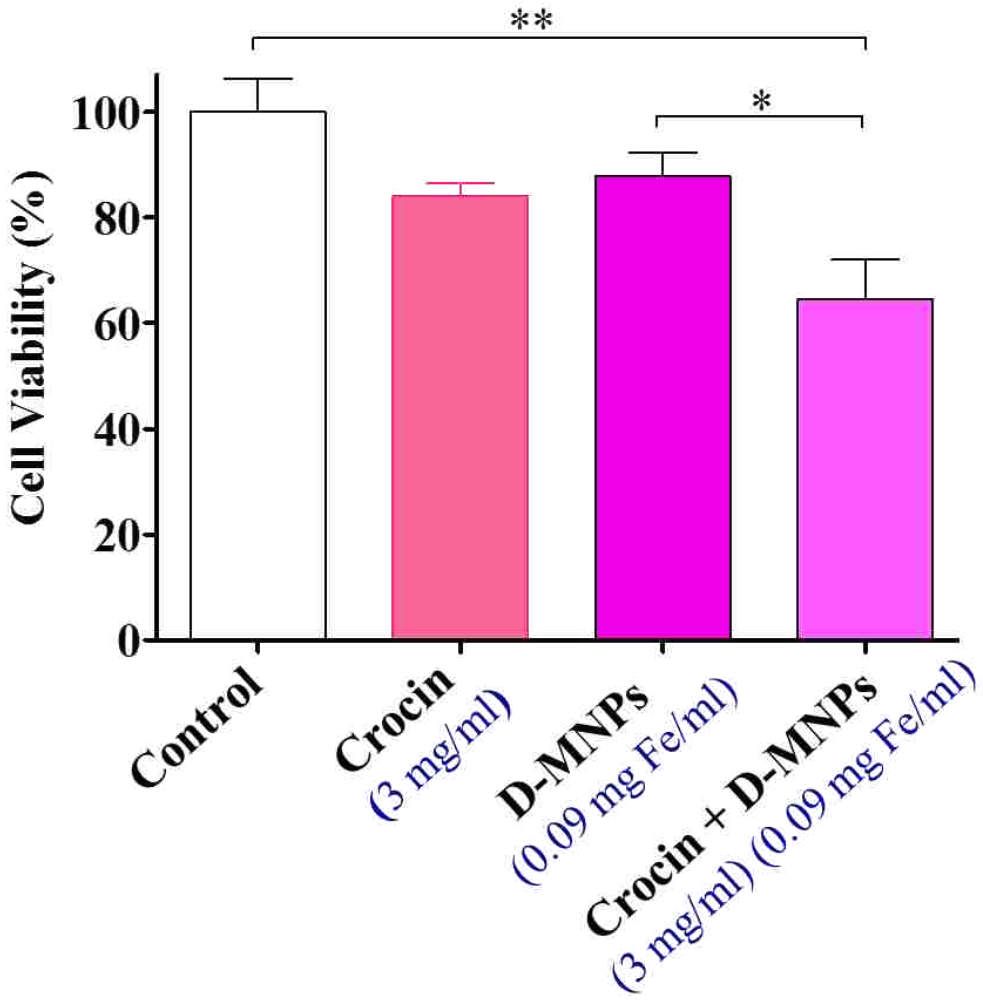

Figure 47: Cytotoxicity effects of media alone as a control, 3 mg/ml crocin alone, D-MNPs with 0.09 mg Fe/ml and 3 mg/ml crocin-loaded D-MNPs with 0.09 mg Fe/ml on HepG2 cells. Values are expressed as mean ±SEM; *$P \leq 0.05$, **$P \leq 0.01$.

In the present study, MTT assay at 72 hrs incubation of HepG2 cells resulted in crocin conjugated D-MNPs significantly decreased ($P \leq 0.01$) the cell viability to 65% compared to non-significant inhibitions 82% of free crocin, and 87% of D-MNPs and all compared to control. The decrease in cell viability associated with D-MNPs group might be due to the degradation of dextran and exposure of MNPs to the cells. There was significant decrease ($^{*}P \leq 0.05$) between crocin-loaded D-MNPs and D-MNPs groups. However, there was no significant difference in cell viability between D-MNPs and control groups.

The D-MNPs either alone or with crocin were stable in the DMEM medium as well as in the deionized or auto-cleaved water (storage solution) during the time of testing and after weeks of storage, indicating that these NPs have stabilizing shell which not only decrease agglomeration but also protect them from external factors.

A carrier like D-MNPs has been shown to increase the uptake by cancer cells via adsorption, fusion, and endocytosis [90, 212, 213]. The increased toxicity of the crocin coated D-MNPs on HepG2 cells might also be due to the anti-proliferation effect of crocin that might be released as shown earlier in the release study (**Figure 44**)**.** Nanoliposomes containing crocin have been shown to improve cytotoxic and apoptotic properties of crocin on HeLa and MCF-7 cancer cell lines compared to free crocin. No cytotoxic effects were however reported on the non-malignant mouse fibroblast cell line L929 [67, 214]. To confirm the cytotoxic effect of the crocin-loaded D-MNPs, further in *vivo* study was performed.

3.7. *In vivo* anti-tumour efficacy

Balb/c mice strain was chosen for this study as it has been used as a model for carcinogenicity in other studies [42, 46, 48, 49, 215-217] and it is relatively

sensitive to the induction of hepatic tumors by chemical carcinogens such as DEN [48].

No previous study has been used multiple injections of DEN to induce pre-neoplastic foci or HCC in pre-weaning Balb/c mice of 3 weeks old. So, in this study we are characterizing a modified pre-cancerous mice model that can be produced in two months only. This model also mimics the human pre-cancerous procedure, as it is a multistep model where cycles of de-generation and re-generation might activate pre-neoplastic transformations. The progression of early dysplastic lesions to malignant tumours is associated with an increased occurrence of genomic alterations [17, 51].

The younger the mice are the faster HCC will develop because of the high hepatocytes proliferation rates of young animals. Also, HCC deveolps in male more than female is because of the stimulating effect of androgens and the inhibitory effect of estrogens on hepatocarcinogenesis [13, 16, 17, 41].

3.7.1. General Observation, Body and Liver Weight

In this study, 50 mg/kg DEN was used to induce hepatic carcinogenesis in 3-weeks old pre-weaning male Balb/c mice. DEN administration caused reduction in the body and liver weights as shown in DEN-induced group compared to normal group as in **Figure 48**. This reduction in body and liver weights was because of the cytotoxic effect induced by DEN. Some animals could not tolerate DEN induced cytotoxic effect and died. DEN exposure affects liver at two stages: initially it reduces the hepatocytes cell proliferation, then cell proliferation and DNA synthesis increase to ultimately form pre-cancerous lesions and cancer. Such initial depression in cell proliferation and DNA synthesis was combined with amount of cell damage or death that was enough to cause some animal to die, before the regenerative response

was triggered. This reduction in the hepatocytes proliferation might decrease the overall body and liver weights in spite of some pre-cancerous changes was taking place in the liver as confirmed by IHC studies section later [31].

In addition, cell proliferation reduction of hepatocytes was associated with the initial interval of cytotoxicity that was reported by Rajewsky et al. in 1966. Male rats were exposed to 5 mg/kg DEN per day in drinking water for 11 weeks. The initial reduction of hepatocytes proliferation was for 3-5 days. After this period, cell proliferation increased to 2-3 times [41]. **Figure 48** shows the body and liver weights in 11 and 22 mg/kg crocin-loaded D-MNPs with 17 mg Fe/kg treated groups recovered and increased compared to DEN-induced or free crocin groups. Indicating better effectiveness of crocin-loaded D-MNPs than free crocin. Crocin-conjugated PEGylated nanoliposomes have been shown to increase the weight of Balb/c mice with C26 tumor when compared with free crocin [218].

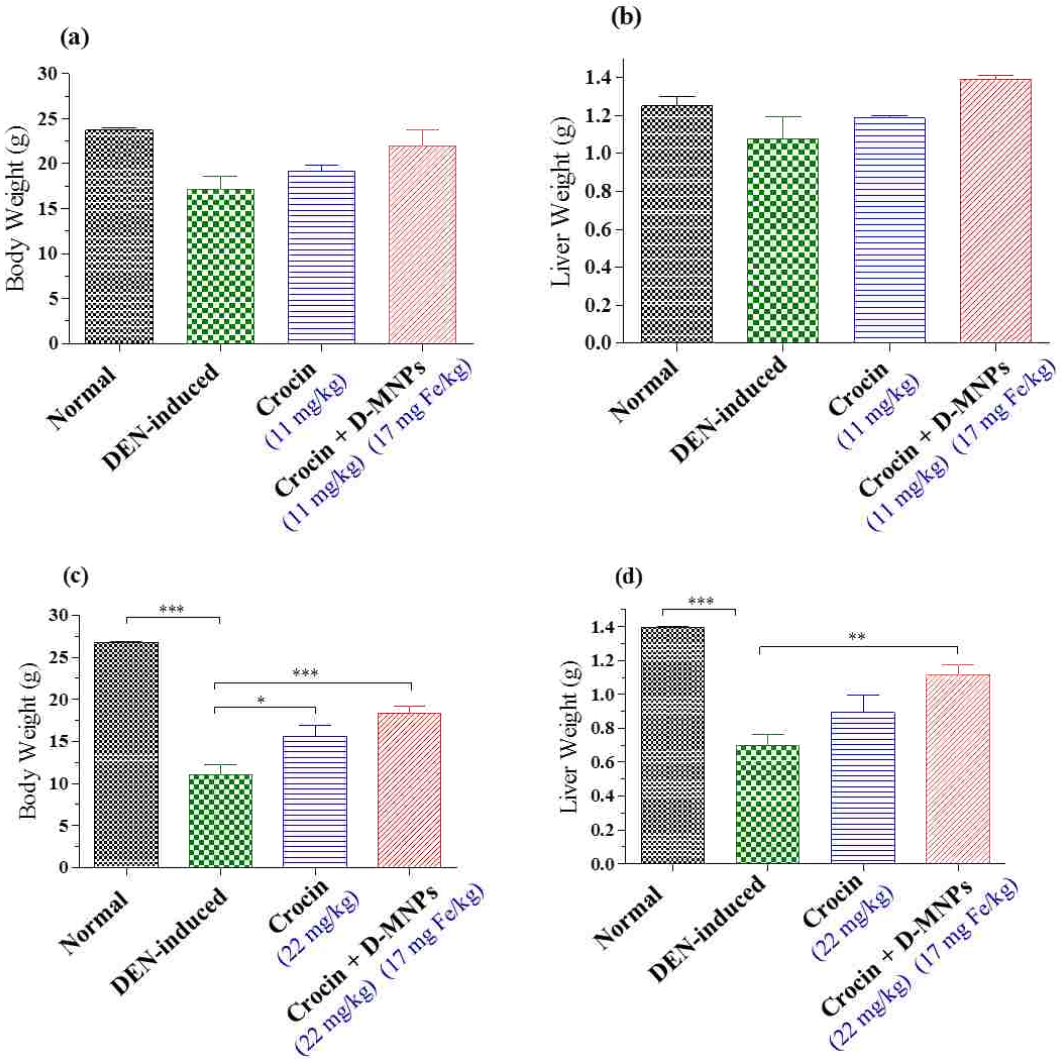

Figure 48: Body and liver weights of Balb/c mice treated with different treatments. a) Body and b) liver weights of normal, DEN injected mice treated with saline (DEN-induced group), 11 mg/kg crocin, and 11 mg/kg crocin-loaded D-MNPs with 17 mg Fe/kg. c) Body and d) liver weights of normal, DEN injected mice treated with saline (DEN-induced group), 22 mg/kg crocin, and 22 mg/kg crocin-loaded D-MNPs with 17 mg Fe/kg. Values are expressed as mean ±SEM; $*P \leq 0.05$, $**P \leq 0.01$, $***P \leq 0.001$.

3.7.2. Histopathological examination

Figures 49 and 50 show normal structure and histology of liver as seen in the normal group of mice. The liver is divided histologically into lobules; each lobule appears hexagonal in shape. The center of the lobule include the central vein, however the portal triads are located at the periphery. The portal triad consists of branches of hepatic artery, portal vein, and bile duct. It also includes lymphatic vessels. The hepatocytes appear mono or bi-nuclear with round and centrally located nuclei. Hepatocytes are also arranged in single-cell thick plates that radiate out from the central vein. These plates are separated or surrounded by vascular sinusoids [10].

In the animal model that has been developed in this study, no gross or macroscopic tumor was observed in the livers of any DEN injected group. However, microscopic histological examination of livers of mice in DEN-induced group showed clear pre-neoplastic changes including large and small cell dysplasia, such as altered hepatocellular foci (AHF), and accumulation of lymphocytes, intrahepatic bile ducts and oval cells. AHF were also considered by some researchers as islands of cellular alteration [42, 217, 219].

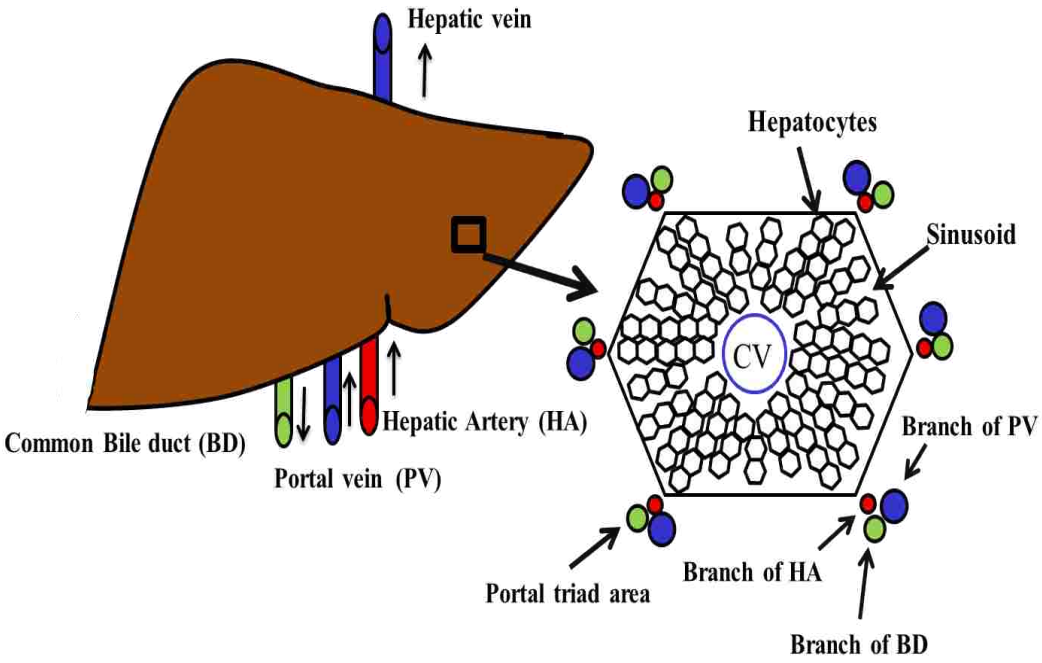

Figure 49: Diagrammatic representation of liver normal structure and blood flow. Hepatic lobules of liver are represented by hexagonal hepatocytes cells structure and surrounded by portal triads at the corners. CV; central vein.

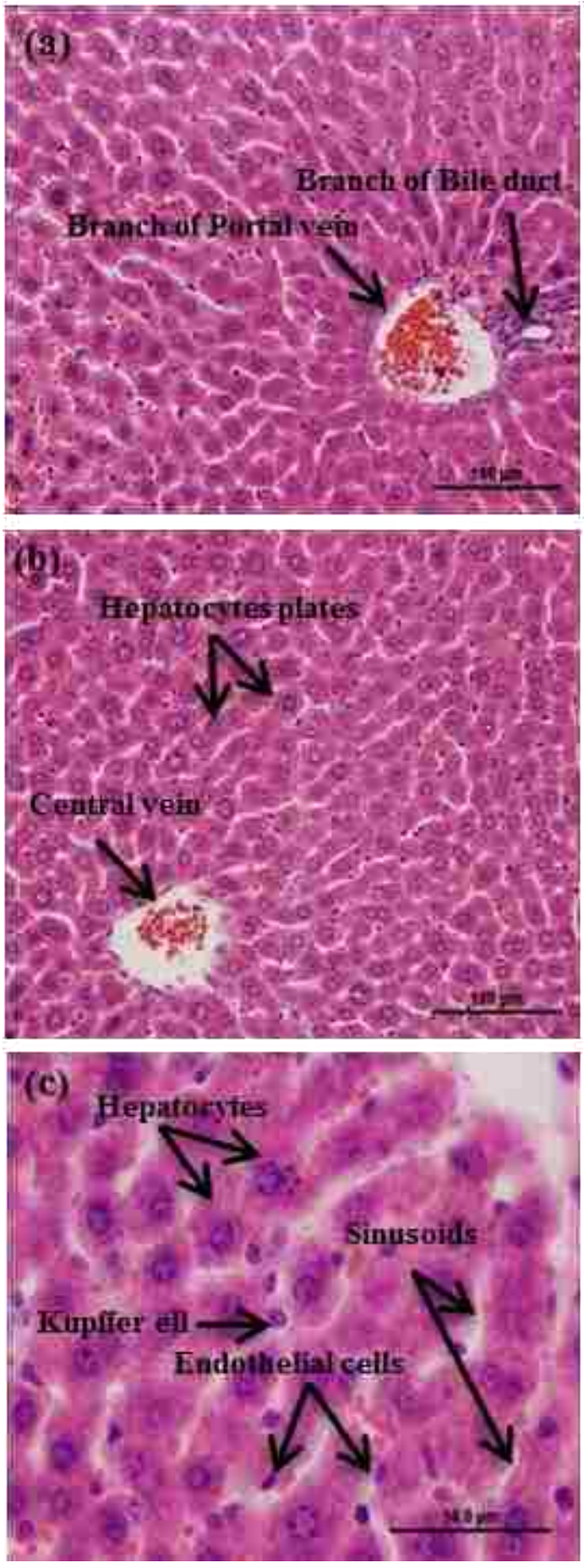

Figure 50: Liver's normal histology (H&E stain). a) Portal triad area consists of branch of portal vein and bile duct, scale bar = 100µm, b) central vein and hepatocytes, scale bar = 100µm, and c) hepatocytes are surrounded by sinusoids, endothelial and kupffer cells, scale bar = 50µm.

Other changes were also determined such as hepatocytes with vacuolated nucleus, nuclear pleomorphism, multi-nucleation, mitotic activity, increased proliferative index, giant cells and hepatic cytolysis (**Figure 51**). Apoptotic bodies were detected in the portal area, suggesting that apoptosis was contributory to clonal growth via removal of adjacent normal cells [42, 217, 219]. In this study, there were also other features of cells undergoing apoptosis and characterized by cell shrinkage, membrane blebbing, chromatin condensation and nuclear fragmentation. Similar features were reported in other DEN models studies [220].

Similar to tumorigenesis in other organs, hepatocarcinogenesis in humans and rodents is a multistep process characterized by the development of cellular intermediates that progressively cause genetic alterations that regulate transformation of normal cells into malignant cells. AHF is one of the major cellular alterations [219] that are known to occur in consequence of liver injury, and are considered to be one of the pre-neoplastic predictive markers associated with HCC. AHF can be categorized into basophilic, eosinophilic, clear, vacuolated, or mixed [221-223].

In the present study, most of the liver foci in mice of the DEN-induced group were identified to be consisted of mixed of basophilic, vacuolated and clear cells **(Figure 51)**. The distribution of all types appeared to be at random with respect to the hepatic lobule. AHF are generally distinguished as circular areas of hepatocytes with altered staining properties. Basophilic AHF are composed of cells that are usually smaller than adjacent normal hepatocytes. In vacuolated AHF, hepatocytes are enlarged with large or small lipid vacuoles in the cytoplasm and mostly central nuclei due to displacement by vacuoles. The cytoplasm of vacuolated AHF showed patchy cytoplasmic staining as seen in **Figure 51**. Cells in clear AHF are normal sized or enlarged with central, often hyperchromatic nuclei, and clear whitish

cytoplasm that must be distinguished from vacuolated one by lack of cytoplasmic lipid vacuoles. Hepatocytes in eosinophilic AHF are generally larger than normal hepatocytes and have diffusely eosinophilic cytoplasm. The cytoplasm in eosinophilic AHF varies from mild to intense. The mild eosinophilic foci were difficult to distinguish in the staining from surrounding parenchyma.

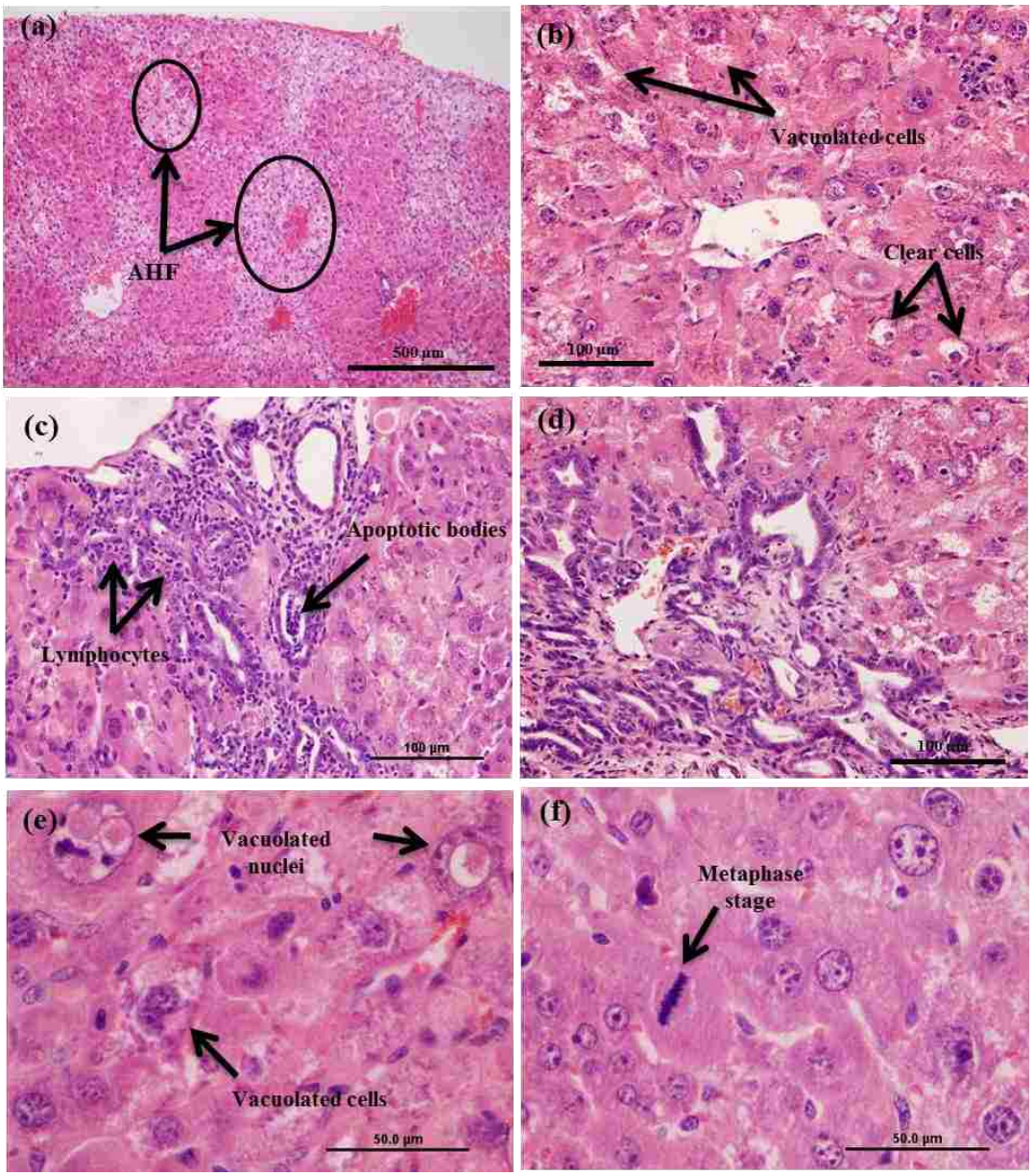

Figure 51: Formation of AHF in the liver of DEN-induced group. a) Mixed cell AHF composed of basophilic, vacuolated and clear cells, scale bar = 500 µm, b) vacuolated and clear cells, scale bar = 100 µm, c) cholangioma, lymoocytes hyperplasia and apoptotic bodies, scale bar = 100 µm, d) cholangioma, scale bar = 100 µm, e) vacuolated nuclei and the cell, scale bar = 50 µm, and f) mitotic figure in Metaphase stage, scale bar = 50 µm.

DEN is a carcinogenic chemical that is found in tobacco smoke, cured or fried meals, cosmetics, agricultural chemicals and some pharmaceutical agents. Previous studies have shown that DEN may induce carcinogenicity by several ways. i) Alkylating DNA structures leading to the formation of mutagenic DNA adducts [13, 16, 17, 33]. ii) Generating ROS that causes carcinogenesis by damaging DNA, protein and lipid molecules [13, 16, 17, 33]. iii) Inducing mutations in *H-ras* proto-oncogene leading to unlimited cell division and, eventually, cancer development [13, 17, 35]. iv) Inducing over-expression of the Bcl-2 gene [17]. v) Stimulating the proliferation of hepatic oval cells and bile duct cells leading to hyperplasia and the formation of microscopic intrahepatic cholangioma [38, 39].

A previous study has utilized pre-weaning Balb/c mice strain where a single dose DEN was used as initiator [216] followed by a promoter such as phenobarbital [48] or partial hepatectomy [215] to accelerate growth of pre-neoplastic focal lesions [42]. In the present study, pre-weaning Balb/c mice were injected with multiple doses of DEN for two months which is considered a modified protocol to induce pre-neoplastic foci and cholangioma.

Similar pre-neoplastic cytological alterations that were observed in this study were also observed in the transgenic mice model. Gillet et al. generated several lines of transgenic mice that develop hepatocarcinoma in response to expression of wild-type SV40 early sequences, under the control of the regulatory sequences of human anti-thrombin III gene (TAg mice, previously named ASV mice). As of second month of life, transgenic livers are characterized by pre-neoplastic cytological alterations, including anisocytosis, anisokaryosis, increased proliferative index, giant cells and hepatic cytolysis. These pre-neoplastic foci become macroscopic from the second month onward. But all animals die before the age of 7 months [219].

In the combined treatment group of D-MNPs loaded with crocin at 11 mg/kg and 22 mg/kg concentrations, there were reduction in the pre-neoplastic changes compared to groups of DEN-induced or free crocin (**Figures 52 and 53**). The overall pre-neoplastic reductions were better in 22 mg/kg than 11 mg/kg crocin-loaded D-MNPs formulation, which might be because of high concentration of crocin. The brown color in the combined treatment in **Figure 53** indicated the presence of D-MNPs that attached to the 11 mg/kg or 22 mg/kg crocin. To confirm the presence of these NPs, Prussian blue stain was used with and without H&E stain.

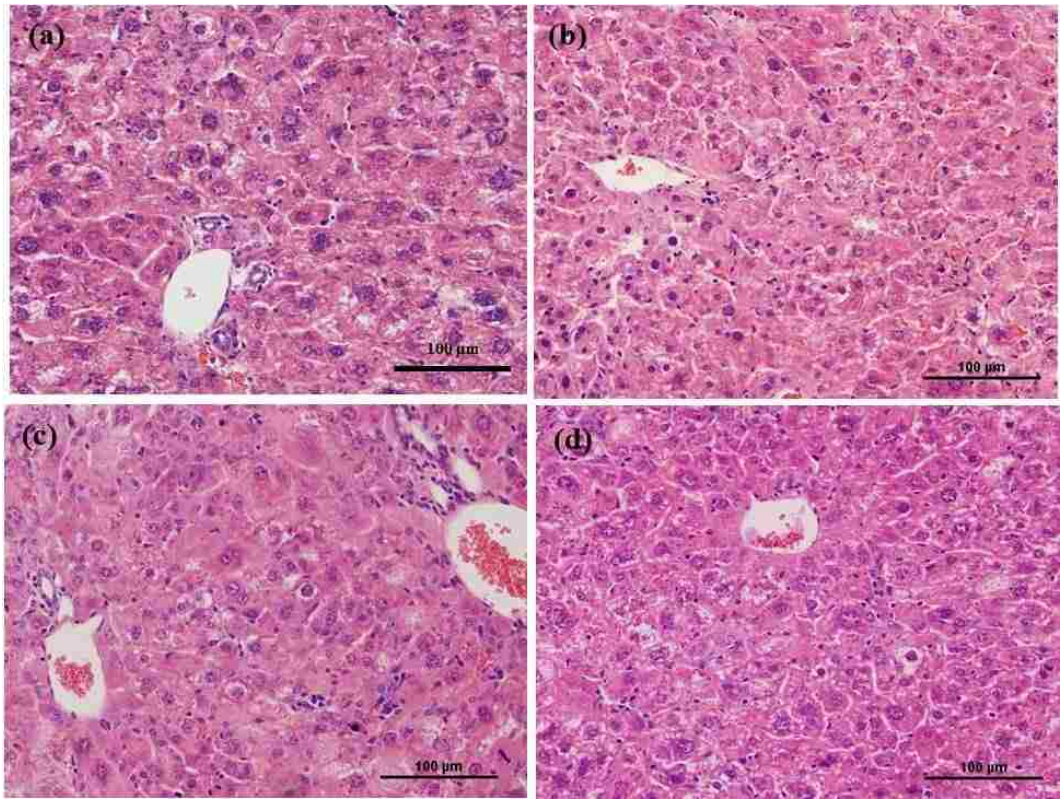

Figure 52: Histological examination of AHF arising in livers of Balb/c mice after DEN administration and treated with 11 mg/kg or 22 mg/kg free crocin. a) Portal area and b) central vein of 11 mg/kg crocin treated animals, each scale bar = 100 µm. c) Portal area and d) central vein of 22 mg/kg crocin treated animals, each scale bar = 100 µm.

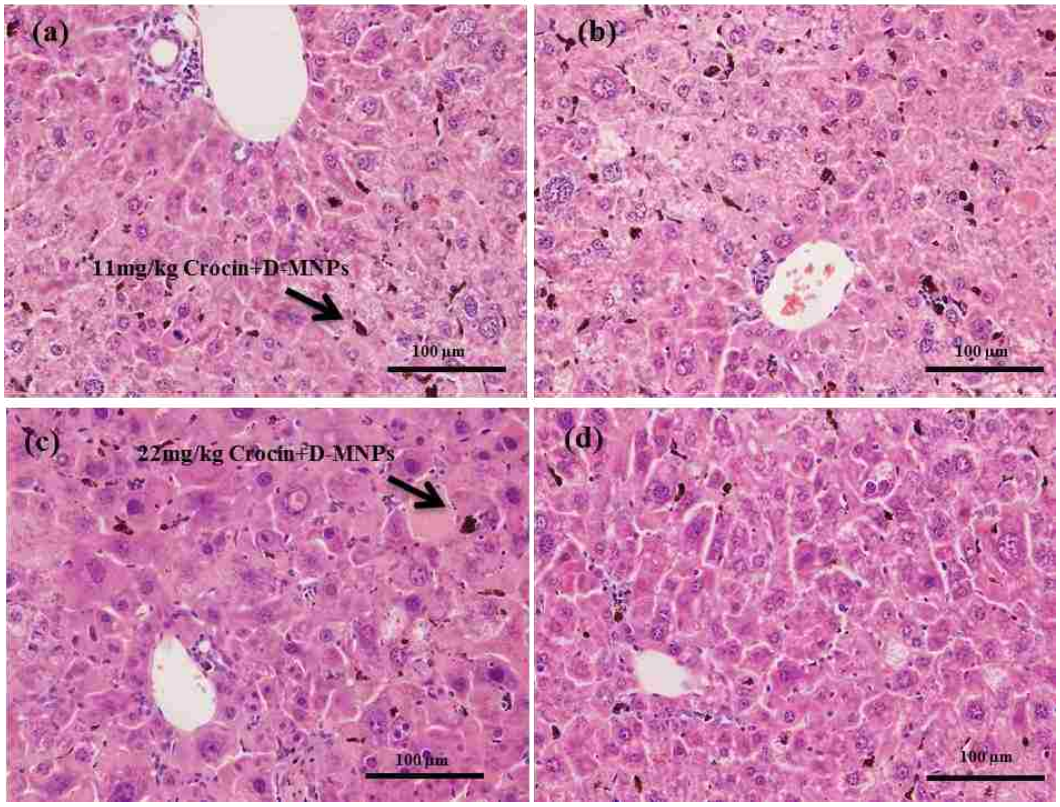

Figure 53: Histological examination of AHF arising in livers of Balb/c mice post DEN administration and treated with 11 mg/kg crocin-loaded D-MNPs or 22 mg/kg crocin-loaded D-MNPs, both doses contained 17 mg Fe/kg. a) Portal area and b) central vein of 11 mg/kg crocin-loaded D-MNPs treated animals, each scale bar = 100 µm. c) Portal area and d) central vein of 22 mg/kg crocin-loaded D-MNPs treated animals, each scale bar = 100 µm. The arrow indicates presence of D-MNPs loaded with 11 or 22 mg/kg crocin in liver tissues.

3.7.3. Detection of D-MNPs *in vivo*

To confirm that the pre-neoplastic lesion size reduction correlated with MNPs accumulation after 24 hrs of last i.v. injection, we used Prussian blue stain to analyze MNPs in liver of normal and 22 mg/kg crocin-loaded D-MNPs contained 17 mg Fe/kg as representative groups (**Figure 54**). Prussian blue staining showed more MNPs accumulation in liver tissue, mostly in kupffer cells, treated with crocin-loaded D-MNPs in the 2 formulations. However, NPs were neither observed in the normal (**Figure 54a**), the DEN-induced nor in the free crocin groups (data not shown).

Despite this widespread distribution of crocin-loaded D-MNPs *in vivo*, it should be emphasized that we did not have any fatalities due to the blocking of blood vessels at the MNPs dose used in this study. The size of D-MNPs with crocin is 16 nm which still is in the acceptable size range to be i.v. injected in the mice [3]. MNPs in the size range 10-100 nm have been considered to be optimal for i.v. administration. Particles more 100 nm and less than 10 nm are isolated by the spleen or removed via renal clearance, respectively [3]. D-MNPs administration and its iron oxide concentration used in this study caused neither adverse effects nor death to any of the examined mice. Thus, the data suggest that D-MNPs are biocompatible and adequate for biomedical experiments.

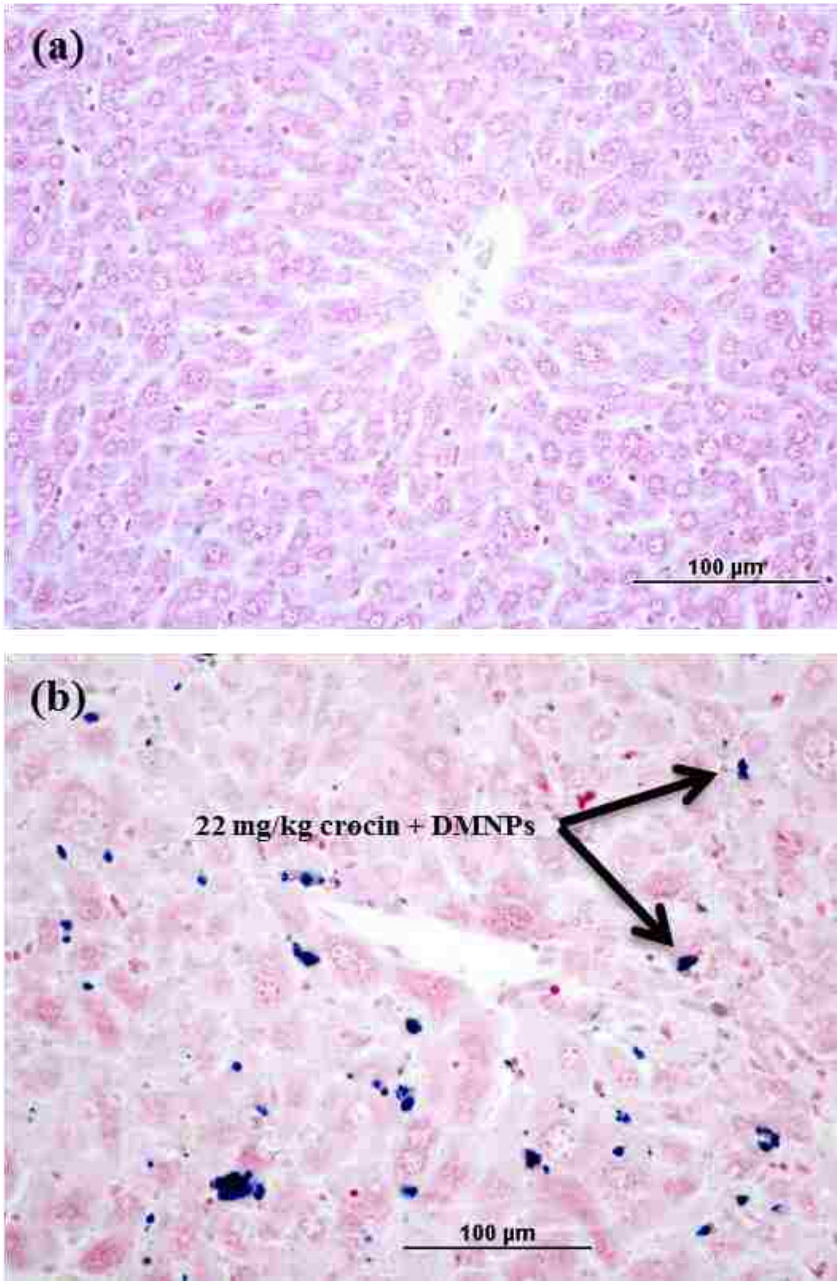

Figure 54: Prussian blue staining of liver sections. a) Normal liver and b) liver section of mouse treated with 22 mg/kg crocin-loaded D-MNPs, each scale bar = 100 µm.

The bright blue clouds around D-MNPs clusters with crocin (**Figure 55**) suggested free iron release from the clusters. The fate of D-MNPs following i.v. administration will mainly be in liver and spleen as a filtration system, which also confirmed by histological studies done by other researchers. Iron-release evidences observed more in the liver tissue compared to spleen. The clusters of D-MNPs were restricted to spleen red pulp. The primary function of red-pulp is to filter the blood from various components and it includes granulocytes and macrophages [224]. While white pulp mainly contains lymphocytes, such as T cells. Lacava et al. observed that D-MNPs decrease in numbers throughout 6 months in liver and spleen of normal mice [224]. In spite of the presence of D-MNPs in both liver and spleen tissues, no damaged cells or any other alterations were observed in the investigated normal tissues. Thus, D-MNPs have proven to be safe and they are currently used clinically in different forms such as Feridex IV and Resovist [90, 91, 146].

Magnetic core may cause toxic effects to organisms if it was left directly exposed to the cells. This may occur if weak bonding between dextran and MNPs exist. Uncoated magnetic cores tend to aggregate and may lead to the precipitation of MNPs that eventually block the blood vessels and kill the organism. Furthermore, uncoated MNPs can induce genotoxicity via generation of ROS. Upon internalization of MNPs into the cell, MNPs might degrade in the lysosomes by hydrolyzing enzymes into free ferrous ions (Fe^{2+}). These free ions might cross the mitochondrial membrane and react with hydrogen peroxide and oxygen to produce highly reactive hydroxyl radicals and ferric ions (Fe^{3+}). The generated hydroxyl radicals can damage DNA, proteins, polysaccharides and lipids. Thus, iron overload and its subsequent homeostatic imbalance may have direct cellular responses including, but not limited to, DNA damage, and inflammatory processes. Ensuring the surface coating of

MNPs is therefore essential to prevent the release of toxic ions from magnetic core [3, 213, 225].

It is also known that MNPs is one of the most iron oxide-based particles used *in vivo*. That is because they are easily degraded and cleared from circulation by the endogenous iron metabolic pathways. The released iron is normally metabolized in the liver and subsequently used in the formation of red blood cells, bind to ferritin or excreted via kidneys [3, 212, 213, 225]. In previous section of this study, both TGA and FTIR analyses have been utilized to insure the presence of dextran as a coating material. Also, the *in vitro* release study confirmed the release of crocin not dextran at different conditions (**Figure 44**).

The distribution of MNPs localized in the liver tissue might indicate presence of endosomes that could merge with lysosomes at later stage of endocytosis. MNPs have already been reported inside endosomes around nucleus in the cytoplasm, but not inside the nucleus of the cells [212]. Lysosomal enzymes might break the bond between the crocin and the cross-linker attached to D-MNPs, and thus releasing the crocin as its intact active structure. The D-MNPs entrapped by Kupffer cells indicates an efficient elimination process of MNPs through phagocytosis in the mice treated with NPs.

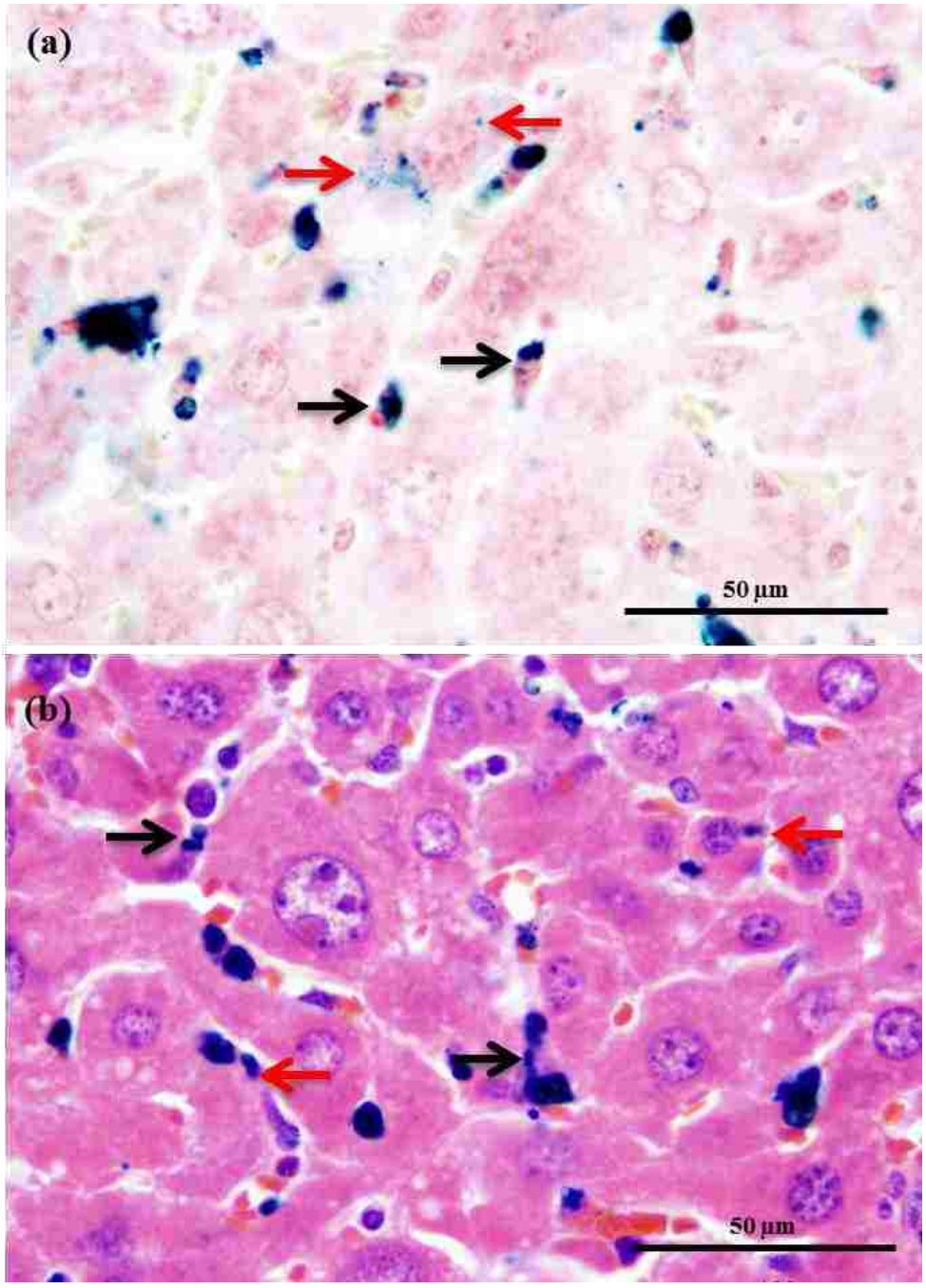

Figure 55: Subcellular localization of 22 mg/kg crocin-loaded-DMNPs and stained with Prussian blue. The tissues were counterstained with a) neutral red, and b) H&E stain, each scale bar = 50µm. Crocin loaded-DMNPs are localized in the cytoplasm. Red arrow: D-MNPs in hepatocytes, and Black arrow: D-MNPs in Kupffer cells.

Once in the bloodstream NPs are rapidly coated by components of the circulation, such as plasma proteins in process known as opsonization. This process is critical in determining the circumstance and the fate of the injected NPs. Normally; opsonization makes the particles identifiable by the body's major defense system, the reticuloendothelial system [226]. It is a system of specialized cells that are phagocytic and can be found in connective tissues area of the liver, spleen and lymph nodes [90, 203, 212]. Kupffer cells and the macrophages of the spleen and circulation play a critical role in the removal of opsonized particles. As a result, the application of MNPs *in vivo* would require surface modification that would ensure that particles are non-toxic, biocompatible and stable like hydrophilic compounds [88, 92, 188, 227]. Hydrophilic compounds such as dextran polymer have been used in this study, and dextran was shown to resist the opsonization process and to slowly clear thus increasing the half-life of MNPs and the crocin.

The leaky nature of vasculatures in pre-neoplastic and tumor microenvironment facilitates the extravasation of NPs (10–500 nm) from the blood circulation and selective penetration into the cancer microenvironment. However, the poor lymphatic drainage system helps them to be retained [228-230].

3.7.4. Immunohistochemistry studies

This section was designed to analyze the anti-cancer efficacy of free crocin versus crocin-loaded D-MNPs on liver has pre-cancerous lesion in Balb/c mice. Immunohistochemistry staining for GST-P was employed to identify the presence of pre-neoplastic foci after DEN administration, which was followed by treatments with saline (DEN-induced group), free crocin or crocin-loaded D-MNPs as detailed in materials and methods section.

3.7.4.1. GST-P expression

Glutathione S-transferases (GSTs) are a major group of phase II enzymes, and among the most powerful cellular detoxifying systems. This family facilitates the catalysis of thioether bonds between glutathione and electrophilic compounds including carcinogens, drugs and a variety of products of cellular metabolism (both endogenous and exogenous compounds). This family is grouped into six classes according to the number of chromosome, Alpha (chromosome 6), Mu (chromosome 1), Omega (chromosome 10), Pi (chromosome 11), Theta (chromosome 22), and Zeta (chromosome 14). There are both structural and functional redundancies between isozyme family members.

GST-P form belongs to the Pi class of GSTs. GST-P was first identified in rat placenta and was hence named the placental form. The GST-P in the rat is markedly induced in pre-neoplastic foci and nodules induced by experimental hepatocarcinogenesis [231, 232]. GST-P could be detected in a single cell as early as 2–3 days after the i.p. administration of DEN. This gene is expressed in response to almost all of the chemical carcinogens, and can be found as a predominant protein in other tumors like breast cancer [231-233].

GST-P levels in normal rat tissues including fetal, adult and regenerating livers, and even in the placenta are very low compared to livers bearing pre-neoplastic foci [232]. This enzyme is not induced by the same eletrophilic xenobiotics which induce the expression of other GST isozymes. The expression patterns of GST-P is closely associated with the early stage of hepatocarcinogenesis [231].

GST-P expression was estimated as the percentage of cells positively stained by the antibody and detected by the DAB substrate (brownish color) in the cytoplasm

and nucleus of the cells. Two months post DEN administration, the expression of GST-P in DEN-induced group increased with strong intensity compared to the normal group. Both tested formulations 11 and 22 mg/kg crocin-loaded D-MNPs had more pre-neoplastic foci inhibition compared to DEN-induced or free crocin **(Figures 56 and 57)** especially in 22 mg/kg crocin formulation.

The percentage of the GST-P positive foci was quantified from relative IHC staining cells of pre-neoplastic foci in twenty fields per group. The quantification analysis was performed using Image Pro 6 software, and was confirming the IHC analysis. The percentage of expression of GST-P foci was significantly increased in DEN-induced group ($P \leq 0.001$) compared to normal group as in **Figure 58**. Sheweita et al. demonstrated that DEN increased the activity of GSTs by 50% after 1 hr only of i.p. injection with 20 mg/kg in Balb/c mice [234]. Also Narumi et al. reported that the expression of GST-P positive single hepatocytes appeared after the initial DEN treatment with 12.5 mg/kg/day and their numbers increased as the number of days of DEN administration increased to 14^{th} days. GST-P positive mini-foci existed on the 7^{th} day of DEN post-treatment and increased prominently on the 14^{th} day post-DEN treatment [235].

Amin et al. indicated that saffron-mediated reduction of nodular hepatocytes that was associated by significant decrease in the number of GST-P positive foci induced by DEN in rats [68]. On the other hand, the percentage of expression areas in the combined treatment group crocin-attached D-MNPs in both 11 and 22 mg/kg formulations were reduced compared to DEN-induced or free crocin groups (**Figure 58).** This might be because of the role of NPs as a carrier in improving the anti-cancer effects of crocin.

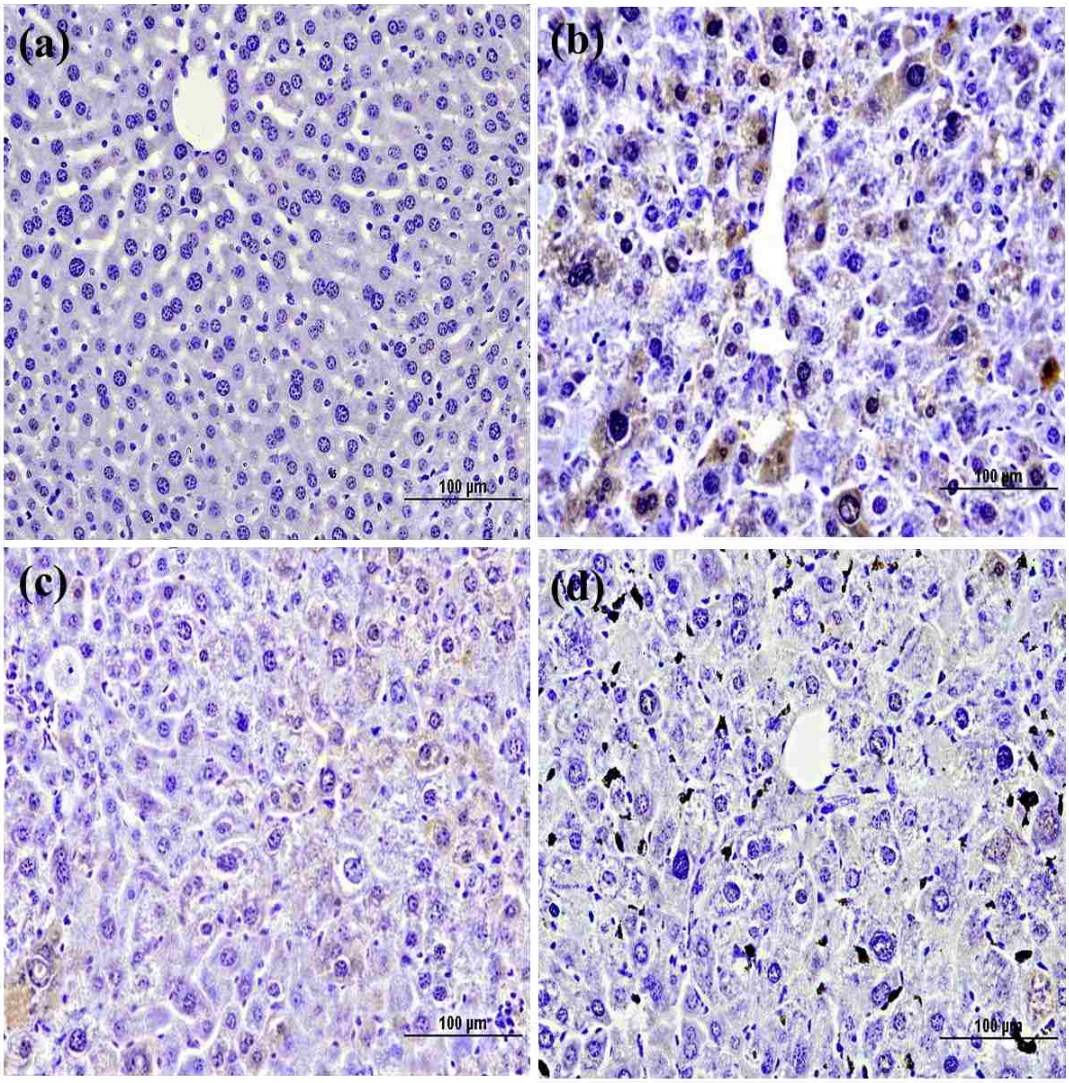

Figure 56: Effects of 11 mg/kg crocin and its NP formulations on GST-P expression in liver. a) Normal, b) DEN-induced, c) free 11 mg/kg crocin, and d) 11 mg/kg crocin-loaded D-MNPs. Each scale bar = 100 µm.

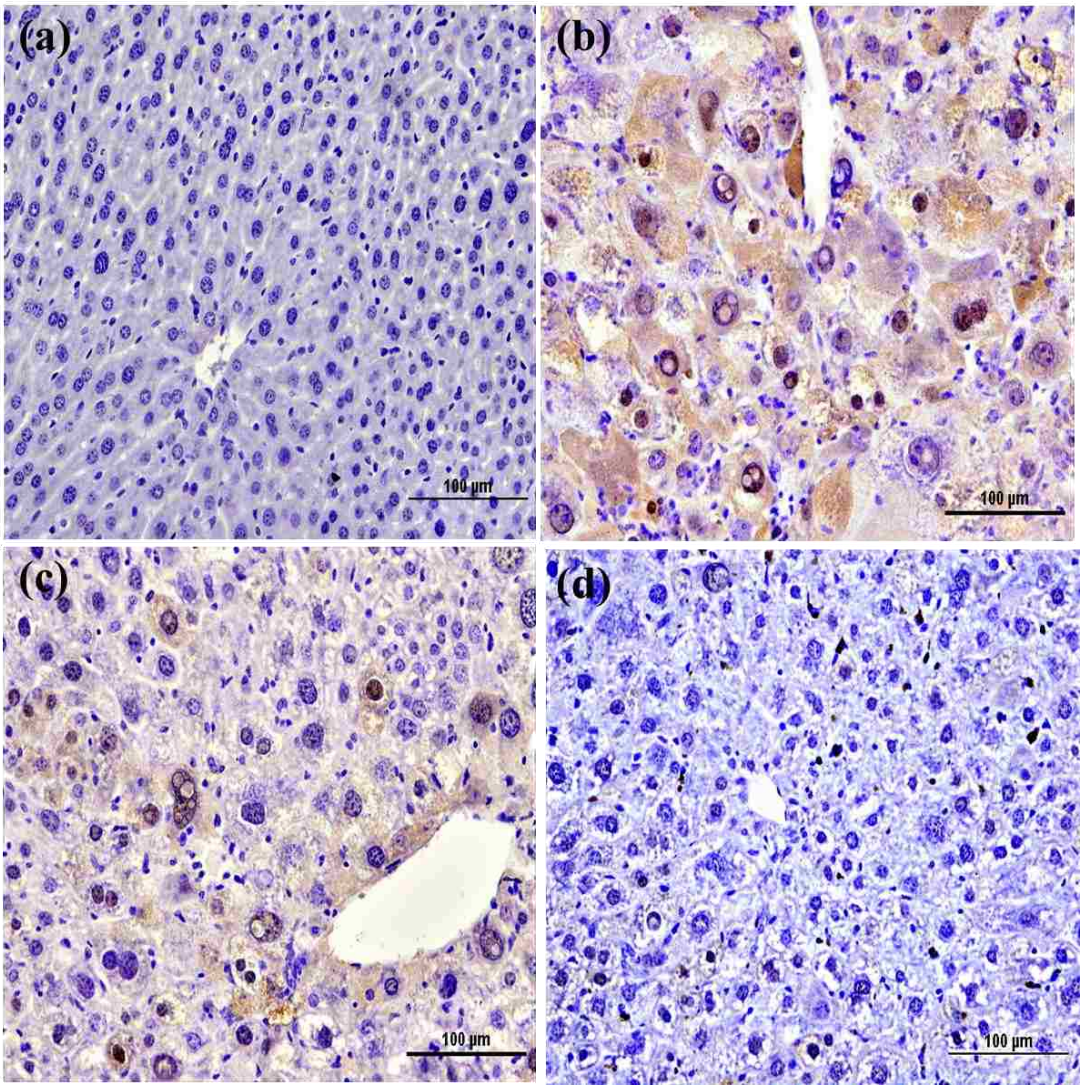

Figure 57: Effects of 22 mg/kg crocin and its NP formulations on GST-P expression in liver. a) Normal, b) DEN-induced, c) free 22 mg/kg crocin, and d) 22 mg/kg crocin-loaded D-MNPs. Each scale bar = 100 µm.

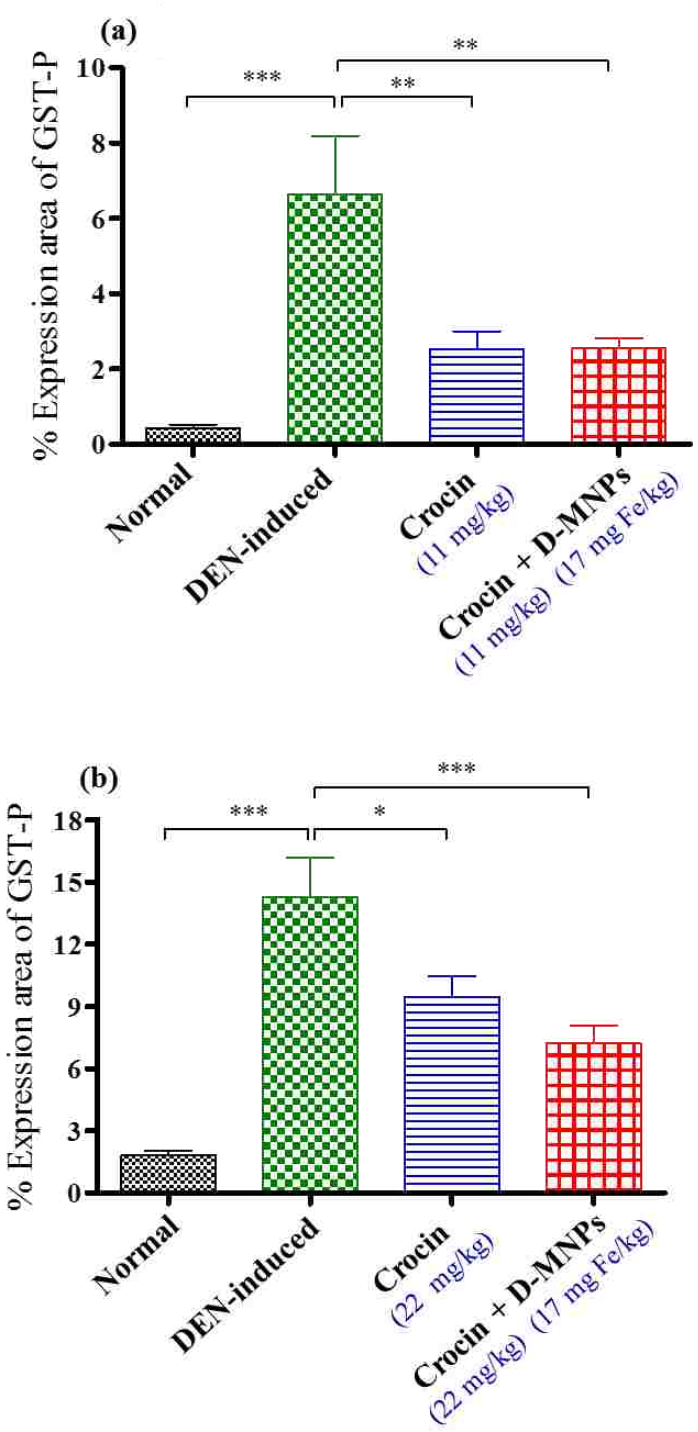

Figure 58: Quantification of percent stained GST-P area in the two tested crocin formulations. a) 11 mg/kg crocin-loaded D-MNPs, and b) 22 mg/kg crocin-loaded D-MNPs. Values are expressed as mean ±SEM; $*P \leq 0.05$, $**P \leq 0.01$, $***P \leq 0.001$.

3.7.4.2. Ki-67 expression

Cell proliferation plays an important role in several steps of carcinogenesis process. Initially carcinogens interact with DNA leading to mutant nucleotide sequences. It's however the induced proliferation of such mutant DNA that will lead to the formation of pre-cancerous lesions, that would, at a later stage, form HCC [236]. The examination of the presence of cell cycle-related proteins may yield important information about the biological behavior of a tumor. Ki-67 is a nuclear protein that has been used as proliferative marker of both normal and cancer cells. It is expressed in all active phases of the cell cycle, including G1, S, G2, and mitosis, with the highest expression seen in G2/M. Ki-67 is however lacking in resting cells (G0). The name of ki-67 is derived from the city of origin (Kiel) and the number of the original clone in the 96 well plate [237-241].

In the present study, Ki-67-specific antibody has been used to evaluate the cellular proliferation rates and analyze liver regeneration and carcinogenesis processes, in the different treated animal groups. Ki-67 immunoreactivity was detected and localized in the nuclei of cells (**Figures 59 and 60**) and the IHC results were quantified (**Figure 61**). Ki-67 expression was estimated as the percentage of expression area that was stained by the antibody and visualized by DAB substrate as dark-brown colour in 20 fields. In normal liver sections a limited number of Ki-67 positive cells was observed, but the number of Ki-67 positive cells was increased significantly (P <0.0001) in DEN-induced liver tissues. According to Youssef et al. the Ki-67 expression was increasing after 6 and 12 weeks. The highest increasing in the number of Ki-67 positive cells was after 18 weeks post DEN injection with 75 and 100 mg/kg, each one a weeks for 3 weeks [241]. Also Narumi et al. observed that the number of Ki-67-positive hepatocytes increased gradually after DEN

exposure in time- and dose- dependent manner compared to control [235]. The expression of Ki-67 positive cells in 11 and 22 mg/kg crocin-loaded D-MNPs groups was reduced compared to DEN-induced or free crocin treated groups. Saffron showed anti-proliferative activity by decreasing the number of Ki-67 positive cells in DEN-treated rats. So this study indicated that attaching crocin on D-MNPs as a delivery vehicle could enhance the anti-proliferative activities of crocin reported earlier in [68].

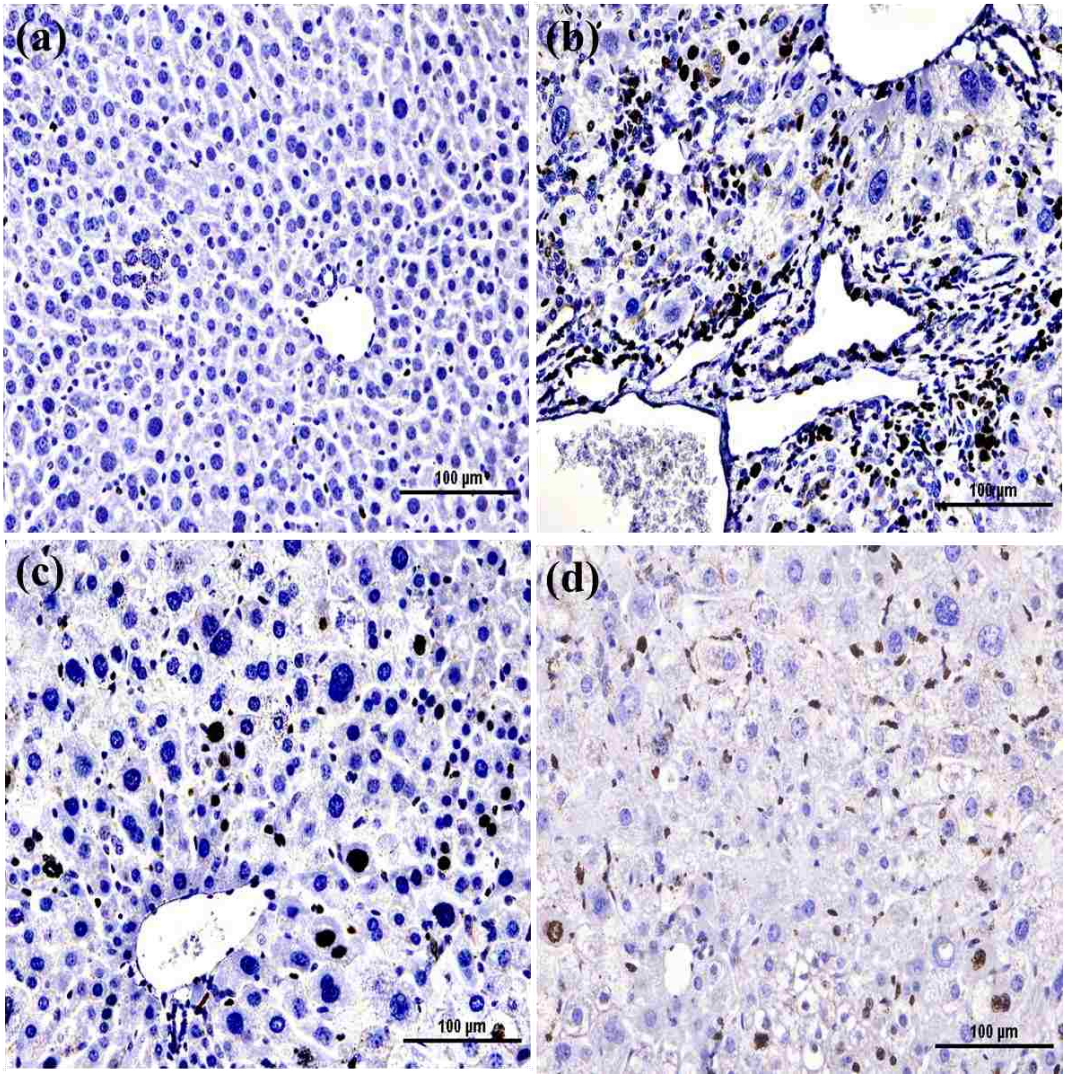

Figure 59: Effects of 11 mg/kg crocin and its NP formulations on Ki-67 expression in liver. a) Normal, b) DEN-induced, c) 11 mg/kg crocin, and d) 11 mg/kg crocin-loaded D-MNPs. Each scale bar = 100 µm.

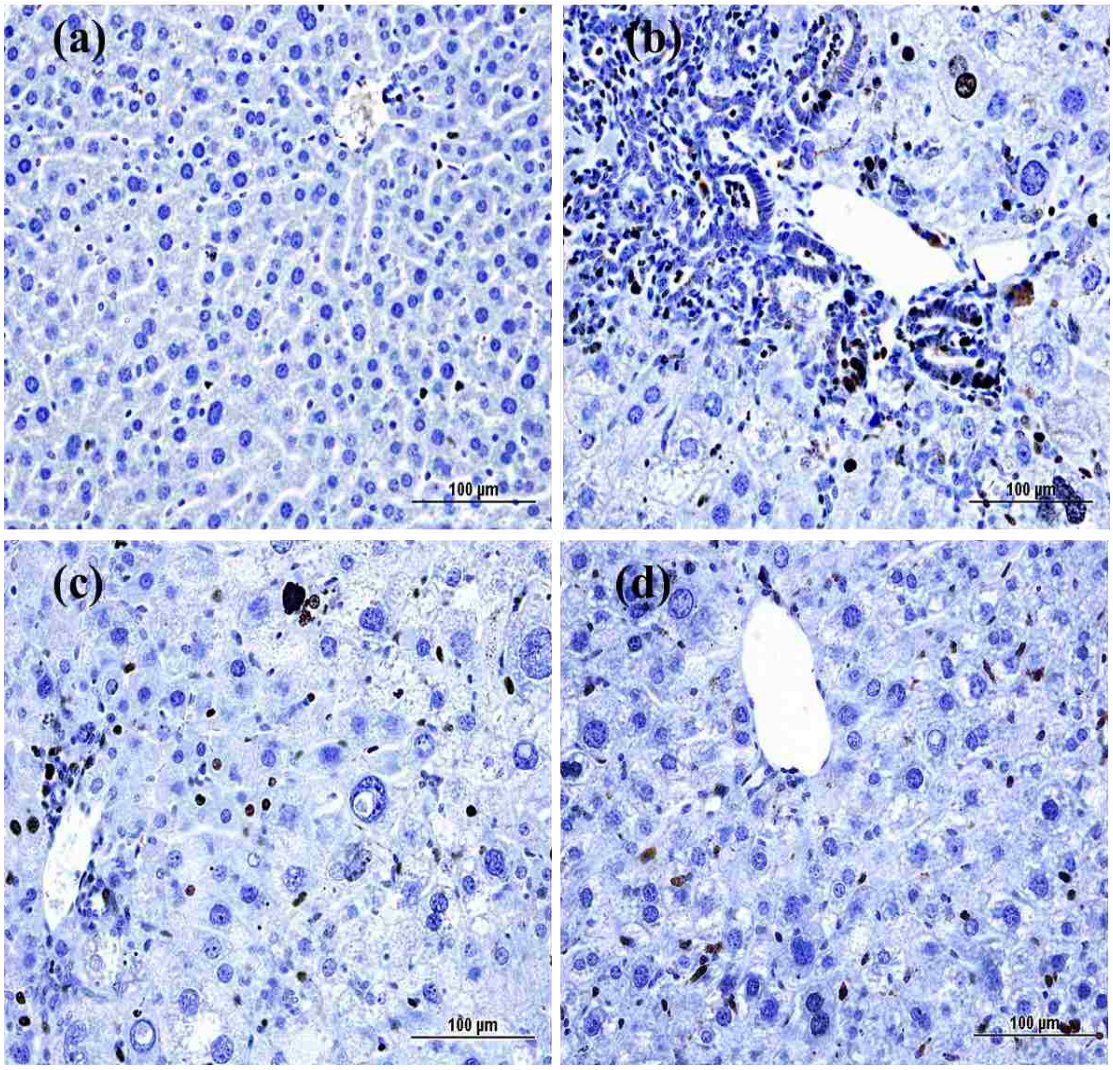

Figure 60: Effects of 22 mg/kg crocin and its NP formulations on Ki-67 expression in liver. a) Normal, b) DEN-induced, c) 22 mg/kg crocin, and d) 22 mg/kg crocin-loaded D-MNPs. Each scale bar = 100 µm.

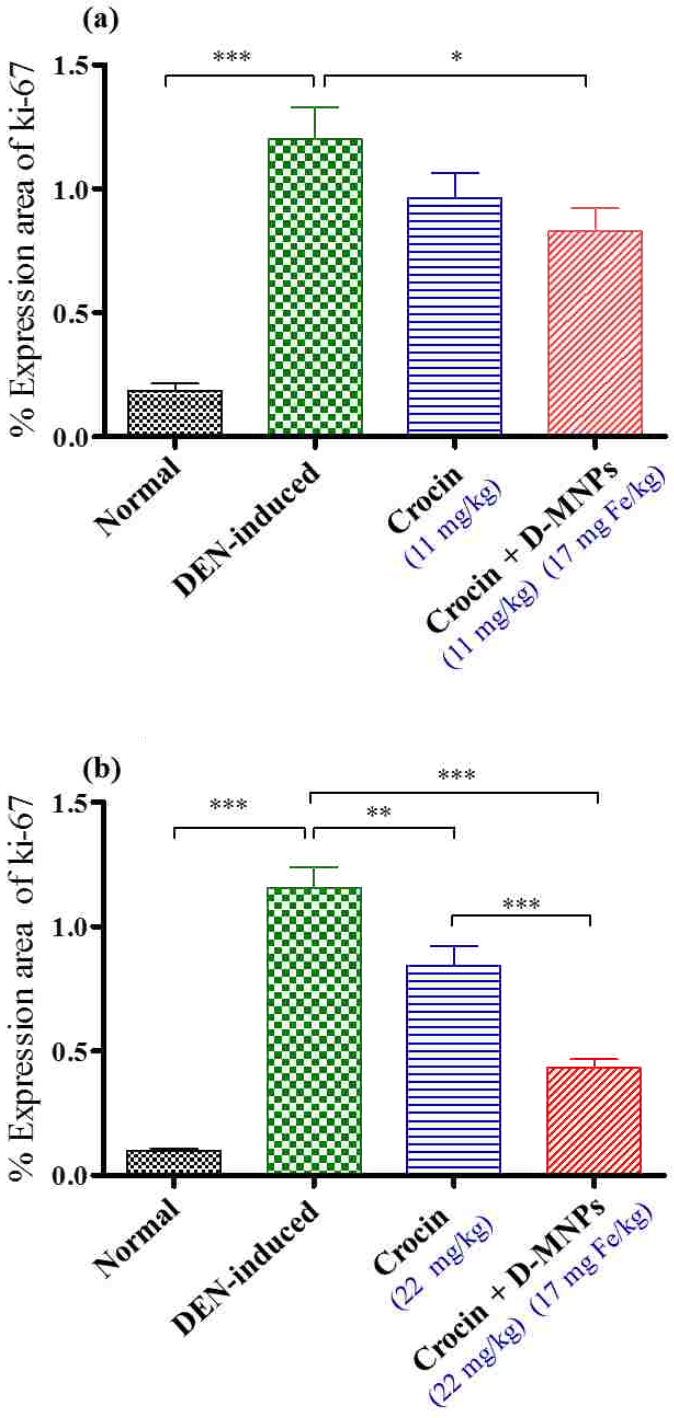

Figure 61: Estimated expression areas of Ki-67 positive cells in the two examined crocin formulations. a) 11 mg/kg crocin-loaded D-MNPs, and b) 22 mg/kg crocin-loaded D-MNPs. Values are expressed as mean ± SEM; * $P \leq 0.05$, ** $P \leq 0.01$, *** $P \leq 0.001$.

3.7.4.3. M30-Cytodeath expression

Several studies indicate that apoptosis is essential in the modulation of hepatocarcinogenesis and pre-neoplastic hepatocytes development. Apoptosis is a physiological cell death that has been suggested to play an important role in the maintenance of homeostasis [219, 220, 242-245].

Dysregulation of apoptosis is an important component of the multistage hepatocarcinogenesis. This dysregulation may result in the decreased ability of cells to undergo apoptosis and provide a selective survival advantage for those cells, therefore leading to altered growth, cellular transformation and tumor progression. During hepatocarcinogenesis, altered hepatic foci display increased rates of cell proliferation and cell death relative to surrounding normal hepatocytes. This increase in the apoptotic process, also called compensatory apoptosis, and occurs irrespective of the oncogenic events generating pre-neoplastic and neoplastic lesions. However, the rate of cell replication process exceeds the apoptosis leading to hyperplasia [219, 243, 246]. Some liver injury like chronic hepatitis is characterized by continuous elimination of hepatic cells, which could lead to cancer formation by cytolysis/regeneration phenomena [219, 243, 246].

Apoptotic pathways have been shown to be activated in several forms of chronic liver injuries including liver cancer. Liver cell apoptosis can be initiated by different complex pathways, the majority involving activation of the caspases. Caspases-2, -8, -9, and -10 are initially activated and, in turn, activate a cascade of downstream effector caspases such as -3,-6, and-7 [220, 242, 244].

Recently, there has been a growing interest in the role of cytokeratin proteins during apoptosis. It has been suggested that caspase cleavage of the cytokeratin proteins facilitate the formation of apoptotic bodies and amplify the apoptotic signal.

Cytokeratin 18, for example, is an intermediate filament protein representing about 5% of total protein in the liver and other tissues such as pancreas and intestine. During early apoptosis cytokeratin18 is cleaved by caspases 3 and 6 (**Figure 62**) at two distinct sites (Aspartate 238 and Aspartate 396). This cleavage pattern is highly specific to apoptosis and leads to the cellular release of caspase-cleaved cytokeratin 18 fragments into the extracellular space and finally to bloodstream causing the characteristic morphologic changes of apoptosis [247, 248].

The computerized estimation of the cytokeratin positive cells has confirmed the results of the IHC analysis of cytokeratin 18. As shown in **Figures 63 and 64** normal group showed weak cytoplasmic cytokeratin 18 positive cells. This expression increased significantly ($P \leq 0.001$) in the DEN-induced compared to normal group (**Figure 65**). The increasing in the apoptosis expression might be because of the process of replacing the normal liver cells by pre-neoplastic cells. This continuous elimination of hepatic cells could lead to cancer formation by cytolysis/regeneration phenomena. The increased apoptosis, also called compensatory apoptosis, occurs irrespective of the oncogenic events triggering pre-neoplastic and neoplastic lesions [219, 243]. Amin et al. demonstrated that saffron treatment increased the number of M30-Cytodeath positive cells in DEN-induced rats [68]. Moreover, the numbers of positive cells were increased in groups treated with 11 mg/kg and 22 mg/kg crocin-loaded D-MNPs formulations compared with DEN-induced group ($P \leq 0.001$) or free crocin.

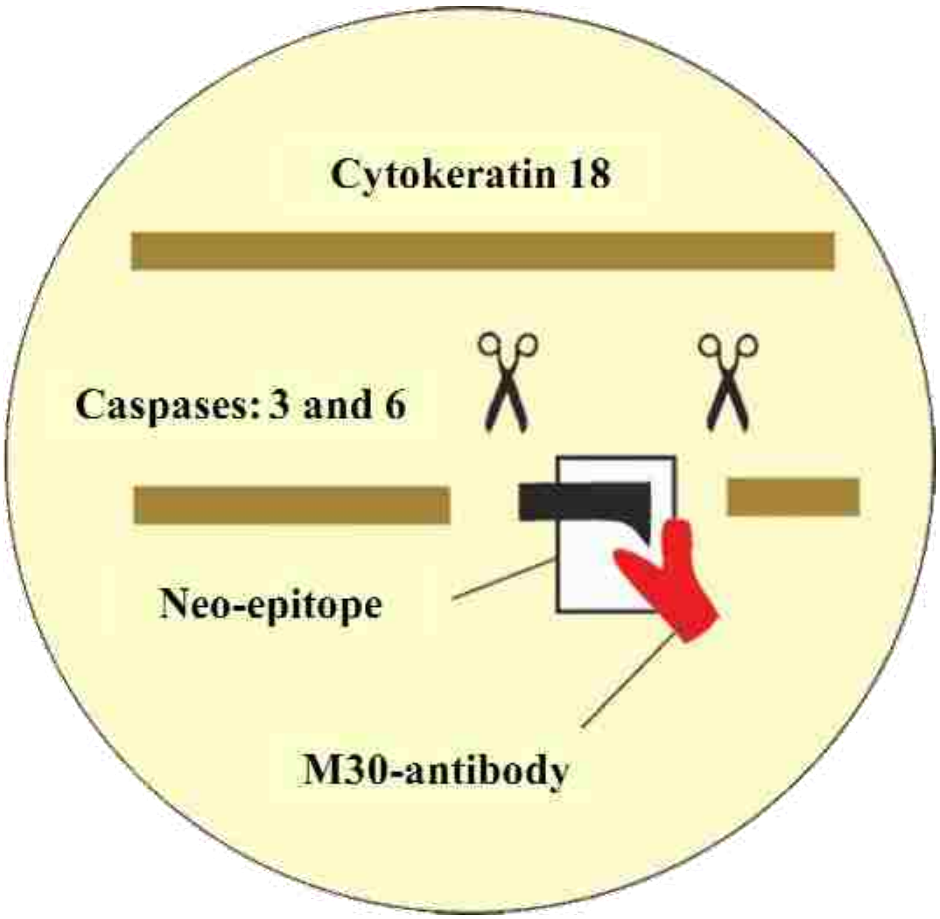

Figure 62: Diagrammatic representation of caspases cleavage of the cytokeratin 18 [249].

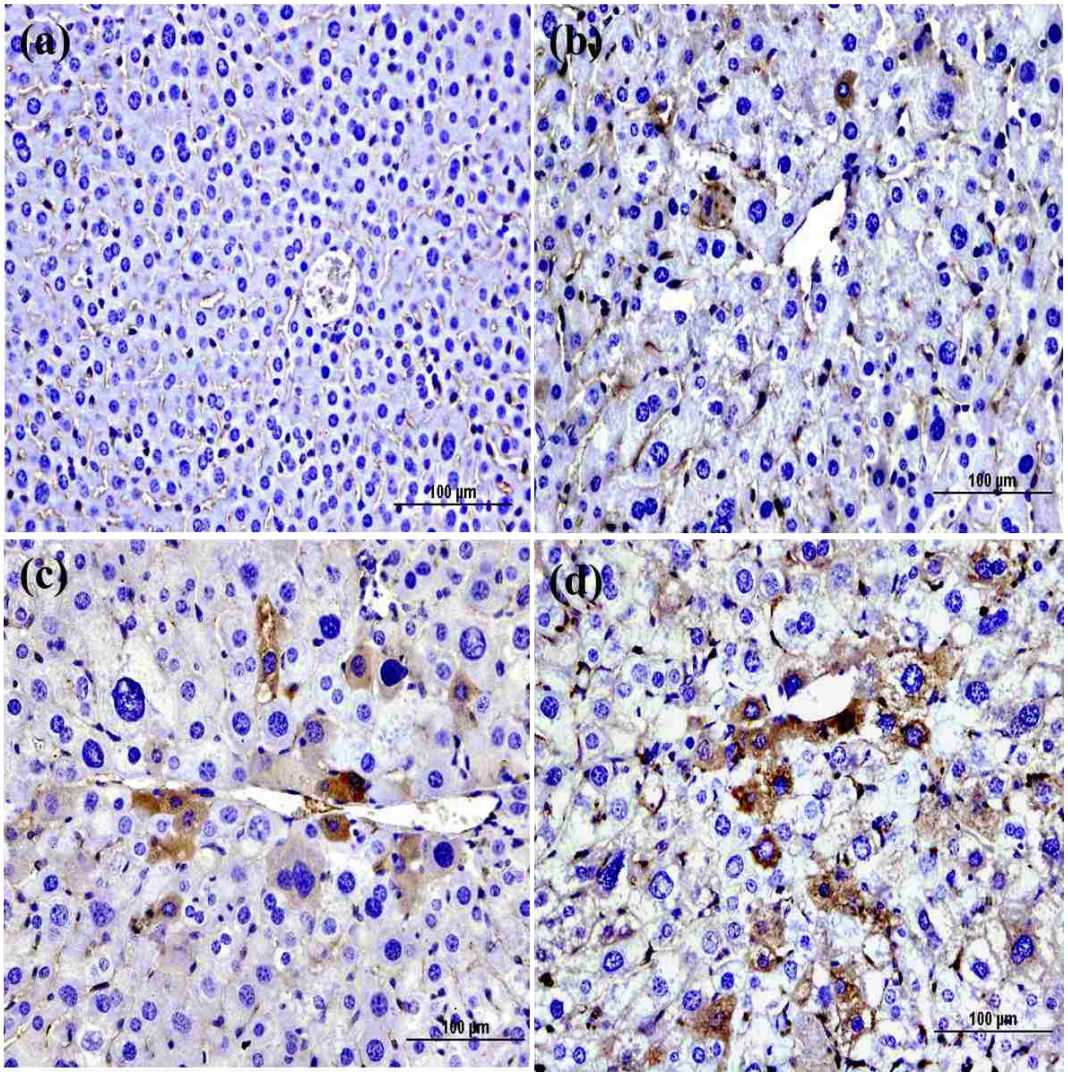

Figure 63: Effects of 11 mg/kg crocin and its NP formulations on M30-Cytodeath expression in liver. a) Normal, b) DEN-induced, c) 11 mg/kg crocin, and d) 11 mg/kg crocin-loaded D-MNPs. Each scale bar = 100 µm.

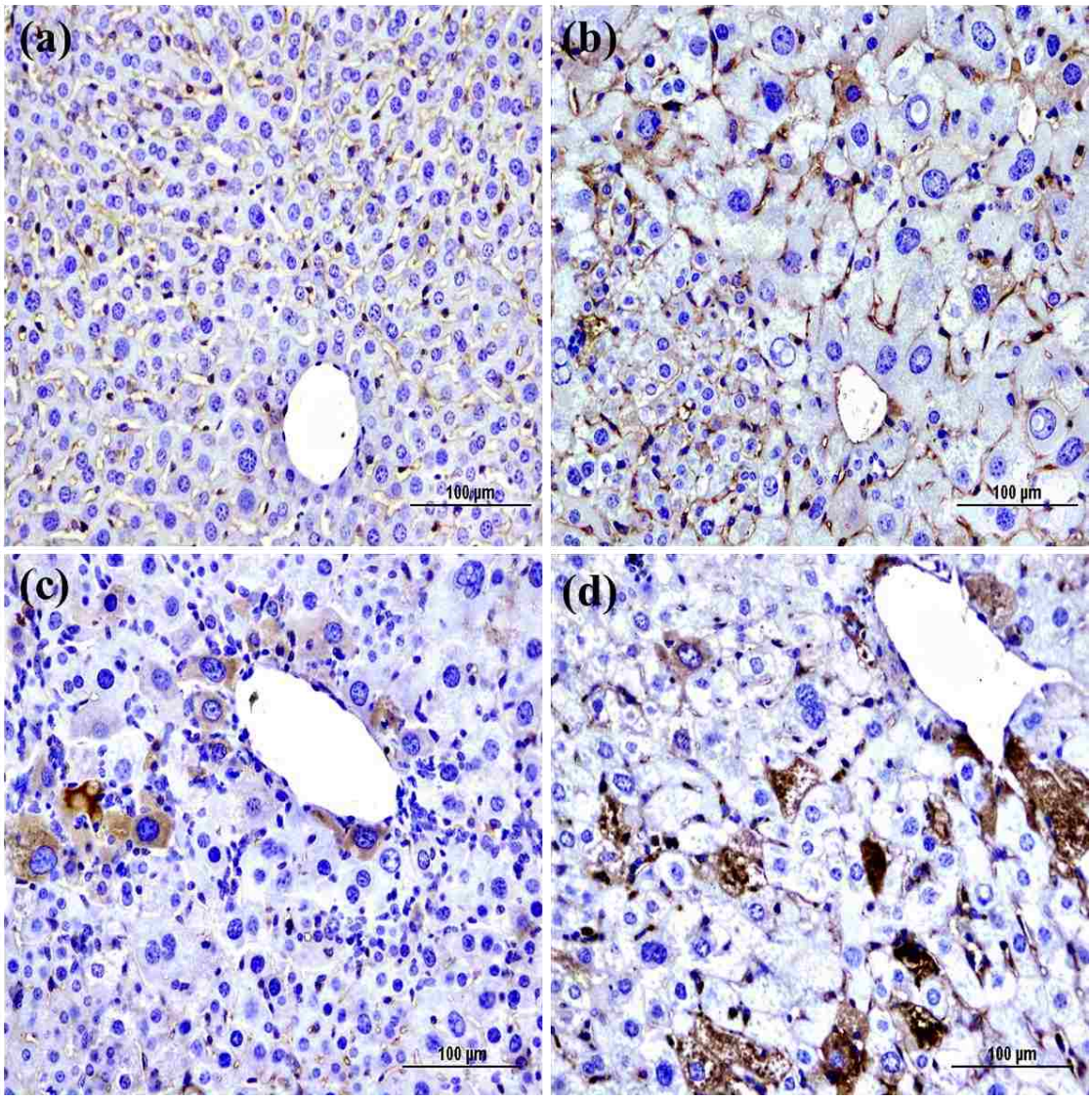

Figure 64: Effects of 22 mg/kg crocin and its NP formulations on M30-Cytodeath expression in liver. a) Normal, b) DEN-induced, c) 22 mg/kg crocin, and d) 22 mg/kg crocin-loaded D-MNPs. Each scale bar = 100 µm.

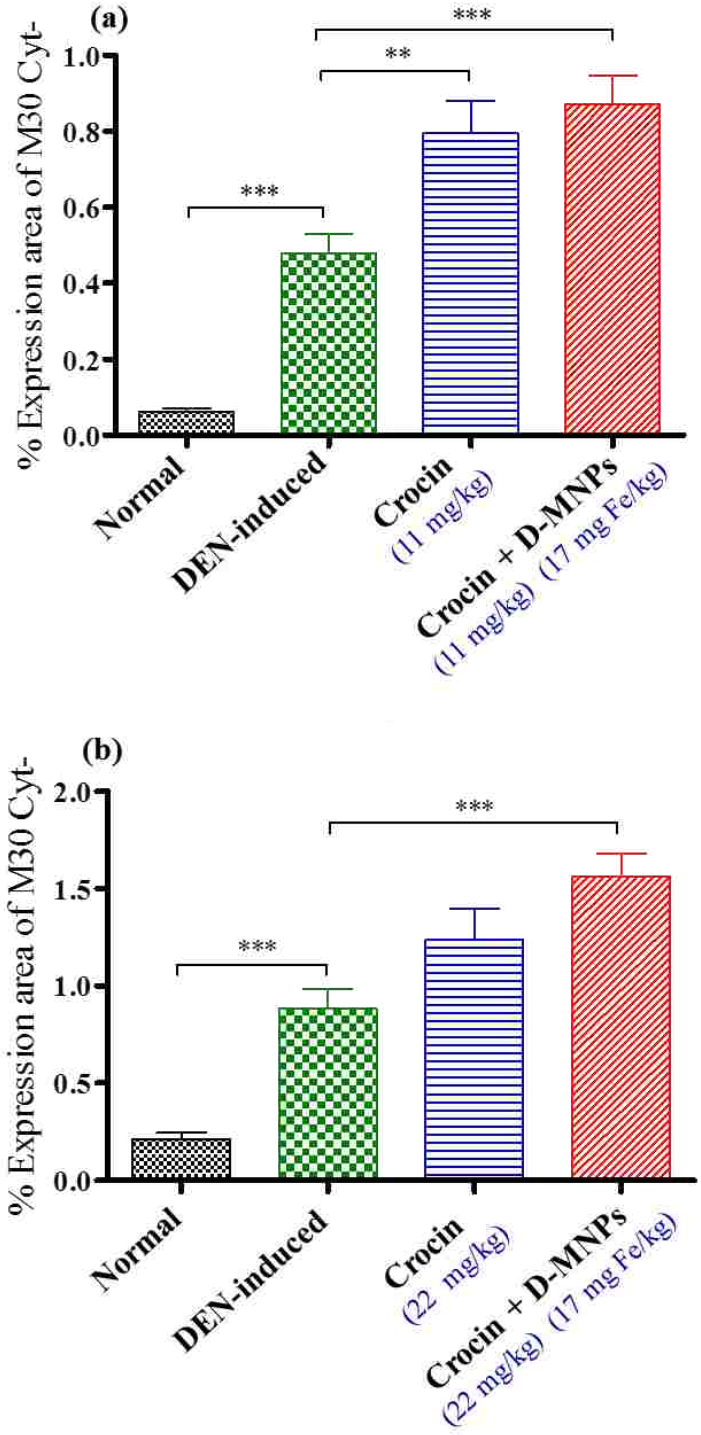

Figure 65: Estimated expression of M30-Cytodeath area in the two examined crocin formulations. a) 11 mg/kg crocin-loaded D-MNPs, and b) 22 mg/kg crocin-loaded D-MNPs. Values are expressed as mean ±SEM; * $P \leq 0.05$, ** $P \leq 0.01$, *** $P \leq 0.001$.

3.7.4.4. Bcl-2 expression

Much attention has been given to the detection of molecular targets that are also involved in the regulation of apoptosis and that might be altered in tumors. Bcl-2 oncogene was originally identified as overexpressed in most human B-cell follicular lymphomas, caused by a chromosomal translocation involving chromosomes 14 and 18. The name of Bcl-2 is derived from B-cell lymphoma 2. Bcl-2 prolongs cell survival by blocking apoptosis rather than regulation of cell replication. There are several Bcl-2 family members that have been identified, including proteins that induce apoptosis (pro-apoptotic), and those prevent apoptosis (anti-apoptotic). Pro-apoptotic proteins, includes Bax and Bak. The anti-apoptotic proteins such as Bcl2 and Bcl-X_L. However, the cellular equilibrium between the promotor and the blocker family members is known to be essential in determining cell fate (**figure 66**). Bcl-2 is normally expressed in abundance in the thymus, spleen, and cerebrum but not in the liver [219, 220, 243, 250-252].

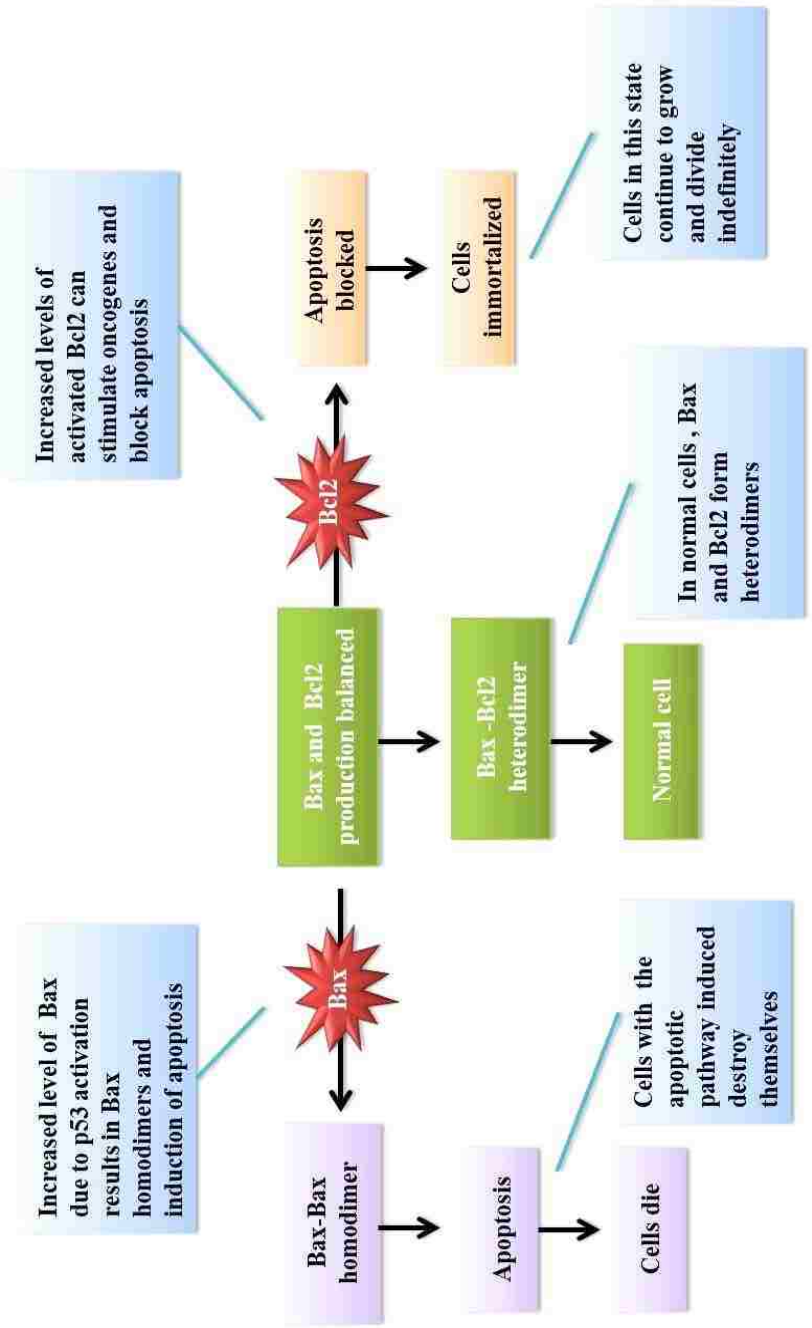

Figure 66: Diagrammatic representation of Bcl-2 and Bax regulate apoptosis, modified from [253].

Bcl-2 was shown to be overexpressed in DEN-induced mouse neoplasia [250]. The objective of the present investigation was to determine whether expression of Bcl-2 was altered *in vivo* following treatment with different crocin formulations.

According to the IHC analysis (**Figures 67 and 68**) that was confirmed by computerized analysis of 20 fields of IHC, most of the AHF in DEN-induced group were positive for Bcl-2 and was significantly ($P \leq 0.001$) increased compared to normal group, which was weakly stained (**Figure 69**). The staining was specifically seen in the cytoplasm of the cells. The expression of Bcl-2 in hepatic tissue of normal animals could not be detect was examined by immunohistochemistry, but positive staining of this protein was located in the cytoplasm of hepatocytes in animals treated with 200 mg/kg DEN [254]. Also Lee et al. concluded that normal mouse hepatocytes did not express Bcl-2, most DEN-induced tumours were positive for this protein [251].

Sun et al. reported that animal injected i.p. with 6.25 and 25 mg/kg crocin showed reduction in the tumour weight and size of HL-60 xenografts in nude mice. These treated animals showed inhibited Bcl-2 expression, and increased Bax expression in xenografts [208]. In the 11 and 22 mg/kg crocin-loaded D-MNPs formulations, the expression of Bcl-2 positive cell in crocin-loaded D-MNPs was reduced compared to DEN-induced or free crocin, indicating that the NPs could induce apoptosis by enhances the suppression of Bcl-2.

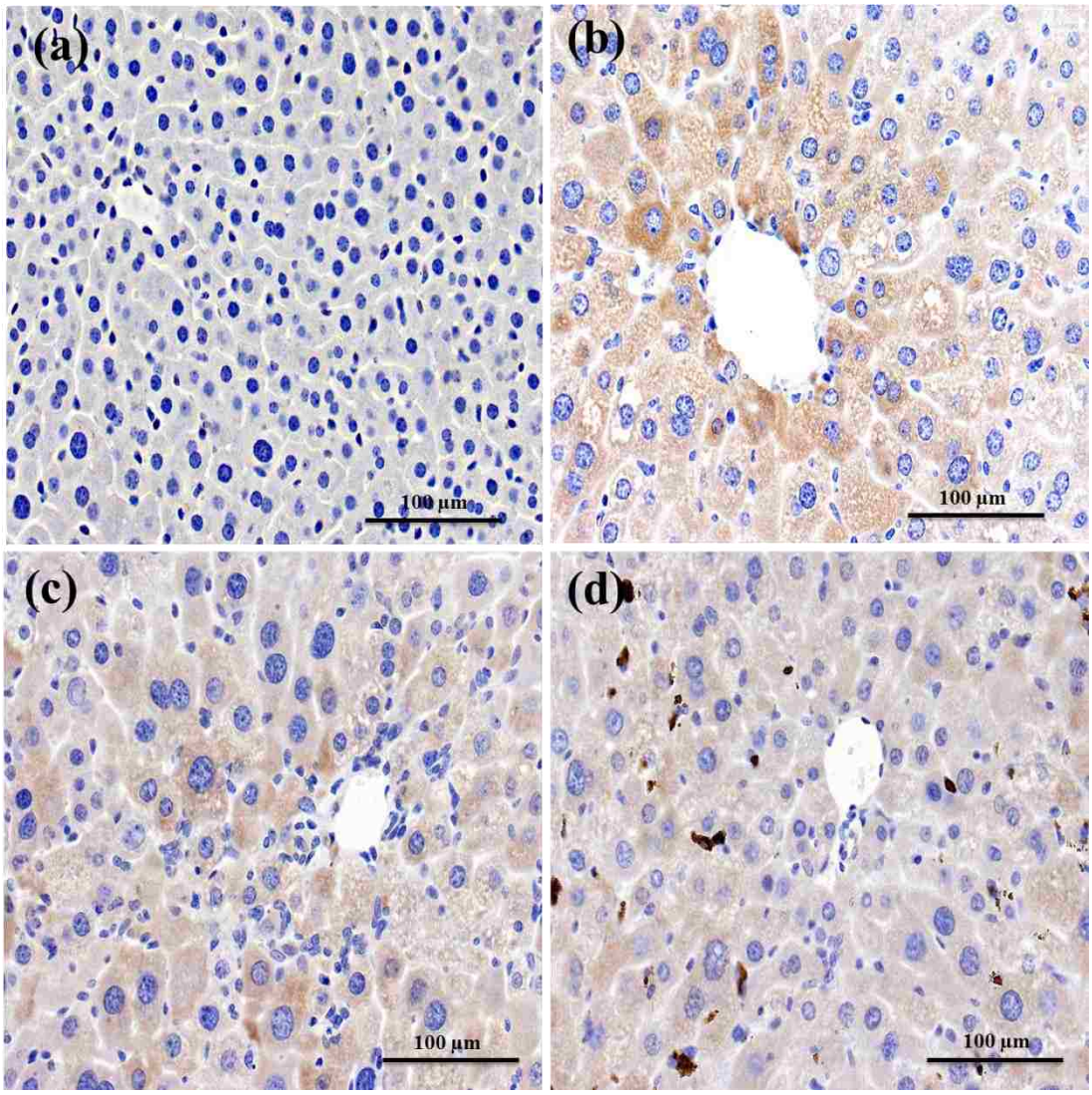

Figure 67: Effects of 11 mg/kg crocin and its NP formulations on Bcl-2 expression in liver. a) Normal, b) DEN-induced, c) 11 mg/kg crocin, and d) 11 mg/kg crocin-loaded D-MNPs formulation. Each scale bar = 100 µm.

.

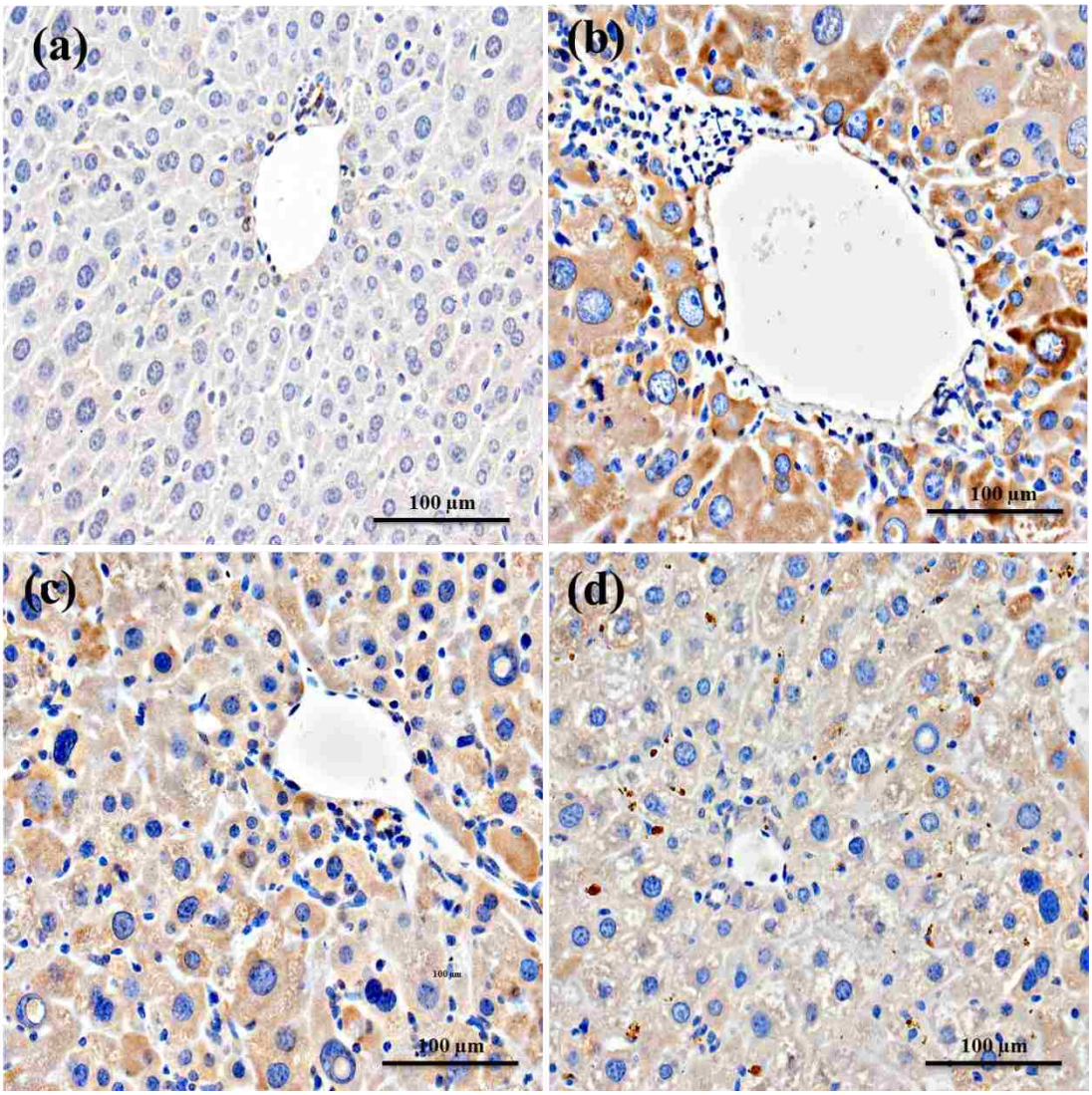

Figure 68: Effects of 22 mg/kg crocin and its NP formulations on Bcl-2 expression in liver. a) Normal, b) DEN-induced, c) 22 mg/kg crocin and d) 22 mg/kg crocin-loaded D-MNPs formulation. Each scale bar = 100 µm.

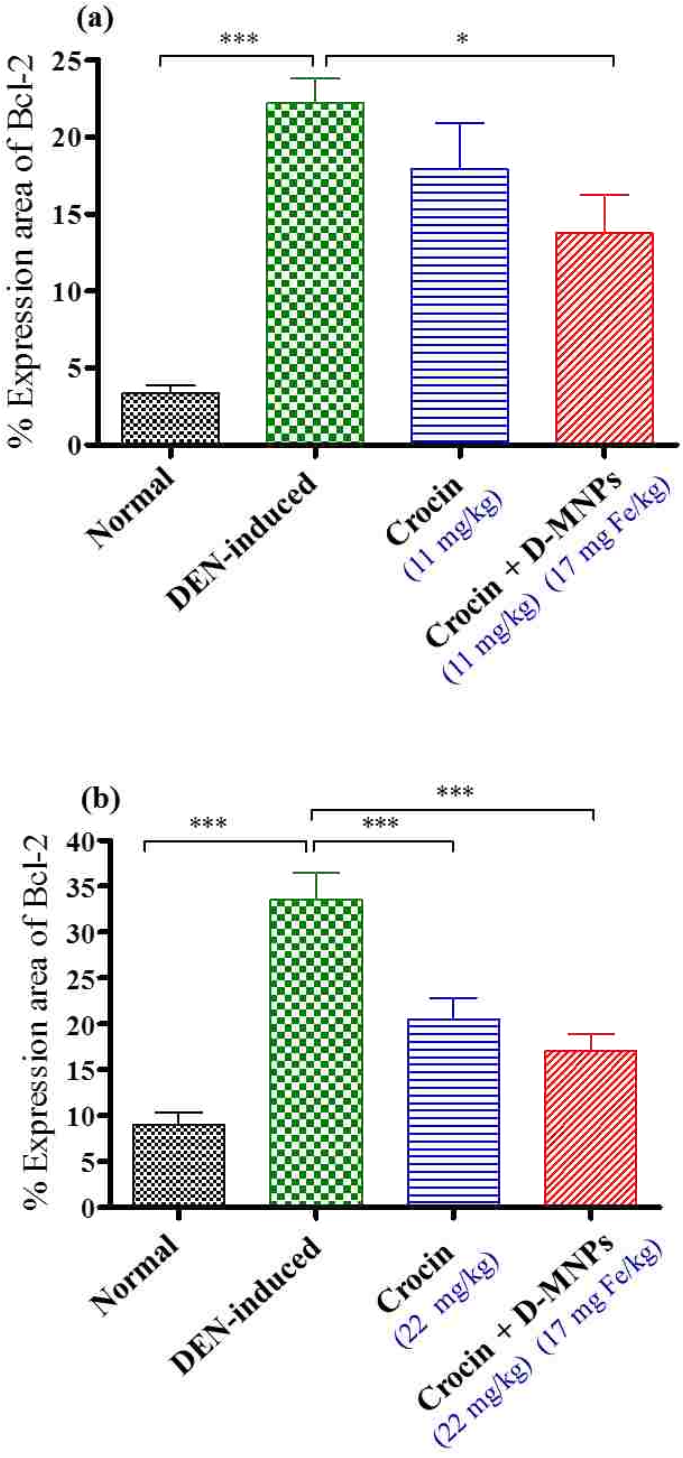

Figure 69: Quantitative analysis of Bcl-2 expression in relative to IHC fields in the two tested crocin formulations. a) 11 mg/kg crocin-loaded D-MNPs, and b) 22 mg/kg crocin- loaded D-MNPs. Values are expressed as mean ±SEM; *$P \leq 0.05$, **$P \leq 0.01$, ***$P \leq 0.001$.

3.7.4.5. COX-2 expression

Liver cancer development is associated with chronic cytotoxic and inflammatory events, indicating that inflammation mediators (such as prostaglandins) are involved in its pathogenesis. Prostaglandins are produced from arachidonic acid by either COX-1 or COX-2. COX-1 is normally and constantly expressed in most tissues and is important for the maintenance of homeostatic functions. COX-2, however, is an inducible enzyme that is normally associated with tumorigenesis events, such as cell proliferation, angiogenesis, invasiveness and resistance to apoptosis. Various studies have reported that increased COX-2 expression may contribute to liver damage and tumorigenesis in animal models and HCC in humans. As COX-2 is thought to contribute to inflammation-mediated cancer development, the expression level of this enzyme has been reported in the different animal studies [223, 255-257].

COX-2 has been localized to the neoplastic cells, endothelial cells, immune cells, and stromal fibroblasts within the cancer. The downstream targets of COX-2 include: (1) production of VEGF ; (2) promotion of vascular sprouting, migration, and tube formation; (3) enhanced endothelial cell survival via Bcl-2 expression and Akt signaling; (4) induction of matrix metalloproteinases (MMP) 2 and 9, and (5) activation of epidermal growth factor receptor-mediated angiogenesis [258].

In this study, IHC results of COX-2 (**Figures 70 and 71**) was quantified and confirmed as shown in **Figure 72.** COX-2 expression was found to be significantly increased ($P \leq 0.001$) in DEN-induced group compared to normal group. Dietary feeding with crocin (50-200 ppm) for 4 weeks was able to inhibit colonic adenocarcinomas in mice and decrease the mRNA expression of inflammation regulators such as COX-2, NF-κB, TNF-α, IL- 1β and IL-6 as reported by Kawabata

et al. [259]. Therefore, free crocin has a role in inhibiting COX-2 expression in animals with cancer. COX-2 expression was significantly reduced in crocin attached D-MNPs of the 11 and 22 mg/kg formulations compared with DEN-induced ($P \leq 0.001$) or free crocin ($P \leq 0.001$). These indicate the role of NPs in improving the anti-cancer activity of crocin. COX-2 expression in all the treatment groups was prominent staining around central vein and portal area.

Investigations by Sivaramakrishnan et al. [257], Amin et al. [68] and Kawabata et al. [259] have shown nuclear translocation of NF-κB-p65 in DEN-induced animals was important for the activation of COX-2 and thereby inflammation and carcinogenesis. Thus, it is possible that crocin-loaded D-MNPs suppress the nuclear localization of NF-κB p65 in DEN injected animals, thus leading to the down-regulation of COX-2 and angiogenesis.

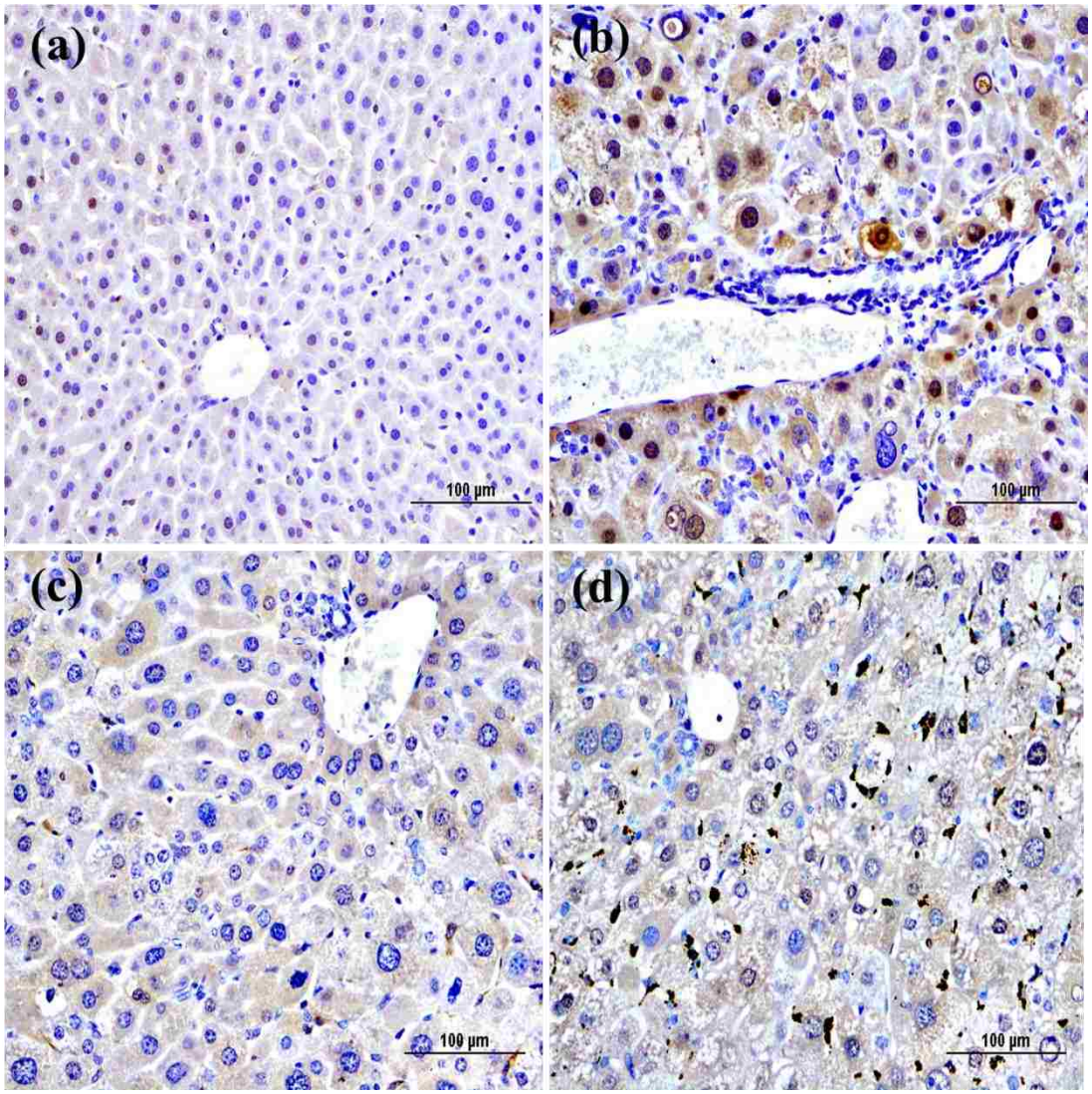

Figure 70: Effects of 11 mg/kg crocin and its NP formulations on COX-2 expression in liver. a) Normal, b) DEN-induced, c) 11 mg/kg crocin and d) 11 mg/kg crocin-loaded D-MNPs. Each scale bar = 100 µm

.

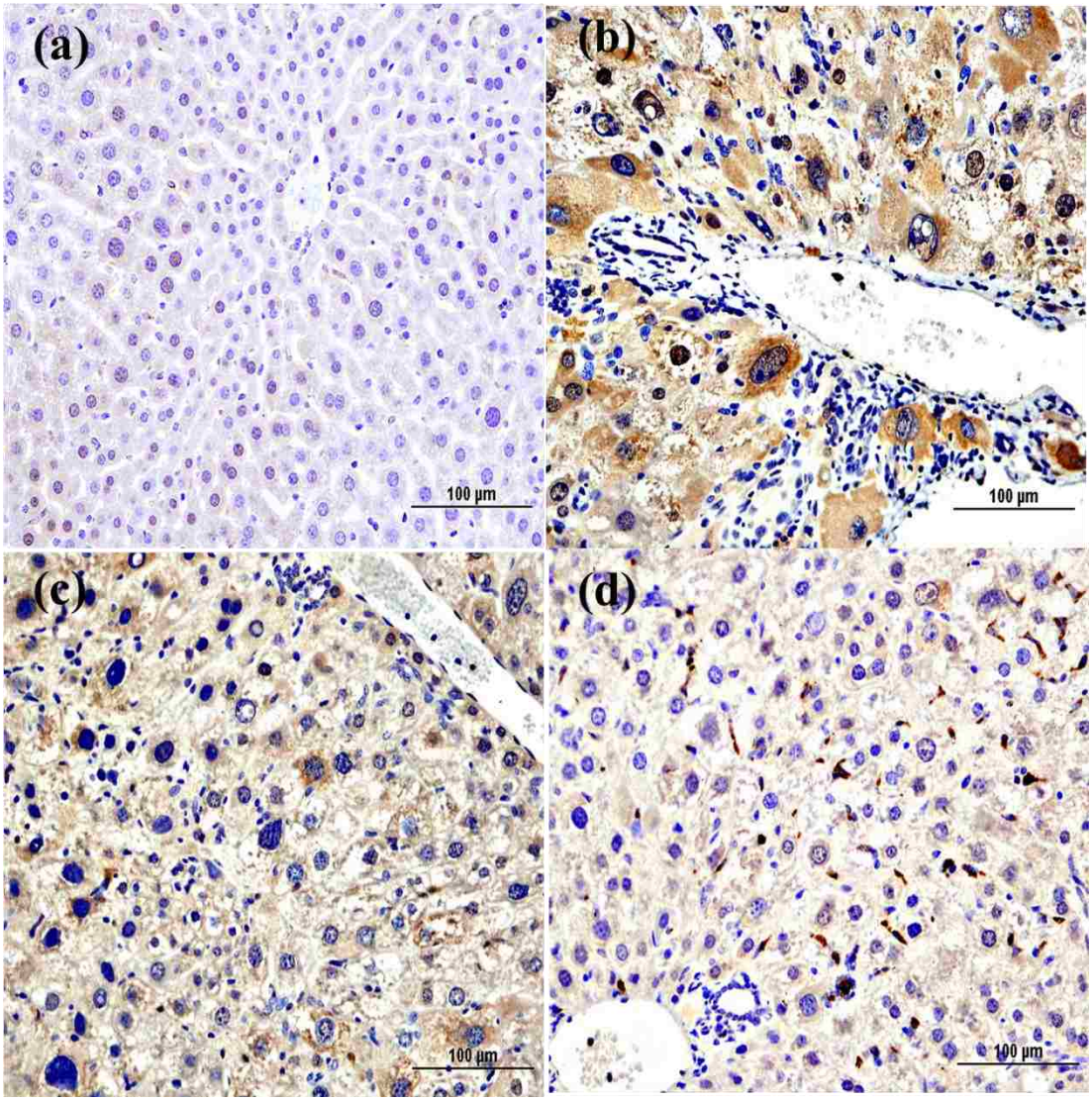

Figure 71: Effects of 22 mg/kg crocin and its NP formulations on COX-2 expression in liver. a) Normal, b) DEN-induced, c) 22 mg/kg crocin and d) 22 mg/kg crocin-loaded D-MNPs. Each scale bar = 100 µm.

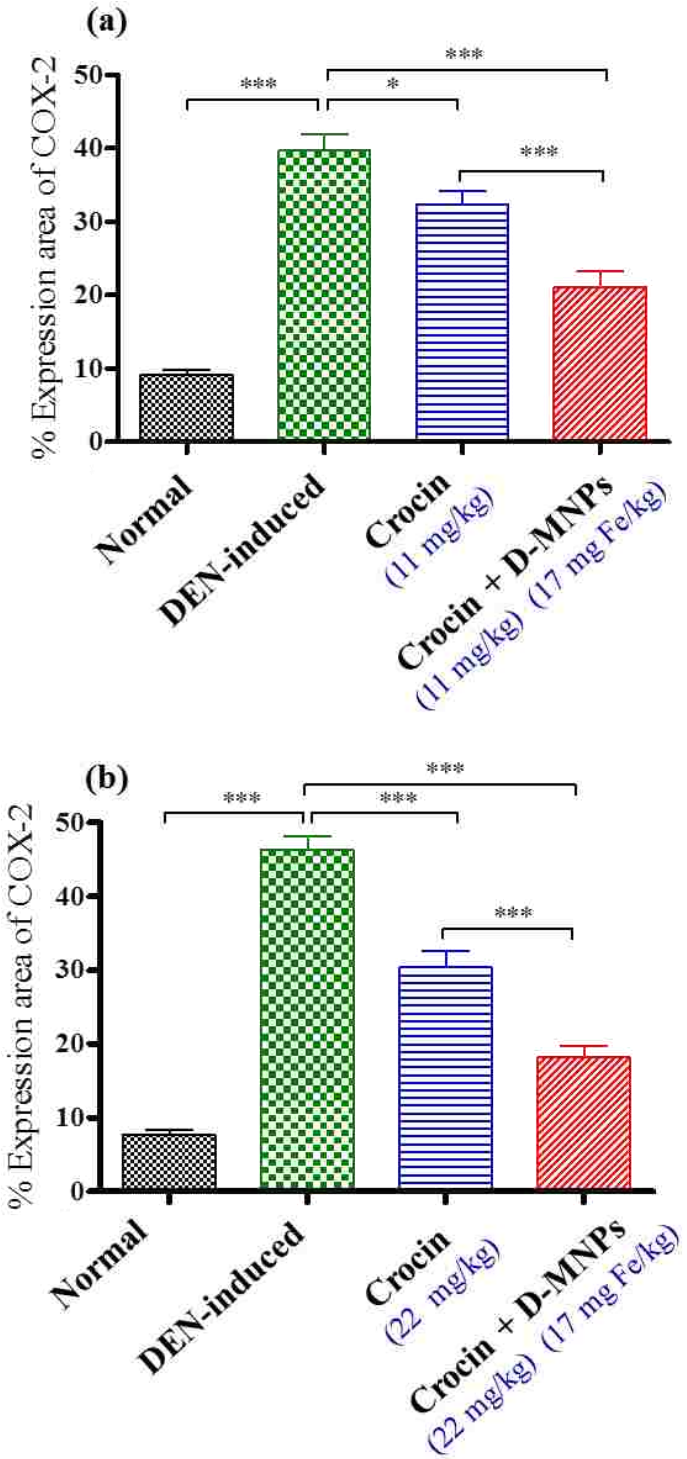

Figure 72: Estimated expression areas of COX-2 positive cells in the two examined crocin formulations. a) 11 mg/kg crocin-loaded D-MNPs, and b) 22 mg/kg crocin-loaded D-MNPs.Values are expressed as mean ±SEM; $*P \leq 0.05$, $**P \leq 0.01$, $***P \leq 0.001$.

3.7.4.6. VEGF expression

Angiogenesis is a complicated and critical process involving proliferation and migration of endothelial cells to form new blood vessels. This phenomenon is required for healing of injured tissue, and proliferation of tumor cells, in order to supply the growth factors, nutrients, and oxygen. Recently, it was demonstrated that angiogenesis starts at a very early (100-300 cells) stage of tumor formation. Various angiogenic factors have been identified, but vascular endothelial growth factor (VEGF) is the most potent and specific growth factor for angiogenesis. VEGF has been demonstrated to play a critical role in division, migration, invasion and tubule formation of vascular endothelial cells [260-265].

Chronic liver injury promotes the progress of genetic alterations leading to dysplastic foci/nodule formation, which can develop into HCC later. Angiogenic gene expression in the dysplastic foci facilitates the carcinogenesis pathway leading to the highly vascularized lesion, which is characterized by the presence of sinusoidal capillarization and subsequently, HCC development [260]. Several studies have been shown that VEGF is secreted abundantly in several human tumors and animal experimental models. VEGF-induced tumor development and angiogenesis are mediated through several receptors, such as VEGFR2 and kinase insert domain-containing receptor/fetal liver kinase 1 (KDR/FLK-1). Through the Ras/Raf/MEK/ERK pathway, activate VEGFr2 triggers cell cycle progression, extracellular matrix remodeling, apoptosis resistance, and angiogenesis [260-264].

Proliferation of sinusoidal endothelial cells is mainly regulated by VEGF [263]. Folkman was first to suggest that inhibiting angiogenesis might have therapeutic potential for treating cancer [266] and since then many anti-angiogenic agents have been introduced as potential therapeutic agents to block angiogenesis

process [262]. In this study, the anti-angiogenic effects of crocin-loaded D-MNPs have been investigated in comparison with free crocin.

VEGF IHC results (**Figures 73 and 74**) was quantified and confirmed as shown in **Figure 75.** VEGF expression was significantly increased ($P \leq 0.001$) during hepatocarcinogenesis in DEN-induced group compared to normal group. This was similar to the results of Liu et al. that demonstrated that VEGF expression, in rats giving DEN at the dosage of 10 mg/kg every day for 16 weeks was highly increased compared to normal animals [261].

Umigai et al. indicated that crocetin (aglycone of crocin carotenoids) might suppress the VEGF-induced angiogenesis by inhibiting the phosphorylated-p38 and protection of VE-cadherin expression [267]. Moreover, VEGF expression was attenuated after the treatment with 11 and 22 mg/kg crocin-loaded D-MNPs formulations compared to DEN-induced or free crocin. These data highlighted the role of NPs in enhancing the anti-angiogenesis activities of crocin.

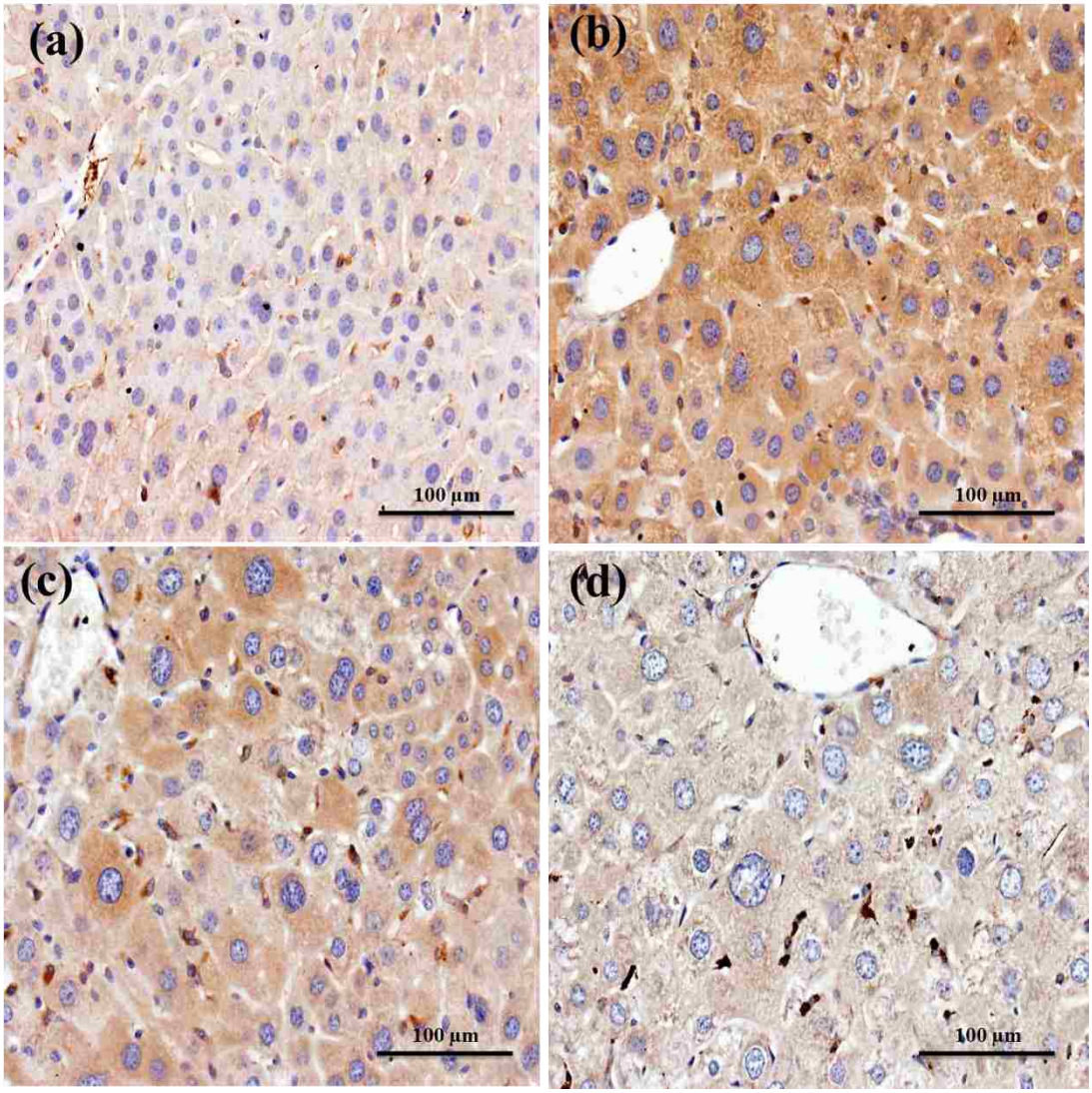

Figure 73: Effects of 11 mg/kg crocin and its NP formulations on VEGF expression in liver. a) Normal, b) DEN-induced, c) 11 mg/kg crocin, and d) 11 mg/kg crocin-loaded D-MNPs. Each scale bar = 100 µm.

.

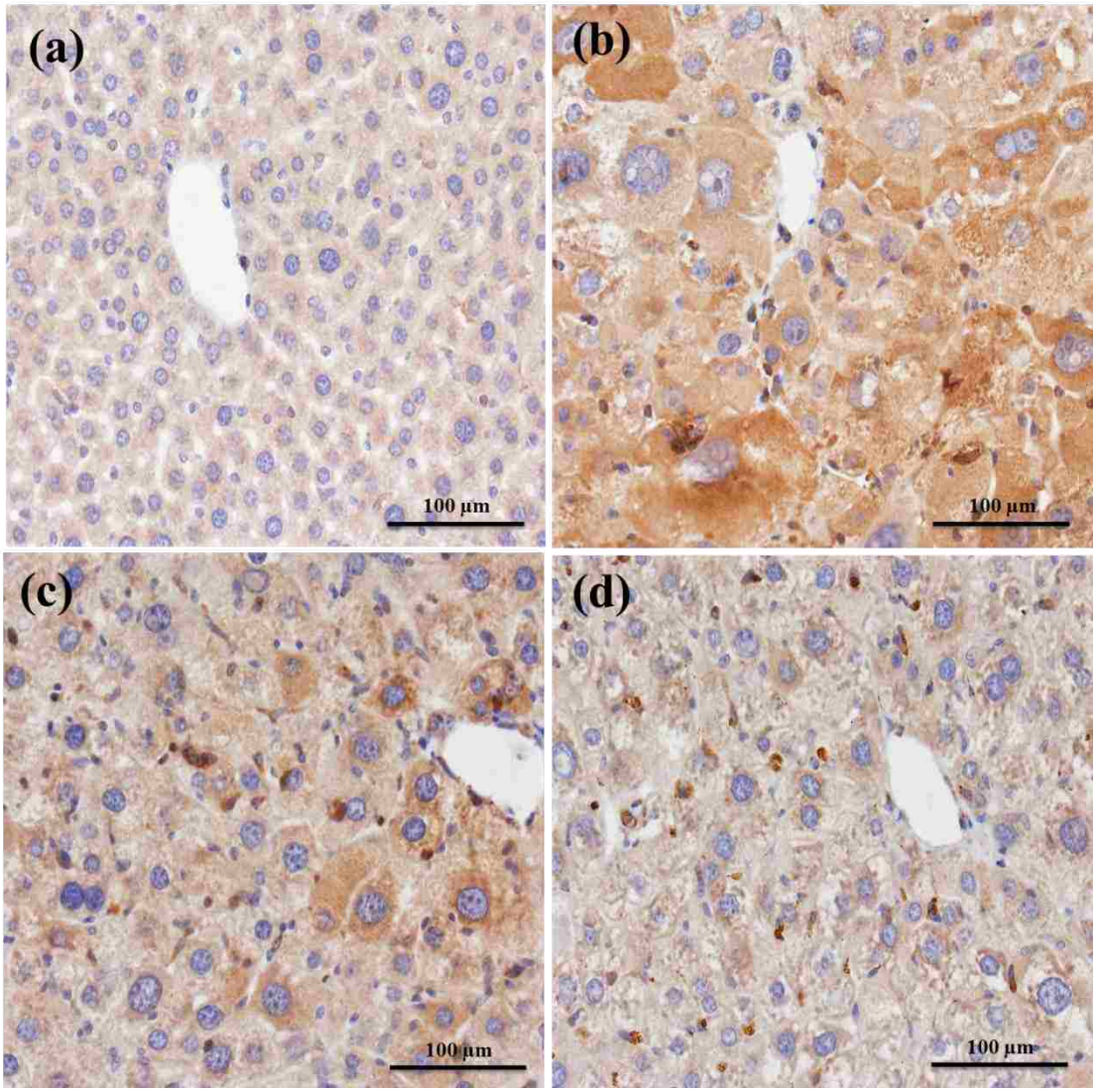

Figure 74: Effects of 22 mg/kg crocin and its NP formulations on VEGF expression in liver. a) Normal, b) DEN-induced, c) 22 mg/kg crocin, and d) 22 mg/kg crocin-loaded D-MNPs. Each scale bar = 100 µm.

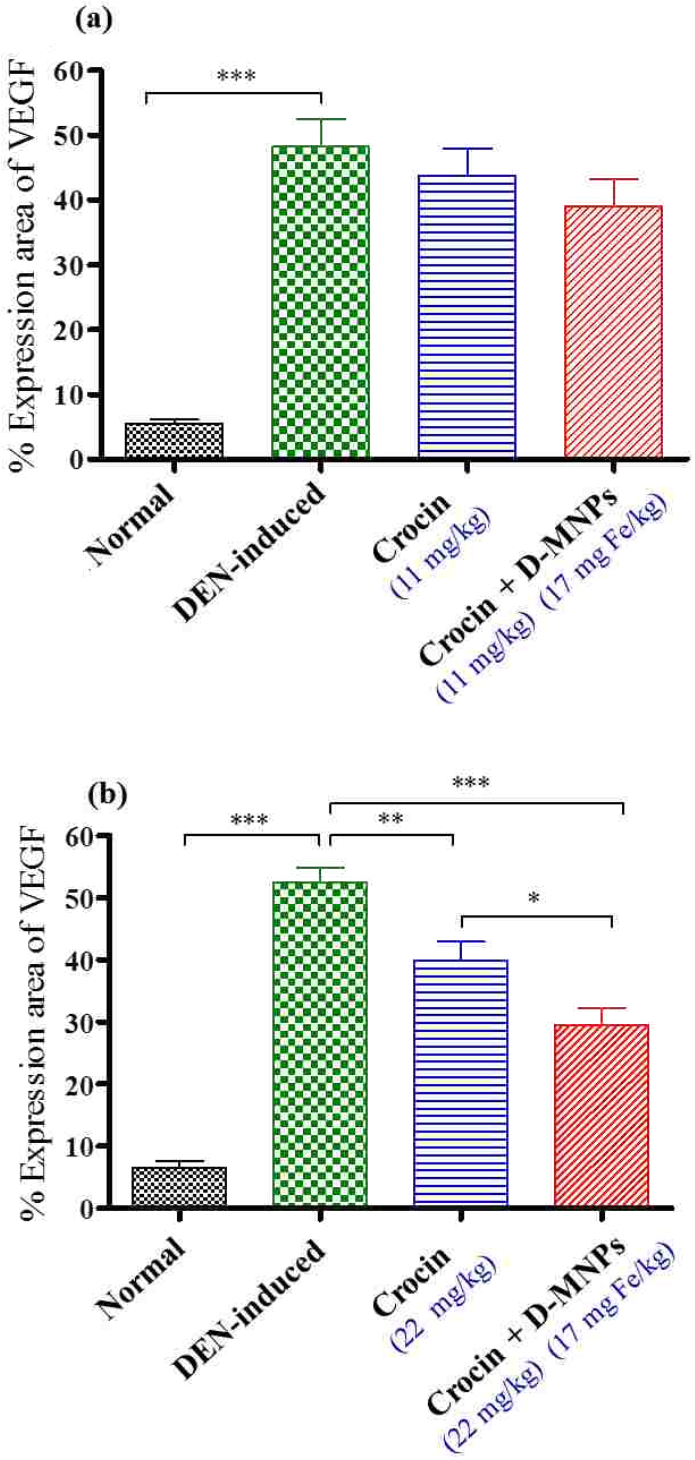

Figure 75: Quantitative analysis of VEGF-expression in the two examined crocin formulations. a) 11 mg/kg crocin-loaded D-MNPs, and b) 22 mg/kg crocin-loaded D-MNPs. Values are expressed as mean ±SEM; *$P \leq 0.05$, **$P \leq 0.01$, ***$P \leq 0.001$.

3.7.5. Proposed mechanism

To achieve effective targeting of pre-cancerous tissues, systemically delivered NPs must first extravasate from the bloodstream and bind to cells. Then NPs must cross the cell membrane of the target cells to reach appropriate intracellular sites. Two targeting strategies, passive and active have been reported by researchers to explain NPs delivery to the tumors. Active targeting, also called ligand-mediated targeting, involves the utilization of specific ligands on the surface of NPs that bind specific surface molecules or receptors overexpressed on the membranes of cancer cells [90, 201-203, 268].

Passive targeting (used in this study) utilizes the distinctive pathological characteristics of tumor blood vessels: highly immature, disorganized and dilated with a high number of pores or fenestrae. These vascular changes may even lead to the formation of wide gaps between endothelial cells and enabling NPs to accumulate in pre-cancerous and cancerous tissues. Therefore, the 'leaky' vascularization enhances permeability and allows migration and entry of NPs (10-500 nm) into the pre-cancerous tissues **(Figure 76).** Moreover, the deficiency of the lymphatic system in the newly formed pre-cancerous tissue does not allow the recapture of these NPs and improves the retention or preservation effect [90, 201-203].

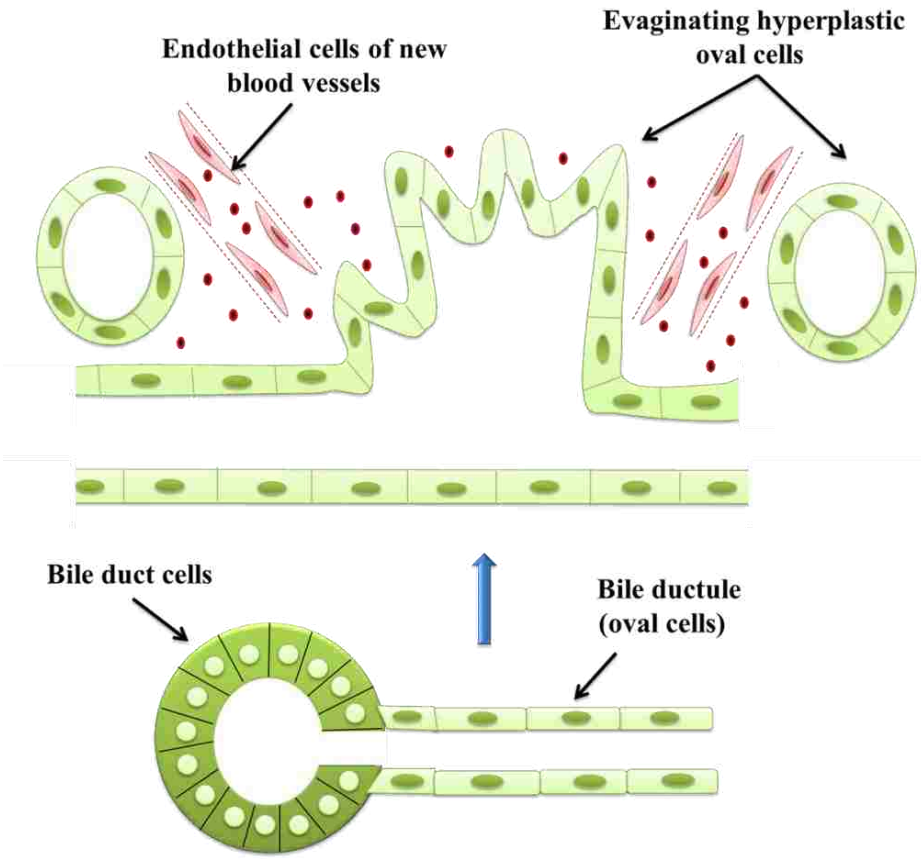

Figure 76: A diagram representing the changes that occur in bile ductule and oval cells due to DEN. Proliferation of oval cells leads to evagination of the epithelium and formation of pre-cancerous lesion. New blood vessels also develop (angiogenesis) around the hyperplastic tissue. These changes might lead to enhanced internalization of crocin-loaded D-MNPs by passive targeting.

Once extravasated from the bloodstream, D-MNPs internalization into the oval cells and hepatocytes starts by their binding or adsorption to cell membranes followed by the formation of endocytotic vesicles or NPs-containing endosomes [269]. Thus, it is possible that in this study, endosomes and lysosomes fuse to form endo-lysosome vesicles in which the crocin is released from crocin-loaded D-MNPs in its active form as illustrated in **Figure 77**. Most of the NPs were captured by kupffer cells via phagocytosis (**Figure 55)**, and then the formation of a phagosome. Phago-lysosome is formed after fusion of phagosome with lysosome, where the crocin is also released from crocin-loaded D-MNPs in its active form.

Dextran will be degraded into sugar components and MNPs will be degraded into free iron II and III. Free Iron in the hepatocytes cytoplasm can be used in essential physiological functions, such as mitochondrial adenosine triphosphate (ATP) generation and DNA damage repair. Meanwhile, unused iron is stored in the iron-binding protein such as ferritin, hemosiderin, and transferrin. Iron might exit the cells by exocytosis, bind to transferrin in blood, and get transported throughout the body as diferric transferrin. Iron homeostasis is preserved by the loss of about 1 mg of iron per day through the sloughing of intestinal mucosa and skin. On the other hand, 20–25 mg of iron is essential each day for the hemoglobinization of new erythrocytes [270].

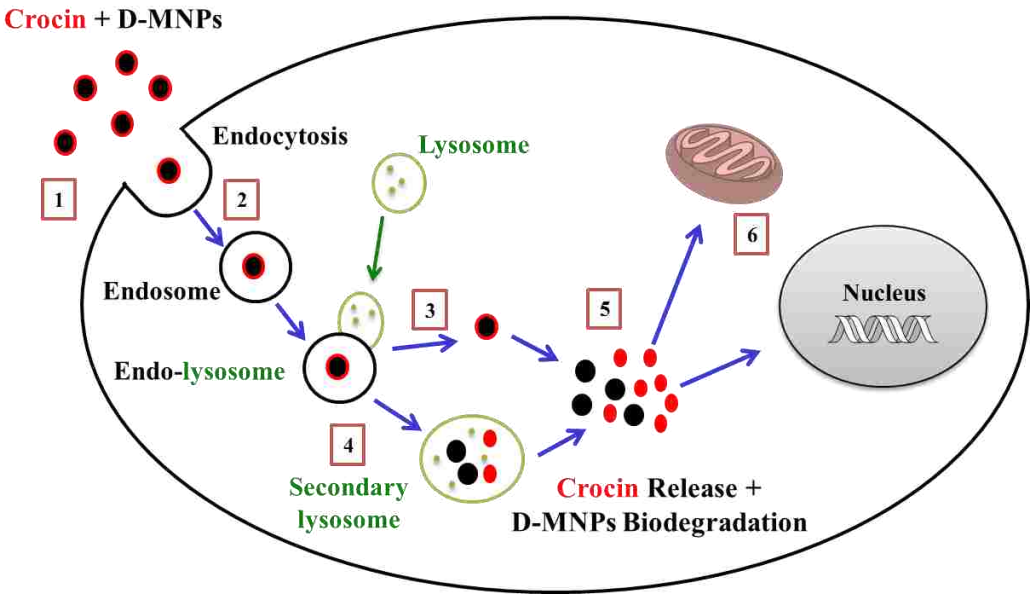

Figure 77: A diagram representing the proposed steps of endocytosis of crocin-loaded D-MNPs into the oval cell and hepatocytes. The NPs go through (1) cellular association, (2) internalization of via endocytosis, (3) endosomal escape or (4) lysosomal degradation, (5) free crocin release into the cytoplasm and D-MNPs biodegradation, (6) cytoplasmic transport of crocin to effect organelles such as nucleus and mitochondria, modified from [271].

Moreover, the microenvironment surrounding pre-cancerous tissue is different from healthy tissue, a physiological phenomenon that also supports passive targeting. Due to high metabolic rate of fast-growing tumor cells, they require more oxygen and nutrients. Consequently, glycolysis is stimulated to obtain extra energy, resulting in an acidic environment. The passive diffusion mechanism will facilitate the crocin-loaded D-MNPs entry to the acidic environment of cells thus releasing crocin in its active form.

The present study shows that the crocin release rate in acidic cancerous condition was higher than the physiological condition (pH 7.4) as in **Figure 44**. This fast crocin release could be explained by induced hydrolysis [3, 200, 272] of ester bond between crocin and cross-linker conjugated to D-MNPs in the acidic microenvironment. Following the successful loading and releasing of crocin in its active from D-MNPs in pre-cancerous lesions location, crocin can affects such lesions via different mechanisms; some of these mechanisms have been investigated in this study. Crocin could decrease GST-P expression in DEN-induced mice (**Figure 58**). This reduced level of GST-P might be due to crocin's anti-antioxidant effect though suppressing the DEN-induced ROS. Ochiai et al. reported that crocin is considered promising for neuroprotection due to their potential ROS-suppressing abilities. Treatment of PC-12 cells with crocin has been reported to inhibit cell membrane lipid peroxidation and to restore intracellular superoxide dismutase and glutathione peroxidase (anti-oxidant enzymes) activity [273].

The anti-proliferative activity of crocin in this study was also associated with the inhibition of Ki-67 (**Figure 61**) and induction of apoptosis. Crocin stimulated apoptosis by up-regulation of caspase cleaved cytokeratin 18 (**Figure 65**) and down-regulation of Bcl-2 expression (**Figure 69**). Crocin might reduce the Bcl-2 through

de-activating PI3K/AKT signaling pathway [274]. Other studies showed that crocin induced broad changes in the expression profile of genes modulating cell cycle via down-regulating the Bcl-2 expression and up-regulating Bax expression. Furthermore, crocin has been shown to increase the number of cells at G0/G1 phase, thus increasing the percentage of apoptotic cells through G1 cell cycle arrest [67, 207, 275].

Liver cancer development is combined with chronic cytotoxicity and inflammation. In this study, crocin displayed an efficacy in significantly reducing DEN-induced liver inflammation by decreasing level of expression COX-2 in the cells as in **Figure 72**. COX-2 is a key enzyme involved in producing inflammatory signals [276]. The overall proposed anti-cancer mechanisms of crocin are shown in **Figure 78**.

To our knowledge this study is the first to show that crocin has an inhibitory effect against angiogenesis and does significantly decreases VEGF expression in DEN-induced mice (**Figure 75**). This effect might be because of suppression of p38 phosphorylation similar to crocetin [267].

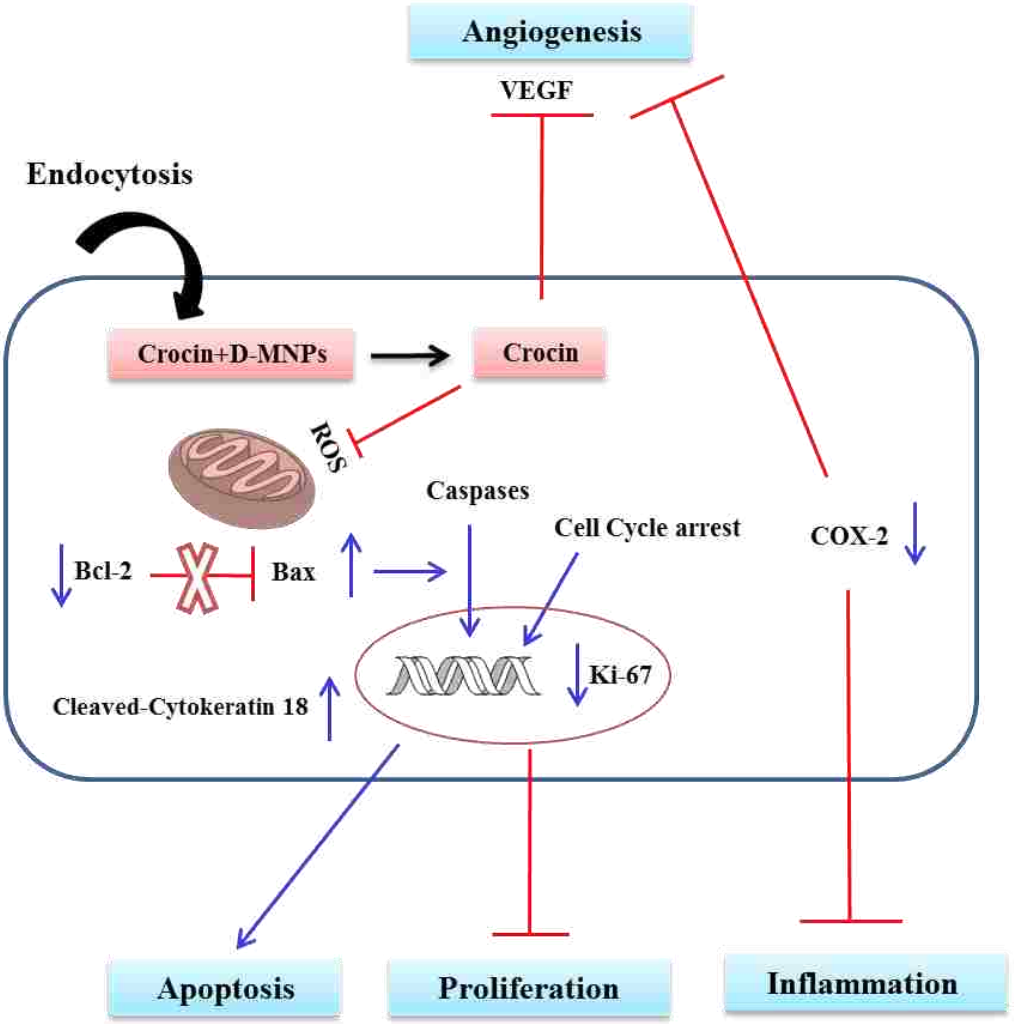

Figure 78: Diagrammatic representation demonstrating the proposed anti-cancer activity of crocin on pre-cancer/cancer cell, *in vitro* and *in vivo*. Crocin has multi-effects on the cell include inhibition of proliferation and inflammation and enhancement of apoptosis. Crocin exhibits inhibitory effect on proliferation by decreasing Ki-67 nuclear protein, while apoptosis activity increases through up-regulation of caspase cleaved cytokeratin 18 and down-regulation of Bcl-2. The anti-inflammatory and anti-angiogenesis effect of crocin is due to down-regulation of COX-2. Anti-angiogenesis also includes inhibition of VEGF growth factor.

Chapter 4: Conclusions

HCC is one of the most widespread cancers worldwide and its incidence and mortality rate are on the rise in many countries. The major drawbacks in current modalities of liver cancer treatment are associated with high toxicity and the lack of specificity to cancer cells. Thus, different controlled drug delivery systems have been developed and natural anti-cancer sources have been investigated to overcome those shortcomings. Modified co-precipitation method in air at low temperature was used to manufacture pure and coated MNPs. After investigating different reaction parameters and coating materials, 1.0 % of dextran was selected as an ideal coating material using a slow feeding rate at 40 ml/hr while maintaining the stirring and soaking temperatures at 60ºC. Crocin was chemically conjugated to D-MNPs via cross-linker. Crocin is a saffron-based natural product that has shown anti-tumour activity both *in vitro* and *in vivo.*

To our knowledge this is the first report indicating that i.v. administration and the controlled release of crocin conjugated onto D-MNPs could improve the anti-cancer therapeutic effect than free crocin in *in vitro* and *in vivo* liver cancer models. HepG2 cells treated with crocin-loaded D-MNPs reduced the cell proliferation when compared to control (non-treated cells) or those treated with free crocin or D-MNPs. In mice injected with diethylnitosamine, and developed several pre-cancerous changes and microscopic intrahepatic cholangioma, immunohistochemical results indicated that D-MNPs conjugated with crocin could increase the anti-cancer activity over free crocin. Thus, to obtain an optimal dose for use in humans, these NPs require further investigation. These results provide insights for designing new modalities for treatment of liver cancer which would hopefully reduce its high mortality rate.

Chapter 5: Future Prospects and Limitations

To reduce the toxic side effects induced by traditional chemotherapy, this dissertation demonstrated a potential means of passive delivery for crocin as a natural anti-cancer agent specifically into cancer sites. With the promising anti-cancer results of crocin attached on D-MNPs reported in this study both *in vitro* and *in vivo*, it would be useful to investigate other pathways and possible mechanisms by which crocin in this NPs system could inhibit the cancer development. Key markers of pathways of interest include, but not limited to, p53 and caspase 3 for apoptosis, and NF-κB, IL-1ß, IL-6 and TNF-α for inflammation.

In addition, it would be interesting to evaluate the effect of crocin-attached D-MNPs system on other cell lines and in different animal models of HCC. Hep3B, SUN-398 and PLHC-1 are examples of other HCC cell lines. Alternative HCC animal models include chemically-induced with aflatoxin B1 or carbon tetrachloride, xenograft model, and transgenic mice such as TAg mice. Being synthesized with magnetite cores would make it beneficial to track these nano-carrier using MRI while simultaneously acting as anti-cancer agent *in vitro* and *in vivo*. MRI can be used to evaluate the reduction in cancer tissues after treating with crocin-load D-MNPs.

Despite the success of developing D-MNPs that enhanced the delivery and activity of crocin, there are still several obstacles to be overcome. First, there was minor cytotoxicity because of de-attachment of dextran as a coating material exposing MNPs core to the cells. Second, crocin release rate was slow and took two weeks to reach 92% at pH 5.5. Third, there was difficulty to reproduce the effective crocin-loaded D-MNPs due to fact that not all MNPs could be coated with dextran and attached to crocin similarly and effectively (heterogeneous production).

Further refinements are needed for these NPs to be used for drug delivery. In spite of that, the developed D-MNPs have important properties that qualify them to be used for cancer treatment, such as, hyperthermia.

Bibliography

1. Hanahan, D. and Robert A. Weinberg, Hallmarks of Cancer: The Next Generation. Cell, 2011. 144(5): p. 646-674.

2. Floor, S.L., et al., *Hallmarks of cancer: of all cancer cells, all the time?* Trends in Molecular Medicine, 2012. **18**(9): p. 509-515.

3. Singh, N., et al., *Potential toxicity of superparamagnetic iron oxide nanoparticles (SPION).* Nano Rev, 2010. **1**.

4. Interntional Agency for Research on Cancer, W.H.O. *GLOBOCAN 2012: Estimated Cancer Incidence, Mortality and Prevalence Worldwide in 2012*. 2012 [cited 22.9.2014].

5. Dhabi, A. and H. Authority, *Health Statistics 2012*. 2013, Health Authority Abu Dhabi: Health Authority Abu Dhabi

6. Clavijo-Cornejo, D., et al., *Acetaldehyde targets superoxide dismutase 2 in liver cancer cells inducing transient enzyme impairment and a rapid transcriptional recovery.* Food and Chemical Toxicology, 2014. **69**(0): p. 102-108.

7. Weeder, P.D., R.J. Porte, and T. Lisman, *Hemostasis in Liver Disease: Implications of New Concepts for Perioperative Management.* Transfusion Medicine Reviews, 2014. **28**(3): p. 107-113.

8. Emanuel Rubin, J.L.F., *Essential Pathology*. Second ed. 1995.

9. Christopher R.W. Edwards, I.A.D.B., Christopher Haslett and Edwin R. Chrilvers, *Davidson's principles and practice of medicine.* 1995(Seventeenth): p. 484-489.

10. Thoolen, B., et al., *Proliferative and nonproliferative lesions of the rat and mouse hepatobiliary system.* Toxicol Pathol, 2010. **38**(7 Suppl): p. 5s-81s.

11. Britannica, E., *Liver*, in *Britannica*, M.G. Abdullah, et al., Editors. 2014.

12. CellPress, *Liver structure*. 2014, Cell Press.

13. Bakiri, L. and E.F. Wagner, *Mouse models for liver cancer.* Molecular Oncology, 2013. **7**(2): p. 206-223.

14. Chen, X. and D.F. Calvisi, *Hydrodynamic Transfection for Generation of Novel Mouse Models for Liver Cancer Research.* The American Journal of Pathology, 2014. **184**(4): p. 912-923.

15. Sengupta, D., et al., *Berberine and S allyl cysteine mediated amelioration of DEN+CCl4 induced hepatocarcinoma.* Biochimica et Biophysica Acta (BBA) - General Subjects, 2014. **1840**(1): p. 219-244.

16. De Minicis, S., et al., *Liver carcinogenesis: Rodent models of hepatocarcinoma and cholangiocarcinoma.* Digestive and Liver Disease, 2013. **45**(6): p. 450-459.

17. Heindryckx, F., I. Colle, and H. Van Vlierberghe, *Experimental mouse models for hepatocellular carcinoma research.* Int J Exp Pathol, 2009. **90**(4): p. 367-86.

18. Llovet, J.M., A. Burroughs, and J. Bruix, *Hepatocellular carcinoma.* The Lancet, 2003. **362**(9399): p. 1907-1917.

19. Marquardt, J.U., P.R. Galle, and A. Teufel, *Molecular diagnosis and therapy of hepatocellular carcinoma (HCC): An emerging field for advanced technologies.* Journal of Hepatology, 2012. **56**(1): p. 267-275.

20. Teufel, A., J.U. Marquardt, and P.R. Galle, *Next generation sequencing of HCC from European and Asian HCC cohorts. Back to p53 and Wnt/β-catenin.* Journal of Hepatology, 2013. **58**(3): p. 622-624.

21. Jain, D., *Tissue Diagnosis of Hepatocellular Carcinoma.* Journal of Clinical and Experimental Hepatology, 2014. **4,** Supplement 3(0): p. S67-S73.

22. Stagos, D., et al., *Chemoprevention of liver cancer by plant polyphenols.* Food and Chemical Toxicology, 2012. **50**(6): p. 2155-2170.

23. Nowak, R., M. Olech, and N. Nowacka, *Chapter 97 - Plant Polyphenols as Chemopreventive Agents*, in *Polyphenols in Human Health and Disease*, R.R. Watson, V.R. Preedy, and S. Zibadi, Editors. 2014, Academic Press: San Diego. p. 1289-1307.

24. Eguchi, H., et al., *Augmentation of antitumor activity of 5-fluorouracil by interferon alpha is associated with up-regulation of p27Kip1 in human hepatocellular carcinoma cells.* Clin Cancer Res, 2000. **6**(7): p. 2881-90.

25. Adnane, L., et al., *Sorafenib (BAY 43-9006, Nexavar®), a Dual-Action Inhibitor That Targets RAF/MEK/ERK Pathway in Tumor Cells and Tyrosine Kinases VEGFR/PDGFR in Tumor Vasculature*, in *Methods in Enzymology*, C.J.D. William E. Balch and H. Alan, Editors. 2006, Academic Press. p. 597-612.

26. Cao, H., H. Phan, and L.X. Yang, *Improved chemotherapy for hepatocellular carcinoma.* Anticancer Res, 2012. **32**(4): p. 1379-86.

27. Nagasue, N., et al., *Incidence and factors associated with intrahepatic recurrence following resection of hepatocellular carcinoma.* Gastroenterology, 1993. 105(2): p. 488-94.

28. Li, Y., Z.-Y. Tang, and J.-X. Hou, *Hepatocellular carcinoma: insight from animal models.* Nat Rev Gastroenterol Hepatol, 2012. **9**(1): p. 32-43.

29. Pradeep, K., et al., *Silymarin modulates the oxidant-antioxidant imbalance during diethylnitrosamine induced oxidative stress in rats.* Eur J Pharmacol, 2007. **560**(2-3): p. 110-6.

30. Barnes, J.M. and P.N. Magee, *The production of malignant primaryheptic tumors in therat by feeding dimethylnitrosamine.* British Journal of Cancer, 1956. **10**(1): p. 114–122.

31. Verna, L., J. Whysner, and G.M. Williams, *N-nitrosodiethylamine mechanistic data and risk assessment: bioactivation, DNA-adduct formation, mutagenicity, and tumor initiation.* Pharmacol Ther, 1996. **71**(1-2): p. 57-81.

32. Pradeep, K., et al., *Protective effect of Cassia fistula Linn. on diethylnitrosamine induced hepatocellular damage and oxidative stress in ethanol pretreated rats.* Biol Res, 2010. **43**(1): p. 113-25.

33. Lewis, D.F., et al., *Nitrosamine carcinogenesis: rodent assays, quantitative structure-activity relationships, and human risk assessment.* Drug Metab Rev, 1997. **29**(4): p. 1055-78.

34. Paula Santos, N., et al., *N-diethylnitrosamine mouse hepatotoxicity: Time-related effects on histology and oxidative stress.* Exp Toxicol Pathol, 2014.

35. Rumsby, P.C., et al., *Analysis of the Ha-ras oncogene in C3H/He mouse liver tumours derived spontaneously or induced with diethylnitrosamine or phenobarbitone.* Carcinogenesis, 1991. **12**(12): p. 2331-6.

36. Buchmann, A., et al., *Mutational activation of the c-Ha-ras gene in liver tumors of different rodent strains: correlation with susceptibility to hepatocarcinogenesis.* Proc Natl Acad Sci U S A, 1991. **88**(3): p. 911-5.

37. Srinivasan, K., et al., *Identification of a farnesol analog as a Ras function inhibitor using both an in vivo Ras activation sensor and a phenotypic screening approach.* Mol Cell Biochem, 2014. **387**(1-2): p. 177-86.

38. He, X.Y., et al., *Short-term diethylnitrosamine-induced oval cell responses in three strains of mice.* Pathology, 1994. **26**(2): p. 154-60.

39. Xu, X.M., et al., *Hepatic oval cells activated by hepatocyte apoptosis in diethylnitrosamine-induced rat liver cirrhosis.* Saudi Med J, 2010. **31**(5): p. 490-4.

40. Hartwell, K.L. and P. Shubick, *Survey of Compounds Which Have Been Tested for Carcinogenic Activity.* National Institutes of Health, 1967. **1**.

41. Rajewsky, M.F., W. Dauber, and H. Frankenberg, *Liver carcinogenesis by diethylnitrosamine in the rat.* Science, 1966. **152**(3718): p. 83-5.

42. Maronpot, R.R., *Biological Basis of Differential Susceptibility to Hepatocarcinogenesis among Mouse Strains.* Journal of Toxicologic Pathology, 2009. **22**(1): p. 11-33.

43. Park, D.H., et al., *Diethylnitrosamine (DEN) induces irreversible hepatocellular carcinogenesis through overexpression of G1/S-phase regulatory proteins in rat.* Toxicol Lett, 2009. **191**(2-3): p. 321-6.

44. Frey, S., et al., *Suppression of apoptosis in C3H mouse liver tumors by activated Ha-ras oncogene.* Carcinogenesis, 2000. **21**(2): p. 161-6.

45. Zimmers, T.A., et al., *Effect of in vivo loss of GDF-15 on hepatocellular carcinogenesis.* J Cancer Res Clin Oncol, 2008. **134**(7): p. 753-9.

46. Shiota, G., et al., *Inhibition of hepatocellular carcinoma by glycyrrhizin in diethylnitrosamine-treated mice.* Carcinogenesis, 1999. **20**(1): p. 59-63.

47. Kushida, M., et al., *Dose-related induction of hepatic preneoplastic lesions by diethylnitrosamine in C57BL/6 mice.* Toxicol Pathol, 2011. **39**(5): p. 776-86.

48. Klaunig, J.E., et al., *Dose-response relationship of diethylnitrosamine-initiated tumors in neonatal balb/c mice: effect of phenobarbital promotion.* Toxicol Pathol, 1988. **16**(3): p. 381-5.

49. da Silva, T.C., et al., *Inhibitory effects of Pfaffia paniculata (Brazilian ginseng) on preneoplastic and neoplastic lesions in a mouse hepatocarcinogenesis model.* Cancer Lett, 2005. **226**(2): p. 107-13.

50. Shirakami, Y., M.E. Gottesman, and W.S. Blaner, *Diethylnitrosamine-induced hepatocarcinogenesis is suppressed in lecithin:retinol acyltransferase-deficient mice primarily through retinoid actions immediately after carcinogen administration.* Carcinogenesis, 2012. **33**(2): p. 268-74.

51. Newell, P., et al., *Experimental models of hepatocellular carcinoma.* J Hepatol, 2008. **48**(5): p. 858-79.

52. Hamid, A.S., et al., *Aflatoxin B1-induced hepatocellular carcinoma in developing countries: Geographical distribution, mechanism of action and prevention.* Oncol Lett, 2013. **5**(4): p. 1087-1092.

53. Kew, M.C., *Aflatoxins as a cause of hepatocellular carcinoma.* J Gastrointestin Liver Dis, 2013. **22**(3): p. 305-10.

54. Fujii, T., et al., *Mouse model of carbon tetrachloride induced liver fibrosis: Histopathological changes and expression of CD133 and epidermal growth factor.* BMC Gastroenterol, 2010. **10**: p. 79.

55. Weber, L.W.D., M. Boll, and A. Stampfl, *Hepatotoxicity and Mechanism of Action of Haloalkanes: Carbon Tetrachloride as a Toxicological Model.* Critical Reviews in Toxicology, 2003. **33**: p. 105-136.

56. Knight, B., et al., *Impaired preneoplastic changes and liver tumor formation in tumor necrosis factor receptor type 1 knockout mice.* J Exp Med, 2000. **192**(12): p. 1809-18.

57. Richmond, A. and Y. Su, *Mouse xenograft models vs GEM models for human cancer therapeutics.* Disease Models & Mechanisms 1, 2008. **1**: p. 78-82

58. Newell, P., et al., *Experimental models of hepatocellular carcinoma.* Journal of Hepatology, 2008. **48**(5): p. 858-879.

59. A.Kalaiselvan, et al., *Preventive Effect of Shorea Robusta Bark Extract against Diethylnitrosamine-Induced Hepatocellular Carcinoma in Rats.* International Research Journal of Medical Sciences, 2013. **1**(2): p. 2-9.

60. Bolhassani, A., A. Khavari, and S.Z. Bathaie, *Saffron and natural carotenoids: Biochemical activities and anti-tumor effects.* Biochimica et Biophysica Acta (BBA) - Reviews on Cancer, 2014. **1845**(1): p. 20-30.

61. Fernández, J.-A., *Anticancer properties of saffron, Crocus sativus Linn*, in *Advances in Phytomedicine*, T.H.K. Mahmud and A. Arjumand, Editors. 2006, Elsevier. p. 313-330.

62. Melnyk, J.P., S. Wang, and M.F. Marcone, *Chemical and biological properties of the world's most expensive spice: Saffron.* Food Research International, 2010. **43**(8): p. 1981-1989.

63. Srivastava, R., et al., *Crocus sativus L.: A comprehensive review.* Pharmacogn Rev, 2010. **4**(8): p. 200-8.

64. Lopresti, A.L. and P.D. Drummond, *Saffron (Crocus sativus) for depression: a systematic review of clinical studies and examination of underlying*

antidepressant mechanisms of action. Hum Psychopharmacol, 2014. **29**(6): p. 517-27.

65. Padmavathy, J., et al., *Pharmacological, Pharmacognostic and Phytochemical Review of Saffron* International Journal Of Pharmacy &Technology, 2011.

66. Saffron, S. *The Saffron*. 2013 [cited 2015; Available from: http://www.saffron-spain.com/ingles/azafran.html

67. Alavizadeh, S.H. and H. Hosseinzadeh, *Bioactivity assessment and toxicity of crocin: A comprehensive review.* Food and Chemical Toxicology, 2014. **64**(0): p. 65-80.

68. Amin, A., et al., *Saffron: A Potential Candidate for a Novel Anticancer Drug Against Hepatocellular Carcinoma.* Hepatology, 2011. **54**: p. 857-867.

69. Singla, R.K. and V.B. G, *Crocin: An Overview.* Indo Global Journal of Pharmaceutical Sciences, 2011. **1**(4): p. 281-286.

70. Asai, A., et al., *Orally administered crocetin and crocins are absorbed into blood plasma as crocetin and its glucuronide conjugates in mice.* J Agric Food Chem, 2005. **53**(18): p. 7302-6.

71. Xi, L., et al., *Pharmacokinetic properties of crocin (crocetin digentiobiose ester) following oral administration in rats.* Phytomedicine, 2007. **14**(9): p. 633-636.

72. Lee, I.A., et al., *Antihyperlipidemic effect of crocin isolated from the fructus of Gardenia jasminoides and its metabolite Crocetin.* Biol Pharm Bull, 2005. **28**(11): p. 2106-10.

73. Debnath, T., et al., *Antioxidant activity of Gardenia jasminoides Ellis fruit extracts.* Food Chemistry, 2011. **128**(3): p. 697-703.

74. Aung, H.H., et al., *Crocin from Crocus sativus possesses significant anti-proliferation effects on human colorectal cancer cells.* Exp Oncol, 2007. **29**(3): p. 175-80.

75. Konoshima, T., et al., *Crocin and Crocetin Derivatives Inhibit Skin Tumour Promotion in Mice.* Phytotherapy Research, 1998. **12**: p. 400–404.

76. Garcia-Olmo, D.C., et al., *Effects of long-term treatment of colon adenocarcinoma with crocin, a carotenoid from saffron (Crocus sativus L.): an experimental study in the rat.* Nutr Cancer, 1999. **35**(2): p. 120-6.

77. Kianbakht, S. and K. Mozaffari, *Effects of Saffron and its Active Constituents, Crocin and Safranal, on Prevention of Indomethacin Induced Gastric Ulcers in Diabetic and Nondiabetic Rats.* Medicinal Plants, 2009. **8**(5): p. 30-38.

78. Xu, G.L., et al., *Preventive effect of crocin in inflamed animals and in LPS-challenged RAW 264.7 cells.* J Agric Food Chem, 2009. **57**(18): p. 8325-30.

79. Bors, W., M. Saran, and C. Michel, *Radical intermediates involved in the bleaching of the carotenoid crocin. Hydroxyl radicals, superoxide anions and hydrated electrons.* Int J Radiat Biol Relat Stud Phys Chem Med, 1982. **41**(5): p. 493-501.

80. Yang, H.J., M. Park, and H.S. Lee, *Antioxidative Activities and Components of Gardenia jasminoides* Food and Science Technology, 2011. **43**: p. 51–57.

81. Sebastin Santhosh, M., et al., *Vipera russelli venom-induced oxidative stress and hematological alterations: amelioration by crocin a dietary colorant.* Cell Biochem Funct, 2013. **31**(1): p. 41-50.

82. El-Beshbishy, H.A., et al., *Crocin "saffron" protects against beryllium chloride toxicity in rats through diminution of oxidative stress and enhancing gene expression of antioxidant enzymes.* Ecotoxicology and Environmental Safety, 2012. **83**(0): p. 47-54.

83. Tamaddonfard, E., et al., *Comparison of the effects of crocin, safranal and diclofenac on local inflammation and inflammatory pain responses induced by carrageenan in rats.* Pharmacol Rep, 2013. **65**(5): p. 1272-80.

84. Wang, C.J., L.S. Hwang, and J.K. Lin, *Reversible hepatic black pigmentation and enzyme alteration induced by prolonged feeding of high dose of crocin dyes in rats.* Proc Natl Sci Counc Repub China B, 1984. **8**(3): p. 246-53.

85. Hosseinzadeh, H., et al., *Acute and Sub-Acute Toxicity of Crocin, a Costituet af Crocus Sativus L. (Saffron), in Mice and Rats.* Pharmacologyonline, 2010. 2: p. 943-951.

86. Mohamadpour, A.H., et al., *Safety Evaluation of Crocin (a constituent of saffron) Tablets in Healthy Volunteers.* Iran J Basic Med Sci, 2013. **16**(1): p. 39-46.

87. Chatterjee, K., et al., *Core/shell nanoparticles in biomedical applications.* Advances in Colloid and Interface Science, 2014. **209**(0): p. 8-39.

88. Grillo, R., A.H. Rosa, and L.F. Fraceto, *Engineered nanoparticles and organic matter: A review of the state-of-the-art.* Chemosphere, 2015. **119C**: p. 608-619.

89. Wu, L., J. Zhang, and W. Watanabe, *Physical and chemical stability of drug nanoparticles.* Adv Drug Deliv Rev, 2011. **63**(6): p. 456-69.

90. Nazir, S., et al., *Nanomaterials in combating cancer: Therapeutic applications and developments.* Nanomedicine: Nanotechnology, Biology and Medicine, 2014. **10**(1): p. 19-34.

91. Wang, R., P.S. Billone, and W.M. Mullett, *Nanomedicine in Action: An Overview of Cancer Nanomedicine on the Market and in Clinical Trials.* Nanomaterials, 2012. **2013**.

92. Mahmoudi, M., et al., *Superparamagnetic iron oxide nanoparticles (SPIONs): Development, surface modification and applications in chemotherapy*. Advanced Drug Delivery Reviews, 2011. **63**(1–2): p. 24-46.

93. Santhosh, P.B. and N.P. Ulrih, *Multifunctional superparamagnetic iron oxide nanoparticles: promising tools in cancer theranostics.* Cancer Lett, 2013. **336**(1): p. 8-17.

94. Veiseh, O., J.W. Gunn, and M. Zhang, *Design and fabrication of magnetic nanoparticles for targeted drug delivery and imaging.* Advanced Drug Delivery Reviews, 2010. **62**(3): p. 284-304.

95. Muthiah, M., I.-K. Park, and C.-S. Cho, *Surface modification of iron oxide nanoparticles by biocompatible polymers for tissue imaging and targeting.* Biotechnology Advances, 2013. **31**(8): p. 1224-1236.

96. Widder, K.J., A.E. Senyel, and G.D. Scarpelli, *Magnetic microspheres: a model system of site specific drug delivery in vivo.* Proc Soc Exp Biol Med, 1978. **158**(2): p. 141-6.

97. McBain, S.C., H.H. Yiu, and J. Dobson, *Magnetic nanoparticles for gene and drug delivery.* Int J Nanomedicine, 2008. **3**(2): p. 169-80.

98. Indira, T.K. and P.K. Lakshmi, *Magnetic nanoparticles- A Review.* International journal of pharmaceutical sciences and nanotechnology, 2010. **2**(3).

99. Naahidi, S., et al., *Biocompatibility of engineered nanoparticles for drug delivery.* Journal of Controlled Release, 2013. **166**(2): p. 182-194.

100. Nadoll, P., et al., *The chemistry of hydrothermal magnetite: A review.* Ore Geology Reviews, 2014. **61**(0): p. 1-32.

101. Mahmoudi, M., et al., *Superparamagnetic iron oxide nanoparticles (SPIONs): development, surface modification and applications in chemotherapy*. Adv Drug Deliv Rev, 2011. **63**(1-2): p. 24-46.

102. Laurent, S., et al., *Magnetic iron oxide nanoparticles: synthesis, stabilization, vectorization, physicochemical characterizations, and biological applications.* Chem Rev, 2008. **108**(6): p. 2064-110.

103. Teja, A.S. and P.-Y. Koh, *Synthesis, properties, and applications of magnetic iron oxide nanoparticles.* Progress in Crystal Growth and Characterization of Materials, 2009. **55**(1–2): p. 22-45.

104. Fanciullino, R., J. Ciccolini, and G. Milano, *Challenges, expectations and limits for nanoparticles-based therapeutics in cancer: A focus on nano-albumin-bound drugs.* Critical Reviews in Oncology/Hematology, 2013. **88**(3): p. 504-513.

105. Wu, L., J. Zhang, and W. Watanabe, *Physical and chemical stability of drug nanoparticles.* Advanced Drug Delivery Reviews, 2011. **63**(6): p. 456-469.

106. Kanapathipillai, M., A. Brock, and D.E. Ingber, *Nanoparticle targeting of anti-cancer drugs that alter intracellular signaling or influence the tumor microenvironment.* Advanced Drug Delivery Reviews, 2014(0).

107. Gupta, A.K. and S. Wells, *Surface-modified superparamagnetic nanoparticles for drug delivery: preparation, characterization, and cytotoxicity studies.* IEEE Trans Nanobioscience, 2004. **3**(1): p. 66-73.

108. Laurent, S., et al., *Magnetic fluid hyperthermia: Focus on superparamagnetic iron oxide nanoparticles*. Advances in Colloid and Interface Science, 2011. **166**(1–2): p. 8-23.

109. Hasany, S.F., et al., *Systematic Review of the Preparation Techniques of Iron Oxide Magnetic Nanoparticles.* Nanoscience and Nanotechnology 2012. **2**(6): p. 148-158.

110. blaney, L., *Magnetite (Fe3O4): Properties, Synthesis, and Applications.* Lehigh Review at Lehigh Preserve, 2007. **15**.

111. Majewski, P. and B. Thierry, *Functionalized Magnetite Nanoparticles—Synthesis, Properties, and Bioapplications*, in *Particulate Systems in Nano- and Biotechnologies*, H. Ei-Shall, et al., Editors. 2008. p. 331–352.

112. Goya, G.F., T.S. Berquo´, and F.C. Fonseca, *Static and dynamic magnetic properties of spherical magnetite nanoparticles.* JOURNAL OF APPLIED PHYSICS, 2003. **94**.

113. Román, S. *Superparamagnetic nanoparticles and the separation problem*. 2014 [cited 2015; Available from: http://mappingignorance.org/2014/03/05/superparamagnetic-nanoparticles-and-the-separation-problem/.

114. Gupta, A.K. and M. Gupta, *Synthesis and surface engineering of iron oxide nanoparticles for biomedical applications.* Biomaterials, 2005. **26**(18): p. 3995-4021.

115. Chomoucka, J., et al., *Magnetic nanoparticles and targeted drug delivering.* Pharmacological Research, 2010. **62**(2): p. 144-149.

116. Laurent, S., et al., *Magnetic iron oxide nanoparticles: synthesis, stabilization, vectorization, physicochemical characterizations, and biological applications.* Chem Rev, 2008. **108**(6): p. 2064-110.

117. Lin, M.M., et al., *Development of superparamagnetic iron oxide nanoparticles (SPIONS) for translation to clinical applications.* IEEE Trans Nanobioscience, 2008. **7**(4): p. 298-305.

118. Shinkai, M., *Functional magnetic particles for medical application.* J Biosci Bioeng, 2002. **94**(6): p. 606-13.

119. Iwasaki, T., et al., *Mechanochemical preparation of magnetite nanoparticles by coprecipitation.* Materials Letters, 2008. **62**(25): p. 4155-4157.

120. Yazdani, F. and M. Edrissi, *Effect of pressure on the size of magnetite nanoparticles in the coprecipitation synthesis.* Materials Science and Engineering: B, 2010. **171**(1-3): p. 86-89.

121. Sun, J., et al., *Synthesis and characterization of biocompatible Fe3O4 nanoparticles.* J Biomed Mater Res A, 2007. **80**(2): p. 333-41.

122. Haw, C.Y., et al., *Hydrothermal synthesis of magnetite nanoparticles as MRI contrast agents.* Ceramics International, 2010. **36**(4): p. 1417-1422.

123. Zhang, Z.J., et al., *Hydrothermal synthesis and self-assembly of magnetite (Fe3O4) nanoparticles with the magnetic and electrochemical properties.* Journal of Crystal Growth, 2008. **310**(24): p. 5453-5457.

124. Zhu, H., D. Yang, and L. Zhu, *Hydrothermal growth and characterization of magnetite (Fe3O4) thin films.* Surface and Coatings Technology, 2007. **201**(12): p. 5870-5874.

125. Teja, A.S. and P.-Y. Koh, *Synthesis, properties, and applications of magnetic iron oxide nanoparticles.* Progress in Crystal Growth and Characterization of Materials. **55**(1-2): p. 22-45.

126. Zheng, Y.-h., et al., *Synthesis and magnetic properties of Fe3O4 nanoparticles.* Materials Research Bulletin, 2006. **41**(3): p. 525-529.

127. Mizutani, N., et al., *Size control of magnetite nanoparticles in hydrothermal synthesis by coexistence of lactate and sulfate ions.* Current Applied Physics, 2010. **10**(3): p. 801-806.

128. Kahani, S.A. and M. Jafari, *A new method for preparation of magnetite from iron oxyhydroxide or iron oxide and ferrous salt in aqueous solution.* Journal of Magnetism and Magnetic Materials, 2009. **321**(13): p. 1951-1954.

129. Si, S., et al., *Size-Controlled Synthesis of Magnetite Nanoparticles inthe Presence of Polyelectrolytes.* chemical material, 2004.

130. Sun, S. and H. Zeng, *Size-controlled synthesis of magnetite nanoparticles.* J Am Chem Soc, 2002. **124**(28): p. 8204-5.

131. Sun, S., et al., *Monodisperse MFe2O4 (M = Fe, Co, Mn) nanoparticles.* J Am Chem Soc, 2004. **126**(1): p. 273-9.

132. Woo, K., J. Hong, and J.-P. Ahn, *Synthesis and surface modification of hydrophobic magnetite to processible magnetite@silica-propylamine.* Journal of Magnetism and Magnetic Materials, 2005. **293**(1): p. 177-181.

133. Li, D., et al., *Nanocrystalline α-Fe and ε-Fe3N particles prepared by chemical vapor condensation process.* Journal of Magnetism and Magnetic Materials, 2004. **283**(1): p. 8-15.

134. Xuan, S., et al., *Preparation of water-soluble magnetite nanocrystals through hydrothermal approach.* Journal of Magnetism and Magnetic Materials, 2007. **308**(2): p. 210-213.

135. Jiaqi, W., et al. *In situ decoration of carbon nanotubes with nearly monodisperse magnetite nanoparticles in liquid polyols*. 2007. **17**, 1188-1192.

136. Li, Z., et al. *One-Pot Reaction to Synthesize Water-Soluble Magnetite Nanocrystals*. 2004. **16**, 1391-1393.

137. Mahmoudi, M., et al., *Superparamagnetic iron oxide nanoparticles (SPIONs): Development, surface modification and applications in chemotherapy.* Adv Drug Deliv Rev, 2010.

138. Morales, M.A., et al., *Synthesis and characterization of magnetic mesoporous particles.* Journal of Colloid and Interface Science, 2010. **342**(2): p. 269-277.

139. Yang, L., et al., *Development of Receptor Targeted Magnetic Iron Oxide Nanoparticles for Efficient Drug Delivery and Tumor Imaging.* Journal of Biomedical Nanotechnology, 2008. **4**: p. 439-449.

140. McCarthy, J.R. and R. Weissleder, *Multifunctional magnetic nanoparticles for targeted imaging and therapy.* Advanced Drug Delivery Reviews, 2008. **60**(11): p. 1241-1251.

141. Chomoucka, J., et al., *Magnetic nanoparticles and targeted drug delivering.* Pharmacol Res, 2010. **62**(2): p. 144-9.

142. Gaumet, M., et al., *Nanoparticles for drug delivery: The need for precision in reporting particle size parameters.* European Journal of Pharmaceutics and Biopharmaceutics, 2008. **69**(1): p. 1-9.

143. Parveen, S., R. Misra, and S.K. Sahoo, *Nanoparticles: a boon to drug delivery, therapeutics, diagnostics and imaging.* Nanomedicine: Nanotechnology, Biology and Medicine, 2012. **8**(2): p. 147-166.

144. Sun, C., J.S.H. Lee, and M. Zhang, *Magnetic nanoparticles in MR imaging and drug delivery.* Advanced Drug Delivery Reviews, 2008. **60**(11): p. 1252-1265.

145. El-kharrag, R., A. Amin, and Y. Greish, *Synthesis and Characterization of Mesoporous Sodium Dodecyl Sulfate-Coated Magnetite Nanoparticles.* Journal of Ceramic Science and Technology, 2011. **2**(4): p. 203-210.

146. Singh, A. and S.K. Sahoo, *Magnetic nanoparticles: a novel platform for cancer theranostics.* Drug Discov Today, 2014. **19**(4): p. 474-81.

147. Yallapu, M.M., et al., *Multi-functional magnetic nanoparticles for magnetic resonance imaging and cancer therapy.* Biomaterials, 2011. **32**(7): p. 1890-1905.

148. Gupta, A.K. and S. Wells, *Surface-modified superparamagnetic nanoparticles for drug delivery: preparation, characterization, and cytotoxicity studies.* IEEE Trans Nanobioscience, 2004. **3**(1): p. 66-73.

149. Peter, M. and T. Benjamin *Functionalized Magnetite Nanoparticles—Synthesis, Properties, and Bio-Applications*. 2007. **32**, 203–215.

150. de Dios, A.S. and M.E. Díaz-García, *Multifunctional nanoparticles: Analytical prospects.* Analytica Chimica Acta, 2010. **666**(1-2): p. 1-22.

151. Donadel, K., et al., *Synthesis and characterization of the iron oxide magnetic particles coated with chitosan biopolymer*. Materials Science and Engineering: C, 2008. **28**(4): p. 509-514.

152. Mykhaylyk, O., et al., *Glial brain tumor targeting of magnetite nanoparticles in rats.* Journal of Magnetism and Magnetic Materials, 2001. **225**(1-2): p. 241-247.

153. Marie, E., K. Landfester, and M. Antonietti, *Synthesis of chitosan-stabilized polymer dispersions, capsules, and chitosan grafting products via miniemulsion.* Biomacromolecules, 2002. **3**(3): p. 475-81.

154. Dash, M., et al., *Chitosan—A versatile semi-synthetic polymer in biomedical applications.* Progress in Polymer Science, 2011. **36**(8): p. 981-1014.

155. Li, G.-y., et al., *Preparation and properties of magnetic Fe3O4–chitosan nanoparticles.* Journal of Alloys and Compounds, 2008. **466**(1-2): p. 451-456.

156. Zhu, L., et al., *Chitosan-coated magnetic nanoparticles as carriers of 5-fluorouracil: preparation, characterization and cytotoxicity studies.* Colloids Surf B Biointerfaces, 2009. **68**(1): p. 1-6.

157. Tran, H.V., L.D. Tran, and T.N. Nguyen, *Preparation of chitosan/magnetite composite beads and their application for removal of Pb(II) and Ni(II) from aqueous solution.* Materials Science and Engineering: C, 2010. **30**(2): p. 304-310.

158. Boddu, V.M., et al., *Removal of arsenic (III) and arsenic (V) from aqueous medium using chitosan-coated biosorbent.* Water Research, 2008. **42**(3): p. 633-642.

159. Peng, Q., et al., *Biosorption of copper(II) by immobilizing Saccharomyces cerevisiae on the surface of chitosan-coated magnetic nanoparticles from aqueous solution.* Journal of Hazardous Materials, 2010. **177**(1-3): p. 676-682.

160. Feng, B., et al., *Synthesis of monodisperse magnetite nanoparticles via chitosan–poly(acrylic acid) template and their application in MRI.* Journal of Alloys and Compounds, 2009. **473**(1-2): p. 356-362.

161. Tsai, Z.-T., et al., *In situ preparation of high relaxivity iron oxide nanoparticles by coating with chitosan: A potential MRI contrast agent useful for cell tracking.* Journal of Magnetism and Magnetic Materials, 2010. **322**(2): p. 208-213.

162. Shen, C.-R., et al., *Preparation, characterization and application of superparamagnetic iron oxide encapsulated with N-[(2-hydroxy-3-trimethylammonium) propyl] chitosan chloride.* Carbohydrate Polymers, 2011. **84**(2): p. 781-787.

163. Hee Kim, E., et al., *Synthesis of ferrofluid with magnetic nanoparticles by sonochemical method for MRI contrast agent.* Journal of Magnetism and Magnetic Materials, 2005. **289**(0): p. 328-330.

164. Bhatt, A.S., D. Krishna Bhat, and M.S. Santosh, *Electrical and magnetic properties of chitosan-magnetite nanocomposites.* Physica B: Condensed Matter, 2010. **405**(8): p. 2078-2082.

165. Singer, M.M. and R.S. Tjeerdema, *Fate and effects of the surfactant sodium dodecyl sulfate.* Rev Environ Contam Toxicol, 1993. **133**: p. 95-149.

166. Shariati, S., et al., *Fe3O4 magnetic nanoparticles modified with sodium dodecyl sulfate for removal of safranin O dye from aqueous solutions.* Desalination, 2011. **270**(1–3): p. 160-165.

167. Adeli, M., Y. Yamini, and M. Faraji, *Removal of copper, nickel and zinc by sodium dodecyl sulphate coated magnetite nanoparticles from water and wastewater samples.* Arabian Journal of Chemistry, 2012(0).

168. Sadighian, S., et al., *Doxorubicin-conjugated core–shell magnetite nanoparticles as dual-targeting carriers for anticancer drug delivery.* Colloids and Surfaces B: Biointerfaces, 2014. **117**(0): p. 406-413.

169. Sundar, S., R. Mariappan, and S. Piraman, *Synthesis and characterization of amine modified magnetite nanoparticles as carriers of curcumin-anticancer drug.* Powder Technology, 2014. **266**(0): p. 321-328.

170. Mejías, R., et al., *Dimercaptosuccinic acid-coated magnetite nanoparticles for magnetically guided in vivo delivery of interferon gamma for cancer immunotherapy.* Biomaterials, 2011. **32**(11): p. 2938-2952.

171. Pourbaix, M., *Tlas of Electrochemical Equilibria in Aqueous Solutions*, in *Tlas of Electrochemical Equilibria in Aqueous Solutions*. 1974, Houston : NACE International.

172. Cotton, F.A. and G. Wilkinson, *Advanced Inorganic Chemistry*. 1988, New York: Wiley Interscience.

173. Zhang, X.L., et al., *Preparation of a chitosan-coated C(18)-functionalized magnetite nanoparticle sorbent for extraction of phthalate ester compounds from environmental water samples.* Anal Bioanal Chem, 2010. **397**(2): p. 791-8.

174. Lee, J., T. Isobe, and M. Senna, *Preparation of ultrafine Fe3O4 particles by precipitation in the presence of PVA at high pH.* Colloid Interface Science, 1996. **177**: p. 490-494.

175. Nishio, K., et al., *Preparation of size-controlled (30–100nm) magnetite nanoparticles for biomedical applications.* Journal of Magnetism and Magnetic Materials, 2007. **310**(2, Part 3): p. 2408-2410.

176. Nedkov, I., et al., *Surface oxidation, size and shape of nano-sized magnetite obtained by co-precipitation.* Journal of Magnetism and Magnetic Materials, 2006. **300**(2): p. 358-367.

177. Liu, S., et al., *Synthesis and characterization of iron oxide/polymer composite nanoparticles with pendent functional groups.* Colloids and Surfaces B: Biointerfaces, 2006. **51**(2): p. 101-106.

178. Casillas, P.E.G., C.A.R. Gonzalez, and C.A.M. Pérez, *Infrared Spectroscopy of Functionalized Magnetic Nanoparticles*, in *Infrared Spectroscopy of Functionalized Magnetic Nanoparticles*, *Infrared Spectroscopy - Materials Science, Engineering and Technology*, T. Theophile, Editor. 2012, InTech.

179. Rouquerol, F., J. Rouquerol, and K. Sing, *Chapter 7 - Assessment of Mesoporosity*, in *Adsorption by Powders and Porous Solids*, F. Rouquerol, J. Rouquerol, and K. Sing, Editors. 1999, Academic Press: London. p. 191-217.

180. Blum, P., *Magnetic susceptibility*, in *Physical Properties Handbook*. 1997.

181. Si, S., et al., *Size-Controlled Synthesis of Magnetite Nanoparticles in the Presence of Polyelectrolytes.* Chemistry of Materials, 2004. **16**(18): p. 3489-3496.

182. Thapa, D., et al., *Properties of magnetite nanoparticles synthesized through a novel chemical route.* Materials Letters, 2004. **58**: p. 2692–2694.

183. Ma, Z. and H. Liu, *Synthesis and surface modification of magnetic particles for application in biotechnology and biomedicine.* China Particuology, 2007. **5**(1–2): p. 1-10.

184. El-kharrag, R., A. Amin, and Y. Greish, *Low temperature synthesis of monolithic mesoporous magnetite nanoparticles.* Ceramics International, 2012. **38**(1): p. 627-634.

185. Palanisamy, K.L., V. Devabharathi, and N.M. Sundaram, *The Utility of Magnetic Iron Oxide Nanoparticles Stabilized by Carrier Oils in Removal of Heavy Metals from Waste Water* International Journal of Research in Applied, Natural and Social Sciences, 2013. **1**(4): p. 15-22

186. Gupta, A.K. and M. Gupta, *Synthesis and surface engineering of iron oxide nanoparticles for biomedical applications.* Biomaterials, 2005. **26**(18): p. 3995-4021.

187. Ladj, R., et al., *Polymer encapsulation of inorganic nanoparticles for biomedical applications.* International Journal of Pharmaceutics, 2013. **458**(1): p. 230-241.

188. Ling, D., M.J. Hackett, and T. Hyeon, *Surface ligands in synthesis, modification, assembly and biomedical applications of nanoparticles.* Nano Today, 2014. **9**(4): p. 457-477.

189. Xu, C. and S. Sun, *New forms of superparamagnetic nanoparticles for biomedical applications.* Advanced Drug Delivery Reviews, 2013. **65**(5): p. 732-743.

190. Gupta, A.K. and A.S. Curtis, *Surface modified superparamagnetic nanoparticles for drug delivery: interaction studies with human fibroblasts in culture.* J Mater Sci Mater Med, 2004. **15**(4): p. 493-6.

191. Guo, S. and L. Huang, *Nanoparticles containing insoluble drug for cancer therapy.* Biotechnology Advances, 2014. **32**(4): p. 778-788.

192. Dobson, K.D., A.D. Roddick-Lanzilotta, and A.J. McQuillan, *An in situ infrared spectroscopic investigation of adsorption of sodium dodecylsulfate and of cetyltrimethylammonium bromide surfactants to TiO2, ZrO2, Al2O3, and Ta2O5 particle films from aqueous solutions.* Vibrational Spectroscopy, 2000. **24**(2): p. 287-295.

193. Qu, J.-B., et al., *PEG-chitosan-coated iron oxide nanoparticles with high saturated magnetization as carriers of 10-hydroxycamptothecin: Preparation, characterization and cytotoxicity studies.* Colloids and Surfaces B: Biointerfaces, 2013. **102**(0): p. 37-44.

194. Sreeja, V. and P.A. Joy, *Effect of Inter-Particle Interactions on the Magnetic Properties of Magnetite Nanoparticles after Coating with Dextran.* International of Nanotechnology, 2011. **8**(10): p. 907 - 915.

195. Herrera, A.P., et al., *Functionalization of Magnetite (Fe3O4) Nanoparticles for Cancer Treatment* in *Technical Proceedings of the 2006 NSTI Nanotechnology Conference and Trade Show*. 2006, Nano Science and Technology Institute (NSTI) Cambridge, Massachusetts, USA. p. 75 - 78.

196. Juríková, A., et al., *Thermal Analysis of Magnetic Nanoparticles Modied with Dextran*, in *European Conference Physics of Magnetism 2011 (PM'11)*. 2012: Pozna«, . p. 1296-1298

197. Lemarchand, C., R. Gref, and P. Couvreur, *Polysaccharide-decorated nanoparticles.* European Journal of Pharmaceutics and Biopharmaceutics, 2004. **58**(2): p. 327-341.

198. DAR, R.A., et al., *Indirect Electrochemical Analysis of Crocin in Phytochemical Sample.* E-Journal of Chemistry, 2012. **9**(2): p. 918-925.

199. Akbarzadeh, A., et al., *Synthesis, characterization and in vitro studies of doxorubicin-loaded magnetic nanoparticles grafted to smart copolymers on A549 lung cancer cell line.* J Nanobiotechnology, 2012. **10**: p. 46.

200. Rajesh Kumar, S., et al., *Quercetin conjugated superparamagnetic magnetite nanoparticles for in-vitro analysis of breast cancer cell lines for chemotherapy applications.* Journal of Colloid and Interface Science, 2014. **436**(0): p. 234-242.

201. Bertrand, N., et al., *Cancer nanotechnology: The impact of passive and active targeting in the era of modern cancer biology.* Advanced Drug Delivery Reviews, 2014. **66**(0): p. 2-25.

202. Schleich, N., et al., *Comparison of active, passive and magnetic targeting to tumors of multifunctional paclitaxel/SPIO-loaded nanoparticles for tumor* imaging *and therapy.* Journal of Controlled Release, 2014. **194**(0): p. 82-91.

203. Theek, B., et al., *Characterizing EPR-mediated passive drug targeting using contrast-enhanced functional ultrasound imaging.* Journal of Controlled Release, 2014. **182**(0): p. 83-89.

204. Escribano, J., et al., *Crocin, safranal and picrocrocin from saffron (Crocus sativus L.) inhibit the growth of human cancer cells in vitro.* Cancer Lett, 1996. **100**(1-2): p. 23-30.

205. Escribano, J., et al., *Crocin, safranal and picrocrocin from saffron (Crocus sativus L.) inhibit the growth of human cancer cells in vitro.* Cancer Letters, 1996. **100**(1–2): p. 23-30.

206. Noureini, S.K. and M. Wink, *Antiproliferative effects of crocin in HepG2 cells by telomerase inhibition and hTERT down-regulation.* Asian Pac J Cancer Prev, 2012. **13**(5): p. 2305-9.

207. Amin, A., et al., *Defective Autophagosome Formation in p53-Null Colorectal Cancer Reinforces Crocin-Induced Apoptosis.* Int J Mol Sci, 2015. **16**(1): p. 1544-61.

208. Sun, Y., et al., *Crocin Exhibits Antitumor Effects on Human Leukemia HL-60 Cells In Vitro and In Vivo.* Evid Based Complement Alternat Med, 2013. **2013**: p. 690164.

209. Hoshyar, R., S.Z. Bathaie, and M. Sadeghizadeh, *Crocin triggers the apoptosis through increasing the Bax/Bcl-2 ratio and caspase activation in*

human gastric adenocarcinoma, AGS, cells. DNA Cell Biol, 2013. **32**(2): p. 50-7.

210. Sun, J., et al., *Crocin inhibits proliferation and nucleic acid synthesis and induces apoptosis in the human tongue squamous cell carcinoma cell line Tca8113.* Asian Pac J Cancer Prev, 2011. **12**(10): p. 2679-83.

211. Bakshi, H., et al., *DNA fragmentation and cell cycle arrest: a hallmark of apoptosis induced by crocin from kashmiri saffron in a human pancreatic cancer cell line.* Asian Pac J Cancer Prev, 2010. **11**(3): p. 675-9.

212. Villanueva, A., et al., *The influence of surface functionalization on the enhanced internalization of magnetic nanoparticles in cancer cells.* Nanotechnology, 2009. **20**(11): p. 115103.

213. Wu, X., et al., *Toxic effects of iron oxide nanoparticles on human umbilical vein endothelial cells.* Int J Nanomedicine, 2010. **5**: p. 385-99.

214. Mousavi, S.H., et al., *Improvement of cytotoxic and apoptogenic properties of crocin in cancer cell lines by its nanoliposomal form.* Pharmaceutical Biology, 2011. **49**(1): p. 1039–1045.

215. Lee, G.H., K. Nomura, and T. Kitagawa, *Comparative study of diethylnitrosamine-initiated two-stage hepatocarcinogenesis in C3H, C57BL and BALB mice promoted by various hepatopromoters.* Carcinogenesis, 1989. **10**(12): p. 2227-30.

216. Lee, J., S.-J. Lee, and K.-T. Lim, *ZPDC glycoprotein (24 kDa) induces apoptosis and enhances activity of NK cells in N-nitrosodiethylamine-injected Balb/c.* Cellular Immunology, 2014. **289**(1–2): p. 1-6.

217. Schulte-Hermainn, R., T. Mmermanntro, and J. Esncehruppler, *Response of liver foci in rats to hepatic tumor promoters.* Toxticology Pathology, 1982. **10**(2).

218. Rastgoo, M., et al., *Antitumor activity of PEGylated nanoliposomes containing crocin in mice bearing C26 colon carcinoma.* Planta Med, 2013. **79**(6): p. 447-51.

219. Gillet, R., et al., *Effect of Bcl-2 expression on hepatic preneoplasia in mice.* Cancer Letters, 2002. **177**(2): p. 189-195.

220. Lowe, S.W. and A.W. Lin, *Apoptosis in cancer.* Carcinogenesis, 2000. **21**(3): p. 485-95.

221. Newsholme, S.J. and C.J. Fish, *Morphology and incidence of hepatic foci of cellular alteration in Sprague-Dawley rats.* Toxicol Pathol, 1994. **22**(5): p. 524-7.

222. Walsh, K.M. and A. Razmpour, *Stereological evaluation of altered hepatocellular foci in control Wistar rats.* Toxicol Pathol, 1992. **20**(1): p. 27-31.

223. Márquez-Rosado, L., et al., *Celecoxib, a cyclooxygenase-2 inhibitor, prevents induction of liver preneoplastic lesions in rats.* Journal of Hepatology, 2005. **43**(4): p. 653-660.

224. Lacava, L.M., et al., *Long-term retention of dextran-coated magnetite nanoparticles in the liver and spleen.* Journal of Magnetism and Magnetic Materials, 2004. 272–276, **Part 3**(0): p. 2434-2435.

225. Mahmoudi, M., et al., *Cell toxicity of superparamagnetic iron oxide nanoparticles.* J Colloid Interface Sci, 2009. **336**(2): p. 510-8.

226. Thanh, N.T.K. and L.A.W. Green, *Functionalisation of nanoparticles for biomedical applications.* Nano Today, 2010. **5**(3): p. 213-230.

227. Chomoucka, J., et al., *Magnetic nanoparticles and targeted drug delivering.* Pharmacol Res, 2010. **62**(2): p. 144-9.

228. Cohen, Y. and S.Y. Shoushan, *Magnetic nanoparticles-based diagnostics and theranostics.* Current Opinion in Biotechnology, 2013. **24**(4): p. 672-681.

229. Singh, A. and S.K. Sahoo, *Magnetic nanoparticles: a novel platform for cancer theranostics.* Drug Discovery Today, 2014. **19**(4): p. 474-481.

230. Kanapathipillai, M., A. Brock, and D.E. Ingber, *Nanoparticle targeting of anti-cancer drugs that alter intracellular signaling or influence the tumor microenvironment.* Advanced Drug Delivery Reviews, 2014. **79–80**(0): p. 107-118.

231. Sakai, M. and M. Muramatsu, *Regulation of glutathione transferase P: A tumor marker of hepatocarcinogenesis.* Biochemical and Biophysical Research Communications, 2007. **357**(3): p. 575-578.

232. Sato, K., et al., *Specific Expression of Glutathione S-transferase Pi Forms in (Pre)neoplastic Tissues : Their Properties and Functions.* Experimental Medecine, 1992. **168**: p. 97-103.

233. MAUGARD, C.M., et al., *Genetic Polymorphism At The Glutathione S-Tranferase (GST-P) P1 Locus Is A Breast Cancer Risk Modifier.* International Journal of Cancer, 2001. **91**: p. 334–339

234. Sheweita, S.A. and M.H. Mostafa, *N-Nitrosamines and their effects on the level of glutathione, glutathione reductase and glutathione S-transferase activities in the liver of male mice.* Cancer Letters, 1996. **99**(1): p. 29-34.

235. Narumi, K., et al., *Persistence and accumulation of micronucleated hepatocytes in liver of rats after repeated administration of diethylnitrosamine.* Mutation Research/Genetic Toxicology and Environmental Mutagenesis, 2013. **755**(2): p. 100-107.

236. Tessitore, L., *Apoptosis and cell proliferation are involved in the initiation of liver carcinogenesis by a subnecrogenic dose of diethylnitrosamine in refed rats.* J Nutr, 2000. **130**(1): p. 104-10.

237. Colleoni, M., et al., *Evaluation of Ki-67 expression as a prognostic feature in hepatocellular carcinoma in cirrhosis.* Eur J Cancer, 1995. **31A**(9): p. 1547-8.

238. Ng, I.O., et al., *Ki-67 antigen expression in hepatocellular carcinoma using monoclonal antibody MIB1. A comparison with proliferating cell nuclear antigen.* Am J Clin Pathol, 1995. **104**(3): p. 313-8.

239. Scholzen, T. and J. Gerdes, *The Ki-67 protein: from the known and the unknown.* J Cell Physiol, 2000. **182**(3): p. 311-22.

240. Yeh, T.S., T.C. Chen, and M.F. Chen, *Dedifferentiation of human hepatocellular carcinoma up-regulates telomerase and Ki-67 expression.* Arch Surg, 2000. **135**(11): p. 1334-9.

241. Youssef, M.I., et al., *Expression of Ki 67 in hepatocellular carcinoma induced by diethylnitrosamine in mice and its correlation with histopathological alterations.*Journal of Applied Pharmaceutical Science 2012. **2**(3): p. 52-59.

242. Feldmann, G., *Liver apoptosis.* Journal of Hepatology, 1997. **26, Supplement 2**(0): p. 1-11.

243. Pierce, R.H., et al., *Bcl-2 Expression Inhibits Liver Carcinogenesis and Delays the Development of Proliferating Foci.* The American Journal of Pathology, 2002. **160**(5): p. 1555-1560.

244. Schulte-Hermann, R., B. Grasl-Kraupp, and W. Bursch, *7 - Apoptosis and hepatocarcinogenesis*, in *Liver Regeneration and Carcinogenesis*, R.L. Jirtle, Editor. 1995, Academic Press: San Diego. p. 141-178.

245. Schwarz, M., A. Buchmann, and K.-W. Bock, *Role of cell proliferation at early stages of hepatocarcinogenesis.* Toxicology Letters, 1995. **82–83**(0): p. 27-32.

246. Schulte-hermann, R., et al., *Role of active cell death (apoptosis) in multi-stage carcinogenesis.* Toxicology Letters, 1995. **82–83**(0): p. 143-148.

247. Feldstein, A.E., et al., *Cytokeratin-18 fragment levels as noninvasive biomarkers for nonalcoholic steatohepatitis: a multicenter validation study.* Hepatology, 2009. **50**(4): p. 1072-8.

248. Yilmaz, Y., A.E. Kedrah, and O. Ozdogan, *Cytokeratin-18 fragments and biomarkers of the metabolic syndrome in nonalcoholic steatohepatitis.* World J Gastroenterol, 2009. **15**(35): p. 4387-91.

249. DIAPHARMA. *APOPTOSISKITS - M30 APOPTOSENSE® ELISA*. 2013 [cited 2015; Available from: http://www.diapharma.com/asp/index.asp.

250. Christensen, J.G., et al., *Altered bcl-2 family expression during non-genotoxic hepatocarcinogenesis in mice.* Carcinogenesis, 1999. **20**(8): p. 1583-90.

251. Lee, G.H., *Correlation between Bcl-2 expression and histopathology in diethylnitrosamine-induced mouse hepatocellular tumors.* Am J Pathol, 1997. **151**(4): p. 957-61.

252. Millan, M.T., et al., *Epstein-Barr virus infection is associated with endothelial Bcl-2 expression in transplant liver allografts.* Transplantation, 2002. **73**(3): p. 465-9.

253. Szauter, P. *Cancer Genetics*. 2013 [cited 2015; Available from: http://www.discoveryandinnovation.com/BIOL202/notes/lecture20.html.

254. Bishayee, A. and N. Dhir, *Resveratrol-mediated chemoprevention of diethylnitrosamine-initiated hepatocarcinogenesis: Inhibition of cell proliferation and induction of apoptosis.* Chemico-Biological Interactions, 2009. **179**(2–3): p. 131-144.

255. Chi-Man Tang, T., R. Tung-Ping Poon, and S.T. Fan, *The significance of cyclooxygenase-2 expression in human hepatocellular carcinoma.* Biomedicine & Pharmacotherapy, 2005. **59, Supplement 2**(0): p. S311-S316.

256. Wu, T., *Cyclooxygenase-2 in hepatocellular carcinoma.* Cancer Treatment Reviews, 2006. **32**(1): p. 28-44.

257. Sivaramakrishnan, V. and S. Niranjali Devaraj, *Morin regulates the expression of NF-κB-p65, COX-2 and matrix metalloproteinases in diethylnitrosamine induced rat hepatocellular carcinoma.* Chemico-Biological Interactions, 2009. **180**(3): p. 353-359.

258. Gately, S. and W.W. Li, *Multiple roles of COX-2 in tumor angiogenesis: a target for antiangiogenic therapy.* Seminars in Oncology, 2004. **31, Supplement 7**(0): p. 2-11.

259. Kawabata, K., et al., *Dietary Crocin Inhibits Colitis and Colitis-Associated Colorectal Carcinogenesis in Male ICR Mice.* Evid Based Complement Alternat Med, 2012. **2012**: p. 820415.

260. Aucejo, F., et al., *Vascular endothelial growth factor receptor 2 expression in non-tumorous cirrhotic liver is higher when hepatoma is beyond Milan criteria.* Liver Transpl, 2009. **15**(2): p. 169-76.

261. Liu, J.-G., et al., *Effect of selenium-enriched malt on VEGF and several relevant angiogenic cytokines in diethylnitrosamine-induced hepatocarcinoma rats.* Journal of Trace Elements in Medicine and Biology, 2010. **24**(1): p. 52-57.

262. Otrock, Z.K., et al., *Is VEGF a predictive biomarker to anti-angiogenic therapy?* Critical Reviews in Oncology/Hematology, 2011. **79**(2): p. 103-111.

263. Taniguchi, E., et al., *Expression and role of vascular endothelial growth factor in liver regeneration after partial hepatectomy in rats.* J Histochem Cytochem, 2001. **49**(1): p. 121-30.

264. Yoshiji, H., et al., *Suppression of renin-angiotensin system attenuates hepatocarcinogenesis via angiogenesis inhibition in rats.* Anticancer Res, 2005. **25**(5): p. 3335-40.

265. Wang, Z., et al., *Broad targeting of angiogenesis for cancer prevention and therapy.* Semin Cancer Biol, 2015.

266. Folkman, J., *Tumor angiogenesis: therapeutic implications.* N Engl J Med, 1971. **285**(21): p. 1182-6.

267. Umigai, N., et al., *Crocetin, a carotenoid derivative, inhibits VEGF-induced angiogenesis via suppression of p38 phosphorylation.* Curr Neurovasc Res, 2012. **9**(2): p. 102-9.

268. Bertrand, N., et al., *Cancer nanotechnology: the impact of passive and active targeting in the era of modern cancer biology.* Adv Drug Deliv Rev, 2014. **66**: p. 2-25.

269. Osaka, T., et al., *Effect of surface charge of magnetite nanoparticles on their internalization into breast cancer and umbilical vein endothelial cells.* Colloids and Surfaces B: Biointerfaces, 2009. **71**(2): p. 325-330.

270. Takami, T. and I. Sakaida, *Iron regulation by hepatocytes and free radicals.* J Clin Biochem Nutr, 2011. **48**(2): p. 103-6.

271. Labs, P.E. *A Review Article On Nanoparticle*. 2015 [cited 2015; Available from:http://www.pharmatutor.org/articles/review-article-nanoparticle.

272. Sabella, S., et al., *A general mechanism for intracellular toxicity of metal-containing nanoparticles.* Nanoscale, 2014. **6**(12): p. 7052-61.

273. Ochiai, T., et al., *Crocin prevents the death of rat pheochromyctoma (PC-12) cells by its antioxidant effects stronger than those of α-tocopherol.* Neuroscience Letters, 2004. **362**(1): p. 61-64.

274. Qi, Y., et al., *Crocin prevents retinal ischaemia/reperfusion injury-induced apoptosis in retinal ganglion cells through the PI3K/AKT signalling pathway.* Experimental Eye Research, 2013. **107**(0): p. 44-51.

275. Niranjana, R., et al., *Carotenoids modulate the hallmarks of cancer cells.* Journal of Functional Foods, 2014(0).

276. Tamaddonfard, E., et al., *Comparison of the effects of crocin, safranal and diclofenac on local inflammation and inflammatory pain responses induced by carrageenan in rats.* Pharmacological Reports, 2013. **65**(5): p. 1272-1280.

List of Publications

Rkia El-kharrag, Amr Amin, Yasser Greish (2011). Synthesis and Characterization of Mesoporous Sodium Dodecyl Sulfate-coated Magnetite Nanoparticles. Journal of Ceramic Science and Technology 2(4): 203-210.

Rkia El-kharrag, Amr Amin, Yasser Greish (2012). Low Temperature Synthesis of Monolithic Magnetite Nanoparticles. Journal of Ceramics International 38(1): 627-634.